Project No. 12-3660

Development and Experimental Benchmark of Simulations to Predict Used Nuclear Fuel Cladding Temperatures during Drying and Transfer Operations

Fuel Cycle Research and Development

Miles Greiner
University of Nevada, Reno

John Orchard, Federal POC
Brady Hanson, Technical POC

NEUP Nuclear Energy University Programs
U.S. Department of Energy

FINAL REPORT

Project Title: Development and Experimental Benchmark of Simulations to Predict Used Nuclear Fuel Cladding Temperatures during Drying and Transfer Operations, CFP 12-3660

Technical Work Scope: FC-4 Used Nuclear Fuel Disposition

Covering Period: Sep 15, 2012 through Dec 30, 2016, Years 1-4

Date of Report: Mar 31, 2017

Recipient: University of Nevada, Reno
1664 N. Virginia Street
Reno, NV 89557

Award Number: 00127534

Principal Investigator: Miles Greiner, (775) 784-4873, greiner@unr.edu

Project Period: September 15, 2012 through December 30, 2016

Project Objective: Radial hydride formation in high-burnup used fuel cladding has the potential to radically reduce its ductility and suitability for long-term storage and eventual transport. To avoid this formation, the maximum post-reactor temperature must remain sufficiently low to limit the cladding hoop stress, and so that hydrogen from the existing circumferential hydrides will not dissolve and become available to re-precipitate into radial hydrides under the slow cooling conditions during drying, transfer and early dry-cask storage. The objective of this research is to develop and experimentally-benchmark computational fluid dynamics simulations of heat transfer in post-pool-storage drying operations, when high-burnup fuel cladding is likely to experience its highest temperature. These benchmarked tools can play a key role in evaluating dry cask storage systems for extended storage of high-burnup fuels and post-storage transportation, including fuel retrievability. The benchmarked tools will be used to aid the design of efficient drying processes, as well as estimate variations of surface temperatures as a means of inferring helium integrity inside the canister or cask. This work will be conducted effectively because the principal investigator has experience developing these types of simulations, and has constructed a test facility that can be used to benchmark them.

1. Project Objectives

The objective of this work is to develop and experimentally-benchmark computational methods to accurately predict used nuclear fuel cladding temperatures during vacuum drying operation. This operation is used to remove moisture from used fuel before it is sealed in gas-filled canisters that are used for storage or transport. At low pressures (rarefied gas) associated with vacuum drying, there is a thermal resistance that develops at the interfaces between the surface and gas interacting with it. This resistance causes a temperature jump at these interfaces, which significantly contributes to the increase of used fuel temperature during vacuum drying. Vendors do not include this low pressure effect in the estimation of peak cladding temperature.

This project was structured to investigate the effect of temperature-jump on the cladding temperature at low pressure during vacuum drying. Experimental and numerical investigations were carried out.

The numerical investigation was carried out using three different computational modeling techniques that were developed to calculate transport across rarefied gas that exists in vacuum drying. First, Discrete Velocity Method (DVM) and Direct Simulation Monte Carlo (DSMC) techniques, which solve the Boltzmann kinetic equation, were used to calculate heat transfer between parallel plates and concentric cylinders (simple geometries). The results from these two techniques were compared to ANSYS/FLUENT simulations with temperature-jump model. Different jump models were tested and it was determined that the Lin & Willis model accurately predicts the heat transfer in moderately rarefied gas. More complex geometry simulations (8×8 array of heated rods) were also carried out using DSMC and results were compared to ANSYS/FLUENT to assess the accuracy of Lin & Willis model. This model was then applied to the simulation of vacuum drying in a nuclear fuel canister. A geometrically-accurate three-dimensional (3D) model of a nuclear canister that represents most of the canister components was constructed. Simulations were run for different heat loads, pressure gases, and accommodation coefficients (characterizes the temperature jump effect).

The experimental investigation was carried out through the construction of two experimental setups that were used to measure heat transfer across rarefied gas. The first experiment consisted of an isothermal heated cylinder centered within a temperature-controlled cylindrical enclosure. The cylinder temperatures were measured for a range of heat generation rates, gas pressures, and enclosure temperatures. These results were used to benchmark computational predictions within a “simple” geometry. The second experiment consisted of a square 7×7 array of heated rods within a square enclosure. This geometry is relevant to a used nuclear fuel assembly within a canister’s support basket structure. Rod temperatures were measured for a range of heat generation rates and gas pressures. The results are used to benchmark ANSYS/FLUENT simulations in this “complex” geometry.

2. Summary of Four Years of Activities

2.1 Publications and Presentations

2.1.1 Published or Accepted Journal Papers

A list of journal papers published during the four years of the project are presented below. Copies of these publications are presented in appendix A.

1- Hadj-Nacer, M., Manzo, T., Ho, M. T., Graur, I. and Greiner, M., 2016 “Effects of Gas Rarefaction on Used Nuclear Fuel Cladding Temperatures during Vacuum Drying”. *Nuclear Technology* Journal, Vol: 3, n: 194, pp: 387-399.
2- Hadj-Nacer, M., Maharjan, D., Ho, M.T., Stefanov, S.K., Graur, I., and Greiner, M., 2017 “Continuum and kinetic simulations of Heat Transfer trough Rarefied Gas in Annular and Planar Geometries in the Slip Regime”. J. Heat Transfer 139(4), 042002.
3- Maharjan, D., Hadj-Nacer, M., Chalasani, N., and Greiner, M., “Experimental Validation of Heat Transfer Simulations for a Vertical Heated Rod Array within a Square-Cross-Section, Helium-Filled Isothermal Enclosure,” ASME Journal of Thermal Science and Engineering Applications (accepted).

2.1.2 Publications in Peer-Reviewed Conferences

A list of papers presented in peer-reviewed conferences is given below. Copies of these papers are presented in Appendix B.

1- Green, R. Manzo, E. T., Greiner, M., Li, J., and Liu, Y. Y., “Experimental Benchmark of Simulations that Predict Temperatures of an 8x8 Array of Heater Rods within a Vessel Filled with Rarefied Helium Gas,” Proceedings of the 17th International Symposium on the Packaging and Transportation of Radioactive Materials, Aug 18-23, 2013, San Francisco, CA.
2- Green, R., Manzo, E. T., Hadj-Nacer, M., and Greiner, M., “Design of an experimental apparatus to measure the thermal accommodation coefficient between stainless steel surfaces and rarefied helium,” Proceedings of the ASME 2014 Pressure Vessels & Piping Conference, July 20-24, 2014, Anaheim, CA.
3- Manzo, E. T., Green, R., Hadj-Nacer, M., Greiner, M., Li, J., and Liu, Y. Y., “Prediction of Cladding Temperature within a Used Nuclear Fuel Transfer Cask Filled with Rarefied Helium,” Proceedings of the ASME 2014 Pressure Vessels & Piping Conference, July 20-24, 2014, Anaheim, CA.
4- Hadj-Nacer, M., Manzo, T., Ho, M. T., Graur, I. and Greiner, M, “Phenomena Affecting Used Nuclear Fuel Cladding Temperatures during Vacuum Drying Operations,” International High-Level Radioactive Waste Management Conference, April 12-16, 2015, Charleston, SC.
5- Green, R., Hadj-Nacer, M., and Greiner, M., “Design of an Experiment to Measure the Thermal Accommodation Coefficient Between Helium and Stainless-Steel in Concentric Cylinders,” Proceedings of the ASME 2015 Pressure Vessels & Piping Conference, July 19-23, 2015, Boston, MA.
6- Manzo, E. T., Hadj-Nacer, M., and Greiner, M., “Geometrically-Accurate Three-Dimensional Simulations of a Used Nuclear Fuel Canister Filled with Helium,” Proceedings of the ASME 2015 Pressure Vessels & Piping Conference, July 19-23, 2015, Boston, MA.
7- Maharjan, D., Hadj-Nacer M., Chalasani, N. R., and Greiner, M., “Experimentally-Benchmarked Computational Fluid Dynamics Simulations of an Array of Heated Rods within a Square-Cross-Section Helium-Filled Pressure Vessel”, 2016 ASME Pressure Vessel and Piping Conference, July 17-21, 2016, Vancouver, BC, Canada.

8- Trujillo, C., Hadj-Nacer M., and Greiner, M., "Effect of Rarefication on Cladding Temperatures within a Used Nuclear Fuel Canister Filled with Dry Helium," International High-Level Radioactive Waste Management Conference, April 9-13, 2017, Charlotte, NC.
9- Maharjan, D., Hadj-Nacer M., and Greiner, M., "Temperature Measurement of an Array of Heated Rods Subjected to Vacuum Drying Conditions," Proceedings of the ASME 2017 Pressure Vessels & Piping Division Conference, July 16-20, 2017, Waikoloa Village, HI.
10- Maharjan, D., Hadj-Nacer M., and Greiner, M., "Experimentally Benchmarked Computational Fluid Dynamics Simulations of a 7×7 Array of Heated Rods within a Square-Cross-Section Enclosure Filled with Rarefied Helium," Proceedings of the ASME 2017 Pressure Vessels & Piping Division Conference, July 16-20, 2017, Waikoloa Village, HI.

2.1.3 Conference/Meeting Presentations

1- Maharjan, D., Hadj-Nacer M., and Greiner, M., "Benchmarking FLUENT for Determining Cladding Temperature of UNF During Vacuum Drying using Experimental Approach," 2016 American Nuclear Society (ANS) Winter Meeting and Nuclear Technology Expo, November 6-10, 2016, Las Vegas, NV.

2.2 Personnel

Funding for this project began on September 15, 2012. This was too late to recruit and hire appropriate graduate research assistants for this project during the 2012-13 academic year. Two senior undergraduate mechanical engineering students, Ms. Rachel Green and Mr. E. Triton Manzo were hired. These students were highly productive, completed their bachelor's degrees in May 2013, and continued working on this project as MS students. They were awarded UNR Graduate Fellowships for Materials and Thermal Science for Nuclear Energy (funded by the US Nuclear Regulatory Commission), and hence were not paid by the NEUP grant. Ms. Green's and Mr. Manzo's fellowships ended in May 2015. They were paid from the grant for the months of June and July 2015 to finish their work. Ms. Rachel Green defended her thesis on September 20, 2015 and she accepted a job at the Lawrence Livermore National Laboratory as Mechanical Engineer. The graduate research assistant funds for this work was used to hire additional students, and/or for different purposes.

Mr. Dilesh Maharjan joined this program in January 2014 as a Ph.D. student and was paid by this grant. MS student, Mr. Hasibul MD Alam, joined this program in August 2014, was paid by this grant, and successfully defended his MS thesis in January 25, 2015. MS student, Mr. Corey Trujillo, joined this program in August 2015 and was paid by this grant until August 2016. Senior undergraduate student Joseph Young joined this project in December 2015, and performed an unpaid special project. Mr. Musnicki joined this program from January to May 2016 and was paid from this grant.

Dr. Paul Laca worked on this project as a post-doctoral research associate from November 1, 2012 to February 28, 2013. Dr. Mustafa Hadj Nacer began work as a postdoctoral research associate in December 2013. He has helped to accelerate the pace of the computational and experimental work. He was promoted to Research

Scientist on October 1, 2014. In 2012 Dr. Hadj Nacer completed the Ph.D. dissertation entitled "Tangential Momentum Accommodation Coefficient in Microchannels with Different Surface Materials (measurements and simulations)," under the supervision of Prof. Irina Graur, Marseille University.

2.3 External Collaborations

We collaborated with our Argonne National Laboratory partners, Dr. Jie Li and Dr. Yung Y. Liu.

We collaborated with Professor Stefan Kanchev Stefanov from the Department of Mathematical Modeling and Numerical Simulations at the Bulgarian Academy of Sciences, Institute of Mechanics. He developed Direct Simulation Monte Carlo (DSMC) calculations for predicting heat transfer in rarefied gases within simple and complex geometries. He also developed a two-dimensional DSMC code for predicting heat transfer in a 7x7 arrays of heating rods within a square, stainless-steel enclosure.

We also collaborated with Prof. Irina Graur and her former student Dr. Minh-Tuan Ho from Marseille University, who have helped us to perform rarefied gas heat transfer calculations using the Discrete Velocity Method (DVM) in concentric cylinders and parallel plate configurations.

2.4 Student Work

In this section, a summary of the students' work during the period of the project is presented.

2.4.1 *Mr. E. Triton Manzo*

Year 1: Mr. Manzo joined the project as a senior undergraduate student in October 2012. He completed his bachelor's degree in May 2013. He then spent May to July 2013 interning at Transnuclear/AREVA in Columbia, Maryland. He learned how that company predicts cladding temperatures during vacuum drying, and introduced to its technical staff methods for including the effects of gas rarefaction. He constructed three, two-dimensional cross-section models of a transfer package loaded with used fuel. All three models represent one quarter of the cross section by taking advantage of the package's symmetry. The first package model uses a homogenized model for the fuel regions (that homogenized model was developed by Transnuclear/AREVA). The second uses a geometrically-accurate fuel region model that Mr. Manzo developed, and has distinct regions for the fuel pellets, cladding and helium gas. The third is also a geometrically-accurate model, but it includes the effect of gas rarefaction. Mr. Manzo visited Transnuclear's spent fuel drying training facility to observe the methods used to dry fuel canisters. He gave a presentation to Transnuclear/AREVA technical staff on his work at the end of July 2013, and then returned to UNR.

Figure 1 shows two views of a NUHOMS 24 PTH canister designed to contain 24 used pressurized-water-reactor (PWR) nuclear fuel assemblies. Figure 2 shows two, two-dimensional models of one-quarter of its cross section. Both include the canister shell, support basket structure, and six openings that contain used fuel assemblies. Figure 2a

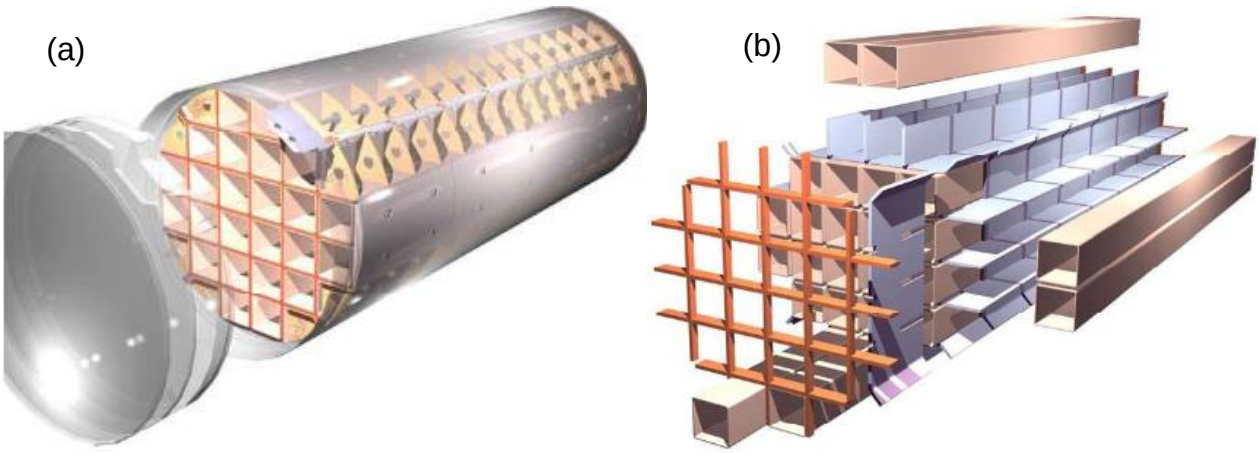

Figure 1: (a) A 3D view of the canister modeled, with the shell and (b) an exploded view without the shell

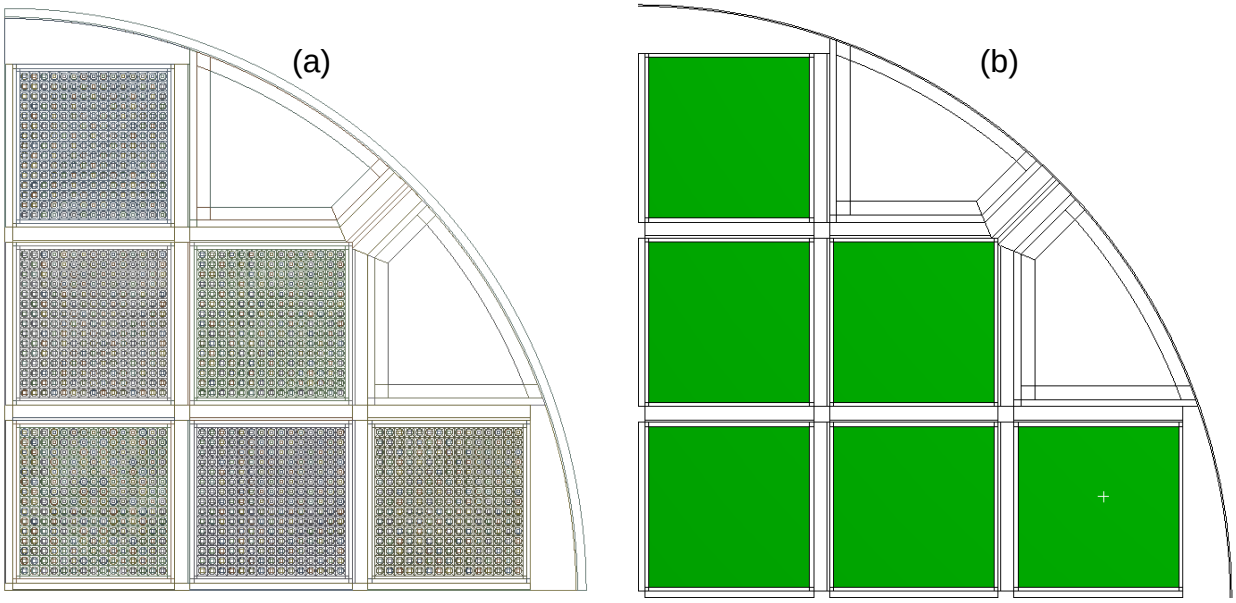

Figure 2: (a) Geometrically accurate model built using the dimensions and materials from the vender's model, (b) A uniform thermal conductivity is applied to the fuel assembly area.

includes geometrically-accurate models of B&W Mark B-2 15x15 used assemblies in each basket opening. The model includes separate regions for the fuel pellets, cladding and helium gas. The fuel pellet, cladding and spacing dimensions are included in Fig. 3. The material properties used in this model were provided by the vendor. In Fig. 2b, a solid region is used in each fuel assembly region. This region is associated with a temperature-dependent effective conductivity that is designed to include the effects of conduction and radiation heat transfer in the fuel regions. This effective conductivity was determined by Transnuclear/AREVA.

Simulations were performed in which each fuel assembly generated 1.7 kW of decay heat. Figures 4a and 4b shows temperature contours from the geometrically-accurate

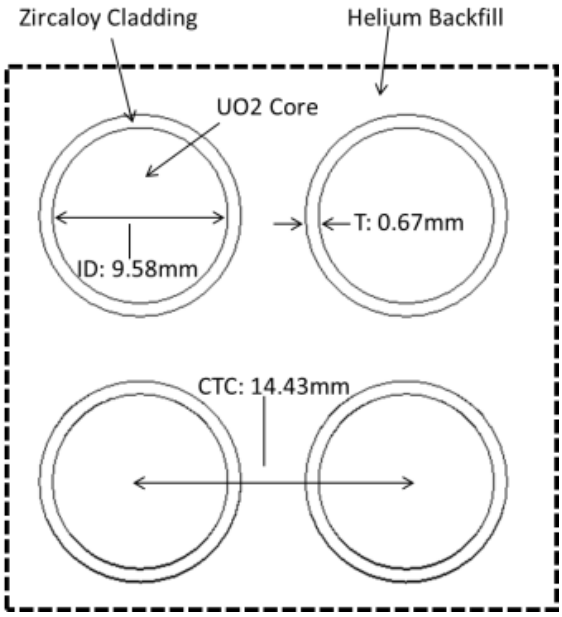

Figure 3: Dimensions of the fuel assembly.

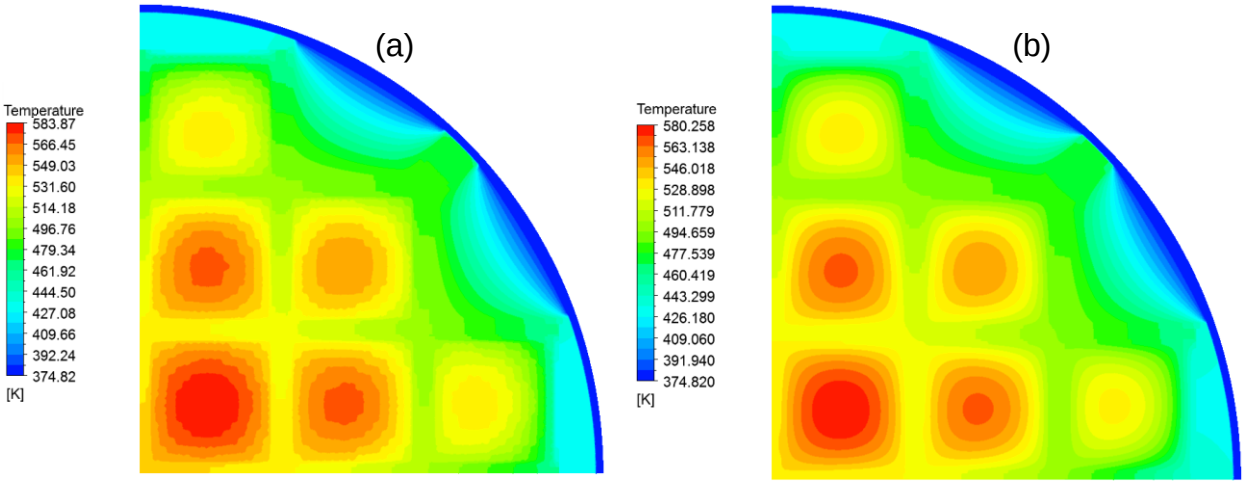

Figure 4: (a) Geometrically accurate model with a maximum temperature of 583.9 K, (b) Homogenized model with a maximum temperature of 580.3 K.

and homogenized-fuel-region models, respectively. The temperature contours from the geometrically accurate model are significantly less smooth than those from the homogenized model. The maximum temperatures in both models are in the fuel region nearest to the package center. The peak fuel temperature from the geometrically-accurate model is 3.6°C hotter than it is from the homogenized model.

A low-pressure simulation was performed using the geometrically-accurate model by implementing a thermal resistance at the interfaces between the solid and gas regions. This thermal resistance is a utility within the ANSYS/FLUENT code, and models the effect of a temperature discontinuity or jump at these interfaces that is present in moderately

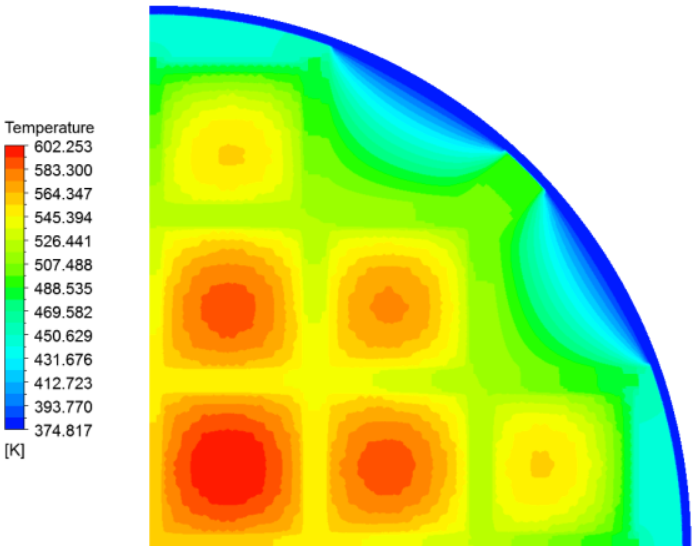

Figure 5: Low pressure temperature slip condition applied to the geometrically accurate model. The maximum temperature is 602.3 K.

rarefied gases at low pressures. In this work, the temperature-jump was calculated for a gas pressure of 200 Pa, a thermal accommodation coefficient of 0.4, and a Lenard-Jones collision diameter of 3.733 Angstroms. The temperature contour from this low pressure simulation is shown in Fig. 5. The maximum temperature in the fuel region closest to the package center is 18.4 K hotter than the maximum for the atmospheric pressure simulation (Fig. 4b).

Figure 6 shows a portion of the geometrically accurate model with an x-axis drawn though three of the fuel-assembly regions. Figure 7 shows temperature profiles along that axis from the three simulations described in this section. The result from the homogenized geometry simulation exhibits a smooth profile in the fuel regions. In the outer shell of the canister and the space between the shell and the basket walls, the geometrically-accurate model gives roughly the same temperature profile as the homogenized model results. However, in the fuel regions, the geometrically-accurate model results exhibit a stair step shape, and as mentioned before a higher peak fuel temperature. The temperature jump model gives the same temperature as the other two simulations in the canister shell, but is hotter starting at the helium gap next to the shell surface.

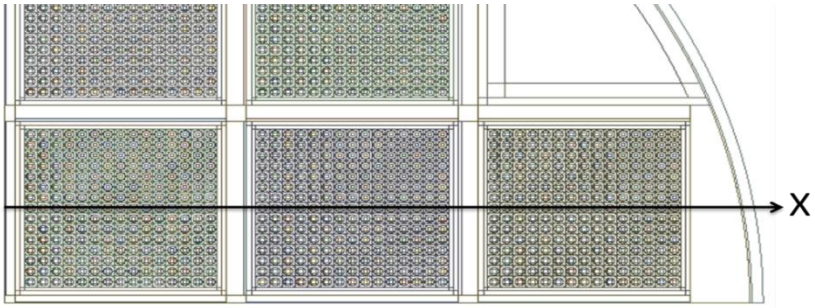

Figure 6: A line drawn across the bottom middle fuel assemblies.

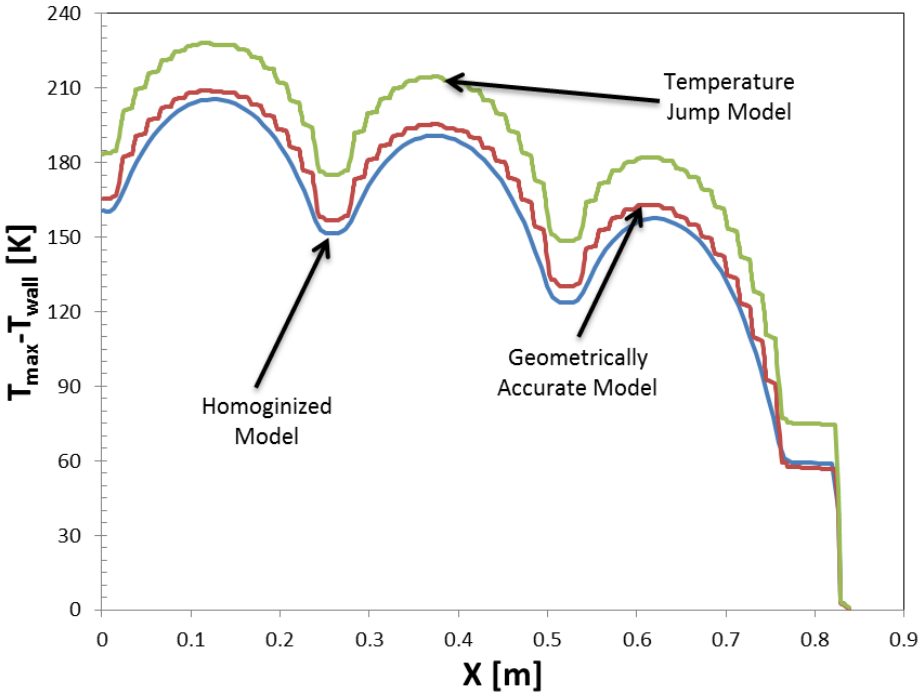

Figure 7: T_{max}- T_{wall} plotted for three different cases against location

<u>Year 2</u>: In the second year of the project, Mr. Manzo constructed a three-dimensional ANSYS/FLUENT model of a one-eighth used nuclear fuel canister. The total number of the elements for this model were roughly 35 million. This number of elements cannot be supported by a quad-cores computer to run ANSYS/FLUENT simulations. Therefore, a request for acquisition of a new high performance computer (12 cores) was submitted and approved by NEUP. The new computer allowed Mr. Manzo to complete his model meshing and to run simulations in reasonable time.

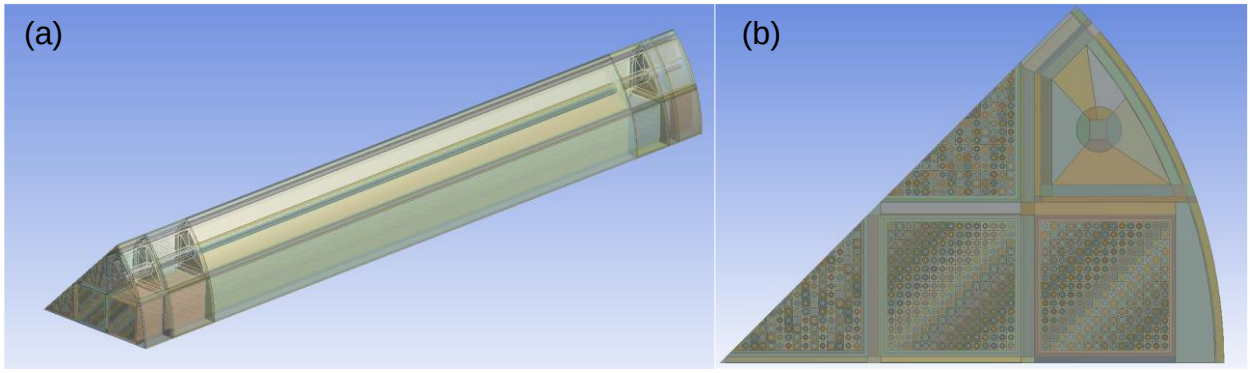

Figure 8: Three-dimensional model of one-eighth of a transfer cask used to calculate temperatures during forced helium dehydration drying operations. (a) Isometric view, (b) cross-section view.

Figure 8a and 8b show isometric and cross-section views of the three-dimensional model that was used to calculate temperature within the package when it is filled with helium or nitrogen at atmospheric and higher pressures. It was also used to calculate enhanced heat transfer caused by turbulation, due to helium injection during forced helium dehydration. The model takes advantage of the canister symmetry, so only one eighth of the canister's cross-section is modeled. The domain shown in Figs. 8a and 8b includes a square array of 15x15 fuel rods within each basket opening, with an UO_2 core surrounded by a Zircaloy cladding. The fuel rod assemblies are centered inside the stainless steel basket openings. The stainless steel basket rests inside aluminum supports along with the neutron poison. The neutron poison is placed in selected locations inside the aluminum support structure.

During this period, Mr. Manzo also conducted two-dimensional ANSYS/FLUENT simulations of a transfer cask with water vapor and helium mixtures at different fractions under atmospheric pressure. Simulations for air and helium under atmospheric and rarefied conditions were also performed.

Data on heat transfer through rarefied gas enclosed between parallel plates and concentric cylinders using DVM (Discrete Velocity Method) were provided by Professor Irina Graur. A comparison with the ANSYS/FLUENT model was performed to assess the Willis temperature jump model which was implemented in ANSYS/FLUENT. The Willis model for temperature jump was found to be more accurate than other models found in the literature. This model was used in the two-dimensional simulations of a transfer cask. Results from this comparison were published in one journal and two conference papers. The references for these papers are given below and copies of these papers are included in Appendices A and B, respectively.

- Hadj-Nacer, M., Manzo, T., Ho, M. T., Graur, I. and Greiner, M., 2016, "Effects of Gas Rarefaction on Used Nuclear Fuel Cladding Temperatures during Vacuum Drying". *Nuclear Technology* Journal, Vol: 3, n: 194, pp: 387-399.
- Manzo, E. T., Green, R., Hadj-Nacer, M., Greiner, M., Li, J., and Liu, Y. Y., "Prediction of Cladding Temperature within a Used Nuclear Fuel Transfer Cask Filled with Rarefied Helium," Proceedings of the ASME 2014 Pressure Vessels & Piping Conference, July 20-24, 2014, Anaheim, CA.
- Hadj-Nacer, M., Manzo, T., Ho, M. T., Graur, I. and Greiner, M, "Phenomena Affecting Used Nuclear Fuel Cladding Temperatures during Vacuum Drying Operations," International High-Level Radioactive Waste Management Conference, April 12-16, 2015, Charleston, SC.

Year 3: During this year, Mr. Manzo completed the construction of the three-dimensional-geometrically-accurate ANSYS/FLUENT model of one-eighth of a spent nuclear fuel canister. He performed mesh sensitivity along the radial direction, which allowed him to reduce the total number of elements. The reduced number of elements allowed us to speed up the simulations and also to increase the number of elements in the axial direction. Mr. Manzo also succeeded in increasing the mesh quality of the 3D model from an orthogonal quality of 0.05 to 0.61. This is on a scale from 0 to 1, with 1 being the best quality.

Simulations using this model were run for forced helium dehydration conditions, including natural convection and stagnant gas (pure conduction) heat transfer. A pressure of 1 atm was considered for the simulations, which is below the actual pressure employed during forced helium dehydration (P ~ 5 atm). Results from this study were published in the 2015 PVP Conference. A copy of this paper is included in Appendix B and the reference is given below:

- Manzo, E. T., Hadj-Nacer, M., and Greiner, M., "Geometrically-Accurate Three-Dimensional Simulations of a Used Nuclear Fuel Canister Filled with Helium," Proceedings of the ASME 2015 Pressure Vessels & Piping Conference, July 19-23, 2015, Boston, MA.

Mr. Manzo also performed some comparisons between the results of the 2D and 3D models of the nuclear canister in order to assess on the accuracy of the 3D model simulations. 3D simulations of the canister with insulated ends were compared to 2D model simulations. Both models should have given essentially the same results. However the results of temperature from the 2D model were off by few degrees compared to the 3D model. Other tests on smaller models were performed to understand the reasons for such discrepancy. This work was continued by Mr. Corey Trujillo.

Mr. Manzo finished his appointment at the University of Nevada Reno in July 2015. Currently he is working as a Mechanical Engineer at the Newmont Mining Corp, Winnemucca, NV. He hasn't defended his Ms. Thesis yet.

2.4.2 Ms. Rachel Green

Year 1: Ms. Rachel Green joined the project in October 2012 as a senior undergraduate student. She completed her bachelor's degree in May 2013 and started working as graduate student on the project. Ms. Green's task was mainly experimental.

An experimental facility, consisting of an 8x8 square array of heater rods within a square-cross section aluminum pressure vessel, was constructed for earlier DOE-funded research, and was proposed for use in the current project. As described in earlier reports, experiments were performed using the same heat generation rate and external conditions as those used when the original experiments were performed. However, the new experiments gave rod temperatures that were lower than those previously observed.

Dr. N.R Chalasani, who constructed the apparatus and performed the original measurements for his Ph.D. dissertation, returned to UNR to help understand the problem. However, he was not able to recreate conditions to repeat his earlier results. Graduate student Rachel Green then disassembled the enclosure and determined that some of the heater and thermocouple wires were no longer properly connected. Figure 9 shows the heater rods removed from the pressure vessel. The foreground of that photo shows that some of the wiring nuts used to connect heaters in series had come off of the power cables. This may have occurred when the pressure vessel seal was being repaired after the original data had been acquired.

The above described experiment was no longer useful for the purpose of the project. A new experimental apparatus was designed. This apparatus can be used to benchmark CFD simulations of the heated rod array for a range of helium gas pressures. However,

these simulations require values of the thermal accommodation coefficient at the interfaces between the gas and solid surface. A literature review of the methods used to predict and/or measure this coefficient for the heat and enclosure materials was conducted.

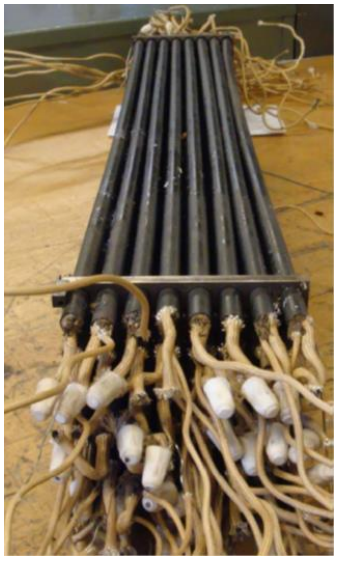

Figure 9: Square 8x8 array of heater rods, held by two spacer plates, removed from its pressure vessel. Heater power cables and thermocouple lead wires are seen in the foreground.

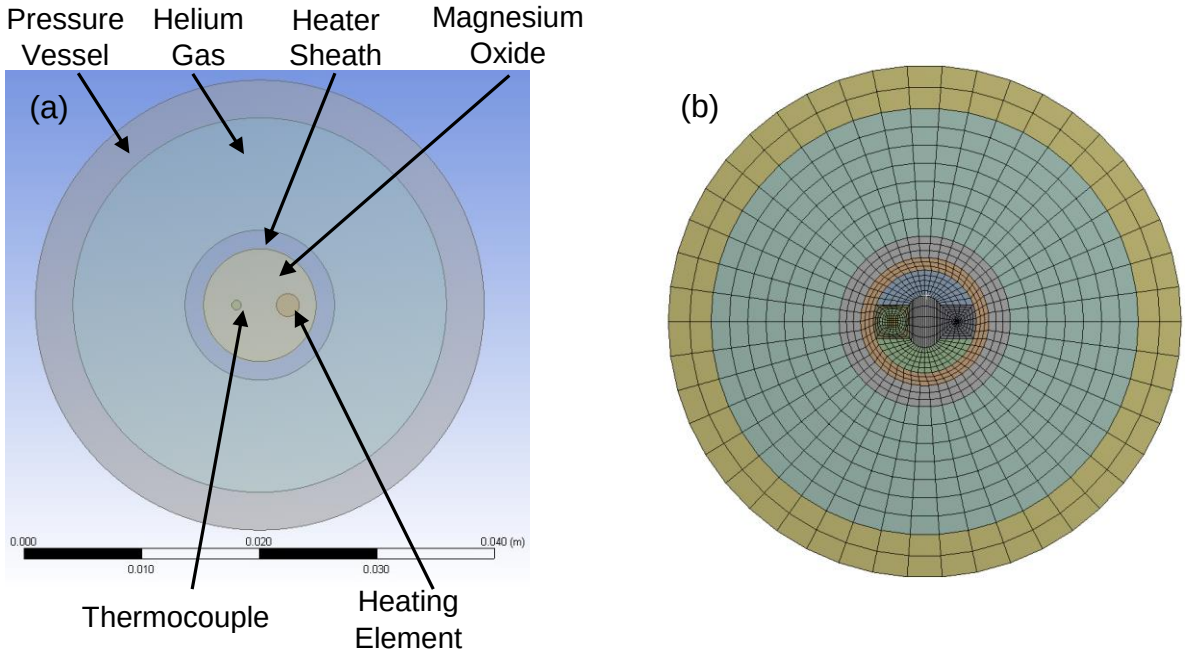

Figure 10: Two-dimensional cross section ANSYS/Fluent model of a single heater centered within a helium-filled pressure vessel. (a) Model regions. (b) Computational Mesh

Ms. Green also performed simulations to help design a simple concentric cylinder experiment in which a single heater rod is centered within a cylindrical pressure vessel containing low pressure helium. This experiment was used to measure heat transfer between concentric cylinders under rarefaction conditions and to determine the thermal accommodation coefficient for helium on stainless steel surface. Figure 10a shows a two-dimensional ANSYS/FLUENT model of the apparatus cross section, and Fig. 10b shows the associated computational mesh. The model includes the pressure vessel, helium gas, and heater sheath and magnesium oxide within the heater, and the heating element and thermocouple within the heater rod.

Simulations using this model were performed to determine the thermocouple temperature versus helium pressure for a range of heater power levels and enclosure diameters, with and without insulation surrounding the vessel. These simulations were used to determine if the thermocouple temperature at low pressure is measurably greater than it is at atmospheric pressure.

A conference paper on the results of the 8×8 experiment and simulation was presented in the 2013 PATRAM Conference. A reference to this paper is given below and a copy of the paper can be found in Appendix B.

- Green, R. Manzo, E. T., Greiner, M., Li, J., and Liu, Y. Y., "Experimental Benchmark of Simulations that Predict Temperatures of an 8x8 Array of Heater Rods within a Vessel Filled with Rarefied Helium Gas," Proceedings of the 17th International Symposium on the Packaging and Transportation of Radioactive Materials, Aug 18-23, 2013, San Francisco, CA.

Year 2: During the second year of the project. Ms. Green completed the design of the experimental apparatus to measure heat transfer between concentric cylinders under rarefaction conditions and started its construction. During the initial construction of the experiment a mishandling of the aluminum and stainless-steel-sheath caused a delay of the experiment assembling. Some modifications to the original design were proposed to enhance its performance and to overcome the problems encountered with the first design. These modifications were performed to minimize the heat losses from the cylinders' end. The diameter of the aluminum, stainless-steel-sheath and stainless-steel-pressure-vessel were reduced and their lengths were increased. The annular gap between the stainless-steel cylinders is reduced to 1 mm (before was 2 mm). This allowed the apparatus to reach rarefaction condition at higher pressures and to minimize the problems related to the outgassing and leakage.

Figure 11 shows the new design of the experimental pressure vessel. Sections from the old pressure vessel were used. The small tubes on the outer surfaces shown in Figure 11a represents the inlet and outlet of the external water jacket, which was used to control the temperature of the pressure vessel. The temperature of the stainless-steel-sheath (inner cylinder) was monitored using 12 thermocouples uniformly distributed on the surface (see Figure 11b).

Ms. Green performed two and three-dimensional ANSYS/FLUENT simulations of the new design of the experimental apparatus. The uniformity of the temperature and heat flux on the stainless-steel sheath and pressure vessel were assessed. Additional three-dimensional simulations of the water jacket performance were conducted. A detailed

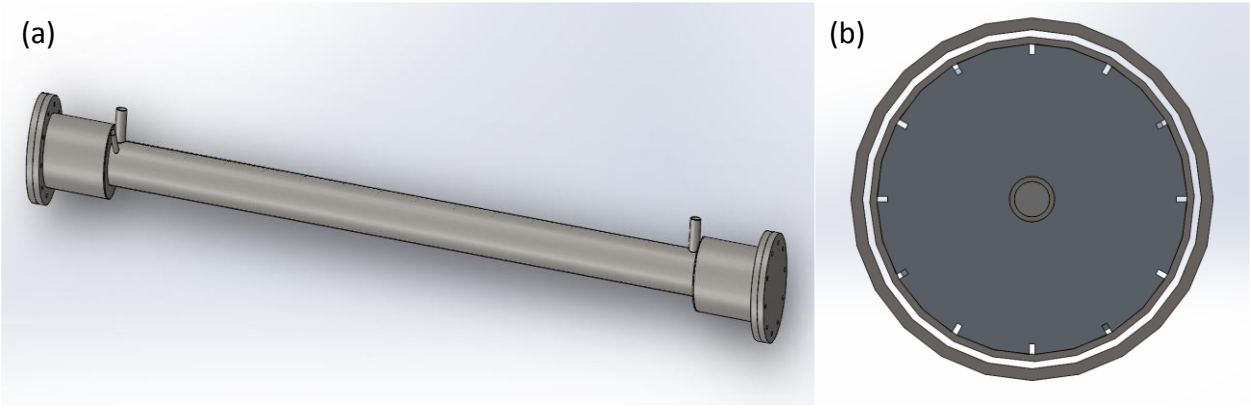

Figure 11: The new design of the experimental apparatus performed under SolidWorks. (a) Isometric view, (b) cross section view.

description of the experimental apparatus design and results of the simulations are presented in the 2014 PVP conference paper. The reference for this paper is given below and a copy of the paper is included in Appendix B.

- Green, R., Manzo, E.T., Hadj Nacer, M., and Greiner, M., 2014, "Design of an Experimental Apparatus to Measure the Thermal Accommodation Coefficient between Stainless Steel Surfaces and Rarefied Helium," PVP2014-29018, Proceedings of the 2014 ASME Pressure Vessels and Piping Conference, July 20-24, 2014, Anaheim, CA, USA

Year 3: During this year, Ms. Green constructed and assembled the different components of the experimental apparatus used to measure heat transfer between concentric cylinders separated by a rarefied gas, and to determine the temperature jump and thermal accommodation coefficients. She also ran three-dimensional ANSYS/FLUENT simulations to validate the experiment design. Other simulations were run to compare the results with the experimental measurements.

Figure 12 shows an axial-section view of the experimental apparatus. It consists of three main parts, the inner cylinder system, the pressure vessel along with the water jacket, and the support system. The inner cylinder system is centered inside the pressure vessel. The inner cylinder system has an outer diameter of 45.48 mm and the pressure vessel cylinder has an inner diameter of 47.49 mm, which leaves an average gap of 1.01 mm between the two cylinders. The length of the inner cylinder system is 1.032 m, however the length of the vessel cylinder is 1.132 m. In order to keep a constant gap between the cylinders the experiment is oriented vertically to limit the problem of inner cylinder system leaning.

The main inner cylinder system is composed of an electrical heating cartridge that is centered inside a thick walled aluminum cylinder. Twelve thermocouples were strategically placed inside precision 0.15 mm deep grooved channels machined on the outer surface of the aluminum cylinder and secured with highly thermal conductive cement so that any potential gaps are minimized. A shrink fit process was used to insert the aluminum cylinder inside 1 mm thickness stainless-steel-sheath, which comprises the outer surface of the inner cylinder system. This process was used to ensure an intimate

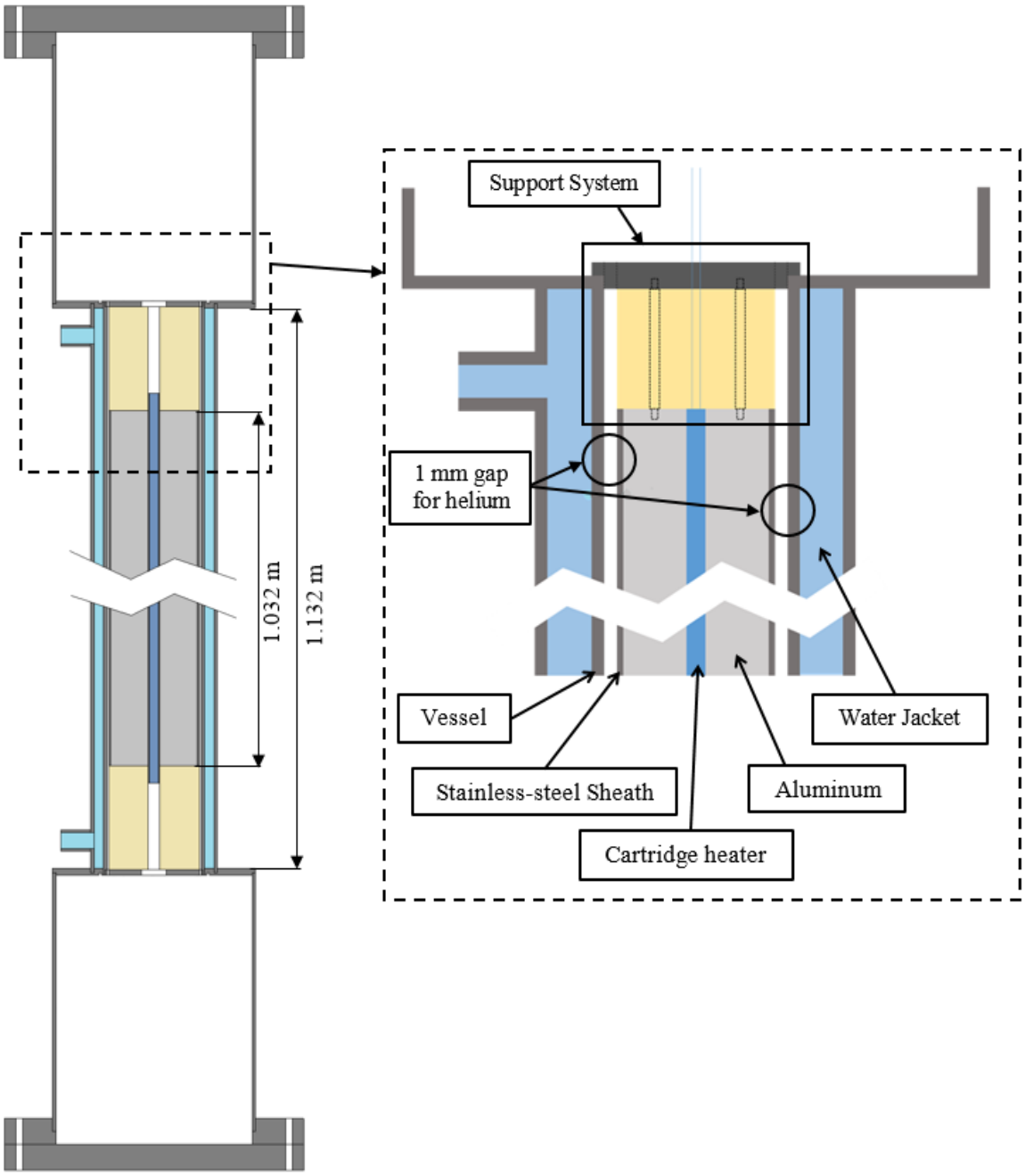

Figure 12: Cross-sectional view of the entire experimental apparatus with detailed view (not to scale) of the inner cylinder assembly and support system.

contact between the outer aluminum surface and inner stainless-steel-sheath surface. Figure 13a shows a picture of the end of the inner cylinder system with the centered heating cartridge, aluminum cylinder and stainless-steel sheath along with the thermocouples channels. The aluminum cylinder has a thick wall to promote a uniform temperature profile on the outer surface of the inner cylinder system. The heating cartridge is secured in place with highly-conductive epoxy.

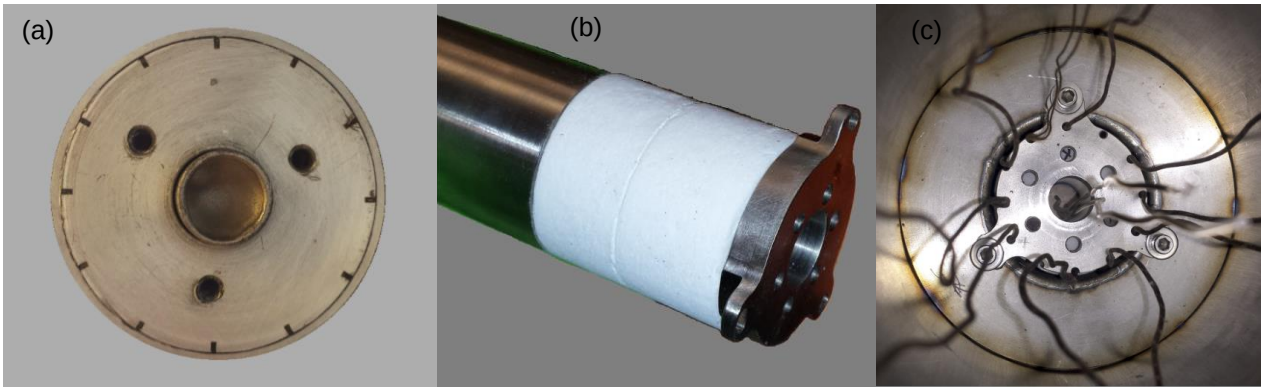

Figure 13: (a) Inner cylinder system; Aluminum and stainless-steel sheath with thermocouple grooves and centered heating cartridge, (b) support system assembled together along with the inner cylinder system, (c) support system secured in place with screws.

Low thermal conductivity (κ = 0.06 W/mK) alumina insulation material, with a thickness of 50 mm, is placed on both ends of the inner cylinder system (see Fig. 13b), then the assembly (inner cylinder system + insulations) is centered inside the outer vessel cylinder with the aid of stainless-steel supports and spacer plates. This low thermal conductivity insulation is employed to minimize the heat losses from the ends of the cylinder system. The supports provide rigidity and ability to hold the inner system concentric to the vessel so that a 1 mm-wide gap is created between the two (see Fig. 13c).

The temperature of the outer vessel is controlled using an external water jacket. Twelve thermocouples are placed inside small grooves machined on the outer surface of the vessel to monitor the vessel temperatures. The thermocouples were secured inside the grooves with epoxy and aluminum straps to ensure their ability to withstand the turbulence of the water flow.

Conflat flanges on both ends of the vessel are used to seal and maintain the pressure inside the vessel. One of the flanges contains thermocouple and power feedthroughs to allow the connection of the thermocouples and power leads from the vacuum chamber to the outside. The other flange contains a vacuum tree that connects the vacuum chamber to the vacuum pump through an open/close valve. To the vacuum tree, also connected is a high pressure helium tank through a metric valve that allows accurate control of the pressure.

Figure 14 shows a pictures of the experimental apparatus fully assembled and placed on the table along with the vacuum pump underneath (red apparatus) and the acquisition system to the left of the experiment.

Ms. Green performed preliminary experimental tests to check vessel leak and outgassing, and determine if the thermocouples were functional. The following tests were performed:

- All inner cylinder assembly and water jacket thermocouples were tested to ensure their full functionality before and after construction or assembling of each component. As a result, all twelve water jacket thermocouples were found to be fully functional.

However, only eight of the inner assembly thermocouples were fully functional after the final assembling.

- The pressure vessel was backfilled and evacuated numerous times to ensure that the only gas present in the system was helium.
- Leak and outgassing tests were performed to find and eliminate any possible leaks and to know the outgassing rate, which can affect the vessel pressure. The tests using the leak detector showed that there were no leaks, however the outgassing rate was important.

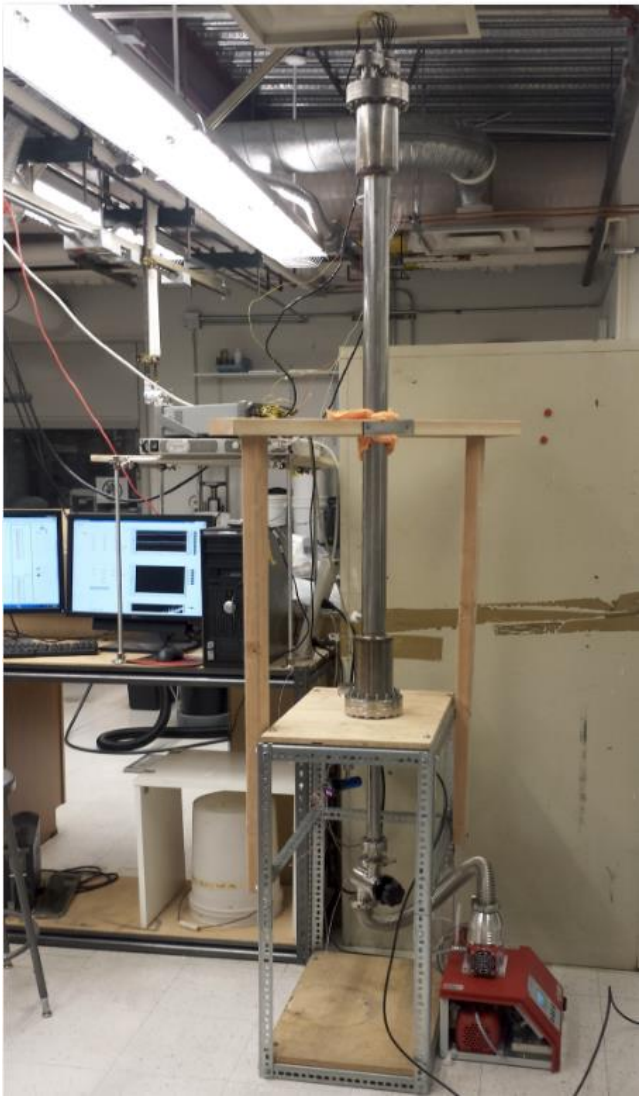

Figure 14: Picture of the experimental apparatus fully assembled

To check and decrease the outgassing rate, the standard '*rate of rise*' method was employed. The pressure in the experiment was set to its possible lower value (10^{-2} Pa) using the vacuum pump and the temperature was increased to 160˚C for several days. Decreasing the pressure and baking the experiment enables adsorbed gas/vapor to be

evacuated, so that outgassing rate was decreased. The vacuum pump was then isolated and the rise of pressure was monitored. If the pressure rose significantly, then the system was still outgassing. This method was repeated several times until the pressure gauge was not sensitive to these effects.

Other tests were conducted to check the time needed for the experiment to attain steady state temperatures, and to verify that there is a measureable temperature difference between the inner cylinder assembly and the pressure vessel walls, even at higher pressures. All the tests showed that the experiment was suitable for the observation of the rarefaction effect and measurements of the temperature jump and thermal accommodation coefficient.

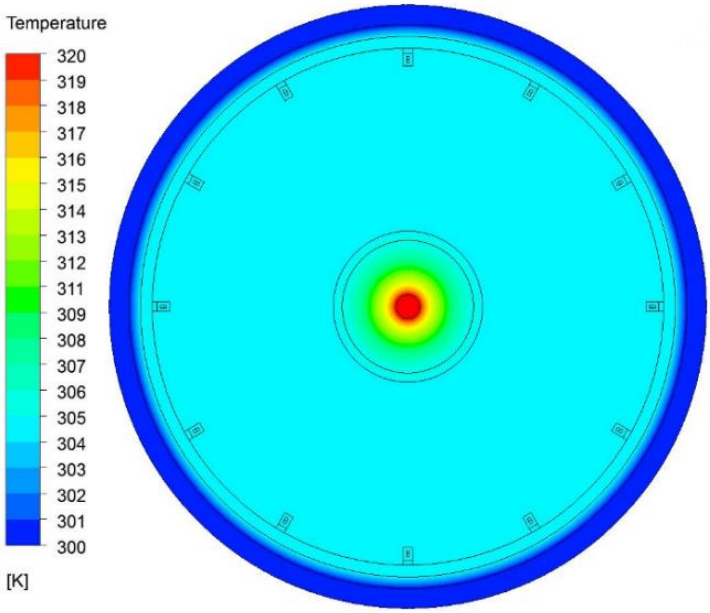

Figure 15: Typical temperature contour of the cross-section for all simulated cases.

Geometrically accurate three-dimensional simulations of the experimental apparatus were performed using ANSYS/FLUENT to validate the design of the experimental apparatus. Simulations that include conduction and radiation heat transfer, and temperature-jump at the interface between solid surfaces and gas were performed. The outer surface of the vessel was maintained at a constant temperature of 300 K and the pressure in the gap was varied from atmospheric pressure to P = 200 Pa. This range of pressures covers both continuum and slip regimes. Three values of the thermal accommodation coefficient, α = 1, 0.4, and 0.2, and different heat generation rates within the cartridge heater (Q=100W, 150W, and 200W) were considered for all the simulations.

Figure 15 shows a typical cross-section-temperature-contour for all of the simulated cases considered. The maximum temperature is located at the center of the inner cylinder assembly with nearly uniform temperature through the aluminum cylinder and stainless steel sheath surrounding the aluminum cylinder. A steep decrease in temperature is observed across the helium gas gap.

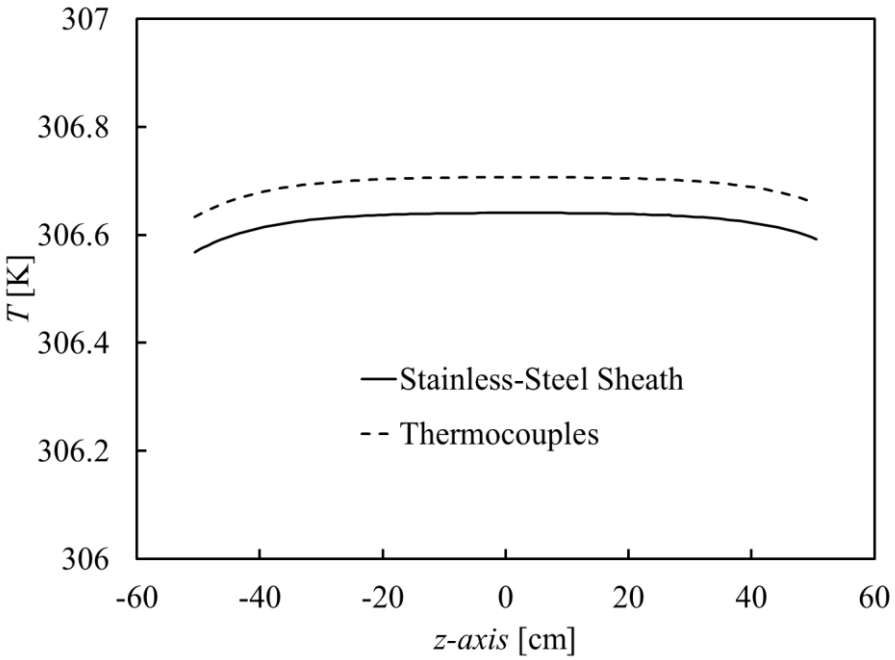

Figure 16: Axial temperature profiles for the outer surface of the stainless steel sheath and the thermocouple region.

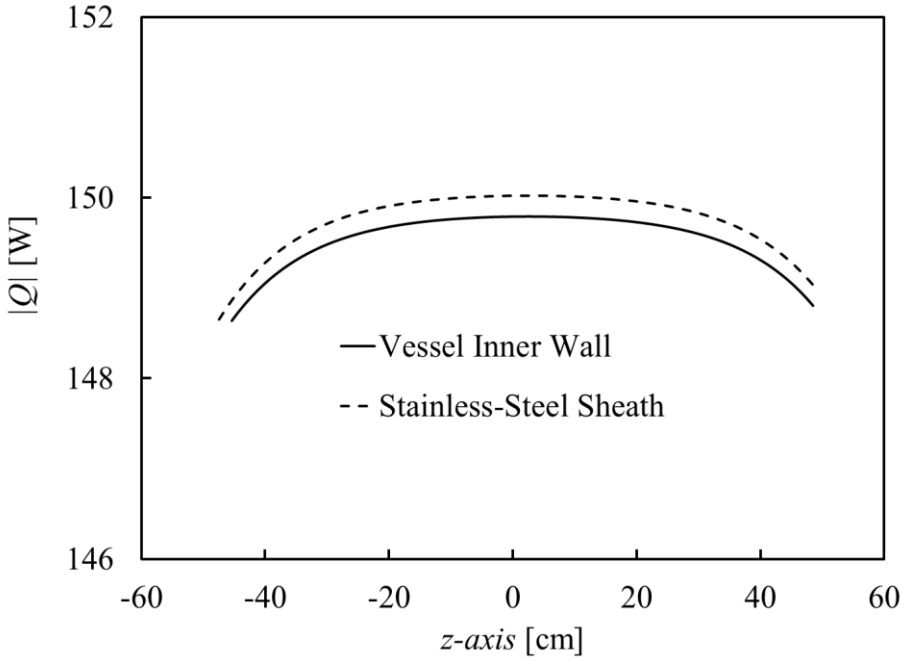

Figure 17: Heat flux along the vessel inner surface and outer surface of the stainless steel sheath.

Temperature profiles along the cylinder axis (*z*-axis) are shown in Fig. 16 for the outer surfaces of the stainless steel sheath and thermocouple region. These profiles are obtained using the continuum model. A nearly uniform temperature along the stainless steel sheath surface is obtained. The maximum variation of temperature along this surface is less than 0.1˚C with the value obtained at the mid-plane.

Axial heat flux profiles along the side surfaces of the stainless steel sheath and vessel are shown in Fig. 17. It is clear from this figure that the heat flux leaving the outer surface of the stainless steel sheath and delivered to the inner surface of the vessel, which are in contact with helium, are nearly identical and uniform along the axial axis direction. The maximum variation of the heat flux along the axial axis is less than 1%.

The uniformity of the temperature and heat flux leaving the surfaces in contact with helium, shown in Figs. 16 and 17, confirms the validity of the actual experimental design to be used for the calculation of the value of the temperature jump coefficient and thermal accommodation coefficient.

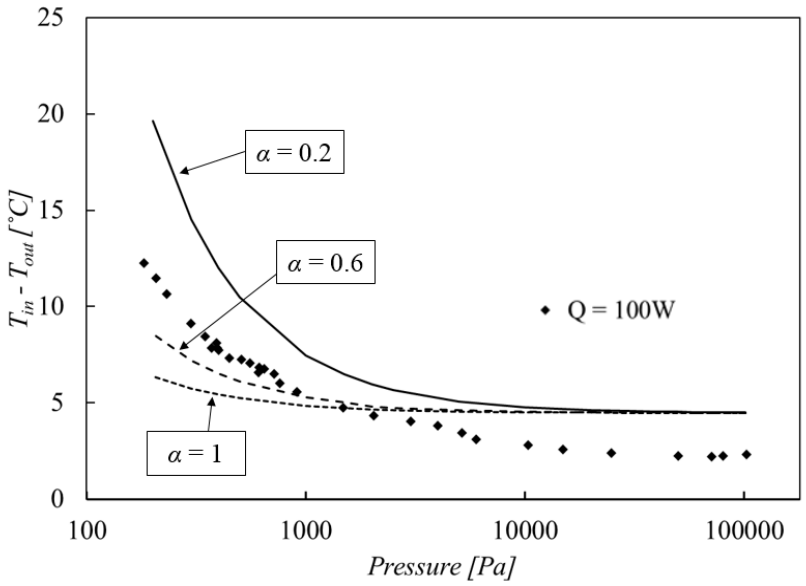

Figure 18: Measured results compared to simulated results for Q=100W and different value of the temperature jump coefficient.

Figures 18–20 show a comparison of the experimentally measured temperature difference between the stainless-steel-sheath inner wall, T_{in}, and the pressure vessel outer wall, T_{out}, with the simulated results, for different heat generation rates, Q=100W, 150W, and 200W, as a function of pressure. The simulation results were obtained for three different values of the thermal accommodation coefficient, α = 1, 0.6, and 0.2. These figures show that the measured temperature difference, T_{in} - T_{out}, is almost constant in the continuum regime (21820 < P < 101325 Pa), however in the slip regime (218.2 < P < 21820 Pa), the temperature difference increases as the pressure decreases. As an example, for the case Q = 100 W and P ≈ 200 Pa, the temperature difference is 10°C higher than it is at $P \approx 10^5$ Pa. This measurable difference is due to the rarefaction effect (decrease of pressure), which proves that the experimental setup was able to observe the rarefaction effect.

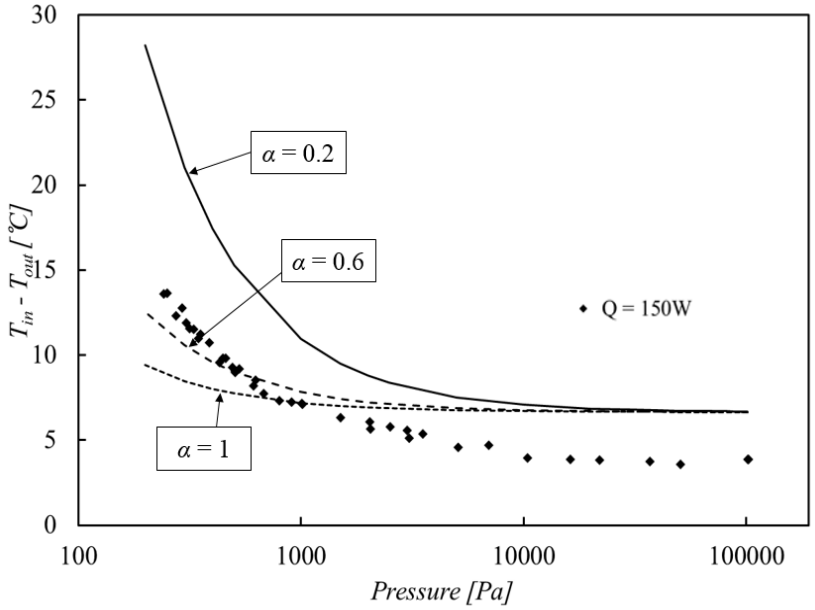

Figure 19: Measured results compared to simulated results for Q=150W and different value of the temperature jump coefficient.

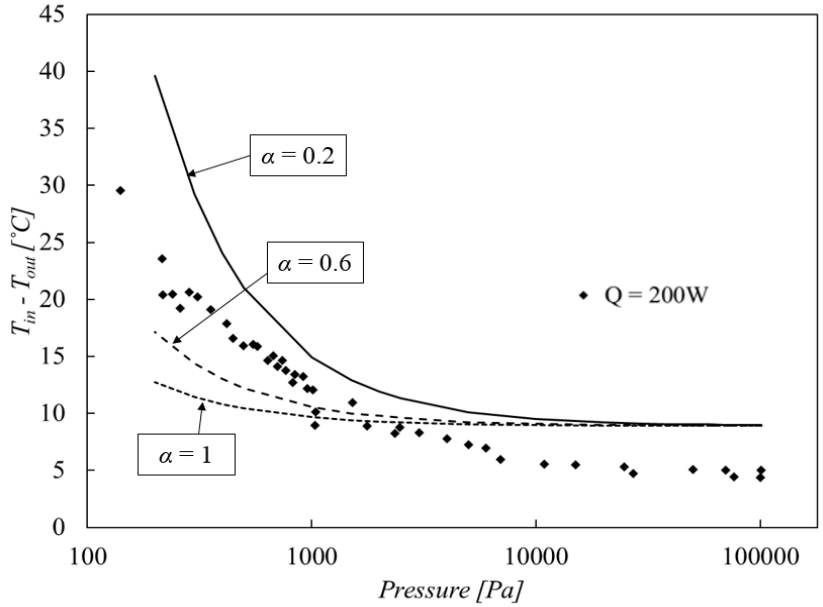

Figure 20: Measured results compared to simulated results for Q=200W and different value of the temperature jump coefficient.

It can also be seen from Figs. 18–20 that the profiles of temperature difference as function of pressure obtained from measurements and simulations follow the same trend. However, at high pressures (continuum regime) there is a measurable difference between the measured and the simulated results. The simulated results predict temperature differences at high pressures that are 4.5°C, 6.7°C, and 9.0°C for the heat generation

rates Q=100W, 150W, and 200W respectively. However, the measured temperature differences are 2.3°C, 3.9°C, and 5.0°C, respectively, which shows a noticeable difference between the measured and simulated results of 2.2°C, 2.8°C, and 4.0°C, respectively. This difference increases with heat generation. Many assumptions have been tested to explain the reasons of this difference. A reason could be an incorrect estimation of the heat loss, a wrong measurement of the pressure vessel inner diameter, or a shift of the inner cylinder assembly inside the pressure vessel. These assumptions were checked by Mr. Walker Musnicki (please see below).

A conference paper on Mr. Green's work was presented at the 2015 ASME Pressure Vessel and Piping Conference. A copy of this paper can be found in Appendix B.

- Green, R., Hadj-Nacer, M. and Greiner, M., "Design of an experiment to measure the thermal accommodation coefficient between helium and stainless-steel in concentric cylinders", 2015 ASME Pressure Vessel and Piping Conference, July 19-23, 2015, Boston, MA.

Ms. Green defended her MS degree, entitled "Measurement of thermal accommodation and temperature jump coefficients for stainless steel surfaces and rarefied helium for coaxial cylinders", on September, 28th 2015. Her thesis can be downloaded following this link: http://innopac.library.unr.edu/record=b3274756~S0

Currently, Ms. Green is working at the Lawrence Livermore National Laboratory, CA as a Mechanical Engineer.

2.4.3 Mr. Dilesh Maharjan

Year 2: Mr. Maharjan joined the project as a graduate student in January 2014 (Year 2 of the project). He started his appointment by collaborating with Professor Stefan Stefanov from the Bulgaria Academy of Science, Bulgaria, and Professor Irina Graur from Aix-Marseille University, France. With the help of Pr. Stefanov, he performed one-dimensional Direct Simulation Monte Carlo (DSMC) calculations in the gap between concentric cylinders and compared the results with Discrete Velocity Method (DVM) calculations performed by Professor Irina Graur. These DSMC and DVM simulations were conducted for different values of the thermal accommodation coefficient, and temperature and aspect ratios.

Mr. Maharjan also designed an experimental setup that consists of an 8x8 square array of heating rods contained within a helium-filled-square-cross-section pressure vessel. Figure 21 shows the experimental apparatus designed under SolidWorks software. This apparatus will be used to model the vacuum drying conditions of a fuel assembly within a package.

During this year, Mr. Maharjan worked with Dr. N. R. Chalasani to perform ANSYS/FLUENT simulations of heated rods array within a square cross-section filled with a pressurized helium or nitrogen and to compare the results with experimental measurements Dr. Chalasani obtained during his appointment at UNR.

Year 3: During the third year of the project, Mr. Maharjan continued to collaborate with Professor Stefan Stefanov and Professor Irina Graur. He performed a one-dimensional Direct Simulation Monte Carlo (DSMC) calculations in the gap between parallel plates

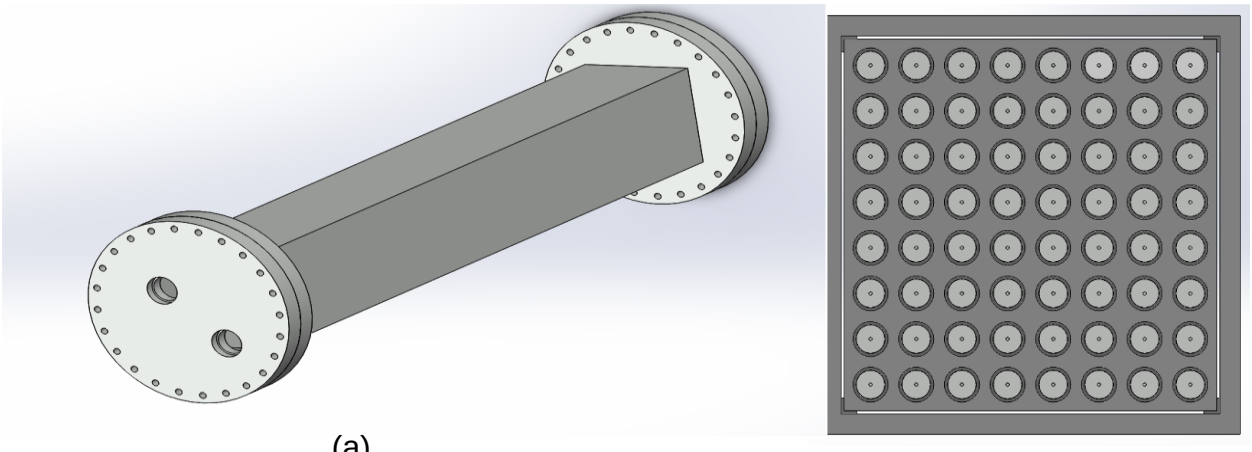

(a) (b)

Figure 21: New experimental apparatus deign of 8x8 array of heating rods within square-section pressure vessel performed under SolidWorks. (a) Isometric view, (b) cross section view.

and compared the results to the Discrete Velocity Method (DVM) calculations performed by Professor Irina Graur and ANSYS/FLUENT simulations. The DSMC simulations were conducted for different values of the thermal accommodation coefficient and wide range of pressure, from 1000 Pa to 10^{-3} Pa. A conference paper summarizing this work was presented at the 2015 ASME International Conference on Nanochannels, Microchannels and Minichannels (ICNMM15). A copy of the paper can be found in Appendix B.

- Maharjan, D., Hadj-Nacer, M., Ho, M. T., Stefanov, S.K., Graur, I. and Greiner, M., "Comparison of Heat Transfer across Rarefied Gas in Annular and Planar Geometries Using FLUENT, DSMC and DVM Methods", 2015 ASME International Conference on Nanochannels, Microchannels and Minichannels (ICNMM) conference, July 6-9, 2015, San Francisco, CA.

Mr. Maharjan continued his work with Dr. N. R. Chalasani to perform ANSYS/FLUENT simulations of 8x8 heated rods array within a square cross-section filled with a pressurized helium or nitrogen. The results of these simulations were compared to the experimental measurements that Dr. Chalasani obtained during his appointment at UNR. The comparison showed a good agreement between the simulation and experimental results.

During this year, Mr. Maharjan completed the design of the experimental apparatus consisting of a 7×7 heating-rod array enclosed within a square pressure vessel. The rod configuration was changed from 8×8 to 7×7 to reduce the cost of the experimental setup.

Figure 22 shows a picture of the experiment that Mr. Maharjan is designing using SolidWorks. The experiment consists of a 7×7 array of heating rods between two spacer plates. Each heating rod has a thermocouple at its center or at ±200 mm from the center in the axial direction. These thermocouples are used to provide a complete temperature profile of the heating rods at different axial locations. Thirteen thermocouples are placed on each side of the square enclosure and fourteen thermocouples are placed in each spacer plates to monitor their temperatures. The spacer plates are held in place by eight

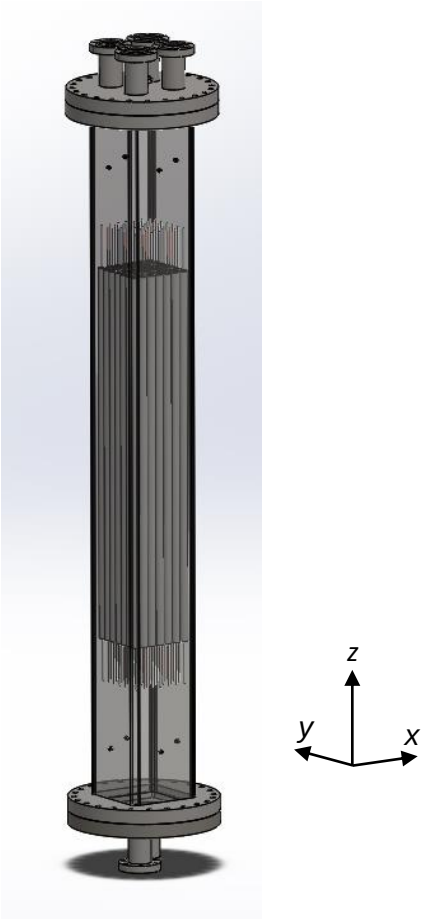

Figure 22: 7×7 experiment designed under SolidWorks.

stainless steel rod supports (four from each side). At the top and bottom of the enclosure, thermocouple and power feedthroughs are used in each side to connect the thermocouple and power wires from the vacuum side to the air side. The total number of thermocouples used in the apparatus is 129. On the outer walls of the enclosure, flat silicon heaters will be placed on each side to control the temperature of the enclosure walls. Insulation will be used to cover the apparatus to minimize the heat losses and to better control the temperature.

Some parts of the apparatus were machined with plastic material to test the procedure of assembling the experiment. Following these tests, some parts were redesigned. All the welding jobs were completed. Hence, the enclosure is ready. Grooves for thermocouple wires have been machined on the outside of enclosure. Other parts like support rods and spacer plates were also fabricated.

Mr. Maharjan performed ANSYS/FLUENT simulations of the experimental apparatus to assess the effect of the square enclosure thickness variation on the heating rods temperatures. It was found that thickness variation has insignificant effects on their temperatures. Mr. Maharjan also conducted simulations to check the effect of small variations of position of heater rods in the square array. The position (in *x* and *y* direction) of half of the heater rods were changed randomly by 0.5 mm. The results showed a maximum variation of approximately 2°C in continuum regime and less than 1°C in

rarefied condition. Other simulations were conducted to check the way to achieve uniform temperature throughout the length of the enclosure. It was observed that this could be achieved if the two ends of the enclosure body could be insulated. Since complete insulation of the ends is not possible, simulations assuming flat heaters are placed on the walls of enclosure were performed to make enclosure temperature uniform. It was observed that the heat generation at the end, beyond the spacer plate, was necessary. However, the uniformity was achievable to about 3 °C and it increased the maximum temperature of the walls by about 25°C compared to condition with no flat heaters.

Further simulations were conducted to check the possibility of getting different temperatures at two adjacent walls compared to the other two walls of the enclosure. It was assumed that flat heaters are placed on two sides of the enclosure and equal heat flux was generated. The results showed that using these flat heaters, a measurable temperature difference can be achieved between the heated and unheated walls of the enclosure.

Year 4: During the fourth year of the project, Mr. Maharjan continued collaborating with Professor Stefan Stefanov and Professor Irina Graur. He prepared a journal paper summarizing the results of heat transfer through rarefied gas in the gap between parallel plates and concentric cylinders using DSMC, DVM and ANSYS/FLUENT. The simulations were conducted for different values of the thermal accommodation coefficient, temperature and aspect ratios, and wide range of pressure, from 1000 Pa to 10^{-3} Pa. The paper was accepted for publication in the Journal of Heat Transfer. A copy of the paper is included in Appendix A.

- Hadj-Nacer, M., Maharjan, D., Ho, M.T., Stefanov, S.K., Graur, I., and Greiner, M., 2017 “Continuum and kinetic simulations of Heat Transfer trough Rarefied Gas in Annular and Planar Geometries in the Slip Regime”. J. Heat Transfer 139(4), 042002.

Mr. Maharjan also collaborated with Professor Stefan Stefanov to perform two-dimensional heat transfer Direct Simulation Monte Carlo (DSMC) in a 7×7 array of heated rods. These DSMC calculations require significant computational time. Dr. Stefanov parallelized the DSMC code to decrease the computational time. Mr. Maharjan is running the code for 1×1 and 2×2arrays of enclosed heaters. The results from the DSMC code will be compared to ANSYS/FLUENT simulation to assess the accuracy of FLUENT in complex geometry.

Mr. Maharjan continued to work with Dr. N. R. Chalasani to perform ANSYS/FLUENT simulations of an 8x8 heated rods array within a square cross-section filled with pressurized helium and held in a vertical position. The results of the simulations were compared to the experimental measurements that Dr. Chalasani obtained during his appointment at UNR. A journal paper summarizing these results was prepared and submitted to the ASME Journal of Thermal Science and Engineering Applications. The paper was accepted for publication. A paper on this work was also presented in the 2016 PVP Conference. Copies of the journal and conference papers are included in Appendices A and B, respectively.

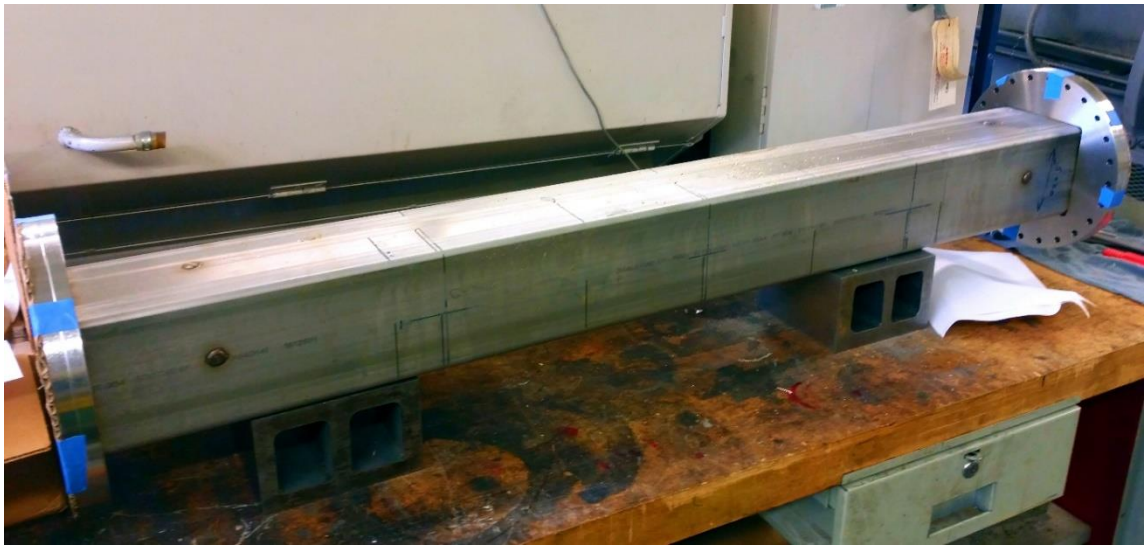

Figure 23: Square cross-section stainless steel pressure vessel.

- Maharjan, D., Hadj-Nacer, M., Chalasani, N., and Greiner, M., "Experimental Validation of Heat Transfer Simulations for a Vertical Heated Rod Array within a Square-Cross-Section, Helium-Filled Isothermal Enclosure," ASME Journal of Thermal Science and Engineering Applications (accepted).
- Maharjan, D., Chalasani, N. R., Hadj-Nacer M., and Greiner, M., "Experimentally-Benchmarked Computational Fluid Dynamics Simulations of an Array of Heated Rods within a Square-Cross-Section Helium-Filled Pressure Vessel", 2016 ASME Pressure Vessel and Piping Conference, July 17-21, 2016, Vancouver, BC, Canada

During this year, Mr. Maharjan completed the fabrication and assembling of the 7×7 experimental apparatus that is used to model the vacuum drying conditions of a fuel assembly within a package and to benchmark ANSYS/FLUENT simulations under rarefied condition. All the welding fabrication operations were completed. Grooves for thermocouple wires have been machined on the outer surfaces of the enclosure. Thermocouple leads are placed in the grooves so their reading is close to the enclosure temperature. Other parts such as the support rods and spacer plates were also fabricated. Figure 23 shows a picture of the stainless steel pressure vessel square enclosure with the thermocouple grooves.

Figure 24 shows pictures of some of the components machined for the 7×7 experiment. Mr. Maharjan made and calibrated all the thermocouples that will be used to measure the temperature boundary conditions. A total of 52 thermocouples were calibrated for temperature range between 20 and 200 °C. He also X-rayed some of the heater rods to measure the length of unheated portions. He found out that the axial locations of the thermocouple in heater rods specified by the manufacturer were not accurate. He also constructed small experiment to locate the positions of the thermocouples inside the heater rods. The manufacturer did not supply a tolerance on their locations. Mr. Maharjan found that some of the heater rods had a thermocouple position that were off by few centimeters from the required position. These heater rods were returned. New ones were received and tested again.

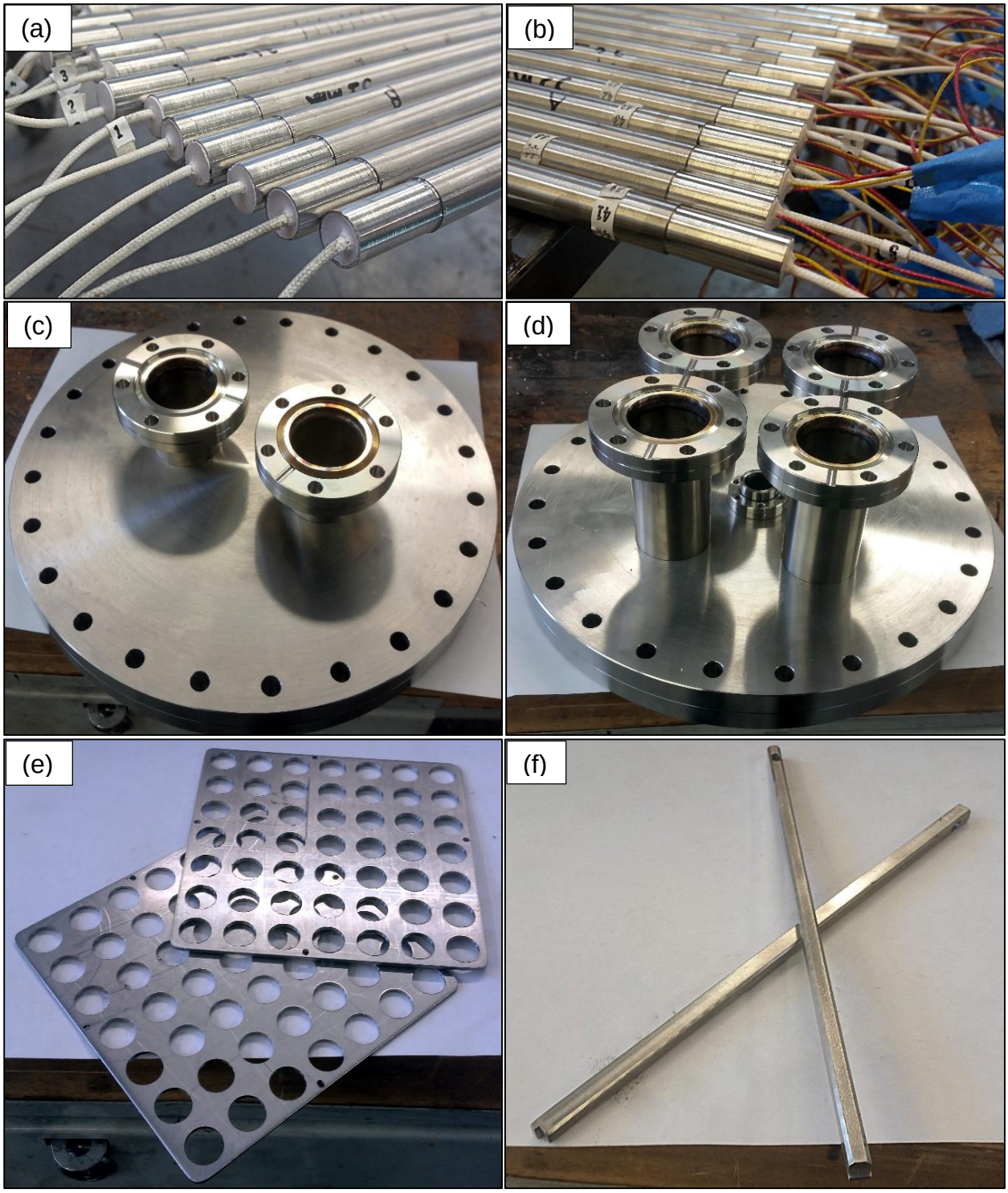

Figure 24: Some components of the 7×7 array of heated rods experiment. (a) and (b) heating rods, (c) and (d) flanges, (e) spacer plates, and (f) support rods.

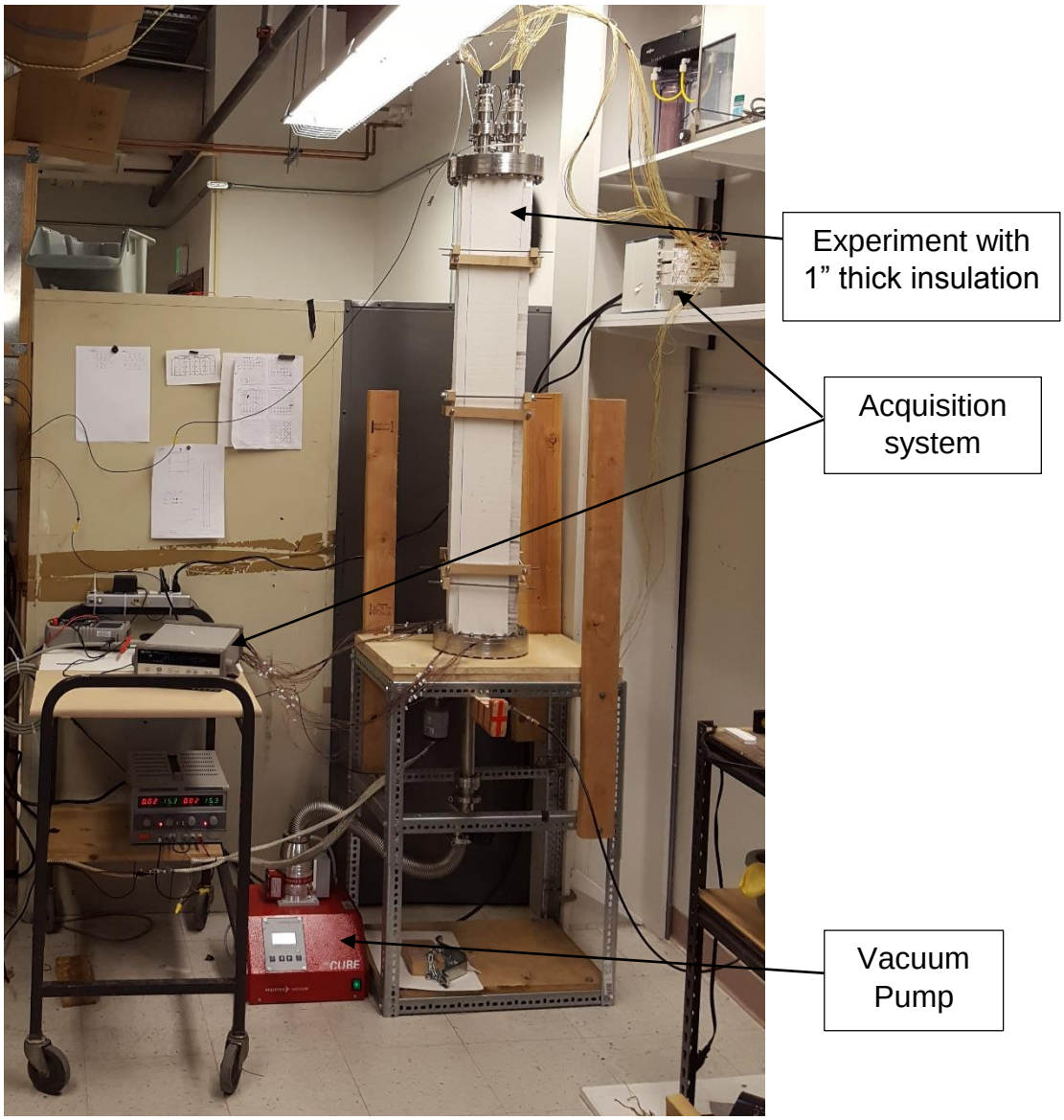

Figure 25: 7×7 array of heated rods experiment assembled.

Figure 25 shows pictures of the experiment fully assembled. The experiment was vacuumed for few weeks to eliminate the residual gases present on the internal surfaces of the experiment. A total of 129 thermocouples were used to obtain the full temperature profile of the rods, spacer plates and enclosure. Also, the experiment was insulated using a 1 inch and 2 inch thick low thermal conductivity material to reduce the effect of the ambient temperature variation on the experimental results, and increase the experiment temperature.

The description of the experimental setup and the preliminary results are given in Milestone 1 and 2 report.

Two papers on Mr. Maharjan’s experimental work were submitted to the 2017 ASME Pressure, Vessel and Pipe (PVP) conference to be held in Hawaii from July 16-20, 2017.

- Maharjan, D., Hadj-Nacer M., and Greiner, M., "Temperature Measurement of an Array of Heated Rods Subjected to Vacuum Drying Conditions," Proceedings of the ASME 2017 Pressure Vessels & Piping Division Conference, July 16-20, 2017, Waikoloa Village, HI.
- Maharjan, D., Hadj-Nacer M., and Greiner, M., "Experimentally Benchmarked Computational Fluid Dynamics Simulations of a 7×7 Array of Heated Rods within a Square-Cross-Section Enclosure Filled with Rarefied Helium," Proceedings of the ASME 2017 Pressure Vessels & Piping Division Conference, July 16-20, 2017, Waikoloa Village, HI.

2.4.4 Mr. Hasibul Alam

Year 2: Mr. Alam started his appointment at UNR as a MS student in August 2014. He learned about nuclear fuel cycles and spent nuclear fuel storage casks. He also studied the forced helium dehydration process to remove any remaining moisture in the canister after water draining. Mr. Alam also worked with Mr. Manzo and Mr. Maharjan to learn how to use ANSYS/FLUENT CFD code.

Year 3: During this year, Mr. Alam learned how to use ANSYS/FLUENT to model heat transfer within nuclear fuel assemblies. He also learned about the Forced Helium Dehydration (FHD) process used to dry nuclear used fuel canister, and the possibility to model this complex process in ANSYS/FLUENT. This process involves a lot of phenomena, such as diffusion, free surface evaporation and desorption of water from the canister surfaces.

Mr. Alam compared different models of evaporation available in ANSYS/FLUENT package to determine the most appropriate one to model FHD process. It was found that the evaporation models available in FLUENT can model only boiling phenomenon but not the free surface evaporation, which is the main phenomenon to remove water during FHD process. For this reason, he wrote a User Define Function (UDF) and implemented it in ANSYS/FLUENT to take into account free surface evaporation. The UDF was tested in simple problems and the results were compared to analytical solutions. The agreement between FLUENT and analytical solutions was very good. The UDF was then implemented in 2D and 3D models representing the nuclear fuel assembly. Some problems related to the convergence of the simulations were observed.

Year 4: During the fourth year of the project, Mr. Alam continued to work on the UDF to take into account the free surface evaporation in complex geometry. This work was carried over by Mr. Trujullo.

Mr. Alam defended his MS thesis on January 25, 2016, in front of a committee composed from Dr. Nicholas Tsoulfanidis, Dr. Miles Greiner, and Dr. Mustafa Hadj-Nacer. His thesis was entitled: "ANSYS/FLUENT Simulation Model Development for Forced Helium Dehydration Process". Mr. Alam compared different models of evaporation available in ANSYS/FLUENT package to determine the most appropriate one to model FHD process. He presented a 2D and 3D simulation results of the nuclear fuel canister subjected to FHD. A copy of Mr. Alam's thesis can be found following this link: http://search.proquest.com/docview/1808419102?pq-origsite=gscholar

2.4.5 Mr. Corey Trujillo

Year 3: Mr. Trujillo joined the project in August 2015. He started by reviewing selected literature on vacuum drying process and rarefied gases. He also began to learn ANSYS/FLUENT by doing some online tutorials. During this period, Mr. Trujillo learned how to build 2D and 3D models of a simplified nuclear fuel assembly.

Mr. Trujillo worked with Ms. Rachel Green to learn about the experimental setup that she built to measure the thermal accommodation coefficient. Ms. Green taught Mr. Trujillo the history of the experiment, how certain components were selected, manufactured, and/or purchased. She also showed him how the LabVIEW software interacts with the hardware. She guided him through startup and shut down procedures, potential flaws of the experiment, and some mistakes she had learned from its construction. She introduced him to people who played key roles in the construction of the experiment, and shared her experience on navigating the university structure to accomplish research goals.

Year 4: The primary focus of Mr. Trujillo's work was to construct a three-dimensional, geometrically-accurate model of a TN-24 PWR nuclear fuel canister filled with 15x15 Westinghouse fuel assemblies (referred to as the "1/8th Model"). With this model, he has conducted simulations using ANSYS/FLUENT software. In addition, Mr. Trujillo has presented his work to a variety of audiences and has collaborated with colleagues on related projects. The details of his work are as follows.

1/8th Model Mr. Trujillo developed geometrically-accurate two and three-dimensional models of a TN-24 nuclear fuel canister containing 15x15 Westinghouse assemblies using ANSYS/FLUENT. This model is similar to that developed by Mr. Manzo (Please see above). The model was re-created to fix the issues with the geometry encountered with Mr. Manzo model. A cross section view of the model is shown in Fig. 26. This model includes distinct regions for uranium dioxide fuel, Zircalloy cladding, helium backfill, steel housing, aluminum support, and steel shell. The canister model is symmetric along the *x* and *y* axes, and two-diagonal lines on the plane *x*, *y*, so only one-eighth of the canister was modeled. To construct the 3D model, the 2D model was extruded in the *z*-direction. Figure 27 shows the top portion of the 3D model. Materials for different regions were assigned such that distinct lids, helium gaps, heated section, header and footer were modeled. In the heated section, separate materials for the fuel rods and their surroundings were assigned and the fuel rods themselves were assigned a heat generation rate. The materials of the header and footer identically match the heated section, but no heat generation rates were used in these sections.

1/8th Model Development Mr. Trujillo began by creating simple models of a 3x3 array – one was two-dimensional while the other was three-dimensional. The 3D model had insulated ends and the same cross section as the 2D model. With these settings, the same results were acquired from the 2D and 3D models.

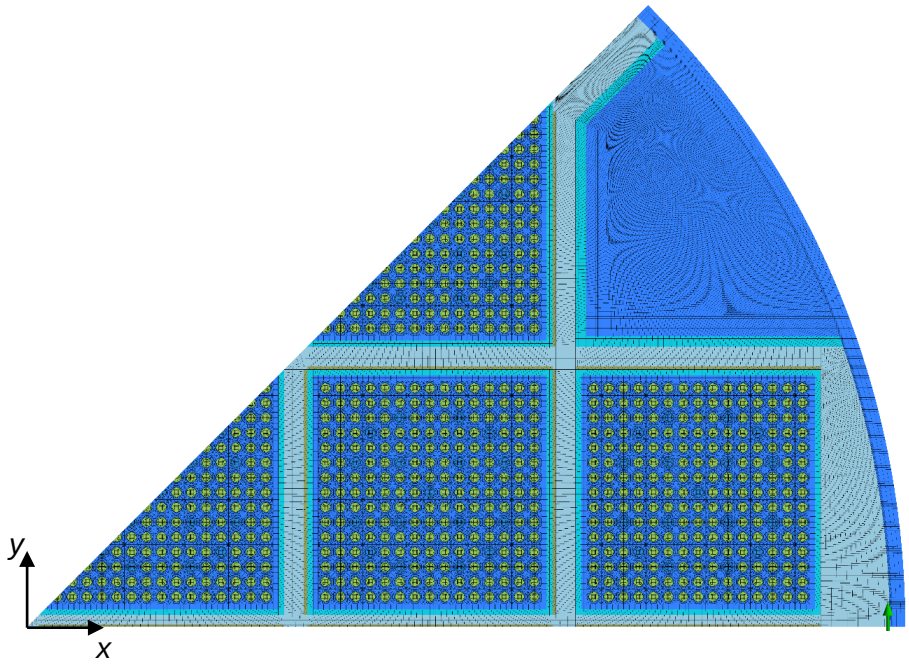

Figure 26: Cross-sectional view of the one-eight model of nuclear fuel canister.

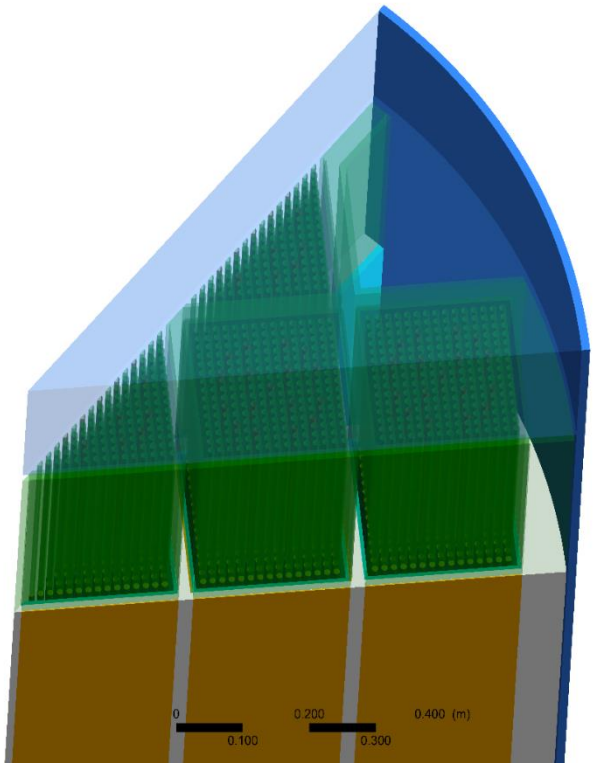

Figure 27: 3D top section view of the one-eight model of nuclear fuel canister.

Next, Mr. Trujillo created a 2D version of the 1/8th Model based on measurements taken from a model created by Mr. Manzo. The greatest hurdle in creating this model was getting the model to mesh properly. It was eventually discovered that very small gaps between bodies (on the order of 10^{-10} m) were inhibiting the model from meshing properly. This was likely due to the fact that Mr. Manzo's model was initially created in Imperial units, while the measurements taken from the model were in SI and the conversion factors used by ANSYS caused these minute discrepancies. When these measurement issues were resolved, the two-dimensional model meshed without error.

The next step in the process was to extrude the 2D 1/8th Model into the third dimension. A 10 cm 3D model was successfully created and meshed. This model used insulated ends and had the same cross section as the 2D model. Both models should essentially give the same results. The results from 2D and 3D models matched within 0.01K

Mr. Trujillo then created 1 m model. Rarefaction was considered with this model. This model was used to conduct a mesh sensitivity study.

Sensitivity Study A sensitivity study was completed by Mr. Trujillo to better understand how mesh resolution affected results from the 2D and 3D simulations. Mesh refinement was conducted in three regions of the model as shown in Fig. 28. More divisions in a region implies more elements and therefore a finer mesh. Simulations of 2D and 3D models with identical meshes were performed and compared to assess accuracy.

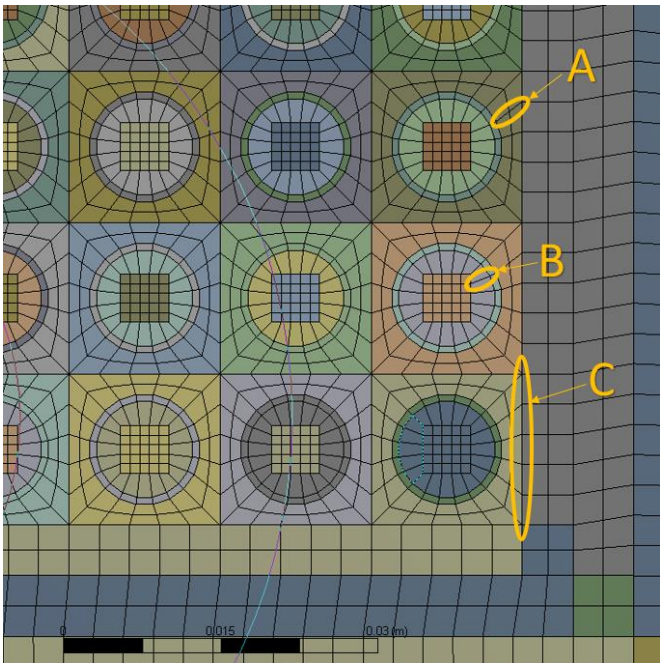

Figure 28: Refined regions of the canister model for mesh sensitivity study

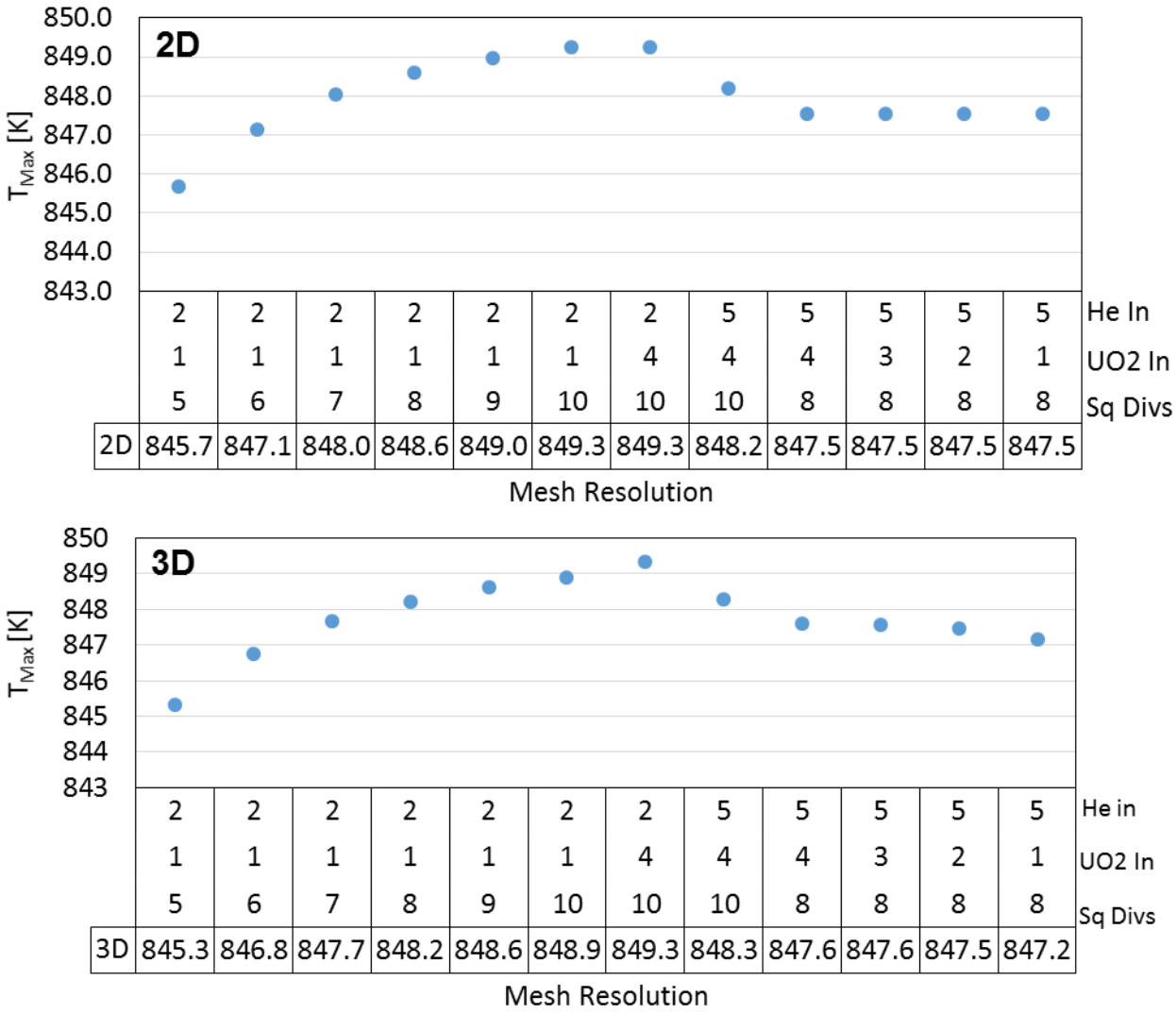

Figure 29: Maximum temperature obtained for different mesh resolutions (a) 2D model, (b) 3D model.

Figure 28 shows the regions considered for mesh refinement. Region A is referred to as “Helium Interior Divisions,” Region B is referred to as “Uranium Dioxide Interior Divisions” and Region C is referred to as “Square Divisions.” In the following discussion, each mesh resolution is identified using this format (He in, UO2 in, Sq Divs). For example, mesh resolution (5, 2, 8) corresponds to the case with 5 divisions in region A, 2 divisions in region B and 8 divisions in region C.

Figure 29 shows the maximum temperatures obtained for the 2D and 3D models with different mesh resolutions. The number of division in each region was increased while keeping the value constant in the other regions. The basic mesh resolution is (2, 1, 5). First, the number of divisions in region C was increased from 5 to 10 with an increment of 1. It is clear from the plots that refining this region caused the maximum temperature

to increase by 3.6°K. However, for the finest meshes the increase was small, so it was concluded that 10 divisions are enough. Second, the number of divisions in region B was increased from 1 to 4 with increment of 1. It was found that refining this mesh does not affect the maximum temperature, therefore only the two extreme cases, (2, 1, 10) and (2, 4, 10), are shown in Fig. 7. Third, the number of divisions in region A was increased from 2 to 5 by increment of 1. The maximum temperature decreased in this case by about 1°K, hence, only the extreme cases are shown. The case (5, 4, 10) represents the finest mesh resolution tested in this study. The use of this mesh resolution will result in a large computational time, especially for the 3D model simulations. So a smaller mesh resolution was needed to conduct the simulation in a reasonable time. The regions B and C were chosen to decrease their number of divisions. It was found that the mesh (5, 2, 8) would be a good alternative for both 2D and 3D models as it gives maximum temperature 0.7°K smaller than the finest mesh and reasonable number of elements.

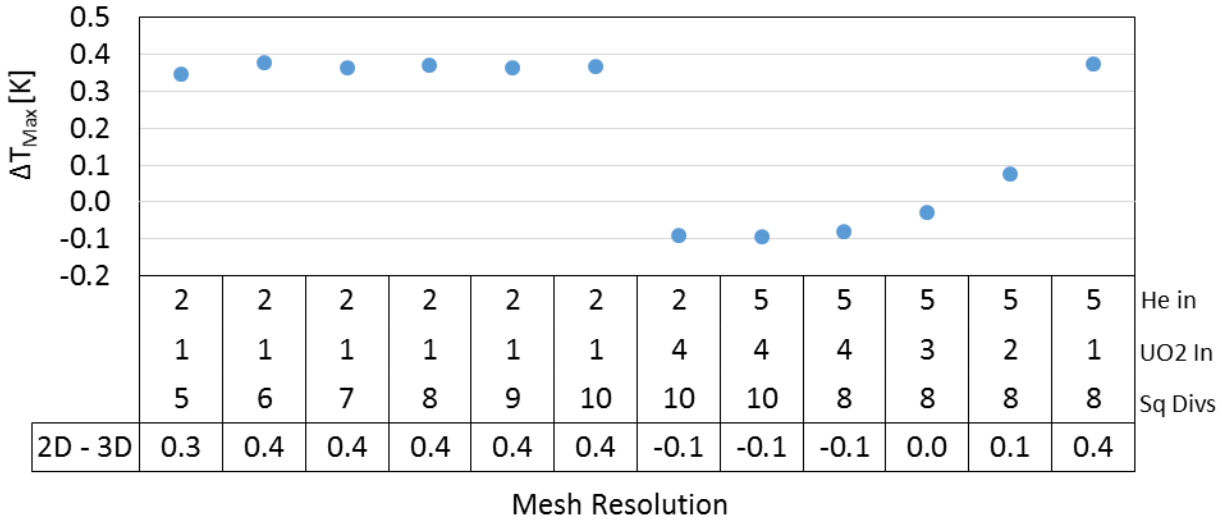

Figure 30: Different of the maximum temperature between the 2D and 3D models obtained for different mesh resolutions

Figure 30 shows the temperature difference between the 2D and 3D models for each mesh resolution. For the case (5, 2, 8), the difference between the 2D and 3D models is 0.1°K, which demonstrates that the 3D model accurately reproduce the 2D model results if its ends are insulated. It should be noted here that the heat generation used for this study is 5660 W/assembly, which is about 3 times the maximum heat generation per assembly in a real canister. The use of low heat generation will result in smaller differences.

Results from the 2D model of the nuclear canister Figure 31 shows results of the maximum temperature as function of heat generation from two 2D models of the nuclear fuel canister. The diagonal black lines show the results from Mr. Manzo's previous work, while the blue lines show the results obtained by Mr. Trujillo. The horizontal lines show the maximum allowable temperature used in the US and Germany, 400°C and 370°C,

respectively. The results are given for continuum (P ≈ 10^5 Pa), rarefied (P = 100 Pa, α = 1, 0.4, 0.2) and hard vacuum (P = 0 Pa) conditions. It is clear from this figure that the results of maximum temperatures obtained by Mr. Trujillo are higher than Mr. Manzo's results. This discrepancy was investigated and it was found that Mr. Manzo failed to consider the actual value of emissivity of the steel basket in his model. Mr. Manzo used an emissivity of 1 for the steel walls, however, the value should be 0.46. This resulted in higher heat transfer by radiation in Mr. Manzo's model, and therefore lower temperatures.

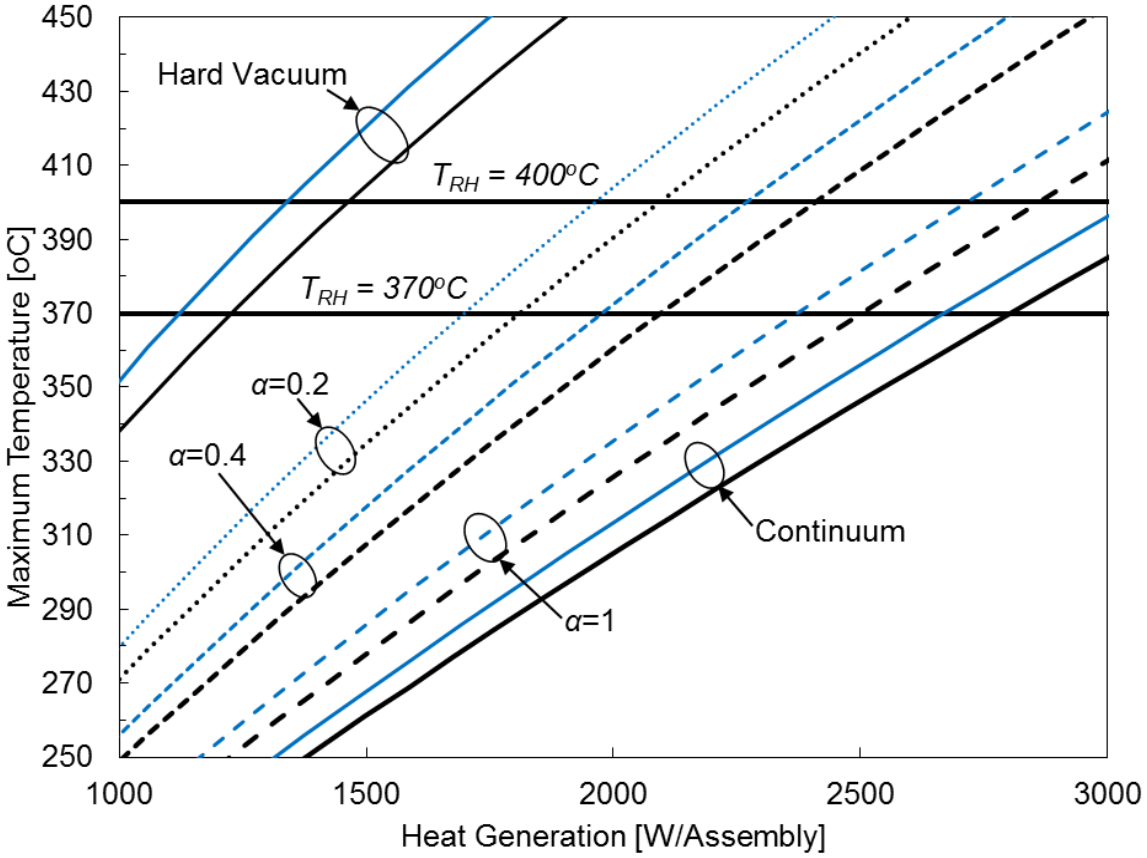

Figure 31: Maximum temperature as function of heat generation for 2D and 3D models.

High Performance Computing The full length 1/8th model requires about 5 days run time in a 24 cores Workstation that has 128GB of RAM. To relieve this burden of the large computational loads of the Full-Length 1/8th Model, a significant portion of Mr. Trujillo's work has been to achieve compatibility between ANSYS software and department- and university-owned high performance computing clusters. This has required Mr. Trujillo to collaborate with both ANSYS support staff and university faculty and staff. Although ideal computational efficiency has yet to be achieved, Mr. Trujillo is now able to run up to eight simulations simultaneously. Although this doesn't decrease computational time of a single simulation, running multiple simulations at once allows data to be acquired more quickly. With collaboration between ANSYS and UNR, it is likely to see runtimes reduced by 75% or more in the near future.

During this year, Mr. Trujillo also worked with Mr. Hasibul Alam to understand phenomena relevant to the forced helium dehydration process (FHD) and how to simulate them in ANSYS. Further work in this area will allow FHD simulations to be conducted with the Full-Length 1/8th model. This is promising work in better understanding flow fields inside the canister during FHD.

Mr. Trujillo worked also with Mr. Manuel Retana, an undergraduate student, over the summer of 2016 to find an appropriate evaporation/condensation model to simulate the FHD process within the geometrically-accurate 3D model.

In addition, Mr. Joseph Young and Mr. Trujillo collaborated to study ANSYS Parametric Design Language (APDL) and its applications for creating larger models with less required memory. APDL is a powerful scripting language that allows a model to be parameterized to automate common tasks. A script was written to generate 2D or 3D square array of heater rods, which can easily be modified to increase or decrease the number of rods. APDL shows promise, but recent conversations with ANSYS staff have suggested the use of ICEM for computational fluid analyses. Both of these systems will be studied for further use.

Mr. Trujillo competed at the University of Nevada Reno's Three-Minute Thesis Competition where he placed third. He also presented at the Mechanical Engineering Departmental Poster Competition where he also placed third.

Mr. Trujillo attended a course titled "ASME Pressure Vessel Code for Nuclear Transport and Storage" from June 20 to 24, 2016 at Argonne National Laboratory. Travel and registration fees to attend this course were not paid from the grant. At this course, Mr. Trujillo presented his work and received feedback from leading experts in the field.

Finally, Mr. Trujillo defended his MS thesis on January 25, 2017, in front of a committee composed from Dr. Nicholas Tsoulfanidis, Dr. Miles Greiner, and Dr. Mustafa Hadj-Nacer. His thesis was entitled: "Computational Model of a TN-24 Nuclear Fuel Canister during the Drying Processes".

2.4.7. Walker Musnicki

Mr. Musnicki started working on the project in January 2016. He redesigned the concentric experiment that Ms. Rachel Green constructed to measure the thermal accommodation coefficient. Unfortunately, the experiment Ms. Green constructed did not give satisfactory results. Troubleshooting the experiment revealed that the supports of the inner cylinder was broken. Mr. Musnicki redesigned new supports and other parts.

Mr. Hadj Nacer assembled the experiment with the help of Mr. Maharjan. Mr. Hadj Nacer wasn't able to run the experiment, because the vacuum pump and vacuum tree were not available. Mr. Maharjan is using them for his 7x7 experiment. After the termination of Mr. Maharjan's experiment, Mr. Hadj Nacer will run the concentric cylinder experiment.

Appendix A (Journal Papers)

1- Hadj-Nacer, M., Manzo, T., Ho, M. T., Graur, I. and Greiner, M., 2016 “Effects of Gas Rarefaction on Used Nuclear Fuel Cladding Temperatures during Vacuum Drying”. *Nuclear Technology* Journal, Vol: 3, n: 194, pp: 387-399.

2- Hadj-Nacer, M., Maharjan, D., Ho, M.T., Stefanov, S.K., Graur, I., and Greiner, M., 2017 “Continuum and kinetic simulations of Heat Transfer trough Rarefied Gas in Annular and Planar Geometries in the Slip Regime”. J. Heat Transfer 139(4), 042002.

3- Maharjan, D., Hadj-Nacer, M., Chalasani, N., and Greiner, M., “Experimental Validation of Heat Transfer Simulations for a Vertical Heated Rod Array within a Square-Cross-Section, Helium-Filled Isothermal Enclosure,” ASME Journal of Thermal Science and Engineering Applications (accepted).

NUCLEAR TECHNOLOGY · VOLUME 194 · 387–399 · JUNE 2016

Effects of Gas Rarefaction on Used Nuclear Fuel Cladding Temperatures During Vacuum Drying

M. Hadj-Nacer,[a]* T. Manzo,[a] M. T. Ho,[b] I. Graur,[b] and M. Greiner[a]

[a]*University of Nevada Reno, 1664 N. Virginia Street, MS 312, Reno, Nevada 89557*
[b]*Aix-Marseille Université, CNRS UMR 7343, 13453 Marseille, France*

Received June 11, 2015
Accepted for Publication October 6, 2015
http://dx.doi.org/10.13182/NT15-82

Abstract — *A two-dimensional computational model of a loaded used nuclear fuel canister filled with dry helium gas was constructed to predict the cladding temperature during vacuum-drying conditions. The model includes distinct regions for the fuel pellets, cladding, and helium within each basket opening, and it calculates the conduction heat transfer within all solid components, heat generation within the fuel pellets, and conduction and surface-to-surface radiation across the gas-filled regions. First, steady-state simulations are performed to determine peak clad temperatures as a function of the fuel heat generation rate, assuming the canister is filled with atmospheric pressure helium. The allowable fuel heat generation rate, which brings the peak clad temperature to its limit, is evaluated. The discrete velocity method is then used to calculate slip-regime rarefied gas conduction across planar and cylindrical helium-filled gaps. These results are used to verify the Lin-Willis solid-gas interface thermal resistance model for a range of thermal accommodation coefficients α. The Lin-Willis model is then implemented at the solid-gas interfaces within the canister model. Finally, canister simulations with helium pressures of 100 and 400 Pa and $\alpha = 1$, 0.4, and 0.2 are performed to determine how much hotter the fuel cladding is under vacuum-drying conditions compared to atmospheric pressure. For $\alpha = 0.4$, the fuel heat generation rates that bring the clad temperature to its allowed limit for helium pressures of 400 and 100 Pa are reduced by 10% and 25%, respectively, compared to atmospheric pressure conditions. Transient simulations show that the cladding reaches its steady-state temperatures ~20 to 30 h after water is removed from the canister.*

Keywords — *Used nuclear fuel, cladding temperatures, vacuum drying.*

Note — *Some figures may be in color only in the electronic version.*

I. INTRODUCTION

Pressurized water reactor (PWR) nuclear fuel assemblies consist primarily of 14 × 14 to 18 × 18 square arrays of Zircaloy cladding tubes that contain fuel pellets and high-pressure gases.[1] During reactor operations, the fuel pellets become highly radioactive and form fission product gases. After being discharged, used nuclear fuel (UNF) assemblies are stored underwater while their radioactivity and heat generation rate decrease.[2] After sufficient time, a canister with an internal basket is placed in a transfer cask and lowered into the pool. The canister is then loaded with used assemblies, covered, and lifted out of the pool. Helium or another nonoxidizing gas is forced into a port near the top of the canister while water flows out through a tube that reaches to the canister bottom.[3] Small amounts of water may remain at the bottom and in crevices of the canister, basket, and assembly surfaces after draining. Essentially all moisture must be removed to prevent corrosion of the assembly and cask materials and/or formation of combustible mixtures of hydrogen and oxygen.[4] After the drying operation, the canister is filled with helium to pressures up to 7 atm (710 kPa) and sealed. It is then placed in an air natural

*E-mail: mhadjnacer@unr.edu

convection–cooled on-site storage module or another packaging for off-site transport.

With the absence of a defined UNF disposal and/or reprocessing path, it is crucial to assure the safety of long-term dry storage systems.[5] Federal regulations (10 CFR 72) require that these systems ensure that external radiation doses are below certain limits and that the fuel configuration remain subcritical, confined and contained, and retrievable. Federal regulations (10 CFR 71) also require that transport package performance be analyzed under normal conditions of transport (which include a 0.3-m drop) and hypothetical accident conditions (which include a 9-m drop). The cladding holds the UNF pellets and fission gas in their analyzed configuration. Adequate cladding ductility must be maintained to assure that after decades in storage, the assemblies can be safely transferred to other packages and/or transported to other locations in their "as-analyzed" configuration.

Radial hydride formation within the cladding has the potential to radically reduce its ductility and suitability for long-term storage or transport.[5] During all postreactor drying, transfer, storage, and transport operations, the fuel cladding must be kept below certain temperatures to avoid (a) dissolution of circumferential hydrides that exist in the cladding and (b) high gas pressures within the tubes, which lead to high cladding hoop stress.[6] If this occurs, then as the heat generation of the UNF decreases during long-term storage, radial hydrides may precipitate and cause the cladding to become brittle.[7–10] The operations in which the fuel canister is dried,[11] moved to an on-site storage facility, and first placed in a storage module are of concern because they are the first in which the fuel is removed from water-cooled environments, and its heat generation rate may still be relatively high. This may cause the cladding to reach high temperatures and trigger events that can lead to radial hydride formation.

U.S. Nuclear Regulatory Commission Interim Staff Guidance-11, Revision 3 (Ref. 6) specifies conditions that are intended to prevent radial hydride formation. For example, the maximum calculated fuel cladding temperature must remain below 400°C for normal conditions of storage and short-term loading conditions (e.g., drying, backfilling with inert gas, and transfer of the cask to the storage module). For low-burnup fuel, a higher short-term temperature limit may be used, provided that the best estimate of the cladding hoop stress is $<$90 MPa. During loading operations, repeated temperature cycling is allowed but is limited to fewer than ten cycles in which the cladding temperature varies by $>$65°C. Until further guidance is developed, high-burnup fuel will be handled on a case-by-case basis.[6] In Germany and Japan, the maximum cladding temperatures for storage and drying are lower and equal to, respectively, 370°C (Ref. 12) and 250°C (Ref. 13).

I.A. Canister Drying Operations

Two methods are currently used by industry for canister moisture removal: vacuum drying and forced helium dehydration.[3,6] In vacuum drying, the canister is evacuated to pressures as low as 67 Pa (0.5 Torr) to promote evaporation and water removal.[11] Several cycles of evacuation and refill may be necessary before operators can demonstrate that the canister meets the drying technical specification of maintaining a low pressure of 400 Pa (3 Torr) for 30 min (Refs. 3 and 11). This process requires ~12 to 24 h for canisters containing metal matrix baskets and 60 to 100 h if BORAL® is used as a neutron absorber.[13]

At the low gas densities associated with vacuum drying, buoyancy-induced gas motion and natural convection heat transfer within the helium-filled regions of the canister are essentially eliminated. Helium thermal conductivity is nearly the same at vacuum-drying pressures as it is at atmospheric conditions. However, as the gas pressure decreases, the mean-free-path length between molecular collisions (described later in this paper) increases. When it approaches the characteristic dimension of the enclosure containing the gas, the gas becomes rarefied. In general, rarefied gases act as a vast collection of discrete colliding molecules that may be modeled using the Boltzmann equation,[14,15] rather than a continuum whose transport can be described using the Navier-Stokes and Fourier equations. Gas rarefaction reduces its ability to conduct heat compared to a continuum. As a result, if vacuum drying causes rarefaction, then the fuel cladding will be hotter than it would be under atmospheric pressure conditions.

Forced helium dehydration is used for drying canisters containing high-burnup and other high-heat-generating fuel.[3] In that process, helium is forced to circulate through the canister, and moisture is removed from the gas while it is outside by condensing, demoisturizing, and then preheating. The gas pressure during helium dehydration is maintained at ~3 to 4 atm (304 to 405 kPa) (Ref. 16), so natural convection is active, and based on the dimension of the canister gaps containing the gas, the gas is not rarefied. Fuel cladding temperatures may be lower when forced helium dehydration is used compared to vacuum drying. However, gas condensing and demoisturizing equipment are required in the former process but are not needed for the latter.

I.B. Cladding Temperature Prediction

Currently, package vendors predict cladding temperatures and the resulting hoop stresses during drying using experimentally benchmarked whole-package computational fluid dynamics (CFD) simulations.[3,17] In some models, the fuel and basket are replaced by a smeared region with an effective thermal conductivity and an effective porosity. Other models use an accurate-geometry computational domain where the fuel rods, gas, and baskets are distinctly modeled.[18–21] These models are used to predict the peak cladding temperature for a range of fuel heat generation rates. That information is used to find the fuel heat generation rate that causes the clad temperature to reach its allowed limits. It may also help determine which loaded canisters may be vacuum dried and which must use the more complex forced-helium-dehydration process.

The whole-package computational models have been validated[22] against measurements performed in an actual evacuated storage package.[23] Currently, the effective properties used during vacuum drying are calculated without regard to gas rarefaction. However, the fuel heat generation in the tests used to validate the current methods was moderately low. For a given package, the effect of gas rarefaction on peak cladding temperatures increases with the fuel heat generation rate. Rarefaction effects may need to be included for high-burnup and other high-heat-generating fuels.

I.C. Current Work

The objective of the current work is to develop computational methods that can be used to predict cladding temperatures under vacuum-drying conditions, including the effects of gas rarefaction. In this work, a finite difference cross-sectional model of a canister designed for 24 PWR assemblies, similar to the NUHOMS® TN-24PTH Horizontal Modular Storage System,[24,25] is constructed using ANSYS/Workbench. It accurately represents 15 × 15 arrays of fuel rods and helium gas within each basket opening and a helium-filled gap between the basket and canister surface. Steady-state simulations that model conduction in all components and surface-to-surface radiation across the helium-filled regions are performed to predict the peak cladding temperature for a range of fuel heat generation rates.

Initial simulations are performed by modeling the helium gas as a continuum at a pressure of 10^5 Pa (~1 atm). Boltzmann equation simulations are then performed to predict conduction heat transfer across rarefied helium within simple gaps between parallel plates and concentric cylinders. These calculations use the Shakhov model (S-model) kinetic equation.[26,27] These results are used to assess the accuracy of a mildly rarefied gas conduction heat transfer model. This model employs a continuum model within the bulk of the gas and the Lin-Willis temperature jump model[28] at the gas-solid interfaces to include rarefaction effects. Based on the quantitative agreement between these models, the Lin-Willis temperature jump model is then implemented in the ANSYS canister simulation. It is used to predict the increased cladding temperatures caused by gas rarefaction at pressures of 100 and 400 Pa. The first pressure is chosen because it is close to the lowest pressure used during vacuum drying.[11] The second pressure is used to test if the moisture has been removed from the system.

Another set of simulations is performed to estimate the amount of time after water is removed from the canister for the cladding to reach its steady-state temperature. This is compared to the typical time required to vacuum dry a canister to assess the appropriateness of using steady-state analysis to estimate the peak cladding temperature during drying. To simplify the modeling in this work, dry helium gas is considered throughout. As a result, evaporation and moisture transport are not included but may be considered in future research.

II. UNF CANISTER COMPUTATIONAL MODEL

In this work, we consider a UNF canister with an internal basket, similar to a Transnuclear NUHOMS TN-24PTH system[24,25] loaded with 24 Westinghouse 15 × 15 PWR assemblies.[29] Figure 1 shows the two-dimensional computational model of the canister cross section employed in this work. The model takes advantage of the canister symmetry along radial-lines, so only one-eighth of its cross section is included. Figure 1a shows the material regions. Each fuel assembly consists of a 15 × 15 array of rods of 10.92-mm outer diameter. Each fuel rod consists of $d = 9.58$-mm-diameter UO_2 pellets surrounded by 0.67-mm-thick Zircaloy cladding. There are also 13 hollow Zircaloy tubes in each assembly. The rod center-to-center pitch is 14.43 mm, and the distance between the walls and the nearest rod center is 12.04 mm. The square cross-section tubes that line each basket opening are constructed from stainless steel, and some surfaces are backed by BORAL neutron poison plates. At this cross section, the tubes are supported by an aluminum structure. The basket and assemblies are enclosed within a stainless steel canister, and there is a large void space in the upper right of the domain. The void spaces contain dry helium.

Figure 1b is a detailed view of one corner of an assembly within a stainless steel basket opening, a BORAL plate, and the aluminum support. Figure 1c

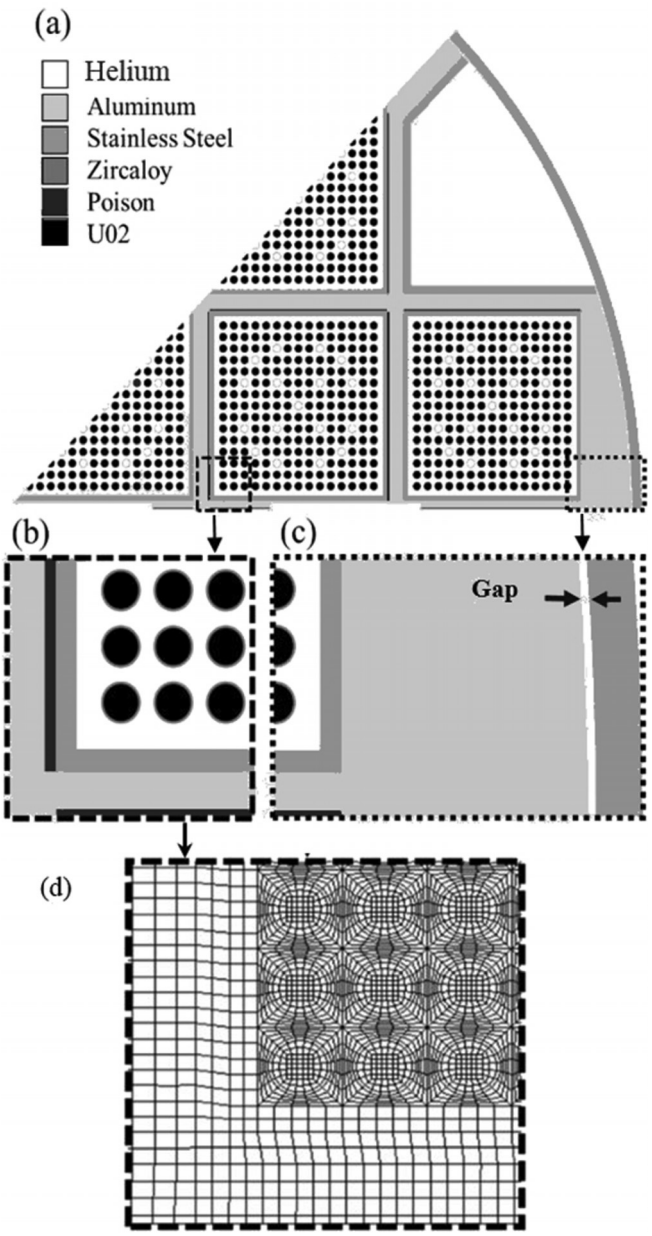

Fig. 1. Two-dimensional model of one-eighth of a UNF canister loaded with 24 PWR assemblies: (a) gray-scale coded material regions; (b) detail showing fuel rods, basket tubes, BORAL plates, and aluminum structure; (c) detail including gap between basket and canister; (d) computational mesh for the region in (b).

shows a region at the periphery of the canister, including a 2.29-mm-wide helium-filled gap between the basket and canister wall. Figure 1d shows the computational mesh within the region shown in Fig. 1b. The entire two-dimensional computational mesh has 131202 elements.

The characteristic dimension of the canister's helium-filled spaces is needed to compare with the gas mean-free-path length in order to determine if the gas is rarefied. However, for the complex space in Fig. 1, this dimension is not easily defined. In this model, the minimum surface-to-surface spacing is 2.3 mm between the outer basket and inner canister surfaces. The maximum spacing is 9.5 mm between diagonally adjacent fuel rods.

Steady-state and transient thermal simulations were performed using ANSYS/Fluent 15, which has been benchmarked for configurations relevant for UNF packaging.[18,19,22] These simulations assume uniform heat generation in all the UO_2 regions and include conduction within the solid and helium-filled regions. Surface-to-surface radiation across helium-filled spaces is included, with surface emissivities of 0.46 for the stainless steel and 0.8 for both the aluminum and Zircaloy.[30] These simulations also have the capacity to include a user-defined resistance at all gas-solid interfaces, which is activated when modeling mildly rarefied helium. During drying operations, the canister is vertical, so that the gravitational field is perpendicular to the plane of Fig. 1. While some natural convection effects may be present in the helium regions, they are not included in these simulations. This is because the gravitational vector is perpendicular to the plane of Fig. 1, and so, the primary flow direction cannot be included in the two-dimensional computational model.

At the package axial location that is represented by this model, the volumetric heat generation within all the UO_2 pellets is assumed to be uniform and equal to

$$q = \frac{P_F Q_F}{NL\frac{\pi}{4}d^2}, \tag{1}$$

where

Q_F = fuel assembly total heat generation rate

N = 212 = number of fuel rods within each assembly containing UO_2 pellets

L = 3.66 m = fuel rod length that contains pellets, based on a 15 × 15 Westinghouse PWR assembly.[29]

The peaking factor P_F = 1.1351 (Ref. 31) is the heat generation rate at the axial location where it reaches its maximum level divided by the average for the assembly.

For all steady-state and transient simulations reported in this paper, symmetry boundary conditions (insulated and radiatively reflective) are applied along the radial lines in Fig. 1a. During drying operations, cooling water is circulated in the gap between the canister outer surface (curved surface in Fig. 1a) and transfer cask inner surface to reduce temperatures. Throughout this work, the canister outer boundary surface temperature is assumed to be

101.7°C (Ref. 32) to conservatively model contact with boiling water at the highest possible pressure during the drying operation.

III. CONTINUUM GAS HEAT TRANSFER WITHIN A CANISTER

This section presents continuum gas simulations. These simulations model the canister filled with roughly atmospheric pressure dry helium (P = 101325 Pa, ~10^5 Pa), do not include the effect of gas rarefaction, and are used to compare to the rarefied gas results. Figure 2 shows continuum model temperature contours for a fuel assembly heat generation of Q_F = 1498 W/assembly. Outlines of the package components are also shown. There are local temperature maximums within each fuel assembly, but the global peak is located near the center of the innermost assembly, on the upper domain boundary. Figure 2 shows the r-axis along that boundary with its origin at the package center. The maximum or peak cladding temperature for this fuel heat generation rate is T_P = 261°C, which is below the nominal allowable limit value used in the United States: T_L = 400°C.

The lower solid line in Fig. 3 marked "Continuum" shows the temperature profile along the r-axis for the conditions used in Fig. 2. The temperature exhibits local peaks within the two fuel assemblies through which the r-axis passes, but the inner assembly temperature is ~25°C warmer than the outer one. Within the fuel assemblies, the temperature profile exhibits a stair-step shape. The more isothermal regions are within the relatively high thermal conductivity solid components. The lower-conductivity gas exhibits steeper gradients. The very steep gradient at r = 83 to 84 cm is within the helium-filled gap shown in Fig. 1c. This gradient is particularly steep because the heat flux through that region is relatively high, and the contribution of radiation to the total heat transfer across this gap is relatively low due to its low temperatures. This region makes a significant contribution to the total temperature difference between the canister outer surface and the hottest cladding.

The upper solid line in Fig. 3 marked "Hard Vacuum" shows the temperature profile along the r-axis assuming the helium is completely evacuated and Q_F = 1498 W/assembly. This eliminates conduction across all void spaces, so all heat transfer in those regions is by radiation. The shape of this profile is nearly identical to that of the continuum simulation. The primary difference is that the temperature gradient in the gap between the basket outer surface and the canister inner surface is much greater for the hard vacuum than for the continuum simulation. We define the basket surface temperature increase ΔT_{BS} as the outer basket surface temperature (at r = 83 cm) at low pressure minus its value under continuum conditions. For the hard vacuum simulation, ΔT_{BS} = 142.4°C. The peak clad temperature increase ΔT_{PC} is the peak clad temperature at low pressure minus its value for continuum conditions. For the hard vacuum simulation, ΔT_{PC} = 143.5°C, which is only 1.1°C larger than ΔT_{BS} (these results are included in Table I). This indicates that the effect of eliminating conduction in the void spaces within the basket openings is much smaller than eliminating it in the gap between the basket and canister. This is because radiation heat transfer carries a larger fraction of the heat within the basket, since that region is relatively hot, compared to the

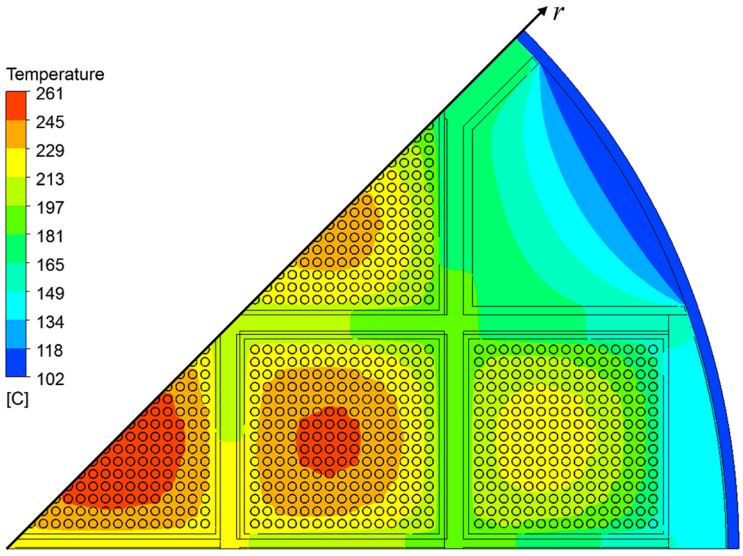

Fig. 2. Loaded canister temperature contours for helium at P = 10^5 Pa and Q_F = 1498 W/assembly.

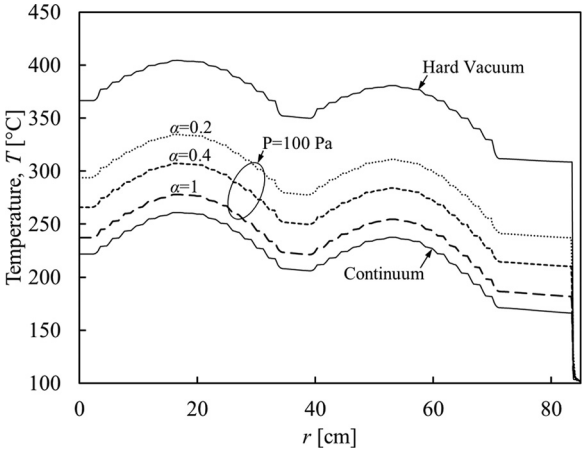

Fig. 3. Temperature profiles along the *r*-axis shown in Fig. 2, for Q_F = 1498 W/assembly. Results are shown for the continuum model, the temperature jump model at P = 100 Pa with three thermal accommodation coefficients, and a hard vacuum model.

TABLE I

Basket Surface and Peak Clad Temperature Differences Caused by Reduced Pressures, Relative to Continuum Conditions

P (Pa)	α	ΔT_{BS} (°C)	ΔT_{PC} (°C)
0	—	142.4	143.5
100	1	15.7	16.8
	0.4	44.1	46.3
	0.2	71.0	73.4
400	1	4.2	4.6
	0.4	14.1	15.1
	0.2	27.9	29.6

gap between the canister and basket, which is relatively cool.

The solid lines in Fig. 4 show the maximum or peak cladding temperatures predicted by the continuum and hard vacuum models as functions of the assembly fuel heat generation. The horizontal lines show the nominal fuel clad temperature limits used in the United States and in Germany: T_L = 400°C (Ref. 6) and T_L = 370°C (Ref. 12), respectively. The continuum and hard vacuum simulations indicate that the fuel cladding will reach 400°C when the fuel heat generation rate reaches limit values of Q_{FL} = 3202 W/assembly and Q_{FL} = 1461 W/assembly (54% smaller), respectively. These limit heat generation rates Q_{FL} are included in Table II. Table II also shows the values of Q_{FL} if the lower temperature limit of 370°C is used and indicates that Q_{FL} is reduced by 12% to 16%.

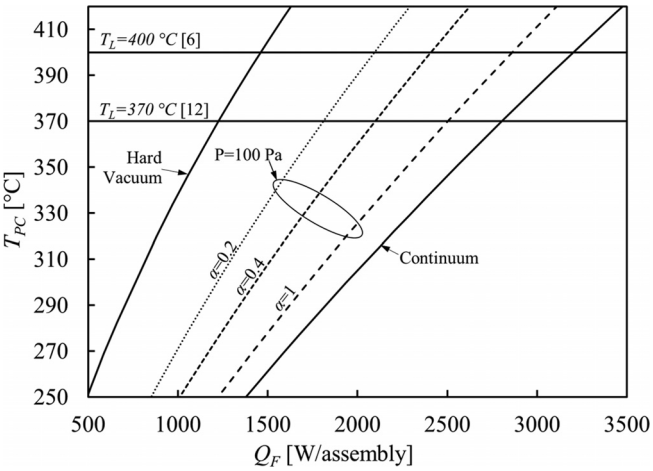

Fig. 4. Peak clad temperature versus fuel heat generation rate for helium at 10^5 Pa (continuum model), 100 Pa (temperature jump model) with three thermal accommodation coefficients, and 0 Pa (hard vacuum model).

We note that the Certificate of Compliance of the NUHOMS TN-24PTH system[24,25] requires the average fuel heat generation rate to be <1000 W/assembly for a standard horizontal storage module or 1700 W/assembly for an enhanced module. These heat generation rates are lower than the limit values presented in Table II for atmospheric pressure helium. For the purposes of this paper, we assume that the Certificate of Compliance limit is calculated by the manufacturer to maintain the cladding safely below 400°C during storage, in which the canister is cooled by air natural convection.

Calculation of cladding temperatures under dry storage conditions is beyond the scope of this work. However, it is reasonable that the canister surface is hotter in the storage module, where it is cooled by air, than in vacuum drying, where it is submerged in water. If the canister is filled with atmospheric pressure helium in both situations, then it is also reasonable that the cladding temperature may be hotter in the storage module than during vacuum drying. However, including the effects of rarefaction during vacuum drying increases the predicted cladding temperature under that condition.

IV. RAREFIED GAS HEAT TRANSFER ACROSS SIMPLE GAPS

We now consider the physical processes that affect conduction heat transfer across rarefied gases and models for predicting that transport. The molecular mean-free-path length λ of a gas is defined as the average distance molecules travel between consecutive collisions. Based on kinetic theory and the hard sphere intermolecular

TABLE II

Maximum Allowable Heat Generation per Assembly Q_{FL} for Two Cladding Temperature Limits

Cladding Temperature Limit, T_L	Continuum $P = 10^5$ Pa	Rarefied						Hard Vacuum $P = 0$ Pa
		$P = 400$ Pa			$P = 100$ Pa			
		$\alpha = 1$	$\alpha = 0.4$	$\alpha = 0.2$	$\alpha = 1$	$\alpha = 0.4$	$\alpha = 0.2$	
400°C	3202	3101	2891	2645	2861	2408	2092	1461
370°C	2804	2715	2529	2309	2502	2096	1810	1226

interaction model for a pure gas with molecule mass m, the mean-free-path length is[33]

$$\lambda = \frac{\sqrt{\pi}}{2}\frac{\mu}{P}\sqrt{\frac{2k_BT}{m}}, \quad (2)$$

where

k_B = Boltzmann's constant

P = gas pressure

T = temperature

μ = dynamic viscosity.

The temperature-dependent viscosity may be calculated based on the hard sphere intermolecular interaction model as

$$\mu = \mu_0\left(\frac{T}{T_0}\right)^{1/2}, \quad (3)$$

where

T_0 = 273.15 K = gas reference temperature

μ_0 = gas viscosity at T_0; for helium, $\mu_0 = 1.865 \times 10^{-5}$Pa · s.

Combining these results indicates that the mean-free-path length is proportional to the temperature and inversely proportional to the pressure, both to the first power.

If a gas is contained within an enclosure of characteristic length L_C and if the molecular mean-free-path length is sufficiently small, then the gas behaves as a continuum, and its momentum and thermal transport are accurately modeled using the Navier-Stokes and Fourier equations. The Knudsen number is defined as the ratio of the molecular mean free path to the enclosure characteristic length, $\mathrm{Kn} = \lambda/L_C$. The continuum approximation is generally valid for $\mathrm{Kn} < 10^{-3}$ (Ref. 14). If the gas pressure is decreased while the characteristic length is kept the same such that $\mathrm{Kn} > 10^{-3}$, the gas no longer behaves as a continuum. The rarefied gas may be modeled as a vast collection of molecules that collide with each other and the enclosure walls. The Boltzmann equation may then be used to calculate transport, but its numerical solution is computationally intensive, especially in complex enclosures.

Whenever an individual molecule collides with a wall, its energy level can remain the same as it was before the collision. Alternately, it can fully accommodate the wall conditions, so that its postcollision energy is in equilibrium with the wall temperature. For a given gas (collection of molecules) and solid surface, the thermal accommodation coefficient α is defined as the fraction of molecules that accommodates the wall conditions. It can be related to the temperatures of the collections of incident and reflected molecules T_i and T_r and the temperature of the wall T_w as[34]

$$\alpha = \frac{T_i - T_r}{T_i - T_w}. \quad (4)$$

The thermal accommodation coefficient is zero if all of the reflected molecules have the same energy they had when they approached the wall, unity if all reflected molecules have the same temperature as the wall, or some value between 0 and 1.

In general, the accommodation coefficient can be a function of the gas and wall compositions and of the wall surface topography and contamination.[35,36] For "engineering surfaces," with typical surface contamination, the value of α is primarily dependent on gas compositions and temperature and is essentially independent of the wall properties.[37] For example, for helium gas it varies from 0.4 to 0.2 as the temperature increases from 300 to 700 K. In general, the value of α is higher for gases with heavier molecular masses than for lighter ones.

In a given enclosure, as the gas pressure goes down and the mean-free-path length increases, the frequency of molecular-molecular collisions is reduced compared to molecular-wall interactions. As a result, the relative importance of molecular-surface interactions increases.

For gases in the continuum regime, energy transfer to the walls is not affected by α because molecular-wall interactions are relatively unimportant. However, as the pressure decreases and the gas becomes rarefied, the importance of molecular-wall interactions increases, and α affects heat transfer across the gas.

Graur et al.[26] and Graur and Polikarpov[27] used the Shakhov kinetic equation as a model (S-model) to simplify the collisional term of the full Boltzmann equation. In the current work, we numerically solve the S-model kinetic equation within two simple enclosures using the discrete velocity method. While the specifics of this calculation are not included in this paper, they may be found in Refs. 26 and 27. Figures 5a and 5b show simple gas-filled computational domains between parallel plates and concentric cylinders, respectively. In both configurations, $T_A = 330$ K and $T_B = 300$ K, and the y-coordinate systems are shown. The planar wall-to-wall spacing is $L_C = 10$ mm, and the inner and outer radii of the annular gap are $R_A = 5$ mm and $R_B = 10$ mm ($L_C = R_B - R_A = 5$ mm), respectively. In this work, the Maxwellian specular-diffuse boundary conditions, with $\alpha = 1$, were implemented at the walls,[38] and the hard sphere intermolecular interaction model was used for the viscosity calculation [Eq. (3)].

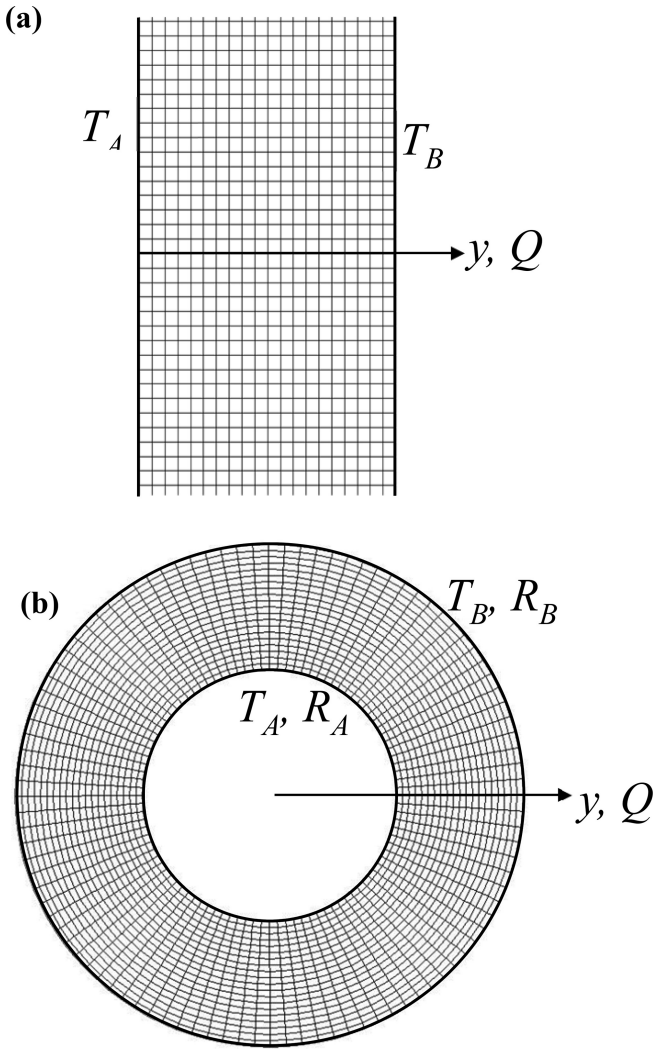

Fig. 5. Domains used to benchmark Lin-Willis temperature jump rarefied gas heat transfer model against S-model kinetic equation, with $T_A = 330$ K and $T_B = 300$ K: (a) planar region between parallel plates and (b) annular region between concentric cylinders, with $R_B/R_A = 2$.

Figures 6a and 6b show the temperature T versus y in the planar and cylindrical domains for helium gas and a thermal accommodation coefficient of $\alpha = 1$. In each plot, results are shown for four pressures P corresponding to Kn = 0.001, 0.01, 0.1, and 1 (the dimensional pressure for each simulation is shown in parentheses). The solid lines show the S-model kinetic simulation results. In both configurations, for the lowest Knudsen number Kn = 0.001

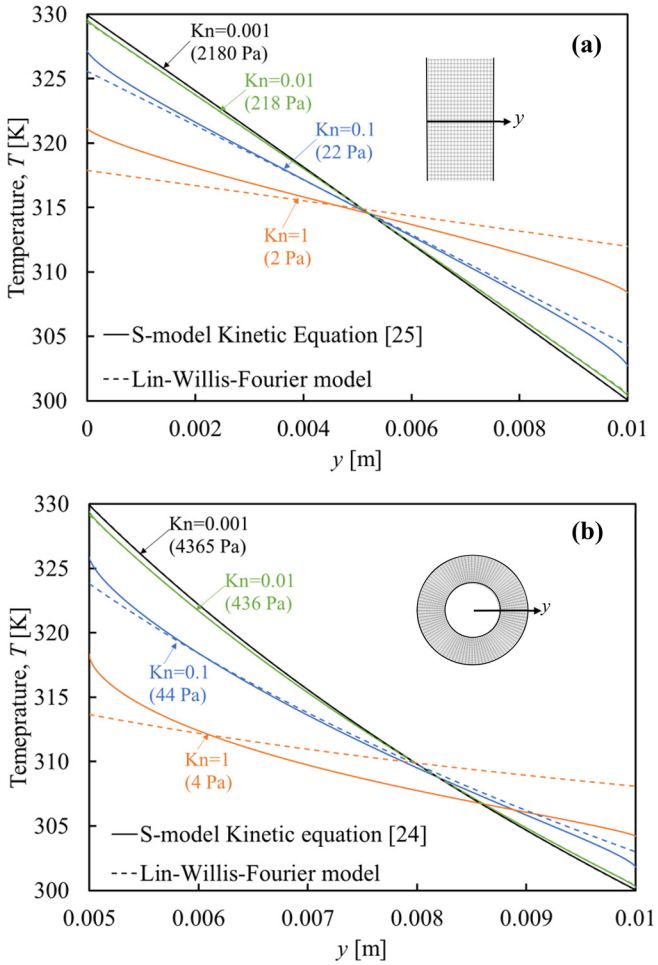

Fig. 6. Temperature profiles within rarefied helium–filled gaps with boundary temperatures of 300 and 330 K using the S-model kinetic equation and the Lin-Willis model: (a) planar gap and (b) annular gap.

(highest gas pressure), the gas temperature at the wall T_g is essentially the same as the wall temperature T_w. However, at higher Kn (lower pressures), there is a temperature difference between the gas and wall (temperature jump), and this jump increases as the pressure decreases. S-model simulation results at the same pressures but smaller values of α (not included in Fig. 6) have larger temperature jumps.

Analysis shows that transport across mildly rarefied gas–filled gaps, i.e., $10^{-3} < \mathrm{Kn} < 10^{-1}$, may be accurately calculated using a continuum model (Navier-Stokes and Fourier equations) completed with the temperature jump conditions at the gas-solid interfaces.[39] This analysis predicts that the difference between the gas and wall temperatures T_g and T_w is proportional to the heat transfer rate conducted by the gas away from the wall Q and may be calculated as

$$T_g - T_w = R_{TJ} Q \,, \tag{5}$$

where R_{TJ} is the temperature jump thermal resistance at the gas-surface interface and Q does not include the heat transported by radiation to other surfaces. The temperature jump thermal resistance is

$$R_{TJ} = \frac{\lambda \zeta_T}{A \kappa} \,, \tag{6}$$

where

A = boundary surface area

κ = gas thermal conductivity

ζ_T = temperature jump coefficient.

The gas conductivity is related to its viscosity μ [Eq. (3)], gas specific heat at constant pressure c_P, and Prandtl number Pr as

$$\kappa = \frac{c_P}{\mathrm{Pr}} \mu \,. \tag{7}$$

For helium, the specific heat and Prandtl number are constants and equal to $c_p = 5193$ J/kg·K and Pr = 2/3.

The literature contains numerous models for the temperature jump coefficient. Lin and Willis[28] developed expression (8), which is based on a solution of the Bhatnagar-Gross-Krook (BGK) kinetic model equation and is dependent on Pr, α, and the gas ratio of specific heat γ:

$$\zeta_T = \frac{2\gamma}{(\gamma + 1)\mathrm{Pr}} \left(\frac{2 - \alpha}{\alpha} + 0.17 \right) . \tag{8}$$

For helium, γ = 5/3. Expression (8) shows that the jump coefficient increases as α decreases.

The dashed lines in Fig. 6 show temperature profiles calculated using the ANSYS/Fluent CFD package in the domains shown in Fig. 5. Those simulations employed a continuum model in the bulk of the gas, with the temperature-dependent gas thermal conductivity in Eqs. (3) and (7), and the temperature jump thermal resistance at the gas-solid interfaces [Eq. (6)] with the Lin-Willis temperature jump coefficient [Eq. (8)]. For the planar and cylindrical configurations, these profiles exhibit excellent agreement with the S-model kinetic calculations for Kn = 0.001, 0.01, and 0.1 (the three highest pressures) but diverge at Kn = 1 (the lowest pressure). These Knudsen numbers are consistent with the mildly rarefied temperature jump regime, i.e., $10^{-3} < \mathrm{Kn} < 10^{-1}$ (Ref. 14).

Figure 7 shows the dimensionless heat transfer reduction ratio $(Q_C - Q)/Q_C$ versus gas pressure for both enclosures in Fig. 5, and α = 1, 0.4, and 0.2. In this

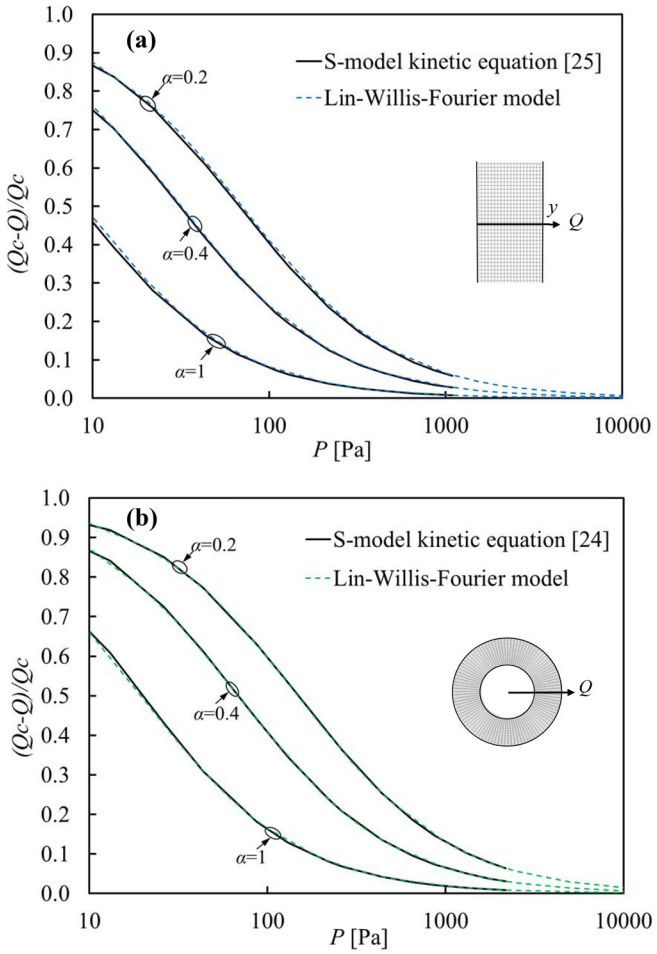

Fig. 7. Heat transfer reduction ratio versus gas pressure and thermal accommodation coefficient from the S-model kinetic equation and the Lin-Willis temperature jump model: (a) planar gap and (b) annular gap.

expression, Q is the conduction heat transfer between the walls for the given pressure and thermal accommodation coefficient, and Q_C is the heat transfer in the continuum regime. The solid and dashed lines show results from the S-model kinetic simulations and the ANSYS/Fluent simulations with the Lin-Willis temperature jump model, respectively. The two models are in excellent agreement for the pressure range included in Fig. 7 ($P > 10$ Pa). They show that the heat transfer reduction increases as the pressure decreases (and the gas becomes more rarefied) and as α decreases (and the gas accommodation to the wall decreases). The quality of the agreement decreases as the pressure decreases. Complete comparisons between the Lin-Willis temperature jump model and S-model kinetic equation results are presented in Ref. 40. The quantitative agreement between the S-model and Lin-Willis temperature jump models justifies implementing the temperature jump model in the domain in Fig. 1 to predict cladding temperatures under mildly rarefied conditions.

V. RAREFIED GAS HEAT TRANSFER WITHIN A CANISTER

As mentioned earlier, Boltzmann equation solutions are needed to calculate temperatures within the canister under rarefied conditions. Those solutions are computationally intensive, particularly in such a complex enclosure. However, for mildly rarefied gases, the effects are concentrated near the gas-solid interfaces. Section IV showed that this effect may be accurately modeled in "simple" gaps between parallel plates and concentric cylinders using continuum (Navier-Stokes and Fourier) equations subjected to the Lin-Willis temperature jump contact resistance at the gas-solid interfaces.

In this section, we implement this temperature jump thermal resistance at all gas-solid interfaces within the computation domain shown in Fig. 1. These interfaces are at the surfaces of the Zircaloy fuel rods, stainless steel basket openings, aluminum basket outer surfaces, and stainless steel canister. Simulations are performed for a range of fuel heat generation rates Q_F and for gas pressures of $P = 100$ and 400 Pa, which are near the lowest values experienced during vacuum drying. Correlations show that the thermal accommodation coefficient for helium gas in contact with engineering surfaces decreases from $\alpha = 0.4$ to 0.2 as the interface temperature increases from 300 to 700 K (Ref. 37). In this work, simulations are performed for $\alpha = 1$, 0.4, and 0.2. However, in the current model, the value of α is the same for all interfaces (regardless of temperature). In future work, an improved model will be implemented in which the local value of α, and its effect on the temperature jump, will be dependent on the local interface temperature.

Temperature contour plots from simulations that use the temperature jump model, a fuel heat generation rate of $Q_F = 1498$ W/assembly, and the range of α and P considered in this work are similar to the one shown in Fig. 2 and are not included in this paper. The dashed lines in Fig. 3 show temperature profiles along the r-axis from the Lin-Willis temperature jump model for $P = 100$ Pa and $\alpha = 1$, 0.4, and 0.2. These profiles are between the continuum and hard vacuum results. The shapes of the rarefied gas simulations are very similar to those from the continuum and hard vacuum results. The major dissimilarity is the temperature difference across the narrow helium-fill gap between the basket and canister, $r = 83$ to 84 cm. This temperature difference is affected by the temperature jumps at the gas-solid interfaces on either side of the helium-filled gap.

Table I summarizes the basket surface temperature difference ΔT_{BS} and peak cladding temperature difference ΔT_{PC} for $\alpha = 1$, 0.4, and 0.2 and $P = 100$ and 400 Pa. As described earlier, these are the increases of these temperatures compared to the continuum simulation results caused by reduced pressure. Table I shows that these temperature differences increase as the accommodation coefficient and the pressure decrease. Moreover, the value of ΔT_{PC} is at most a few degrees larger than ΔT_{BS}. This indicates that the effect of rarefaction is much smaller in the gas-filled regions within the basket openings than it is in the gap between the basket and canister. This is because the heat flux in the basket opening is small compared to the flux at the basket exterior. Also, radiation heat transfer carries a larger fraction of the heat within the basket than it does near the canister, due to the temperatures of these regions.

The dashed lines in Fig. 4 show the peak clad temperature versus fuel heat generation rate from the rarefied gas simulations. These lines are not parallel to the continuum simulation result, which shows that the difference between the peak clad temperature under rarefied and continuum conditions increases slightly with the fuel heat generation rate. Table II summarizes the maximum allowable heat generation rates Q_{FL} (the values of Q_F in Fig. 4 that cause the peak clad temperature to reach T_L) for each pressure, thermal accommodation coefficient, and cladding limit temperature considered in this work. It indicates that for $T_L = 400$°C and $P = 100$ Pa, the maximum allowable heat generation rates are 11%, 25%, and 35% less for $\alpha = 1$, 0.4, and 0.2, compared to the continuum conditions. For $P = 400$ Pa, the respective reductions are 3%, 10%, and 17%. For $T_L = 370$°C, the limit fuel heat generation rate Q_{FL} is reduced by 12% to 14% compared

to $T_L = 400°C$. Even though the values of Q_{FL} for the rarefied gas simulations are less than the values for the continuum simulations, they are greater than the average fuel assembly heat generation rates allowed in the standard or enhanced horizontal storage module Certificate of Compliance: 1000 and 1700 W/assembly (Refs. 24 and 25).

We wish to confirm that the helium-filled void spaces within the canister are actually in the slip flow regime for the conditions considered in this paper. This regime is characterized by the Knudsen number range $0.001 \leq Kn = \lambda/L_C \leq 0.1$. As mentioned earlier, the characteristic dimension L_C of the helium-filled spaces within the canister shown in Fig. 1 is not as easily defined as those of the simple enclosures shown in Fig. 5. The range of surface-to-surface spacing is between 2.3 and 9.5 mm. Moreover, the different gas temperatures and pressures from each simulation affect the mean-free-path length λ. For the higher pressure $P = 400$ Pa, the Knudsen number is in the range $0.01 \leq Kn \leq 0.05$, which is well within the slip flow regime. However, for the lower pressure $P = 100$ Pa, the Knudsen number is in the range $0.03 \leq Kn \leq 0.19$. Under those circumstances, the gas may be slightly in the transitional regime, which is more rarefied than the slip region. However, this depends on the choice of the characteristic length scale used in Kn.

VI. TRANSIENT TEMPERATURE RESPONSE WITHIN A CANISTER

The analysis to predict cladding temperatures under vacuum-drying conditions described so far assumes that the fuel and canister reach their steady-state temperatures. However, at the beginning of the drying process, the fuel is relatively cool because it was recently removed from a water-filled pool. As mentioned earlier, the vacuum-drying process requires between 12 and 100 h to complete.[13] In this section, we determine if the fuel and basket approach steady-state conditions during this time.

To do this, we assume that at the beginning of the drying process, the temperature throughout the canister is uniform at 101.7°C. This temperature is conservatively based on assuming that the water within and outside the canister is boiling. Transient simulations are then performed to calculate the fuel and canister temperatures versus time after the water within the canister is replaced by dry helium. This simplified calculation neglects several aspects of the actual drying process, including the period to drain the liquid water, and vaporization and transport of the remaining liquid. Simulations assuming the void spaces are filled with dry rarefied helium, with $P = 100$ Pa and $\alpha = 0.4$, and dry atmospheric pressure helium are performed with $Q_F = 1498$ W/assembly.

Figure 8 shows the peak cladding temperatures versus time from both simulations. The continuum simulation temperature rises quickly for 15 h. It goes 98% of its way from its initial to its steady-state temperature after 20.3 h. The rarefied simulation temperature goes 98% of the way to its steady-state value after 29.6 h. Rarefaction reduces conduction heat transfer in the helium and increases the steady-state fuel temperatures, and this increases the transition time. The simulations were repeated using the limit assembly heat generation rates in Table II, which are $Q_F = Q_{FL} = 3202$ and 2408 W/assembly for the continuum and rarefied gas conditions, respectively. The 98% transition times for these simulations are 4% to 7% shorter than they are for the 1498 W/assembly calculations. Radiation heat transfer transports more energy at the high temperatures associated with the higher heat generation rate and causes them to reach steady state more quickly. Since these transient times are of the same order as the amount of time required to dry canisters (12 to 100 h), we conclude it is reasonable to use steady-state simulations to estimate the peak cladding temperature during drying.

VII. SUMMARY

Currently, cask vendors do not include the effect of gas rarefaction when predicting the temperature of UNF cladding during vacuum-drying operations. The objective of this work was to determine the effect of gas rarefaction during those operations.

A geometrically accurate two-dimensional computational mesh of a helium-filled UNF canister similar to the

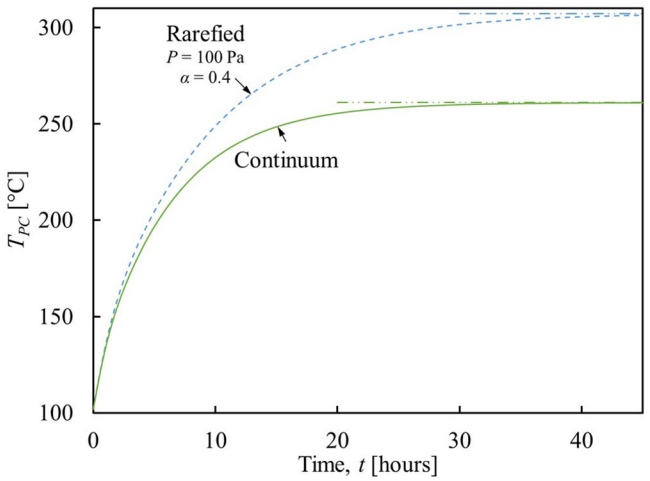

Fig. 8. Peak clad temperature versus time after helium replaces water in the canister. Results are shown from the continuum model and the Lin-Willis rarefied model with $P = 100$ Pa and $\alpha = 0.4$, with $Q_F = 1498$ W/assembly.

NUHOMS TN-24PTH was constructed. A model for heat transfer across mildly rarefied helium was developed using thermal resistance at gas-solid interfaces. This model was based on results from Lin and Willis,[28] dependent on the thermal accommodation coefficient α, and found to accurately reproduce temperature profiles and heat transfer across simple gaps calculated by the Shakhov kinetic model[26,27] of the Boltzmann equation. While the value of α actually depends on surface temperature, in the current implementation it is uniform at all gas-solid interfaces (which may be at different temperatures).

Steady-state simulations were performed to predict the peak cladding temperature for a range of fuel heat generation rates under both continuum conditions (no interface resistance) and for mildly rarefied helium at P = 100 and 400 Pa and α = 1, 0.4, or 0.2. For atmospheric pressure (continuum) helium, the fuel heat generation rate that brings the peak cladding temperature to 400°C is Q_{FL} = 3202 W/assembly.

The effect of rarefaction was mostly concentrated in the narrow gap between the basket and canister walls. If the helium is rarefied at 100 Pa, for α = 1, 0.4, or 0.2, Q_{FL} is reduced by 11%, 25%, or 35%, respectively. For a helium pressure of 400 Pa, the respective reductions are 3%, 10%, and 17%. However, even under these rarefied conditions, the heat generation rates that bring the peak cladding temperature to 400°C during vacuum drying are larger than that allowed by the canister's Certificate of Compliance. A transient simulation shows that the cladding temperature approaches steady-state conditions between 20 and 30 h after water is removed from the package. This indicates that steady-state simulations accurately predict clad temperatures at the end of canister drying processes that require 12 to 100 h to complete. The current work did not include the effects of water vaporization or transport during the drying process. These phenomena may be considered in future research.

Acknowledgment

This work was supported by the U.S. Department of Energy Office of Nuclear Energy University Program. The authors thank the Mesocentre of Aix-Marseille University for the supercomputing resources under project number 13b015.

References

1. "Characteristics of Spent Nuclear Fuel, High-Level Waste, and Other Radioactive Wastes Which May Require Long-Term Isolation," DOE/RW-0184, U.S. Department of Energy, Office of Civilian Radioactive Waste Management (Dec. 1987).
2. J. H. SALING and A. W. FENTIMAN, *Radioactive Waste Management*, 2nd ed., Taylor and Francis, New York (2002).
3. "HI-STORM 100 FSAR," Report HI-2002444, Rev. 8, Holtec International (2010).
4. D. COLMONT and P. ROBLIN, "Improved Thermal Modeling of SNF Shipping Cask Drying Process Using Analytical and Statistical Approaches," *Packag. Transp. Storage Secur. Radioact. Mater.*, **19**, *3*, 160 (2008); http://dx.doi.org/10.1179/174651008X362593.
5. B. HANSON et al., "Gap Analysis to Support Extended Storage of Used Nuclear Fuel," FCRD-USED-2011-000136 Rev. 0, U.S. Department of Energy Used Fuel Disposition Campaign (2012).
6. "Cladding Considerations for the Transportation and Storage of Spent Fuel," Interim Staff Guidance 11, Rev. 3, U.S. Nuclear Regulatory Commission (2003).
7. R. S. DAUM et al., "Radial-Hydride Embrittlement of High-Burnup Zircaloy-4 Fuel Cladding," *J. Nucl. Sci. Technol.*, **43**, *9*, 1054 (2006); http://dx.doi.org/10.1080/18811248.2006.9711195.
8. R. S. DAUM, S. MAJUMDAR, and M. C. BILLONE, "Experimental and Analytical Investigation of the Mechanical Behavior of High-Burnup Zircaloy-4 Fuel Cladding," *J. ASTM Int.*, **5**, *5*, 1 (2008); http://dx.doi.org/10.1520/JAI101209.
9. M. C. BILLONE, T. A. BURTSEVA, and R. E. EINZIGER, "Ductile-to-Brittle Transition Temperature for High-Burnup Cladding Alloys Exposed to Simulated Drying-Storage Conditions," *J. Nucl. Mater.*, **433**, 431 (2013); http://dx.doi.org/10.1016/j.jnucmat.2012.10.002.
10. M. C. BILLONE, T. A. BURTSEVA, and Y. Y. LIU, "Baseline Properties and DBTT of High-Burnup PWR Cladding Alloys," *Proc. Int. Symp. Packaging and Transportation of Radioactive Materials (PATRAM 2013)*, San Francisco, California, August 18–23, 2013.
11. W. S. LARGE and R. L. SINDELAR, "Review of Drying Methods for Spent Nuclear Fuel," WSRC-TR-0075, Westinghouse Savannah River Company (1997).
12. H. G. KIM, Y. H. JEONG, and K. T. KIM, "The Effects of Creep and Hydride on Spent Fuel Integrity During Interim Dry Storage," *Nucl. Eng. Technol.*, **42**, *3*, 249 (2010); http://dx.doi.org/10.5516/NET.2010.42.3.249.
13. W. BRACEY and P. SMITH, "Transnuclear Drying Experience and Lessons Learned," presented at ASTM Workshop, Atlanta, Georgia, 2012.
14. S. A. SCHAAF and P. L. CHAMBRE, *Flow of Rarefied Gases*, Princeton University Press, Princeton, New Jersey (1961).

15. L. B. LOEB, *Kinetic Theory of Gases*, 2nd ed., McGraw-Hill Book Company (1934).

16. K. SINGH, "Method and Apparatus for Dehydrating High Level Waste Based on Dew Point Temperature Measurement," U.S. Patent 8,266,823 B2, Holtec International (2012).

17. Y. S. TSENG et al., "Thermal Design Investigation of a New Tube-Type Dry-Storage System Through CFD Simulations," *Ann. Nucl. Energy*, **38**, 1088 (2011); http://dx.doi.org/10.1016/j.anucene.2011.01.001.

18. N. R. CHALASANI, P. ARAYA, and M. GREINER, "Benchmark of Computational Fluid Dynamics Simulations Using Temperatures Measured Within Enclosed Vertical and Horizontal Arrays of Heated Rods," *Nucl. Technol.*, **167**, *3*, 371 (2009); http://dx.doi.org/10.13182/NT167-371.

19. N. R. CHALASANI and M. GREINER, "Benchmark of Computational Fluid Dynamics Simulations Using Temperatures Measured Within Enclosed Vertical and Horizontal Arrays of Heated Rods," *Proc. ASME 2010 Pressure Vessels and Piping Division/K-PVP Conf.*, Bellevue, Washington, July 18–22, 2010, American Society of Mechanical Engineers (2010).

20. S. H. YOO et al., "Full-Scope Simulation of a Dry Storage Cask Using Computational Fluid Dynamics," *Nucl. Eng. Des.*, **240**, 4111 (2010); http://dx.doi.org/10.1016/j.nucengdes.2010.08.009.

21. R. A. BREWSTER et al., "CFD Analyses of the TN-24P PWR Spent Fuel Storage Cask," *Proc. ASME 2012 Pressure Vessels and Piping Conf.*, Toronto, Ontario, Canada, July 15–19, 2012, American Society of Mechanical Engineers (2012).

22. "Topical Report on the HI-STAR/HI-STORM Thermal Model and Its Benchmarking with Full-Size Cask Test Data," HI-992252, Holtec International (2000).

23. "The TN-24P PWR Spent Fuel Storage Cask: Testing and Analyses," EPRI NP-5128, Electric Power Research Institute (1987).

24. "Certificate of Compliance for Spent Fuel Storage Casks, NUHOMS®-24P," Certificate Number 1004, Docket Number 72-1004, U.S. Nuclear Regulatory Commission (Jan. 23, 1995).

25. "Standardized Advanced NUHOMS® Horizontal Modular Storage System for Irradiated Nuclear Fuel," NUH-003, Rev. 8, Transnuclear, Inc. (June 2004).

26. I. GRAUR, M. T. HO, and M. WÜEST, "Simulation of the Transient Heat Transfer Between Two Coaxial Cylinders," *J. Vac. Sci. Technol. A*, **31**, *6*, 061603 (2013); http://dx.doi.org/10.1116/1.4818870.

27. I. A. GRAUR and A. POLIKARPOV, "Comparison of Different Kinetic Models for the Heat Transfer Problem," *Heat Mass Transfer*, **46**, 237 (2009); http://dx.doi.org/10.1007/s00231-009-0558-x.

28. J. T. LIN and D. R. WILLIS, "Kinetic Theory Analysis of Temperature Jump in a Polyatomic Gas," *Phys. Fluids*, **15**, 31 (1972); http://dx.doi.org/10.1063/1.1693750.

29. J. M. CREER et al., "The TN-24P PWR Spent Fuel Storage Cask: Testing and Analyses," PNL-6054, Pacific Northwest National Laboratory (1987).

30. M. F. MODEST, *Radiative Heat Transfer*, 2nd ed., Academic Press, New York (2003).

31. R. H. BAHNEY and T. L. LOTZ, "Spent Nuclear Fuel Effective Thermal Conductivity Report," U.S. Department of Energy, TRW Environmental Safety Systems, Inc. (1996).

32. "NUHOMS®-24PTH DSC Thermal Evaluation for Storage and Transfer Conditions," Project No. NUH24PTH, Transnuclear Inc.

33. G. A. BIRD, "Definition of Mean Free Path for Real Gases," *Phys. Fluids*, **26**, 3222 (1983); http://dx.doi.org/10.1063/1.864095.

34. E. H. KENNARD, *Kinetic Theory of Gases*, McGraw-Hill Book Company, New York (1938).

35. F. O. GOODMAN, "Thermal Accommodation Coefficients," *J. Phys. Chem.*, **84**, 1431 (1980); http://dx.doi.org/10.1021/j100449a002.

36. S. C. SAXENA and R. K. JOSHI, *Thermal Accommodation & Adsorption Coefficients of Gases*, CRC Press (1989).

37. S. SONG and M. M. YOVANOVICH, "Correlation of Thermal Accommodation Coefficient for 'Engineering' Surfaces," *Proc. 24th ASME Natl. Heat Transfer Conf. and Exposition: Fundamentals of Conduction and Recent Developments in Contact Resistance*, Pittsburgh, Pennsylvania, August 9–12, 1987, p. 107, American Society of Mechanical Engineers (1987).

38. F. SHARIPOV, "Data on the Velocity Slip and Temperature Jump on a Gas-Solid Interface," *J. Phys. Chem. Ref. Data*, **40**, 023101 (2011); http://dx.doi.org/10.1063/1.3580290.

39. F. SHARIPOV, "Data on the Velocity Slip and Temperature Jump Coefficients," *Proc. 5th Int. Conf. EuroSimE: Thermal and Mechanical Simulation and Experiments in Micro-Electronics and Micro-Systems*, Brussels, Belgium, 2004, p. 243, IEEE (2004); http://dx.doi.org/10.1109/ESIME.2004.1304046.

40. D. MAHARJAN et al., "Simulation of Heat Transfer Across Rarefied Gas in Annular and Planar Geometries: Comparison of Navier-Stokes, S-Model and DSMC Methods Results," *Proc. Int. Conf. Nanochannels, Microchannels, and Minichannels (InterPACK/ICNMM2015)*, San Francisco, California, July 6–9, 2015, American Society of Mechanical Engineers (2015).

Mustafa Hadj-Nacer[1]
Mechanical Engineering Department,
University of Nevada, Reno,
Reno, NV 89557
e-mail: mhadjnacer@unr.edu

Dilesh Maharjan
Mechanical Engineering Department,
University of Nevada, Reno,
Reno, NV 89557
e-mail: dileshz@gmail.com

Minh-Tuan Ho
Department of Mechanical and
Aerospace Engineering,
University of Strathclyde,
Glasgow G1 1XJ 5, UK
e-mail: minh-tuan.ho@strath.ac.uk

Stefan K. Stefanov
Professor
Institute of Mechanics,
Bulgarian Academy of Science,
Sofia 1113, Bulgaria
e-mail: stefanov@imbm.bas.bg

Irina Graur
Aix Marseille Université,
CNRS, IUSTI UMR 7343,
13453, Marseille, France
e-mail: irina.martin@univ-amu.fr

Miles Greiner
Professor,
Fellow ASME
Mechanical Engineering Department,
University of Nevada, Reno,
Reno, NV 89557
e-mail: greiner@unr.edu

Continuum and Kinetic Simulations of Heat Transfer Trough Rarefied Gas in Annular and Planar Geometries in the Slip Regime

Steady-state heat transfer through a rarefied gas confined between parallel plates or coaxial cylinders, whose surfaces are maintained at different temperatures, is investigated using the nonlinear Shakhov (S) model kinetic equation and Direct Simulation Monte Carlo (DSMC) technique in the slip regime. The profiles of heat flux and temperature are reported for different values of gas rarefaction parameter δ, ratios of hotter to cooler surface temperatures $\mathcal{T}$, and inner to outer radii ratio $\mathcal{R}$. The results of S-model kinetic equation and DSMC technique are compared to the numerical and analytical solutions of the Fourier equation subjected to the Lin and Willis temperature-jump boundary condition. The analytical expressions are derived for temperature and heat flux for both geometries with hotter and colder surfaces having different values of the thermal accommodation coefficient. The results of the comparison between the kinetic and continuum approaches showed that the Lin and Willis temperature-jump model accurately predicts heat flux and temperature profiles for small temperature ratio $\mathcal{T} = 1.1$ and large radius ratios $\mathcal{R} \geq 0.5$; however, for large temperature ratio, a pronounced disagreement is observed. [DOI: 10.1115/1.4035172]

1 Introduction

Used nuclear fuel assemblies consists primarily of square arrays of zircaloy cladding tubes containing highly radioactive solids and gases [1]. They are initially stored underwater, while their heat generation and radioactivity decrease [2]. After sufficient time, individual assemblies are placed in square openings within helium-fill canisters. Before a canister is sealed, vacuum drying is used to remove remaining moisture [3]. During periods of time of this process, the helium within the canister's narrow spaces is in the rarefied-gas slip regime. This causes the cladding temperature to increase compared to continuum gas conditions. The cladding temperature must be accurately predicted to assure its temperature does not exceed certain important-to-safety limits [4].

The ultimate goal of this research is to develop and experimentally benchmark computational methods to predict surface temperatures of complex void spaces containing slip-regime gases. For moderately low-surface temperature differences and for surfaces with radii of curvature that are larger than the mean-free path (mean distance traveled by molecules between two successive collisions), transport across slip-regime gases may be approximated using continuum Fourier conduction in the gas' bulk and temperature-jump boundary condition at its interfaces with heated surfaces [5].

In the current paper, conduction across annular gaps filled with slip regime helium calculated from two kinetic gas methods (Shakhov-model [6–8] and direct simulation Monte Carlo [9]) are compared to calculations from continuum models with temperature-jump boundary conditions. Annular gaps with a range of radius ratios are simplified models for regions within used fuel canister and other engineering systems. In this paper, comparisons are made between the continuum and kinetic models for a range of radius ratios, surface temperature ratios, gas rarefaction parameters, and surface accommodation coefficients. These comparisons are used to determine the conditions where the continuum models with temperature-jump boundary conditions may be used with confidence for the *simple* annular gap geometry. Future work will compare continuum and kinetic models for calculating heat transfer within an enclosed array of heated rods with experiment data in order to determine when the continuum models may be used in *complex* configurations.

[1]Corresponding author.
Contributed by the Heat Transfer Division of ASME for publication in the JOURNAL OF HEAT TRANSFER. Manuscript received April 12, 2016; final manuscript received November 3, 2016; published online January 10, 2017. Assoc. Editor: George S. Dulikravich.

2 Problem Formulation

The problem of conduction heat transfer between parallel plates and coaxial cylinders separated a gas at rest is considered here (see Fig. 1). The radii and temperatures of the inner and outer cylinders are (R'_1, T'_{w1}) and (R'_2, T'_{w2}), respectively, with $R'_1 < R'_2$ and $T'_{w1} > T'_{w2}$. For simplicity, the same notation is used for parallel plates: the r' axis is normal to both plate's surfaces. The bottom and upper plates have the locations and temperatures (R'_1, T'_{w1}) and (R'_2, T'_{w2}), respectively, with $R'_2 = -R'_1 = H'/2$. The cylinders and plates are assumed to have infinite length in the direction perpendicular to the figure.

Both problems are similar; however, the coaxial cylinder problem is governed by three physical parameters (temperature and radius ratios, and rarefaction parameter; see definitions below). The parallel plate problem is defined by only two parameters (temperature ratio and rarefaction parameter). It is convenient to introduce the following parameters:

- the temperature ratio between the cylinders or plates: $\mathcal{T} = T'_{w1}/T'_{w2}$
- the aspect ratio for the cylinders and plates: $\mathcal{R} = |R'_1/R'_2|$,
- the rarefaction parameter

$$\delta = \frac{R_0}{\ell}, \quad \text{where} \quad \ell = \frac{\mu_0 \upsilon_0}{p_0}, \quad \upsilon_0 = \sqrt{\frac{2k_B T_0}{m}} \tag{1}$$

In these expressions, ℓ is the equivalent mean-free path at reference pressure p_0, m is the molecular mass of the gas, k_B is the Boltzmann constant, and υ_0 is the most probable molecular velocity at reference temperature T_0.

In expression (1), R_0 and T_0 are the reference space dimension and temperature, respectively, and μ_0 is the gas viscosity calculated at the reference temperature; $\mu_0 = \mu(T_0)$.

It is convenient to take the distance between the cylinders (or plates) as the reference space dimension, $R_0 = R'_2 - R'_1$. The temperature of the external cylinder (or upper plate) is used as the reference temperature, $T_0 = T'_{w2}$. The problem of heat transfer considered here is one-dimensional; therefore, the heat flux has only one component in the direction normal to the surfaces, denoted by q'.

For practical reasons, the following dimensionless variables are introduced:

$$r = \frac{r'}{R_0}, \quad p = \frac{p'}{p_0}, \quad T = \frac{T'}{T_0}, \quad \text{and} \quad q = \frac{q'}{p_0 \upsilon_0} \tag{2}$$

The influence of the gas–surface interaction is taken into account by the thermal accommodation coefficient, denoted as

$$\alpha = \frac{T_i - T_r}{T_i - T_w} \tag{3}$$

where T_i and T_r are the temperature of the incident and reflected molecules, respectively.

3 Continuum Approach

The analytical expressions for heat flux and temperature can be obtained from an energy balance. The hypothesis of zero macroscopic velocity and constant pressure between the plates or cylinders are used to derive the analytical expressions. The Fourier law can be applied to calculate the heat flux

$$q' = -\kappa' \frac{dT'}{dr'} \tag{4}$$

For monatomic gases, the gas thermal conductivity κ' is related to the gas viscosity μ' as follows [9]:

$$\kappa' = \frac{15}{4}\frac{k_B}{m}\mu' \tag{5}$$

In order to define the dependence of viscosity on temperature, the molecular interaction potential must be specified. In this work, the inverse power law potential [9] is employed, which leads to a power law temperature dependence for the viscosity

$$\mu' = \mu_0 \left(\frac{T'}{T_0}\right)^{\omega} \tag{6}$$

where ω is the viscosity index, which is equal to 0.5 for the hard-sphere (HS) model and 1 for the Maxwell model. Its value varies as a function of the gas nature in the case of variable hard-sphere (VHS) model, see Ref. [9]. In this paper, the hard-sphere model is retained for all calculations, so $\omega = 0.5$ for all gases.

In the continuum regime, the temperature continuity condition may be assumed on the surfaces. However, in the slip regime, the temperature-jump conditions [10] must be used as boundary conditions

$$T'_g = T'_w + \xi_T \ell \left.\frac{dT'}{dr'}\right|_w \tag{7}$$

where T'_g is the gas temperature near the wall and ξ_T is the temperature-jump coefficient [11]. The dimensionless form of the temperature-jump boundary condition at the cylinders' and plates' walls can be written as

$$T = \begin{cases} T_{w1} + \dfrac{\xi_{T1}}{\delta} T_{w1}^{\omega+1/2} \dfrac{dT}{dr}, & r = R_1 \\ T_{w2} - \dfrac{\xi_{T2}}{\delta} T_{w2}^{\omega+1/2} \dfrac{dT}{dr}, & r = R_2 \end{cases} \tag{8}$$

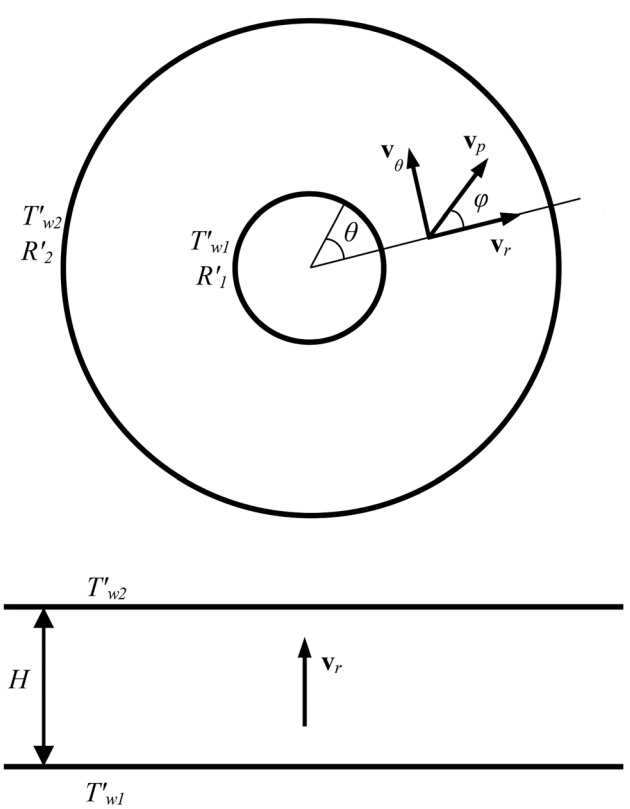

Fig. 1 Cross section of (*a*) two coaxial cylinders and (*b*) two parallel plates configurations: dimensions (r, θ) in physical space; dimensions $(\upsilon_r, \upsilon_\theta)$ (or (υ_p, φ)) in molecular velocity space

Here, ξ_{T1}, ξ_{T2} are the temperature-jump coefficients of the hotter and colder surfaces, respectively. The assumption of the constant pressure between the cylinders and plates is used to obtain the previous expressions. The coefficient ξ_T in Eqs. (7) and (8) depends on the gas nature and surface state through the thermal accommodation coefficient. Lin and Willis [12] proposed the following expression for polyatomic gases:

$$\xi_T = \left(\frac{2-\alpha}{\alpha} + 0.17\right)\frac{\sqrt{\pi}}{\mathrm{Pr}}\frac{\gamma}{\gamma+1} \tag{9}$$

obtained by applying a variational method to the Morse equation [13] and to the Holway model [14]. In Eq. (9), γ is the gas specific heat ratio and Pr is the Prandtl number. For monatomic gases, this expression is reduced to the one proposed by Welander [15]. For the case of complete accommodation ($\alpha = 1$) and a monatomic gas ($\gamma = 5/3$ and $\mathrm{Pr} = 2/3$), the value of this coefficient is $\xi_T \sim 1.95$.

In this paper, Eq. (4) subjected to the boundary condition (8) is solved numerically using an iterative method for parallel plates and coaxial cylinders having different temperature and aspect ratios at different values of the rarefaction parameter δ in the slip regime and various values of the thermal accommodation coefficient α.

3.1 Analytical Solution. To obtain the completely explicit expression of the temperature distribution between the cylinder and plates, a linearization of the temperature is carried out and the terms of the order of ε^2 are neglected, where $\varepsilon = (T_w - T_g/T_w)$ (Eq. (7)), so the temperature profile between the cylinders and plates is obtained analytically with accuracy of ε^2.

3.1.1 Parallel Plates. The following dimensionless analytical expressions are obtained for the temperature profile

$$T(r) = \left\{\frac{1}{2}\left[\left(T_{g1}^{\omega+1} + T_{g2}^{\omega+1}\right) + C(\omega+1)(R_1 + R_2 - 2r)\right]\right\}^{\frac{1}{\omega+1}} \tag{10}$$

and heat flux profile

$$q(r) = \frac{15}{8\delta}C \tag{11}$$

where

$$C = \frac{\left(T_{w1}^{\omega+1} - T_{w2}^{\omega+1}\right)/(\omega+1)}{R_2 - R_1 + \frac{\xi_{T1}}{\delta}T_{w1}^{\omega+1/2} + \frac{\xi_{T2}}{\delta}T_{w2}^{\omega+1/2}} \tag{12}$$

The gas temperatures near the walls are

$$\begin{aligned} T_{g1}^{\omega+1} &= T_{w1}^{\omega+1}[1 - \eta_1(\omega+1)] \\ T_{g2}^{\omega+1} &= T_{w2}^{\omega+1}[1 - \eta_2(\omega+1)] \end{aligned} \tag{13}$$

where

$$\eta_1 = \frac{\xi_{T1}}{\delta}C\frac{1}{T_{w1}^{1/2}}, \quad \eta_2 = -\frac{\xi_{T2}}{\delta}C\frac{1}{T_{w2}^{1/2}} \tag{14}$$

Here, the dimensionless coordinates R_1 and R_2 for parallel plates are $R_1 = -0.5$ and $R_2 = 0.5$.

3.1.2 Coaxial Cylinders. By implementing the same technique, the temperature and heat flux profiles for coaxial cylinders were obtained, as in Ref. [16]. The dimensionless temperature profile with an accuracy of ε^2 is

$$T(r) = \left\{\frac{1}{2}\left[\left(T_{g1}^{\omega+1} + T_{g2}^{\omega+1}\right) + C(\omega+1)\left(\ln\left(\frac{R_1}{r}\right) + \ln\left(\frac{R_2}{r}\right)\right)\right]\right\}^{\frac{1}{\omega+1}} \tag{15}$$

and the dimensionless heat flux profile is

$$q(r) = \frac{15}{8\delta}\frac{C}{r} \tag{16}$$

where

$$C = \frac{\left(T_{w1}^{\omega+1} - T_{w2}^{\omega+1}\right)/(\omega+1)}{\ln\frac{R_2}{R_1} + \frac{\xi_{T1}}{\delta}\frac{T_{w1}^{\omega+1/2}}{R_1} + \frac{\xi_{T2}}{\delta}\frac{T_{w2}^{\omega+1/2}}{R_2}} \tag{17}$$

In this paper, two aspect ratios are considered, $\mathcal{R} = 0.5$ and $\mathcal{R} = 0.1$. The corresponding dimensionless coordinate [R_1, R_2] for each case are [1, 2] and [0.11, 1.11], respectively. The gas temperature in the vicinity of the walls is calculated with the same expressions (13) as for the two parallel plates, with the parameters ε_1 and ε_2 calculated as

$$\eta_1 = \frac{\xi_{T1}}{\delta}\frac{C}{R_1}\frac{1}{T_{w1}^{1/2}}, \quad \eta_2 = -\frac{\xi_{T2}}{\delta}\frac{C}{R_2}\frac{1}{T_{w2}^{1/2}} \tag{18}$$

The analytical model is more convenient to calculate the temperature profile between the cylinders and plates than the numerical model as it needs no iteration.

4 Kinetic Approach

Two kinetic models are used in this paper to simulate heat transfer between parallel plates and coaxial cylinders in the slip regime.

4.1 S-Model Kinetic Equation. In the steady-state case, the S-model kinetic equation [6] reads

$$\mathbf{v}\frac{\partial f'}{\partial \mathbf{r}'} = \nu'\left(f^{S\prime} - f'\right) \tag{19}$$

where $f'(\mathbf{r}', \mathbf{v})$ is the one particle molecular velocity distribution function, $\mathbf{v}$ is the molecular velocity vector, $\mathbf{r}'$ is the position vector, and ν' is the molecular collision frequency. It should be underlined that Eq. (19) is valid if a Cartesian frame is used in the velocity space. In the case of the two coaxial cylinders, an axisymmetric problem, the transport part of Eq. (19), can be written in the form used in Refs. [8] and [17].

The equilibrium distribution function $f^{S\prime}$ is

$$\begin{aligned} f^{S\prime} &= f^{M\prime}\left[1 + \frac{2m\mathbf{V}\mathbf{q}'}{15n'(k_BT')^2}\left(\frac{m\mathbf{V}^2}{2k_BT'} - \frac{5}{2}\right)\right] \\ f^{M\prime}(n', T') &= n'\left(\frac{m}{2\pi k_BT'}\right)^{3/2}\exp\left[-\frac{m(\mathbf{v}-\mathbf{u}')^2}{2k_BT'}\right] \end{aligned} \tag{20}$$

where $f^{M'}$ is the local Maxwellian distribution function, $\mathbf{u}'$ is the bulk velocity vector, $\mathbf{V} = \mathbf{v} - \mathbf{u}'$ is the peculiar velocity vector, and $\mathbf{q}'$ is the heat flux vector.

In the frame of this model, the molecular collision frequency is assumed to be independent of the molecular velocities and may be found as follows [6]:

$$\nu' = \frac{p'}{\mu'} \tag{21}$$

The macroscopic parameters are calculated from the solution of the molecular distribution function f' obtained by solving Eq. (19), as

$$T'(r') = \frac{m}{3n'k_B}\int\int \mathbf{V}^2 f'(\mathbf{r}', \mathbf{v})d\mathbf{v}$$
$$q'(r') = \frac{m}{2}\int\int \mathbf{V}V^2 f'(\mathbf{r}', \mathbf{v})d\mathbf{v} \quad (22)$$

Considering the axial symmetry of the problem, the S-model kinetic equation in the completely conservative form is found in Refs. [8], [18], and [19]. The generalization of a kinetic model for the case of the polyatomic gases is presented in Ref. [20].

The discrete velocity method (DVM) is used to divide the continuum-molecular velocity space c_p in the system of kinetic equations (see Ref. [8]) into a discrete velocity set c_{p_k}. The system of kinetic equations with discrete velocity set c_{p_k} is then discretized in space by the finite-difference method (FDM). The spatial derivatives are approximated by the second order-of-accuracy upwind-type numerical scheme. The Gauss–Hermite quadrature formulas are used to evaluate the integrals for calculating the macroscopic parameters (Eq. (22)).

In the physical space, the reduced distribution functions depend only on the spatial variable r, which is either the distance from the cylinder's axis or the distance from midway between the plates. For coaxial cylinders, the distance between the walls is split into N_r intervals, $N_r = 800$ for $\delta \leq 10$ and $N_r = 6400$ for $\delta > 10$. For parallel plates, $N_r = 4000$ for all δ. In the velocity space, the distribution functions depend on two variables: the magnitude and orientation of the molecular velocity vector c_{p_k} and φ, respectively. The velocity vector magnitude c_{p_k} is distributed according to the Gaussian quadrature rule, which is characterized by Gaussian abscissas N_{c_p} and their corresponding weights. The number of implemented points N_{c_p} depends on gas rarefaction: $N_{c_p} = 25$ for $\delta < 0.5$ and $N_{c_p} = 12$ for $\delta \leq 0.5$. The range of molecular velocity orientations $(0 \leq \varphi \leq \pi)$ is divided into N_φ equal intervals. For coaxial cylinders, $N_\varphi = 6400$ for $\delta \leq 10$ and $N_\varphi = 100$ for larger δ. For parallel plates, $N_\varphi = 100$ for all δ. Moreover, this range of φ is divided into two subdomains, according to the sign of the molecular velocity components. This set of the numerical grid parameters guarantees the accuracy for energy conservation law of the order of 0.1%.

4.2 Direct Simulation Monte Carlo (DSMC). The traditional DSMC technique proposed by Bird [9] is employed in this paper for the calculation of heat transfer between parallel plates and coaxial cylinders. The DSMC technique enables gas flows to be modeled on a molecular level by simulating the motion of individual particles according to their physical properties. This technique can be viewed as a Monte Carlo method for solving the time-dependent nonlinear Boltzmann equation. Within each time step t of the simulation, this method combines deterministic aspects for modeling particle motions with statistical aspects for computing collisions between particles. The collision technique that is used is the NoTime Counter scheme suggested by Bird, with a slight modification in the calculation of maximum number of collision in a cell, as described in Ref. [21].

The procedure for axis-symmetric flows is employed as given in Ref. [9]. For each particle, only the radial coordinate r and the three velocity components $\mathbf{v}_x$, $\mathbf{v}_r$, and $\mathbf{v}_\theta$ are stored. Then, the molecules are moved according to their velocities and acquire a new radial coordinate r^+ given by

$$r^+ = \sqrt{(r + \mathbf{v_r}\Delta t)^2 + (\mathbf{v}_\theta \Delta t)^2} \quad (23)$$

Following this procedure, the new velocity components, $\mathbf{v}_x^+$, $\mathbf{v}_r^+$, and $\mathbf{v}_z^+$, are

$$\mathbf{v}_x^+ = \mathbf{v_x},$$
$$\mathbf{v}_r^+ = \frac{\mathbf{v_r}(r + \mathbf{v_r}\Delta t) - \mathbf{v}_\theta^2 \Delta t}{r^+} \quad \text{and}$$
$$\mathbf{v}_z^+ = \frac{\mathbf{v_r}\mathbf{v}_\theta \Delta t - \mathbf{v}_\theta(r + \mathbf{v_r}\Delta t)}{r^+}$$

The domain is discretized in the radial direction using N_r computational cells (N_r ranges from 400 to 4000), and the particles are initially distributed in such a way that the minimum number of particles in each cell of the domain is $N_p = 50$. Since no weighting factors are used, the region where the number of particles per cell is the smallest corresponds to the area near the inner cylinder for geometrical reasons. The time step Δt is chosen to be less or equal to one-third the cell traversal time, $\Delta r/\sqrt{2kT_0/m}$. The macroscopic properties are obtained for the steady-state solution by time averaging over $N_T = 10{,}000$ time steps. The heat flux and other macroscopic quantities are volume based calculated by averaging the microscopic values of the particles at a given cell, $q_r = \overline{\mathbf{v_r}\mathbf{v}^2}$. For these grid and time parameters, the total computational error (systematic and statistical) is less than 1% in all the computed cases. Here, the available analyses of the splitting scheme and domain discretization [22,23] suggest a first-order systematic approximation error of $(O(\Delta t, \Delta r))$, with respect to the Boltzmann equation. The statistical error [24] is estimated as $O(1/\sqrt{N_T N_p})$.

It should be noted here that the computer code described above was employed for two coaxial cylinders with $\mathcal{R} = 0.1$ and 0.5, and two parallel plates with $\mathcal{R} = 0.999$.

5 Results and Discussions

In this section, results of steady-state heat transfer, between parallel plates and coaxial cylinders in the slip regime, obtained from kinetic and continuum approaches, are presented. The results are showed in graphical form for the macroscopic quantities (temperature, heat flux, and pressure) in term of all the quantities involved in the problem. For all three geometries, parallel plates ($\mathcal{R} = 1$) and coaxial cylinders ($\mathcal{R} = 0.5$ and 0.1), two temperature ratios $\mathcal{T} = 1.1$ and 2 are examined. The value of the rarefaction parameter δ is varied from 500 to 3, which covers the continuum, slip, and near transitional regimes [25]. In this work, we wish to determine the conditions where the difference between the continuum and kinetic results is of the same order as the difference between the S-model and DSMC results.

5.1 Dimensionless Temperature Profiles. In order to assess the limit of applicability of the continuum models, first, a comparison of the dimensionless temperature profiles obtained from the S-model and DSMC technique is performed. Figure 2 shows the dimensionless temperature distribution along the r-axis, obtained from the kinetic (S-model and DSMC) approaches and the continuum (numerical and analytical) models for the temperature and radius ratios considered in this work, in the case of full accommodation of the molecules at the walls ($\alpha_1 = \alpha_2 = 1$) and for different values of rarefaction parameter $\delta = 100$, 50, 10, and 3.

Comparison between the profiles of dimensionless temperature obtained from the kinetic model shows that the S-model and DSMC technique are in good agreement for all $\mathcal{T}$, $\mathcal{R}$, and δ employed in this paper. Both models exhibit the same profile even in the Knudsen layers (local nonequilibrium region with a thickness $\sim O(\ell)$ from the wall).

As expected, for $\mathcal{T} = 1.1$, the profiles of dimensionless temperature from the continuum numerical and analytical (10, 15) models exhibit a nearly linear trend for parallel plates and a nearly logarithmic trend for coaxial cylinders. This is due to the relatively small thermal conductivity variation across the gaps. For the smaller temperature ratio ($\mathcal{T} = 1.1$, left plots), the numerical and analytical temperature profiles are very similar for all values of δ, but the difference increases as $\mathcal{R}$ decreases. For the larger temperature ratio ($\mathcal{T} = 2$, right plots), the difference between the two continuum models is larger and increases as δ decreases. In all cases, the temperatures predicted by the numerical model are systematically larger than that from the analytical model, but within 2%. This difference comes from the linearization of the temperature used in the analytical model; see Secs. 3.1.1 and 3.1.2.

The comparison between dimensionless temperature profiles obtained from the continuum and kinetic models is divided into two categories according to the temperature ratio $\mathcal{T}$.

- For $\mathcal{T} = 1.1$ and all $\mathcal{R}$, there is a good agreement between the two types of models for $\delta = 100$ and 50. For $\delta = 10$, the agreement is good in the core of the gap (away from the walls), except for the case $\mathcal{R} = 0.1$. Deviations are observed close to the walls. For smaller δ, there is disagreement even within the core of the gap for all aspect ratios $\mathcal{R}$.
- For $\mathcal{T} = 2$, the agreement between the continuum and kinetic models for $\delta = 100$ and 50 is not as close as it is for $\mathcal{T} = 1.1$. However, for smaller $\delta \leq 10$, the disagreement increases as δ decreases.

Figure 2 visibly shows that the temperature-jump at the walls increases as δ decreases. The temperature-jump at the hotter wall is larger than the corresponding one at the cooler wall and it increases as $\mathcal{R}$ decreases. Furthermore, as $\mathcal{T}$ increases, the temperature-jump at both walls increases. However, the increase

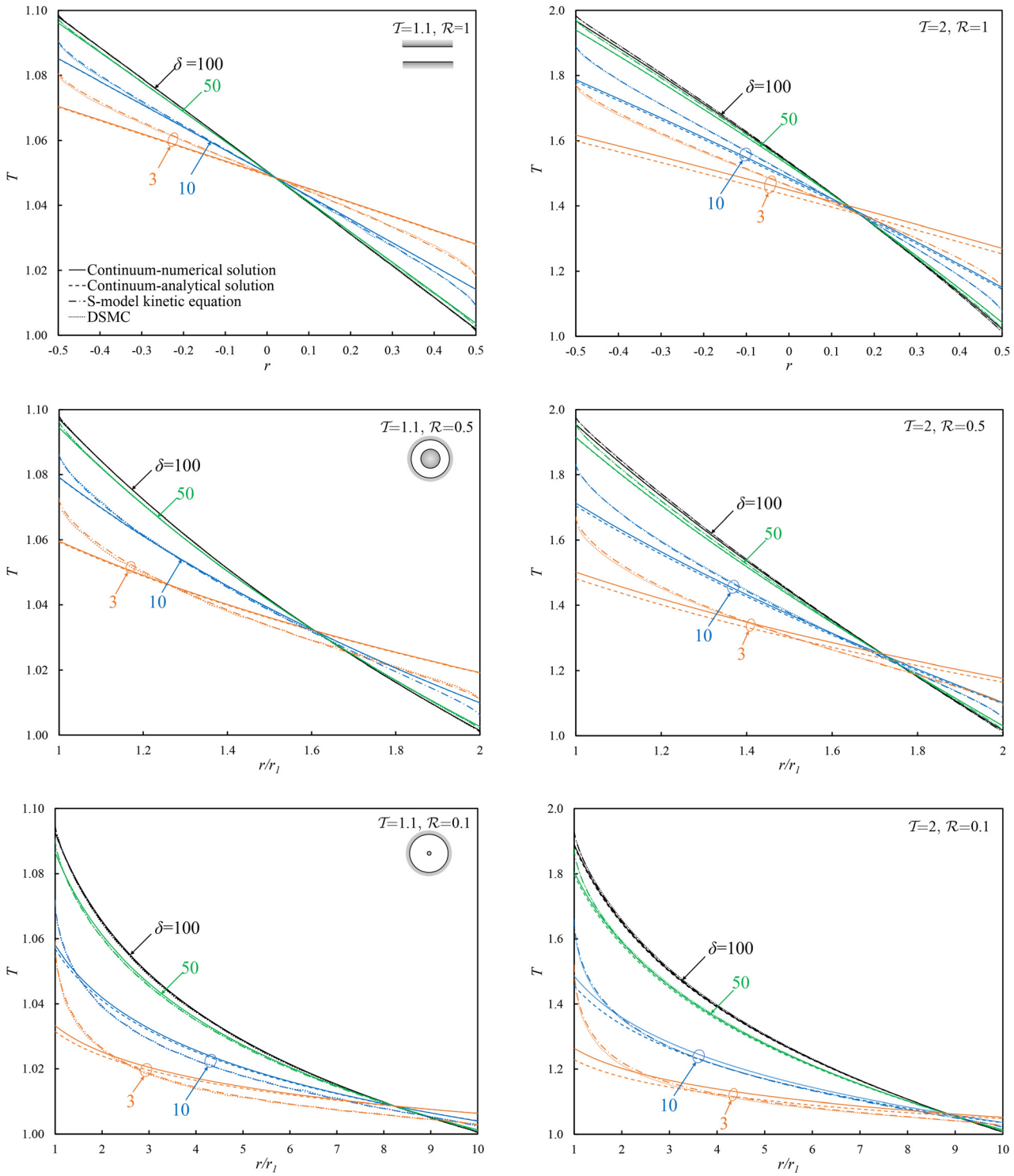

Fig. 2 Dimensionless temperature profiles between plates and cylinders for all combination of $\mathcal{R}$ and $\mathcal{T}$ and different values of rarefaction parameters $\delta = 100$, 50, 10, and 3 in case $\alpha = 1$

of $\mathcal{T}$ has a larger effect on the jump at the inner wall than the outer wall. This is because the gas becomes more rarefied as its temperature increases.

Overall, the temperature-jumps at the walls predicted by the continuum models increase as δ and $\mathcal{R}$ decrease, and $\mathcal{T}$ increases and they are larger than those predicted by the kinetic models.

5.2 Dimensionless Heat Flux. Figure 3 shows the dimensionless heat flux q, which is the quantity of practical interest in this paper, plotted as a function of rarefaction parameter δ for all combinations of $\mathcal{T}$ and $\mathcal{R}$ considered in this paper and for $\alpha = 1$, 0.6 and 0.2 with $\alpha = \alpha_1 = \alpha_2$. Results from kinetic (S-model and DSMC) and continuum (numerical and analytical) approaches are included.

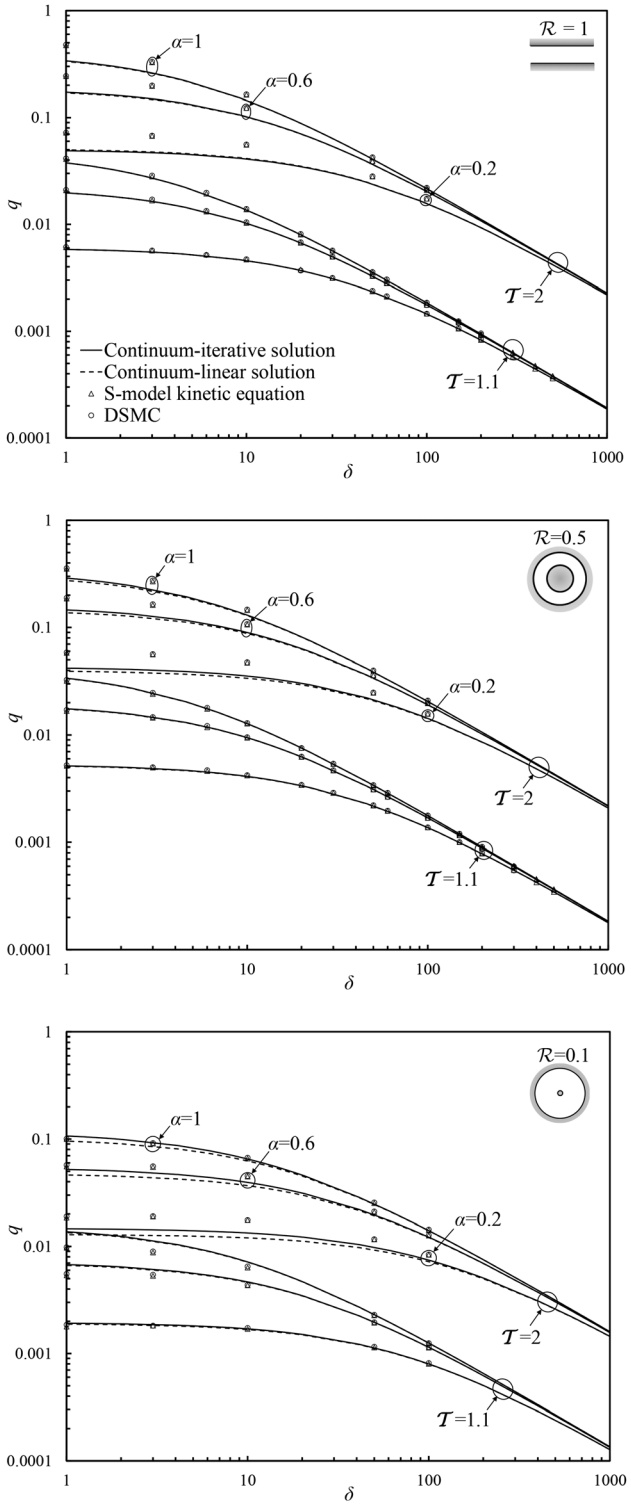

Fig. 3 Dimensionless heat flux as function of the rarefaction parameter δ obtained for all combination of $\mathcal{R}$ and $\mathcal{T}$ and different values of thermal accommodation coefficient α

It is clear from this figure that the value of q increases as δ decreases and α and $\mathcal{T}$ increase. The values of q obtained from both continuum models (numerical and analytical) are in a good agreement for case $\mathcal{T} = 1.1$, regardless $\mathcal{R}$ and α. For $\mathcal{T} = 2$, the discrepancy between the two models increases as δ, α, and $\mathcal{R}$ decrease. The value of q for the continuum numerical model is systematically larger than the continuum-analytical model.

At $\mathcal{T} = 1.1$, the continuum and kinetic results are in good agreement for all values of δ, except for cases $\mathcal{R} = 0.1$ and $\alpha = 1$. The reason of this discrepancy is not clear and may be investigated further. For $\mathcal{T} = 2$, the agreement is good for $\mathcal{R} = 0.1$ and $\alpha = 1$, but is less good as α decreases and $\mathcal{R}$ increases.

The disagreement between the continuum and kinetic models, especially at large $\mathcal{T}$, may be explained from the profiles of dimensionless pressure along the r-axis. Figure 4 shows that these profiles between the cylinders and plates are obtained from the S-model kinetic equation in the case of full accommodation of the molecules at the walls. The results are plotted for $\mathcal{T} = 1.1$ and 2, $\mathcal{R} = 1$, 0.5, and 0.1, and $\delta = 100$, 50, 10, and 3. The r-axis was scaled to be between 1 and 2 as described in the caption for convenience of comparison. From this figure, it can be seen that, in all cases, the pressure varies along the r-axis between the cylinders and plates and this variation is larger as δ and $\mathcal{R}$ decrease, and $\mathcal{T}$ increases. As mentioned earlier, the continuum models assume that the pressure is constant along the r-axis. Figure 4 shows that the pressure variation is very small for $\mathcal{T} = 1.1$, which explains the good agreement obtained between the continuum and kinetic approaches. However, for $\mathcal{T} = 2$, the pressure variation is significant for $\delta \leq 10$; therefore, the assumption of the constant pressure is not valid. This may explain the disagreement obtained in these cases.

Figure 5 gives the percentage difference of dimensionless heat flux q between DSMC and S-model and the continuum-numerical and S-model for both temperature and aspect ratios, and for three values of the thermal accommodation coefficient considered in this work. It can be seen from this figure that the heat fluxes obtained from the DSMC and S-model are within 3% of each other in all configurations. This difference decreases as δ increases and the gas approaches the continuum regime. It is also

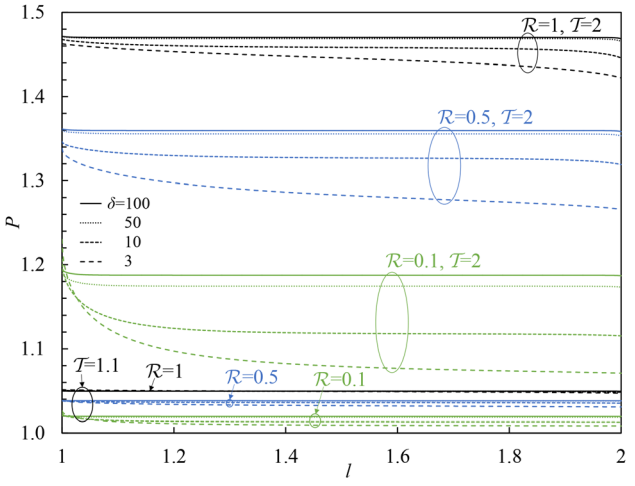

Fig. 4 Dimensionless pressure profiles between plates and cylinders for all combination of $\mathcal{R}$ and $\mathcal{T}$ and different values of rarefaction parameters $\delta = 100$, 50, 10, and 3 in case $\alpha = 1$. $l = r$ for $\mathcal{R} = 0.5$ and $l = 1 - R_1 + r$ for $\mathcal{R} = 1$ and 0.1.

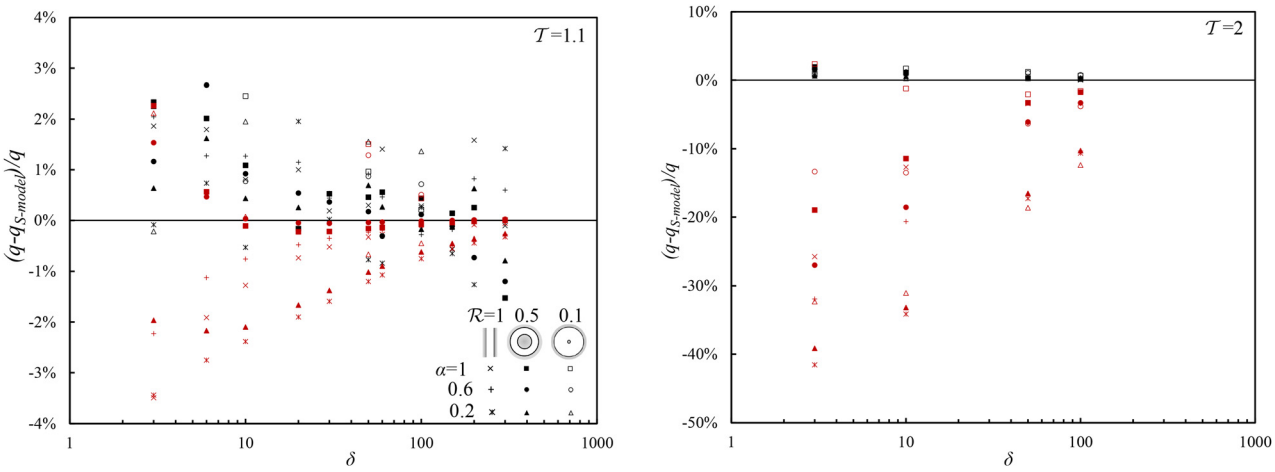

Fig. 5 Percent deference of the dimensionless heat flux q between S-model and DSMC, and Numerical-continuum models as function of the rarefaction parameter δ obtained for all combinations of $\mathcal{T}$ and $\mathcal{R}$ and different values of thermal accommodation coefficient α

clear from Fig. 5 that, for the case $\mathcal{T} = 1.1$, the percentage difference between the continuum-numerical and S-model is smaller than 4% for all values of $\mathcal{R}$, α, and δ, which is of the order of the difference between the DSMC and S-model approaches. However, in case $\mathcal{T} = 2$, the percentage difference between the continuum-numerical and S-models is significantly larger than the corresponding difference between DSMC and S-model and of the order of 50% at small δ. This quantitative comparison between the continuum and kinetic approaches clearly demonstrates that the continuum models are appropriate for simulating heat transfer for small temperature ratio; however, for large ratio, their ability is largely reduced even at large value of $\delta \geq 50$.

In general, it can be concluded that the continuum models are accurate for $\delta \geq 10$ and $\mathcal{T} = 1.1$, and for $\delta \geq 50$ and $\mathcal{T} = 2$, regardless the aspect ratio.

6 Conclusion

The steady-state heat transfer through rarefied gas confined between coaxial cylinders and parallel plates is studied using continuum and kinetic approaches in the slip regime. The calculations were conducted for different temperature and radius ratios. Both walls were assumed to have the same value of thermal accommodation coefficient α.

The dimensionless temperature and heat flux were obtained from S-model and DSMC were compared to continuum numerical and analytical solutions of the Fourier equation subjected to the Lin and Willis temperature-jump boundary condition at the walls.

The two continuum models were in good agreement for all values of δ and α, with maximum difference less than 2%, observed for case $\mathcal{T} = 2$ and $\mathcal{R} = 0.1$. The comparison between the continuum and kinetic approaches showed that the continuum models are valid in the slip regime for a temperature ratio of $\mathcal{T} = 1.1$; however, for $\mathcal{T} = 2$, they are only valid for $\delta \geq 50$.

It should be noticed that here the temperature boundary conditions are employed in the paper. However, sometimes in practice, it is important to be able to employ constant heat flux boundary conditions so that the heat exchange between the system and the surroundings can be controlled. The examples of the implementation of the heat flux boundary conditions are given in Refs. [26] and [27] for the DSMC and kinetic approaches, respectively.

Acknowledgment

This work was supported by the U.S. Department of Energy Office of Nuclear Energy University Program. This work was granted access to the HPC resources of Aix-Marseille Université, under the project number 13b015, financed by the project Equip@Meso (ANR-10-EQPX-29-01) of the program"Investissements d'Avenir" supervised by the Agence Nationale pour la Recherche.

References

[1] U.S. Dept. of Energy, Office of Civilian Radioactive Waste Management (OCRWM), 1987, "Characteristics of Spent Nuclear Fuel, High-Level Waste, and Other Radioactive Wastes Which May Require Long-Term Isolation," Report No. DOE/RW-0184.
[2] Saling, J. H., and Fentiman, A., 2002, *Radioactive Waste Management*, 2nd ed., Taylor and Francis, New York.
[3] Colmont, D., and Roblin, P., 2008, "Improved Thermal Modeling of SNF Shipping Cask Drying Process Using Analytical and Statistical Approaches," Packag. Transp. Storage Secur. Radioact. Mater., **19**(3), pp. 160–164.
[4] USNRC staff, 2003, "Cladding Considerations for the Transportation and Storage of Spent Fuel," U.S. Nuclear Regulatory Commission, Memorandum No. 11, Revision No. 3.
[5] Kennard, E. H., 1938, *Kitetic Theory of Gases*, McGraw-Hill, New York.
[6] Shakhov, E. M., 1968, "Generalization of the Krook Kinetic Relaxation Equation," Fluid Dyn., **3**(5), pp. 95–96.
[7] Graur, I. A., and Polikarpov, A., 2009, "Comparison of Different Kinetic Models for the Heat Transfer Problem," Heat Mass Transfer, **46**(2), pp. 237–244.
[8] Graur, I., Ho, M. T., and Wuest, M., 2013, "Simulation of the Transient Heat Transfer Between Two Coaxial Cylinders," J. Vac. Sci. Technol. A, **31**(6), p. 061603.
[9] Bird, G. A., 1994, *Molecular Gas Dynamics and the Direct Simulation of Gas Flows*, Oxford Science Publications, Oxford University Press, New York.
[10] Cercignani, C., 1990, *Mathematical Methods in Kinetic Theory*, Premuim Press, New York.
[11] Kogan, M. N., 1969, *Rarefied Gas Dynamics*, Plenum Press, New York.
[12] Lin, J. T., and Willis, D. R., 1972, "Kinetic Theory Analysis of Temperature Jump in a Polyatomic Gas," Phys. Fluids, **15**(1), pp. 31–38.
[13] Morse, T. F., 1964, "Kinetic Model for Gases With Internal Degrees of Freedom," Phys. Fluids, **7**(2), pp. 159–169.
[14] Holway, L. H., 1966, "New Statistical Models in Kinetic Theory: Methods of Construction," Phys. Fluids, **9**(9), pp. 1658–1673.
[15] Welander, P., 1954, "On the Temperature Jump in a Rarefied Gas," Ark. Fys., **7**(5), pp. 507–553.
[16] Graur, I., and Ho, M. T., 2014, "Rarefied Gas Flow Through a Long Rectangular Channel of Variable Cross Section," Vacuum, **101**, pp. 328–332.
[17] Sone, Y., and Sugimoto, H., 1995, "Evaporation of a Rarefied Gas From a Cylindrical Condensed Phase Into a Vacuum," Phys. Fluids, **7**(8), p. 2072.
[18] Larina, I. N., and Rykov, V. A., 1998, "A Numerical Method for Calculating Axisymmetric Rarefied Gas Flows," Comput. Math. Math. Phys., **38**(8), pp. 1335–1346.
[19] Shakhov, E. M., and Titarev, V. A., 2009, "Numerical Study of the Generalized Cylindrical Couette Flow of Rarefied Gas," Eur. J. Mech. B/Fluids, **28**(1), pp. 152–169.
[20] Hsu, S. K., and Morse, T. F., 1972, "Kinetic Theory of Parallel Plate Heat Transfer in a Polyatomic Gas," Phys. Fluids, **15**(4), pp. 584–591.
[21] Stefanov, S., Gospodinov, P., and Cercignani, C., 1998, "Monte Carlo Simulation and Navier-Stokes Finite Difference Solution of Rarefied Gas Flow Problems," Phys. Fluids, **10**(1), pp. 289–300.

[22] Gallis, M. A., Torczynski, J. R., Rader, D. J., and Bird, G. A., 2009, "Convergence Behavior of a New DSMC Algorithm," J. Comput. Phys., **228**(12), pp. 4532–4548.
[23] Stefanov, S. K., 2011, "On DSMC Calculations of Rarefied Gas Flows With Small Number of Particles in Cells," SIAM J. Sci. Comp., **33**(2), pp. 677–702.
[24] Hadjiconstantinou, N. G., Garcia, A. L., Bazant, M. Z., and He, G., 2003, "Statistical Error in Particle Simulations of Hydrodynamic Phenomena," J. Comput. Phys., **187**(1), pp. 274–297.
[25] Schaaf, S. A., and Chambre, P. L., 1958, "Flow of Rarefied Gases," *Fundamental of Gasdynamics*, H. W. Edmmons, ed., Vol. III., Princeton University Press, Princeton, NJ, pp. 687–739.
[26] Akhlaghi, H., Roohi, E., and Stefanov, S., 2012, "A Newiterative Wall Heat Flux Specifying Technique in DSMC for Heating/Cooling Simulations of MEMS/NEMS," Int. J. Therm. Sci, **59**, pp. 111–125.
[27] Meng, J., Zhang, Y., and M. R. J., 2015, "Numerical Simulation of Rarefied Gas Flows With Specified Heat Flux Boundary Conditions," Commun. Comput. Phys., **17**(5), pp. 1185–1200.

Experimental Validation of Heat Transfer Simulations for a Vertical Heated Rod Array within a Square-Cross-Section, Helium-Filled Isothermal Enclosure

Dilesh Maharjan[1]
University of Nevada Reno
1664 North Virginia St MS 312
Reno, NV 89557
dileshm@nevada.unr.edu

Mustafa Hadj-Nacer
University of Nevada Reno
1664 North Virginia St MS 312
Reno, NV 89557
mhadjnacer@unr.edu

Narayana Chalasani
Johns Manville
10100 W Ute ave.
Littleton, CO80127
NarayanaRao.Chalasani@jm.com

Miles Greiner
University of Nevada Reno
1664 North Virginia St MS 312
Reno, NV 89557
greiner@unr.edu

ABSTRACT

Computational fluid dynamics simulations of an 8x8 array of vertical heater rods within a square cross-section, helium-filled pressure vessel are performed for a range of enclosure temperatures, helium pressures and rod heat generation rates. This configuration is relevant to a used nuclear fuel assembly within a dry storage canister. To assess the accuracy of the simulations, the temperature results are compared to measurements made in the same configuration. The simulations use the measured enclosure temperatures as boundary conditions, so they essentially calculate the temperature difference between the rods and

[1] Corresponding author

enclosure. These differences are as large as 72°C for some experiments. The measured temperature of rods near the periphery of the array are highly dependent on to small, uncontrolled variations in their location. As a result, those temperatures are not as useful for validating the simulations as measurements from rods nearer the array center. The simulated rod temperatures exhibit random differences from the measurements that are as large as 5.7°C, but the systematic (average) error is 1°C or less. The random differences between the simulated and measured maximum array temperature is 2.1°C, which is less than 3% of the maximum rod-to-wall temperature difference.

BACKGROUND AND OBJECTIVE

Nuclear fuel assemblies consist primarily of 7x7 to 17x17 arrays of fuel rods held in place by periodic spacer plates [1, 2]. Each rod is a sealed zircaloy cladding tube containing uranium dioxide fuel pellets and pressurized gas. The pellets become highly radioactive and generate heat while they are within a reactor. After removal from a reactor, used fuel is stored under water while its radioactivity and heat generation decrease. After sufficient time, a canister with an internal basket, which has multiple square-cross-section openings to support individual assemblies, is placed in a transfer cask. The cask and canister are lowered into the water, loaded with assemblies, covered, lifted from the pool and drained. Vacuum drying [3, 4] is commonly used to remove remaining moisture. This reduces possible corrosion and/or formation of combustible oxygen/hydrogen mixtures. The canister is then filled with atmospheric or higher pressure helium, sealed, and placed in other packaging for onsite dry storage or offsite transport.

In some storage facilities, the canister is placed vertically inside a concrete structure. These structures have ports at the top and bottom to allow atmospheric air to cool the canister by natural convection. Within the canister, heat generated by the assemblies causes helium to flow upward in the basket openings, and downward in vertical passages near the canister periphery. This thermal syphoning cools the fuel assembles beyond the levels that would exist due to conduction

and thermal radiation alone. Thermal syphoning is governed by the ratio of buoyancy to viscous forces, which is characterized by the Grashof number [5]

$$Gr = \frac{g\mathrm{B}(T_M - \bar{T}_W)\rho^2 L^3}{\mu^2} \qquad \text{Eqn. 1}$$

In this expression, g is gravitation acceleration, B is the coefficient of thermal expansion, T_M is the maximum cladding temperature, ρ and μ are, respectively the average gas density and dynamic viscosity, and L is the height of the heated fuel rods. Based on simulations for a canister that contains 24 fuel assemblies [6], the Grashof number is of the order $Gr \sim 10^9$.

After an assembly is removed from a reactor, its cladding must not exceed temperatures of approximately 400°C [7]. This helps to avoid the formation of radial hydrides, which may embrittle the cladding and make the used fuel assembly unsuited for subsequent transport and/or processing. The fuel cladding may reach its highest temperature during vacuum drying because that is the first operation when it is not in direct contact with water, and the fuel's heat generation rate is relatively high. Moreover, during vacuum drying, the helium is evacuated to pressures as low as 70 Pa [8, 9]. At these pressures the gas inside some regions of the canister is rarefied to the extent that there are thermal resistances at the interfaces between the gas and heated surfaces [4, 6, 10, and 11]. These resistances increase the cladding temperature relative to those experienced when the gas acts as a continuum. In order to manage cladding temperatures during vacuum drying, water is circulated in a gap between the canister and transfer cask to cool the canister surface.

After vacuum drying the canister is re-pressurized with helium, eliminating rarefied-gas thermal resistances. If the canister is placed in an air-cooled storage facility, its surface

temperature may increase compared to when it is in water. As a result, another candidate event when the cladding may reach its highest temperature is early dry storage. It is therefore important to develop and experimentally-validate computational tools to predict cladding temperatures during and after vacuum drying.

The computational models Heating5, ANSYS/Mechanical, COBRA-SFS and ANSYS/Fluent have been used to construct two and three-dimensional models of whole loaded canisters [12-15]. These models are used to predict cladding temperatures relative to different canister environments, for a range of fuel heat generation rates and helium pressures. Some of these simulations accurately model the geometry of fuel rods within each basket opening [6], while others use a "smeared" fuel blocks with an effective thermal conductivity to model each assembly [16, 17]. Internal temperatures at a limited number of locations within loaded canisters have been measured in a variety of packaging designs and pressures [18, 19]. Comparison of simulated temperatures with these data have been used to assure that the simulations accurately predict (or conservatively over-predict) canister temperatures [20].

These validated whole-canister simulations are useful for predicting the total temperature difference between the cladding and the canister environment, and the relative magnitude of temperature-differences across certain canister components. For example, the temperature difference between the environment and canister surface, as well as those across helium-fill regions within the canister, are generally larger than the differences across metal components, whose thermal conductivities are relatively high [6]. However, loaded canisters are very large and complex structures. If a whole-canister simulation correctly predicts certain measured temperatures, there is no assurance that it accurately calculates conduction, convection and radiation heat transfer in every portion of the canister. As a result, the validated simulation may

have limited utility when predicting how design changes of individual canister components effect cladding temperatures.

The temperature differences across the helium-filled regions between the basket and cladding surfaces are significantly larger than those across metal components [6]. Heat transfer across those regions is affected by conduction, natural convection and radiation, and its geometry is somewhat complex. A number of experiments [21-24] have measured temperatures of enclosed arrays of heated rods, which are similar to a used fuel assembly within a support basket opening. These data have been used to validate computational fluid dynamics simulations [25-28]. However, the range of rod heat generation rates, contained gas composition and pressure, and/or enclosure temperatures are not sufficient to validate the whole range of operating conditions.

The goal of the current work is to experimentally-validate results from ANSYS/Fluent computational fluid dynamics (CFD) simulations for a configuration that is relevant to a helium-filled region inside a basket opening of a used fuel canister. An earlier experiment measured temperatures within an apparatus consisting of a vertical 8x8 array of electrically heated rods held in place by stainless steel spacer plates at either end, within an aluminum helium-filled pressure vessel [27, 28]. In this paper we consider data from that work for atmospheric and higher pressures, which are relevant to post-drying conditions. An ANSYS/Fluent model of the apparatus is developed, and simulations are performed for a range of gas pressures, vessel and spacer plate temperatures, and rod heat generation rates. The ability of ANSYS/Fluent to accurately reproduce the measured temperatures is assessed. In this work we define configuration errors as temperature variations that are caused by experimental geometric and boundary conditions that cannot be precisely controlled. This work attempts to identify locations where these errors are large, because those measurements are not as useful for validating simulations as those where the errors are small.

EXPERIMENTAL APPARATUS

The experimental apparatus is designed to represent a section of a fuel assembly between consecutive spacer plates, within a helium-filled basket opening [27, 28]. A disassembled view is shown in Fig. 1. It consists of (a) an 8x8 array of heater rods, (b) two stainless steel spacer plates, and (b) a square anodized aluminum enclosure. Each heater rod is 1.1 cm in diameter and 67.3 cm long. The sheath of each rod is made of 0.7-mm-thick Incoloy with compressed Magnesium Oxide (MgO) inside. Most of the rods are mildly bowed, such that the center of some rods are as much as 3 mm away from a line connecting the rod ends. Each rod contains a Nichrome heater coil. The coil ends are anchored to metal pins in both rod ends, which are connected to external power leads. The manufacturer specifies that heat generation is uniform along the length of the heater rods to within ±6%, except for 3.2 cm sections on both ends, which are unheated. For the 64 rods, the average and standard deviation of the heater resistances are, respectively 4 Ω and 0.12 Ω. Sets of eight heater rods are connected in series. The resulting eight sets are connected in parallel to a 0-1000W regulated DC power supply.

The stainless steel spacer plates are 0.635-cm-thick and 11.9 cm on each side. Both contain sixty-four 1.15-cm-diameter holes that hold the heater rods in position. The hole center-to-center pitch is 1.44 cm. A small threaded hole is centered between each set of four rod holes. To hold the heater rods in position, a bolt with an expansion ring is tightened in the threaded holes. The expansion ring pushes the rods to make them contact the far sides of the rod holes. This eccentricity and the rod bowing lead to small but random (uncontrolled) variations of the rod locations.

To make the enclosure as isothermal as possible, it is constructed by tungsten inert gas-welding four 2.54-cm thick aluminum plates, and then black anodized. Its interior forms a square 12 cm by 12 cm square, and its total length is 91.5 cm. Figure 2a shows an axial section of the assembled experiment. The heater rod array is centered axially within the enclosure, so there are 12-cm voids on each end to house power and thermocouple wires. The z-axis is shown, with its origin at the axial mid-plane. When in operation the heater rods are vertical, and the gravity vector $\vec{g}$ is oriented in the negative *z*-direction. The inner surfaces of the spacer plates are at $z = \pm 30.5$ cm, and are coplanar with the ends of the heated regions of the rods.

Forty-seven of the 64 heater rods contain Type-K (chromel/alumel) thermocouples, at one of four axial locations, z = -17.3, 0, 17.3 and 29.2 cm. These locations are known to tolerances of ±1.3 cm, and are indicated in Fig. 2a. In each instrumented rod, a chromel wire exits one end while an alumel wire exits the other. Stainless steel endplates with O-rings are bolted to both ends to seal the enclosure. The top endplate has extension tubes with feedthroughs at their ends for thermocouple leads. The bottom endplate has a thermocouple/power feedthrough and another tube that is used to evacuate and backfill the enclosure. That tube is connected to a tree with an atmospheric valve, an evacuation valve connected to an oil filter attached to an oil-based vacuum pump, and high and low pressure gauges. To increase the enclosure temperature, fiberfrax insulation blankets, with thickness of either I = 2.5 or 5 cm, are used on enclosure and endplates. Figure 2b is a picture of the assembled apparatus wrapped in insulation.

In this sealed enclosure, buoyancy is expected to cause helium to flow upward in the warm center of the rod array, and downward near the relatively cool enclosure walls. This is somewhat different from the thermal syphoning pattern that exists in vertical storage canisters described earlier.

Figure 3 is a schematic of the experimental apparatus cross section. The *x* and *y* coordinate system is also shown. The circles represent heater rods. Each is named according to its row (A to H) and column (1 to 8) location. The number inside certain rods represents the *z*-location of the thermocouple within that rod. The 17 rods without numbers do not contain a thermocouple. Twelve thermocouples are installed in the enclosure walls to measure its temperature. Figure 3 shows wells in the middle of each walls whose end is 0.25 cm from the inner surface. Each wall has wells at *z* = -29, 0, and 29 cm. In Fig. 3 the four black-filled X's near center, top and upper corners of the rod array show the x,y-locations of thermocouples that are on both the top and bottom spacer plates. The open X near the bottom right corner indicates the position of a thermocouple that is only on the top spacer plate.

The section of the experiment in Fig. 3 is symmetric about the x and y axes, and diagonal lines connecting heater rods A1-H8 and rods H1-A8. Due to the nearly isothermal enclosure walls, symmetry of the experiment geometry and the expected natural convection flow pattern, rods that are symmetrically located on either side of the symmetry planes are expected to have nearly the same temperatures. Greek letters α, β, γ, δ, ε, ζ and η in Fig. 3 identify rods in seven symmetry groups that contain thermocouples. Table 1 lists the rods in each groups, and the z-locations of the thermocouples within them. The α group is the one that is closest to the array center, and the β, γ, δ, ε, ζ and η groups are located increasing further away.

Table 1 and Fig. 3 show that symmetry groups α, β and η have thermocouples at all four elevations, z = -17, 0, 17 and 29 cm. Measurements from each group may be assembled to construct an axial profile for a typical rod in that group. Based on distances of each group from the center of the array, groups α, β and η are expected to contain, respectively, the hottest, second hottest and coolest rods in the array.

All the thermocouples in symmetry groups γ, δ , ε and ζ are at z = 0. Based on symmetry, the temperature of the N = 6 or 7 thermocouples within each of these groups will be nearly identical. However, within each group the indicated temperature may differ by normally-distributed random amounts due to measurement and configuration errors. Configuration errors are caused by small but uncontrolled variations in the heater resistances, rod bowing, thermocouple placement in a rod, small variations in the enclosure temperature and other factors. While measurement errors are expected to be roughly the same for all symmetry groups, configuration errors will not be the same. In this work the variation in temperatures within each of these groups is used to determine the variation of configuration errors with group location.

TEMPERATURE MEASUREMENTS

Table 2 describes the twelve experiments that are presented in this paper. Experiments are performed for two insulation thicknesses I = 2.5 or 5 cm, three nominal helium pressures P_N = 1, 2, and 3 atm (which are measured when the apparatus is at room temperature), and three rod heat generation rates Q = 100, 300, and 500 W. For each experiment, Table 2 gives its Roman numeral experiment number, Exp#, the measured pressure P when the experiment reached steady state conditions (which is higher than P_N due to the higher steady state temperature), and Grashof number (eqn. 1). For the Grashof calculation, T_M and $\bar{T}_W$ are the maximum-rod and average-wall temperatures, and L is the heater rod length. The experiment Grashof numbers range from $Gr \sim 10^7$ *to* 10^8, which are one to two order of magnitude smaller than a nominal value for a vertical used fuel canister, $Gr \sim 10^9$. As described earlier, the flow pattern in the current experiment is also somewhat different from that of canisters.

All twelve experiments were performed in a laboratory where the temperature was controlled to be approximately 23°C. The enclosure, spacer plate and rod temperatures were measured using a data acquisition system at a sampling rate of 1 samples/minute. When the heaters were off and the apparatus reached steady state, all the thermocouples indicated approximately the same temperature, within a standard deviation of 0.5°C. After the heater rods are powered, approximately 25 hours were required for the temperatures to reach steady-state conditions. After steady state was reached, all temperatures were sampled for at least 30 minutes, and then averaged. The uncertainty of each thermocouple measurement was ±1.1°C.

The symbols in Fig. 4 show measured enclosure, spacer plate and heater rod temperatures versus axial (z) location for Experiments III (I = 2.5 cm, P = 3 atm, Q = 100 W) and VII (I = 2.5 cm, P = 1 atm, Q = 500 W). The temperature profile shapes in the two plots are similar, but their temperature scales are different. The solid circles at the bottom of each plot show the temperatures on all four enclosure walls at the three axial locations. At each elevation, the temperatures are not the same on the four walls, but the average temperature increases with elevation due to natural convection. For each experiment the four triangles at z = -29 cm and five triangles at z = 29 cm show, respectively, the temperatures of bottom and top spacer plates. Both plates are warmer than the enclosure, and the top plate temperature is higher than the bottom plate, again due to the natural convection inside the apparatus. As expected, on both spacer plates, the plate centers are hotter than locations near the enclosure walls.

For both experiments, the open squares, diamonds and circles show temperatures measured at four different axial locations within the α (hottest), β (second hottest) and η (coolest) rod symmetry groups. The α and η temperatures are measured in four different rods, as described in Table 1. The β temperatures (diamonds) are measured in eight different rods, and have two

measurements at all four elevations. For all experiments, the multiple temperature measurements at locations z = -17, 0 and 17 cm are approximately the same, whereas at z = 29 cm the temperatures differ by 1°C to 3°C. As described earlier, these differences are caused by configuration and measurements errors.

The Grashof number for Experiment III is seven times larger than that for Experiment VII. For Experiment III, in rod groups α and β, the temperatures at z = -17 cm are lower than they are at z = 17 cm. However the temperatures at these locations are closer to each other in Experiment VII, in which the effect of natural convection is less significant. The solid and dotted lines in Fig. 4 are simulated temperatures for the α, β and η group rods, which are described in a later section. The boundary conditions for those simulations are the measured enclosure wall and spacer plate temperatures, which are described in the next section.

Boundary Temperatures

In this work the average measured enclosure wall temperature, $\bar{T}_W$, is used to characterize each experiment. The horizontal lines in Figs. 4a and 4b shows averages in Experiments III and VII which are, respectively, $\bar{T}_W = 67$℃, and 218℃. In Fig. 5a the symbols connected by solid lines shows $\bar{T}_W$ versus the total rod heat generation rate *Q*, for all twelve experiments. As expected the average enclosure temperature increases with heat generation rate and insulation thickness. The data for *I = 2.5 cm* indicate that the average enclosure temperature is essentially independent of the gas pressure.

Figure 5a also shows the average temperature differences between the spacer plates and the enclosure walls. The symbols connected by dotted lines show data for the top spacer plate, $\bar{T}_T - \bar{T}_W$, while dashed lines are used for the bottom spacer plate, $\bar{T}_B - \bar{T}_W$. For all experiments the

upper spacer plate is warmer than the bottom. For I = 2.5 cm, the temperature differences are more strongly affected by the heat generation rate than the pressures considered in this work. As the pressure increases, the top spacer plate gets slightly hotter and the bottom spacer gets slightly cooler, but the change for these pressures is less than 2°C. Increasing the pressure increases the gas density, Grashof number, and the effect of natural convection. This causes the hottest locations on the rods to move to higher z-elevations, and explains why the top spacer plate temperature increase and the lower one decreases as pressure increases. Figure 5a also shows that the temperature difference between the spacer plates and the wall is significantly smaller for $I = 5\ cm$ than for $I = 2.5\ cm$. As already noted, the thicker insulation makes the apparatus hotter, which increases radiation heat transfer. This increase in heat transfer decreases the temperature difference between the enclosure walls and spacer plates.

To quantify the temperature variations within the enclosure wall, we define the temperature range that statistically contains 95% of the measure values, assuming they are normally distributed. This deviation temperature is twice as large as the sample standard deviation, and is calculated as [30]:

$$D_W = 2\sqrt{\frac{\sum\left(\bar{T}_W - T_{W,i}\right)^2}{N_W - 1}}. \qquad \text{Eqn. 2}$$

In this expression, $T_{W,i}$ is each individual measured wall temperature, and $N_W = 12$ is the number of wall measurements. The non-isothermality of the walls, and measurement errors, cause D_W to be non-zero. The top and bottom spacer plate deviations, D_T and D_B, which are calculated using Eqn. 2 but employing the top (*T*) and bottom (*B*) plate temperature measurements, assess measured temperature variations within those objects.

Figure 5b presents the measured temperature deviation versus heat generation rate for the three objects: enclosure wall (symbols connected with solid lines), and bottom (dashed lines) and top (dotted lines) spacer plates. The temperature deviation increases as the heat generation (and consequently object temperature) increases. For I = 2.5 cm the enclosure wall deviations increase marginally with gas pressure. The wall temperature deviation increases with insulation thickness because the insulation increases the wall temperature. For the top and bottom spacer plates, the deviations are nearly the same at P = 2 atm. However, as the pressure increases, the deviations on the top spacer plate increase (as its average temperature increases), while those of the bottom spacer plate decrease (as its average decreases). The temperature deviations on the spacer plates are smaller for I = 5 cm than they are for I = 2.5 cm. This is because as the insulation thickness increases the experiment temperature and the radiation heat transfer increase, which makes the experiment temperatures more uniform. Even though the enclosure is physically larger than the spacer plates, its deviations are smaller. This is due to higher thermal conductivity of aluminum compared to that of stainless steel. Comparing Figs. 5a and 5b shows that the temperature deviation in the spacer plates is not negligible compared to the average temperature difference between those plates and the enclosure.

Configuration Errors

As described earlier, all rods in symmetry groups γ, δ, ε and ζ have thermocouples at z = 0. The variations within each of these groups are used to quantify each group's configuration errors, which are caused by uncontrolled experimental geometric and boundary conditions. Figure 6 shows histograms of the measured temperatures in the $\gamma, \delta, \varepsilon$ and ζ symmetry groups for Experiment VII. The average and deviation (Eqn. 1) temperatures of each group are displayed in

its plot. As expected, the average temperature within each group decreases as its distance from the array center increases.

The average and deviation temperatures for the ζ group are $\bar{T}_\zeta = 247°C$ and $D_\zeta = 11°C$. While most of temperatures in this group are clustered between 247 and 251°C, an outlier is observed at 236°C, which was measured in rod A7. According to the Modified Thompson Tau test [30], for a quantity with normally-distributed variations, it is statistically unlikely that a value that is more than $|T - \bar{T}|_{max}/D = 0.856$ deviations from the average will be observed when only $N = 7$ measurements are acquired. The 236°C thermocouple reading is 1.1 deviations from the mean. Based on Modified Thompson Tau test, we conclude that the 236°C reading is caused by some factor that does not affect the other six readings (suspected to be an intermittent thermocouple junction) and may be rationally excluded from the group. With that measurement excluded, the revised average and deviation temperatures are $\bar{T}_{\zeta,R} = 249°C$ and $D_{\zeta,R} = 3°C$ (these values are given in the ζ figure). The thermocouple within the rod A7 produced outliers in a 9 experiments (I to IX) out of the 12, and those 9 measurements were excluded. While less apparent, according to the Modified Thompson Tau test, the lowest temperature in the δ symmetry group (within rod H5) in Fig. 6 was an outlier in all 12 experiments, and was excluded. No data from the γ or ε symmetry groups were eliminated.

After the Modified Thompson Tau test was used to eliminate 21 thermocouple measurements, the average ($\bar{T}_\gamma, \bar{T}_\delta, \bar{T}_\varepsilon,$ and $\bar{T}_\zeta$) and deviation ($D_\gamma, D_\delta, D_\varepsilon,$ and D_ζ) temperatures were determined for all four symmetry groups and all twelve experiments. Figure 7 is a plot of the temperature deviation for each group D_j (for j = γ, δ, ε and ζ) versus the average temperature difference between the group and the wall $\bar{T}_{kj} - \bar{T}_w$. Data from all twelve experiments are presented. Dotted

lines that are fit to the results of each group are included to better show trends in the data. For each group the deviation in temperature increases roughly linearly with the temperature difference.

The deviations in Fig. 7 are caused by both measurement and configuration errors. We expect the measurement errors from each group to be roughly the same, so the differences between groups is caused by the difference in configuration errors in each symmetry group. The configuration error is smallest for the γ group, which is the one that is closest to the array center. The error for the δ and ε groups, which are the second and third closest groups, are larger than those for the γ group. The ζ group, which is the furthest from the array center, has a lower error than those of the δ and ε groups.

To understand this behavior, we need to consider the temperature profiles along lines that radiate from the array axis (x = y = 0). These temperature profiles pass through the gas and rods. They are fairly flat near the axis, but exhibits steeper gradients near the walls. Bowing of the heater rods causes the thermocouples at z = 0 to be shifted in the x- and y-directions by small but random amounts. The rods in the γ group rods are relatively close to the array center, so small shifts in their location will not cause a large change in their temperatures. However, rods in the δ, ε and ζ groups are close to the walls where the radial temperature gradient is steep, so their temperatures are relatively sensitive to small location variations. However the temperature deviations within the ζ group are relatively small. It is possible that the rods in that group are relatively straight compared to that of the other groups. Unfortunately, it is not possible to test that hypothesis because the bowing of those rods were not observed before the experiment was disassembled.

Figure 7 shows that the configuration error within a symmetry group is larger for groups that are nearer the array periphery, because their temperatures are more sensitive to random location

variation than those in groups near the array axis. We conclude that measurements made near the array axis are more valuable for assessing the accuracy of simulations than ones near the periphery.

NUMERICAL SIMULATIONS

Computational Domain

Two and three-dimensional computational meshes representing the experimental apparatus were generated using ANSYS Meshing. Figure 8a shows an x,y-plane of a computational mesh. The outer portion of the plane consists of a 0.25-cm-thick aluminum region which represents the portion of the enclosure that is inside the locations where temperatures are measured. It also contains regions for the 64 heater rods (magnesium oxide core and zircaloy sheath), and the helium between the rods and enclosure. This mesh was extruded in the z-direction (normal to the plane of the mesh) to form the three-dimensional mesh.

At the ends of the extrusion, the properties of 0.635-cm-long regions are modified to represent the two stainless steel spacer plates. Figure 8b is an expanded view of Section 1 from Fig. 8a, showing the solid and gas regions near the spacer plates. Darker shaded regions show the helium-filled gaps. These gaps are between the spacer plate and enclosure wall (except at the corners where the spacer plates are supported), and between the rods and plate holes. As described earlier, expansion rings between each set of four rods press the rods against the portions of the spacer holes that are away from the rings. The resulting eccentricity of the rods and holes are represented in the mesh as a 45°-arc contact surface. The total number of mesh elements in the three-dimensional domain is 1,834,880. For comparison, another mesh was constructed with the rods symmetrically centered within the holes.

Temperature dependent material properties were assigned to all of the magnesium oxide, zircaloy, stainless steel, aluminum and helium regions. The emissivities of the anodized aluminum

enclosure walls, Incoloy heater rod sheaths, and stainless steel spacer plates were measured. However, after the experiments were completed and the enclosure was reopened, all interior surfaces were found to be coated with a film of vacuum pump oil. The emissivity of the coated surfaces were not measured, but were approximated to be very near unity [29].

In the model, heat is generated uniformly throughout the magnesium oxide, except in the z-locations within the spacer plates. For the simulation of each experiment, the total heat generation rate is equal to that of the experiment. The outer surfaces of the aluminum region is set uniformly to the average measured temperature of the enclosure walls.

At the top and bottom of the domain (outer surfaces of the spacer plates), the end surfaces of the heater rods and the helium gaps are insulated. Three different types of boundary conditions are applied to the stainless spacer plates. The first is the Regional Temperature condition, in which the spacer plates are divided into nine regions, which are shown in Fig. 8a separated by the vertical and horizontal lines. The temperature in Middle region of the top and bottom plates (marked M in Fig. 8a) is set to the temperature measured at the center thermocouple for each plate (center X in Fig. 3). The temperature of all four Side regions (marked S) is the value measured by the thermocouple at the side of each plate (X near the top of Fig. 3). The Corner region temperature (marked C) is set to a value that is the average of the measured two or three corner regions for that plate, which was then averaged with the measured enclosure temperature. This second average was used because simulation results show that significant portions of the corner regions are cooler than the location where the temperature is measured. The second type of spacer plate boundary condition is a Uniform Temperature, in which the area-weighted-average temperature for each plate is applied to that plate's entire outer surface. In the third type of boundary conditions, the outer surfaces of the spacer plates were simply Insulated.

Conduction, natural convection, and radiation heat transfer within the domain were simulated using ANSYS/Fluent. The steady-state momentum and energy equations were solved using a pressure-based solver where the pressure-velocity coupling was achieved using the SIMPLE scheme and discretization was achieved using a second order upwind scheme [31]. The discrete ordinate model was used to calculate radiation heat transfer. For natural convection, buoyancy induced flow was generated using gravitational acceleration in negative *z*-direction. Temperature-based density was applied to helium for the steady-state pressure measured for each experiment.

To check the sensitivity of the mesh, two finer meshes were constructed with 2,111,992 and 4,730,080 elements. Simulations representing Experiments I and IX (see Table 2) were performed using all three meshes. The difference between the maximum temperatures for each mesh was less than 0.3°C. Hence, the coarse mesh shown in Fig. 8 was used for all presented simulations.

Simulations Results

Figure 9 shows simulation results for the rod heat generation rate, gas pressure and enclosure wall and spacer plate temperatures measured for Experiment VII. These simulations employed the Regional Temperature spacer plate boundary conditions. Figure 9a shows rod surface temperature contours. Half of the rods are removed to expose the center of the array. The hottest region is slightly above the array mid-height, at z = 4.4 cm. Much of the central rod surface temperatures are fairly uniform, but the temperature exhibits rapid drop offs at the rod tops and bottoms, and on rods close to the walls. Figure 9b shows the vertical component of gas velocity at the mid-height (z = 0). The surface is colored according to the gas temperature. It shows that natural convection causes the warm gas near the center to move upward with a maximum speed of around 4 cm/s, and downward along the walls with a peak of around -3

cm/sec. The gas moves in rounded-cross-section up-flowing and down-flowing jets in between the heater rods.

The solid lines in Fig. 4 show the temperatures within the α, β and η rods from simulations that use the Regional Temperature spacer plate boundary conditions. Even though there are multiple rods in each of these groups, only one line is needed since, due to the precise symmetry of the simulation domain and boundary conditions, the temperatures in all the rods are identical. For both Experiment III and VII, the rod temperatures are fairly uniform in the middle 20 cm of the rods and drop off near the top and bottom spacer plates, and the α and β rods are significantly warmer than the η rods. The simulations show that the heat loss through the outer surfaces of the spacer plates is less than 8% of the total rod heat generation rate. In the α and β rods, the location of the maximum temperature is at a larger value of z for Experiment III than for Experiment VII. This is caused by natural convection, and is similar to the trend exhibited by the measurements.

Temperature profiles from simulations that use the Uniform Temperature spacer plate condition are nearly the same as those from the Regional Temperature boundaries, and so are not included. The dotted lines in Fig. 4 show rod temperatures results assuming the spacer plate outer surfaces are insulated. While insulation increases the temperatures of the rod ends, it has little effect on the middle 10 cm of the rods, where the highest temperatures reside. From this we conclude that the majority of the heat generated within the center region of the rods is transferred radially to the enclosure walls, and not axially to the endplates. To confirm this, simple two-dimensional simulations were performed using the mesh shown in Fig. 8a. The $\times, +$ and $*$ symbols at z = 0 of Fig. 4 show temperatures within the α, β and η rods groups, respectively. The good agreement between the two-dimensional and three-dimensional simulations for both

Experiment III and VII indicate that the spacer plate thermal boundary conditions have very little effect on maximum rod temperatures, which are located near the rod mid-height.

COMPARISON BETWEEN SIMULATED AND MEASURED ROD TEMPERATURES

In Fig. 4, the simulated temperature for all three rods (α, β, and η) in both Experiment III and VII are within 3°C of the measured values at all four elevations where they are measured, z = -17, 0, 17 and 29 cm. For the η rods, which are near the array corners, the simulated temperature is below the measured value at z = 17 cm, but above it at z = -17 cm. An additional simulation was performed using an axially varying enclosure temperature that was hotter at the top than at the bottom, based on the measured enclosure temperatures. The resulting simulated temperatures for the η rod is in better agreement with the measurements than curves in Fig. 4, and had little effect on the α and β rods. This suggests that temperatures of rods in the periphery of the array are more affected by the wall temperature than those near the center. This supports the assessment that rods near the array periphery have larger configuration errors than ones near the array center, since they are more sensitive to the enclosure temperature profile.

Since the measured enclosure wall and spacer plate temperatures are used as boundary conditions, the simulations essentially calculate the temperature *difference* between the rods and the enclosure. To compare the simulated and measured temperatures, for all 47 thermocouples in each of the 12 experiments, we calculate the measured rod temperature minus the average wall temperature, $\Delta T_M = T_M - \bar{T}_W$, and the simulated rod temperatures minus the wall temperature, $\Delta T_S = T_i - \bar{T}_W$. Since 21 measurements were excluded based on the Modified Thompson Tau test, there are 543 measurements and simulation results. Figure 10 is a plot of the simulated versus

measured temperature differences. These temperature differences are as large as 72°C. As expected, the simulated temperature difference increases as the measure difference increases, and the correlation appears to be linear.

If the simulations perfectly recreated the measured data, then all of the data would lie along $\Delta T_S = \Delta T_M$, which is shown in Fig. 10 using a thin solid line. The simulated results are scattered in a fairly narrow band above and below that line. The dotted line in Fig. 10 shows the best linear fit to the data, $\Delta T_{S,Fit} = m\Delta T_M + b$, where m and b are respectively the slope and intercept found from the least-squares technique. For the results in Fig. 10, $m = 1.02$ and $b = -1.2°C$. The difference between the best fit line and the ideal line $\Delta T_S = \Delta T_M$ is an indication of the systematic differences between the simulated and measured temperatures. The solid and dotted lines in Fig. 10 show that this difference is small compared to the random differences.

The scatter of the results above and below the best fit line is an indication of the random differences between the simulations and measurements. The estimate of the best fit line's random error, with a 95%-confidence level [30], is calculated as:

$$E_{95} = 2\sqrt{\frac{\sum(m\Delta T_m + b - \Delta T_S)^2}{N-2}} \quad . \qquad \text{Eqn. 3}$$

The summation is carried out for the N = 543 pairs of ΔT_m and ΔT_S. In terms of Fig. 10, this is the vertical distance above and below the best fit line that statistically contains 95% of the data. For the results in Fig. 10, $E_{95} = 5.7°C$, and dashed lines are placed $5.7°C$ above and below the best fit line. The region between these two lines contain roughly 95% of the results.

Table 3 reports the best fit slope, intercept and random error for several simulations and comparisons. The baseline comparison, which is presented in Fig. 10, uses (a) the simulation mesh with rods placed eccentrically within the spacer plate holes, (b) the Regional Temperature spacer plate boundary condition, and (c) all 543 qualified measurements. The best fit slope, intercept and random error for the baseline are given in the first line of Table 3. Under ideal conditions, $m = 1$, $b = 0$ and $E_{95} = 0$, and simulations that give parameters that approach those values are judged to be superior to ones whose values are further away. Table 3 shows that simulations using the computational domain with rods placed concentrically (rather than eccentrically) in the spacer holes gave parameters that are slightly more favorable than the baseline. Simulations that use the Uniform Temperature (Area-Weighted Average) spacer plate boundary condition gave larger random errors than the baseline.

The random differences between the measured and simulated temperatures are affected by inaccuracies of the simulations, configuration errors, and thermocouple measurement errors. The objective of this work is to assess the inaccuracies of the simulations. As discussed earlier, the configuration errors are larger in the array periphery than they are near its center. Table 3 shows that if the outermost rods (all rods in rows A and H, and column 1 and 8 of Fig. 3) are eliminated from the comparison between the simulations and measurements, then the random differences between the measured and simulation results is reduced to $4.4°C$. If only the maximum measured and simulated temperatures are compared, the random error is only $2.0°C$, a 63% reduction compared to the baseline comparison. This is not substantially larger than the thermocouple measurement uncertainty of $1.1°C$. However, the simulations systematically over predicted the maximum temperature. We view these latter comparisons to be a better assessment of the

uncertainties of the simulation methods than the ones that include all of the rods, because the outer rod are more affected by configuration errors.

CONCLUSION

The goal of the current work is to use experimental measurements to validate computational fluid dynamics (CFD) simulations of conduction, natural convection and radiation heat transfer in a configuration that is relevant to a used nuclear fuel assembly within a square basket opening of a vertical storage canister. An experimental apparatus was constructed consisting of an 8x8 array of vertical heated rods within a square cross-section, helium-filled aluminum pressure vessel. The temperature of the enclosure, heater rods, and spacer plates that hold the rods, were measured using thermocouples with an uncertainty of $1.1°C$ in twelve experiments for a range of helium pressures, rod heat generation rates, and thickness of insulation surrounding the vessel (to increase the vessel temperature).

Temperatures measured in the rods are affected by both measurement and configuration errors. Configuration errors are caused by small systematic and random deviations from the intended experiment geometry and boundary conditions, such as variations in the heater resistances, rod curvatures, thermocouple locations within each rod, and enclosure wall temperatures. The variation of measured temperatures within symmetrically-placed rods was used to assess configuration errors. These errors were larger in rods that are close to the array periphery, than for ones near the array center. Measurements with larger configuration errors are less useful for validating simulation results than ones with smaller errors.

ANSYS/Fluent CFD simulations that model conduction, natural convection and radiation heat transfer within the rods, spacer plates, enclosure, and helium gas of the experiment were performed. These simulations used the measured spacer plate and enclosure temperatures as boundary conditions. The simulated difference between the rod and enclosure temperatures were compared to the measured differences for all rods and all twelve experiments. The simulations systematically predicted all the trends in the measured data, but had random differences of ±5.7°C. If the outmost rods are excluded, the random differences are only ±4.4°C. If only the maximum rod temperatures are considered, the random errors are ±2°C, but the simulations consistently predict higher temperatures than the measured ones.

ACKNOWLEDGMENT

This work was supported by the U.S. Department of Energy Office of Nuclear Energy University Programs.

NOMENCLATURE

Gr	Grashof number, eqn. 1
m, b	Best fit slope and intercept for $\Delta T_S = m\Delta T_M + b$
N	Number of samples
P	Helium pressure when the experiment is at steady state
P_N	Nominal helium pressure when the experiment apparatus is at room temperature
Q	Assembly heat generation rate
$D = 2\sqrt{\frac{\sum(\bar{T}_M - T_M)^2}{N-1}}$	Measured temperature sample deviation with 95% confidence level
$E_{95} = 2\sqrt{\frac{\sum(mT_m + b - T_S)^2}{N-2}}$	Random Error of the simulations with 95% confidence level
$\Delta T = T - \bar{T}_W$	Difference between local temperature and average enclosure wall temperatures
$\Delta\bar{T} = \bar{T} - \bar{T}_W$	Difference between average spacer plate temperature and average enclosure wall temperatures
T	Temperature
$\bar{T}$	Average Temperature
x, y, z	Coordinate systems with origin at heater rod array center (Fig. 2a and 3)

Subscripts

J	Index
W	Enclosure wall
T	Top spacer plate
B	Bottom spacer plate
S	Simulated
M	Measured
R	Revised based on the Thompson Modified Tau test.
$\alpha, \beta, \gamma, \delta, \varepsilon, \zeta, \eta$	Symmetry groups (Table 1)

REFERENCES

[1] U.S. Dept. of Energy, Office of Civilian Radioactive Waste Management (OCRWM), 1987, "Characteristics of Spent Nuclear Fuel, High-Level Waste, and Other Radioactive Wastes Which May Require Long-Term Isolation," DOE/RW-0184, December.

[2] Saling, J.H., and Fentiman, A.W., 2002, *Radioactive Waste Management*, 2nd Edition, Taylor and Francis, New York.

[3] Holtec International, 2010, "HI-STORM 100 FSAR," Revision 8, Report HI-2002444.

[4] Colmont, D. and Roblin, P., 2008, "Improved thermal modeling of SNF shipping cask drying process using analytical and statistical approaches," Packaging, Transport, Storage & Security of Radioactive Material, Vol. 19, No. 3, pp. 160–164.

[5] Incropera, F. and DeWitt, 1996, *Introduction to Heat Transfer*, 3rd Edition, Wiley.

[6] Hadj-Nacer, M., Manzo, T., Ho, M. T., Graur, I. and Greiner, M, 2016, "Effects of Gas Rarefaction on Used Nuclear Fuel Cladding Temperatures during Vacuum Drying," *Nuclear Technology*, Vol. 194, No. 3, pp. 387-399.

[7] NRC, 2003, "Cladding Considerations for the Transportation and Storage of Spent Fuel," ISG-11 R3, Interim Staff Guidance Report for the Spent Fuel Project Office of the U.S. NRC.

[8] Large, W.S. and Sindelar, R.L., 1997, "Review of Drying Methods for Spent Nuclear Fuel," Westinghouse Savannah River Company, Savannah River Site, Aiken, SC, report number WSRC-TR-0075

[9] Bracey, W. and Smith, P., 2012, "Transnuclear Drying Experience and Lessons Learned," ASTM Workshop, Atlanta, GA.

[10] Schaaf, S.A. and Chambre, P.L, 1961, Flow of Rarefied Gases, Princeton University Press, New Jersey.

[11] Maharjan, D., Hadj-Nacer, M., Ho, M.T., Stefanov, S.K., Graur, I. and Greiner, M., 2015, "Simulation of heat transfer across rarefied gas in annular and planar geometries: Comparison of Navier-Stokes, S-model and DSMC methods results," *Proceeding of the International Conference on Nanochannels, & Microchannels, and Minichannels (InterPACK/ICNMM2015)*, San Francisco, CA.

[12] NRC Docket Number 71-9225, *NACLWT Legal Weight Truck Cask System Safety Analysis Report*, June 2005, Rev. 37, Nuclear Assurance Corporation International, Norcross, Georgia, U.S.A.

[13] Adkins, H. E., Koeppel, B. J. Jr., Cuta, J. M., Guzman, A. D., Bajwa, C. S., 2006, "Spent Fuel Transportation Package Response to the Caldecott Tunnel Fire Scenario," NUREG/CR-6894, Rev.1, Pacific Northwest National Laboratory, Washington D.C.

[14] Michener TE, DR Rector, JM Cuta, RE Dodge, and CW Enderlin, 1995, *COBRA-SFS: A Thermal-Hydraulic Code for Spent Fuel Storage and Transportation Casks,* PNL-10782, Pacific Northwest Laboratory, Richland, Washington.

[15] Tseng, Y.S, Wang, J.R., Tsai, F.P., Cheng, Y.H., and Shih, C., 2011, "Thermal design investigation of a new tube-type dry-storage system through CFD simulations," *Annals of Nuclear Energy*, 38, 1088–1097.

[16] Li, J., and Liu, Y.Y., 2015, "Validation of Thermal Analysis of Dry Storage Casks at Diablo Canyon," *Proceedings of PVP 2015, 2015 ASME Pressure Vessels and Piping Division Conference*, July 19–23, 2015 Park Plaza, Boston, MA.

[17] Kamichetty, K.K., Venigalla, V., and Greiner, M., 2014, "Development, Use, and Accuracy of a Homogenized Fuel Region Model for Thermal Analysis of a Truck Package under Normal and Fire Accident Conditions," *Journal of Pressure Vessel Technology*, Vol. 136, No. 2, 021208-1-12.

[18] Pacific Northwest Laboratory, et al., 1987, "The TN-24P PWR Spent Fuel Storage Cask: Testing and Analyses," EPRI NP-5128.

[19] Creer, J.M., Michener, T.E., McKinnon, M.A., Tanner, J.E., Gilbert, E.R. and Goodman, R.L., 1987, "The TN-24P PWR spent fuel storage cask: testing and analyses," Pacific Northwest National Laboratory (PNL), Interim Report PNL-6054.

[20] Holtec International, 2000, "Topical Report on the HI-STAR/HI-STORM Thermal Model and its Benchmarking with Full-Scale Cask Test Data," Holtec Report No. HI-992252.

[21] Lovett, P. M., 1991, "An Experiment to Simulate the Heat Transfer Properties of a Dry, Horizontal Spent Nuclear Fuel Assembly," M.S. Thesis, Nuclear Eng., Massachusetts Institute of Technology

[22] Canaan, R.E., and Klein, D.E., 1996, "An Experimental Investigation of Natural Convection Heat Transfer within Horizontal Spent-Fuel Assemblies," *Nuclear Technology*, December, Vol.116, pp. 306-318.

[23] Dalton, T.E., 1994, "An Experimental Study of Natural Convection in Horizontal Rod-Bundle Enclosures," MS thesis, University of Tennessee, Knoxville

[24] Keyhani, M., Kulacki, F.A., and Christensen, R.N., 1985, "Experimental Investigation of Free Convection in a Vertical Rod-Bundle-A General Correlation for Nusselt Numbers," *ASME Journal of Heat Transfer*, Vol. 107, pp. 611-623

[25] Canaan, R E., and Klein, D.E., 1998, "A Numerical Investigation of Natural Convection Heat Transfer within Horizontal Spent-Fuel Assemblies", *Nuclear Technology*, Vol. 123, Aug. pp. 193-208.

[26] Chalasani, N.R., Araya, P., and Greiner, M., 2009, "Benchmark of Computational Fluid Dynamics Simulations using Temperatures Measured within Enclosed Vertical and Horizontal Arrays of Heated Rods," *Nuclear Technology*., Vol. 167, No. 3, pp. 371–383.

[27] Chalasani, N.R. and Greiner, M., 2010, "Benchmark of Computational Fluid Dynamics Simulations Using Temperatures Measured Within Enclosed Vertical and Horizontal Arrays of Heated Rods," PVP2010-25803, *Proceedings of the ASME 2010 Pressure Vessels and Piping Division/K-PVP Conference*, Bellevue, Washington, USA.

[28] Chalasani, N.R., 2010, "Benchmark of CFD Simulations Using Temperatures Measured Within an Enclosed Array of Heater Rods Oriented Vertically and Horizontally," Doctoral of Philosophy Dissertation, Mechanical Engineering Department, University of Nevada, Reno.

[29] Emissivity Table, http://www.optotherm.com/emiss-table.htm

[30] Wheeler, A.J., and Gangi, A.R., 2010, *Introduction to Engineering Experimentation*, 3rd Edition, Pearson.

[31] ANSYS Inc., 2015, "ANSYS Fluent User's Guide," www.ansys.com.

Figure Caption List

Fig. 1 Dissembled Experimental Apparatus (a) Heater rod array, (b) Spacer plates, and (c) Enclosure

Fig. 2 Assembled experimental apparatus. (a) Axial cross section showing internal components (b) Photograph showing external insulation, and top extension tubes with wire feedthroughs

Fig. 3 Experimental apparatus cross section showing heater rods, enclosure walls, coordinate system and row and column names. Numbers in rods indicate z-location of thermocouples, and Greek letters indicate symmetry group (Table 2)

Fig. 4 Measured thermocouple (open and filled symbols) and simulated (solid and dotted lines and $\times + *$ symbols) temperatures within boundaries and rods for experiments III and VII

Fig. 5 Measured enclosure wall and top and bottom spacer plate temperatures for different insulation thicknesses and helium pressures versus heat generation rate (a) Average temperatures (b) 95%- deviation temperatures

Fig. 6 Temperature histograms for Experiment 7 for the γ, δ, ε and ζ symmetry groups, which have thermocouples at $z = 0$

Fig. 7 Deviation temperatures within each symmetry group versus group average temperature minus wall temperature

Fig. 8 Computational domain (a) Full x, y-plane divided into nine middle, m, side, s, and corner, c, regions (b) Enlarged view of section 1 from part (a), showing eccentricity of the heater rods

Fig. 9 Computational results for Experiment VII. (a) Rod surface temperature contours (half of the rods are removed to show highest temperatures) (b) Vertical component of gas velocity in the mid-plane, z = 0, colored according to the gas temperature

Fig. 10 Simulated versus measured thermocouple-to-wall temperature differences for all 12 experiments

Table Caption List

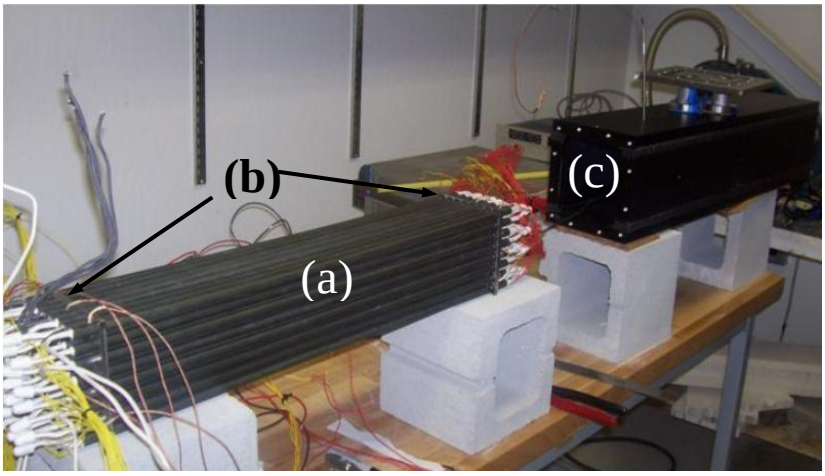

FIGURE 1 Dissembled experimental apparatus (a) Heater rod array, (b) Spacer plates, and (c) Enclosure

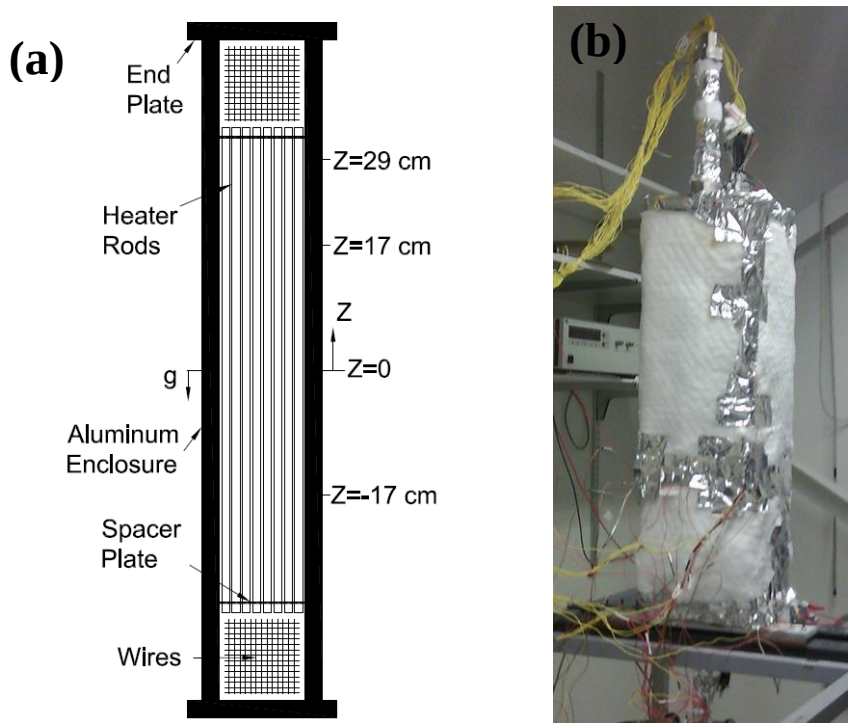

FIGURE 2 Assembled experimental apparatus. (a) Axial cross section showing internal components (b) Photograph showing external insulation, and top extension tubes with wire feedthroughs

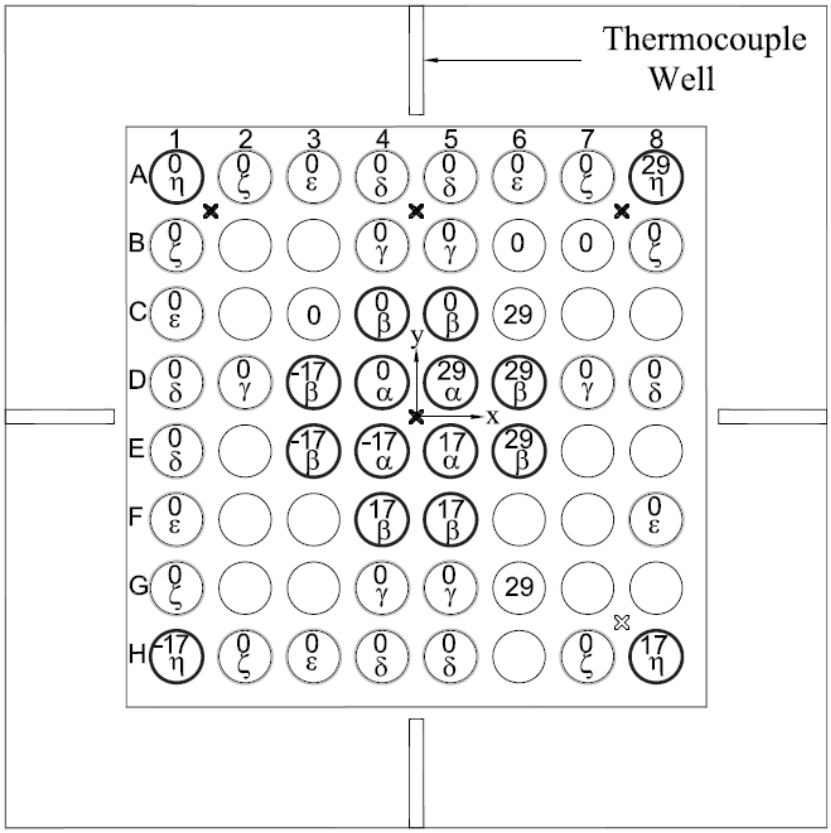

FIGURE 3 Experimental apparatus cross section showing heater rods, enclosure walls, coordinate system and row and column names. Numbers in rods indicate z-location of thermocouples, and Greek letters indicate symmetry group (Table 2)

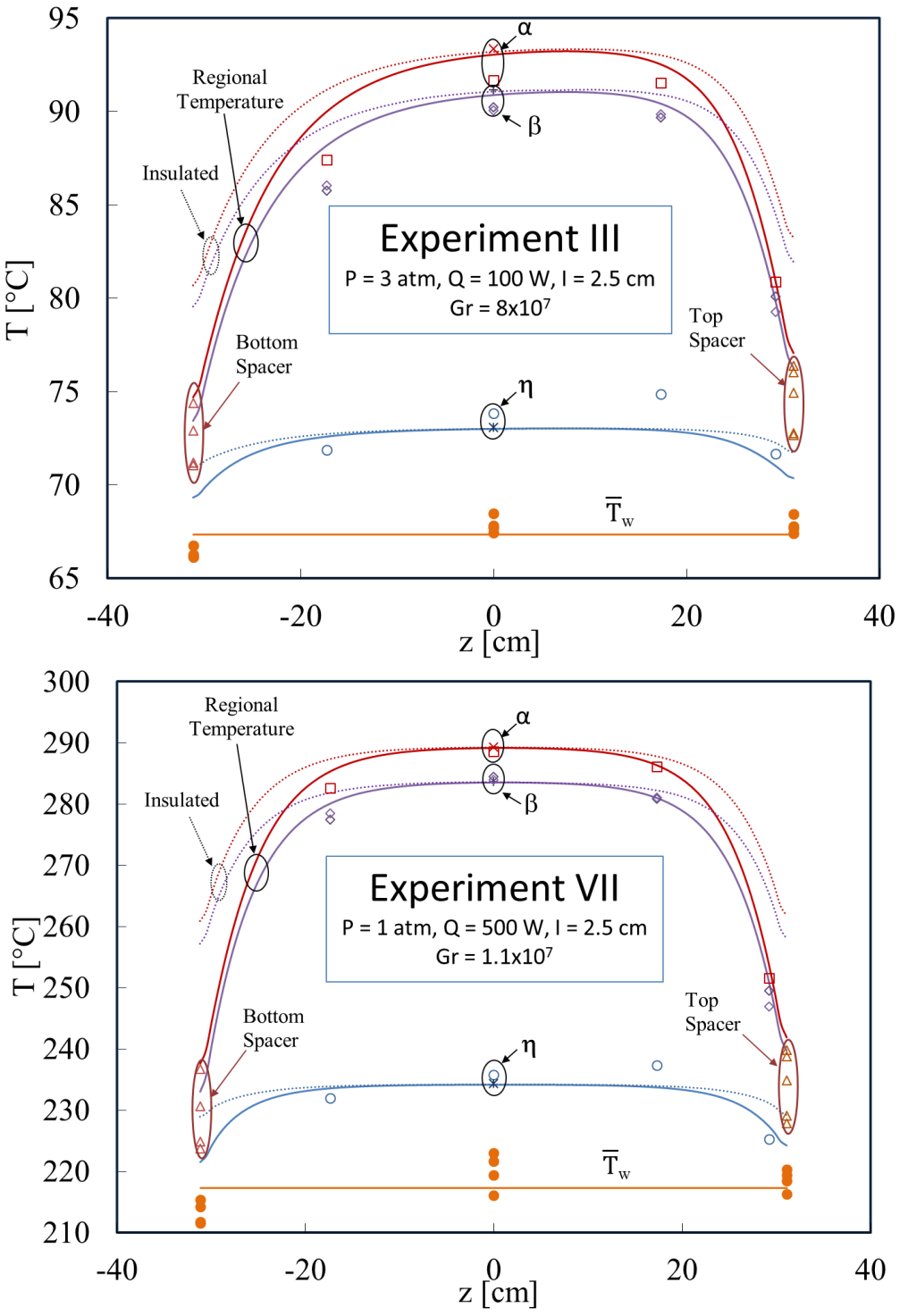

FIGURE 4 Measured thermocouple (open and filled symbols) and simulated (solid and dotted lines and $\times + *$ symbols) temperatures within boundaries and rods for experiments III and VII

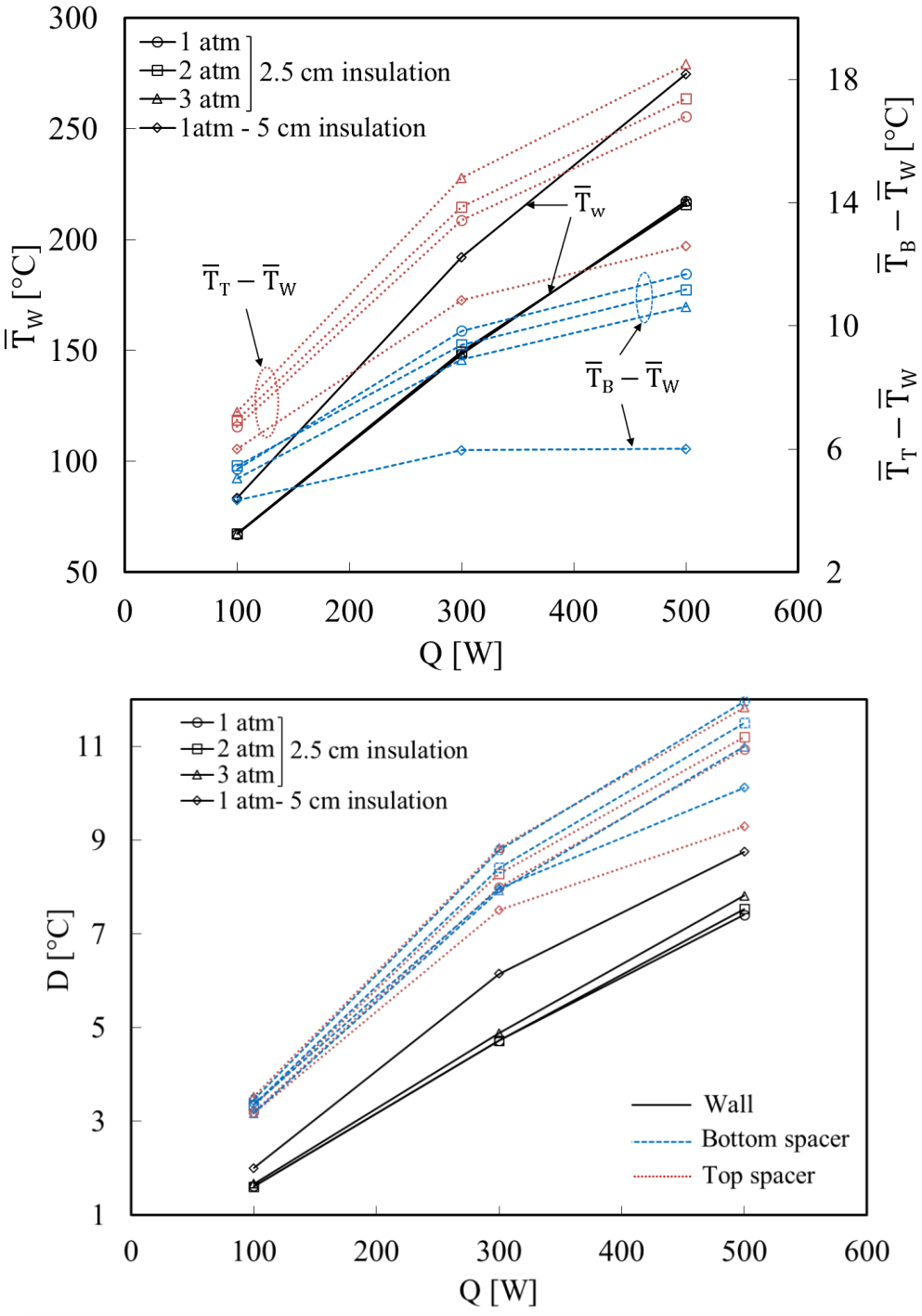

FIGURE 5 Measured enclosure wall and top and bottom spacer plate temperatures for different insulation thicknesses and helium pressures versus heat generation rate (a) Average temperatures (b) 95%- deviation temperatures

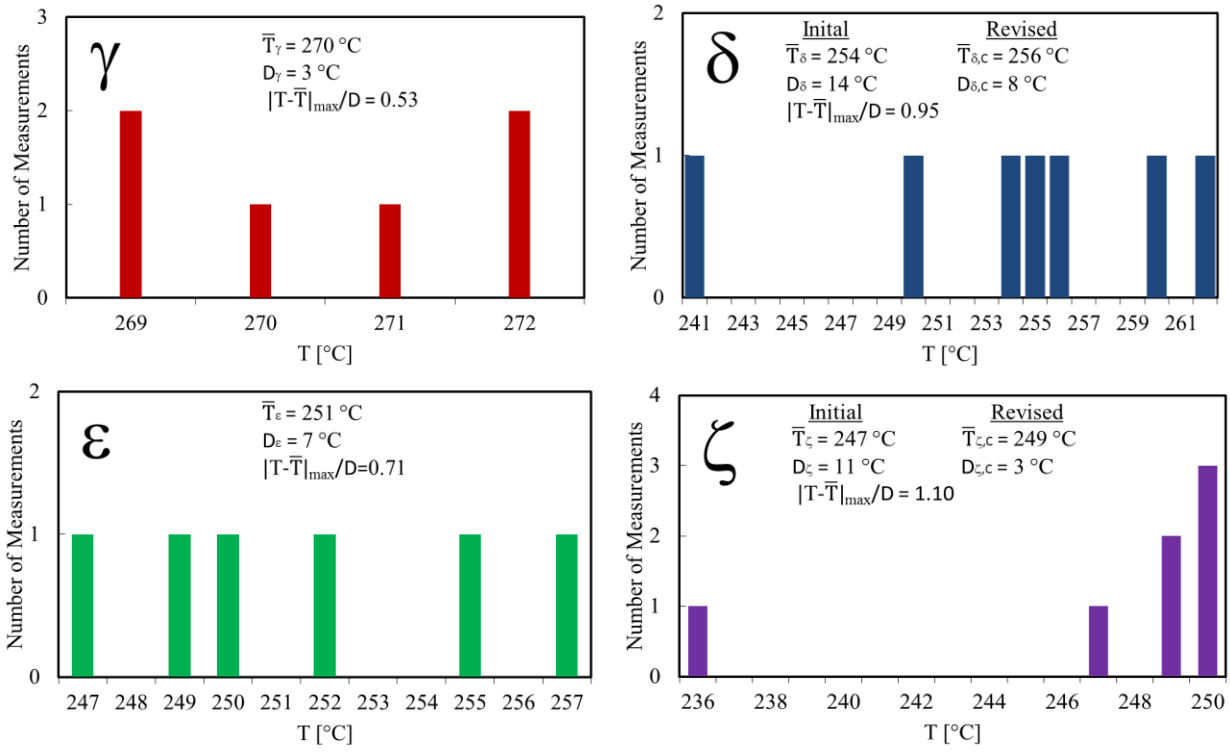

FIGURE 6 Temperature histograms for Experiment 7 for the γ, δ, ε and ζ symmetry groups, which have thermocouples at z = 0

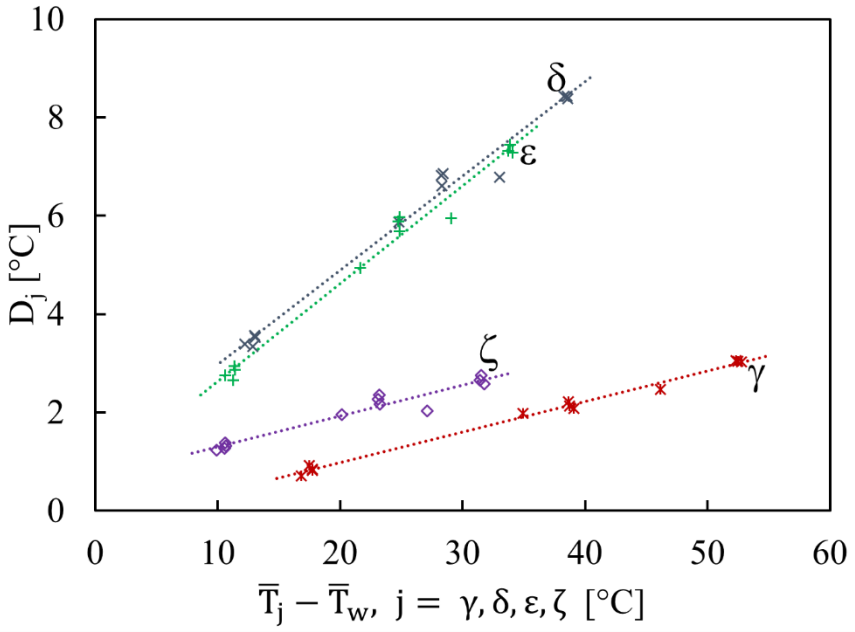

FIGURE 7: Deviation temperatures within each symmetry group versus group average temperature minus wall temperature

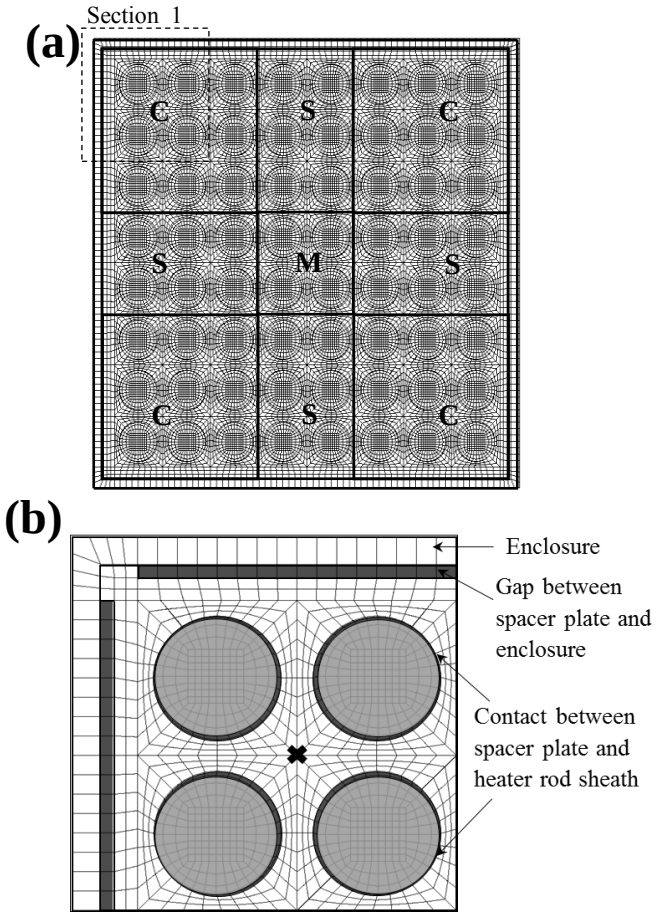

FIGURE 8 Computational domain (a) Full x,y-plane divided into nine middle, m, side, s, and corner, c, regions (b) Enlarged view of section 1 from part (a), showing eccentricity of the heater rods

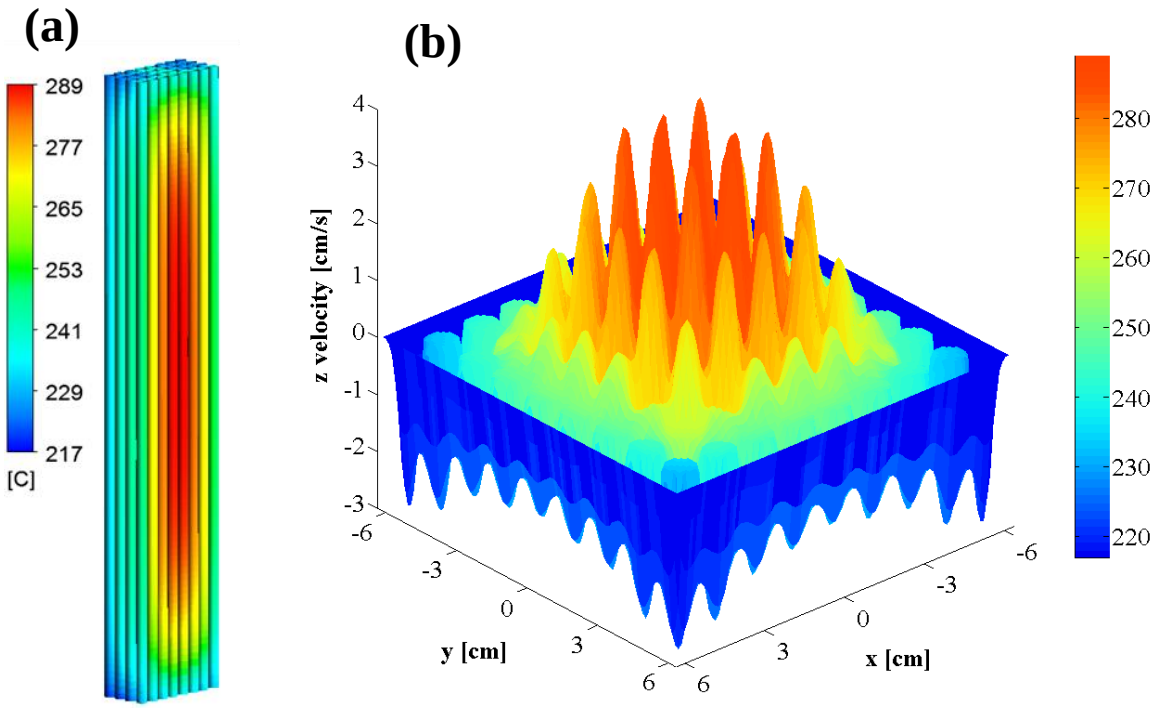

FIGURE 9 Computational results for Experiment VII. (a) Rod surface temperature contours (half of the rods are removed to show highest temperatures) (b) Vertical component of gas velocity in the mid-plane, z = 0, colored according to the gas temperature.

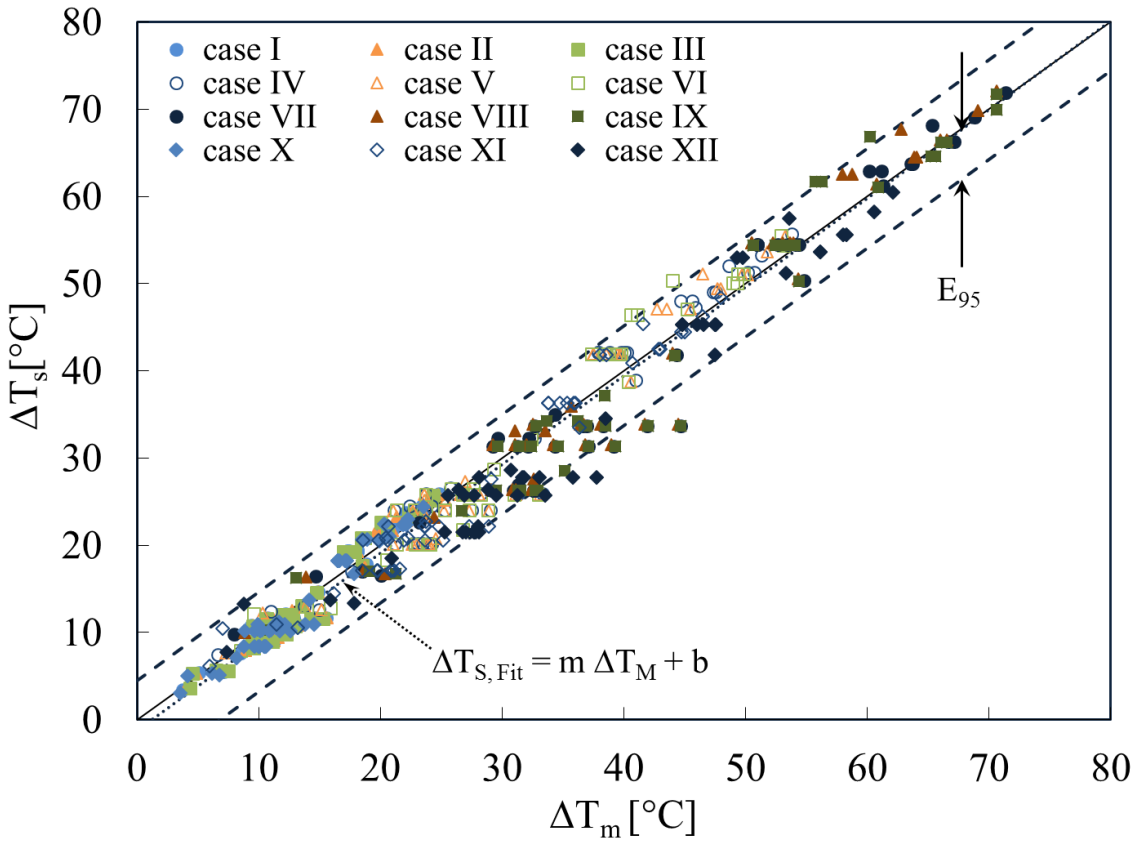

FIGURE 10 Simulated versus measured thermocouple-to-wall temperature differences for all 12 experiments.

TABLE 1 Heater rods within each symmetry group

Group Name	Group Heater Rods	Locations of Thermocouples
α	D4, D5, E4, E5	All z
ß	C4, C5, D3, D6, E3 E6, F4, F5	All z
γ	B4, B5, D2, D7, G4, G5	z = 0
δ	A4, A5, D1, D8, E1, H4, H5	z = 0
ε	A3, A6, C1, F1, F8, H3	z = 0
ζ	A2, A7, B1, B8, G1, H2, H7	z = 0
η	A1, A8, H1, H8	All z

TABLE 2 Insulation thickness, gas pressure, and total rod heat generation rate for all 12 experiments

Insulation Thickness, I [cm]	Nominal Pressure, P_N [atm]	Total Rod Heat Generation, Q [W]								
		100			300			500		
		Exp#	P [Atm]	$Gr \cdot 10^{-7}$	Exp#	P [Atm]	$Gr \cdot 10^{-7}$	Exp#	P [Atm]	$Gr \cdot 10^{-7}$
2.5	1	I	1.38	0.91	IV	2.30	1.1	VII	3.02	1.0
	2	II	1.53	3.6	V	2.62	4.4	VIII	3.36	4.1
	3	III	1.66	8.0	VI	2.82	9.9	IX	3.56	9.0
5	1	X	1.16	0.78	XI	1.42	0.81	XII	1.62	0.72

Table 3 Slope and Intercept values of regression line for difference boundary conditions and models tested

Simulation	**Slope m**	**Intercept b [°C]**	**Random Error E_{95} [°C]**
Baseline	1.02	-1.2	5.7
Concentric Heater Rods	1.02	-1.1	5.6
Area-Weighted Average Spacer Plate Temperature	1.02	-1.5	6.2
Baseline (without Outermost Heater Rods)	1.02	-0.1	4.4
Baseline (Maximum Temperature Only)	0.99	1.4	2.0

Appendix B (Conference Papers)

1- Green, R. Manzo, E. T., Greiner, M., Li, J., and Liu, Y. Y., “Experimental Benchmark of Simulations that Predict Temperatures of an 8x8 Array of Heater Rods within a Vessel Filled with Rarefied Helium Gas,” Proceedings of the 17th International Symposium on the Packaging and Transportation of Radioactive Materials, Aug 18-23, 2013, San Francisco, CA.

2- Green, R., Manzo, E. T., Hadj-Nacer, M., and Greiner, M., “Design of an experimental apparatus to measure the thermal accommodation coefficient between stainless steel surfaces and rarefied helium,” Proceedings of the ASME 2014 Pressure Vessels & Piping Conference, July 20-24, 2014, Anaheim, CA.

3- Manzo, E. T., Green, R., Hadj-Nacer, M., Greiner, M., Li, J., and Liu, Y. Y., “Prediction of Cladding Temperature within a Used Nuclear Fuel Transfer Cask Filled with Rarefied Helium,” Proceedings of the ASME 2014 Pressure Vessels & Piping Conference, July 20-24, 2014, Anaheim, CA.

4- Hadj-Nacer, M., Manzo, T., Ho, M. T., Graur, I. and Greiner, M, “Phenomena Affecting Used Nuclear Fuel Cladding Temperatures during Vacuum Drying Operations,” International High-Level Radioactive Waste Management Conference, April 12-16, 2015, Charleston, SC.

5- Green, R., Hadj-Nacer, M., and Greiner, M., “Design of an Experiment to Measure the Thermal Accommodation Coefficient Between Helium and Stainless-Steel in Concentric Cylinders,” Proceedings of the ASME 2015 Pressure Vessels & Piping Conference, July 19-23, 2015, Boston, MA.

6- Manzo, E. T., Hadj-Nacer, M., and Greiner, M., “Geometrically-Accurate Three-Dimensional Simulations of a Used Nuclear Fuel Canister Filled with Helium,” Proceedings of the ASME 2015 Pressure Vessels & Piping Conference, July 19-23, 2015, Boston, MA.

7- Maharjan, D., Hadj-Nacer M., Chalasani, N. R., and Greiner, M., “Experimentally-Benchmarked Computational Fluid Dynamics Simulations of an Array of Heated Rods within a Square-Cross-Section Helium-Filled Pressure Vessel”, 2016 ASME Pressure Vessel and Piping Conference, July 17-21, 2016, Vancouver, BC, Canada.

8- Trujillo, C., Hadj-Nacer M., and Greiner, M., “Effect of Rarefication on Cladding Temperatures within a Used Nuclear Fuel Canister Filled with Dry Helium,” International High-Level Radioactive Waste Management Conference, April 9-13, 2017, Charlotte, NC.

9- Maharjan, D., Hadj-Nacer M., and Greiner, M., “Temperature Measurement of an Array of Heated Rods Subjected to Vacuum Drying Conditions,” Proceedings of the ASME 2017 Pressure Vessels & Piping Division Conference, July 16-20, 2017, Waikoloa Village, HI.

10- Maharjan, D., Hadj-Nacer M., and Greiner, M., “Experimentally Benchmarked Computational Fluid Dynamics Simulations of a 7×7 Array of Heated Rods within a Square-Cross-Section Enclosure Filled with Rarefied Helium,” Proceedings of the ASME 2017 Pressure Vessels & Piping Division Conference, July 16-20, 2017, Waikoloa Village, HI.

Proceedings of the 17th International Symposium on the
Packaging and Transportation of Radioactive Materials
PATRAM 2013
August 18-23, 2013, San Francisco, CA, USA

Experimental Benchmark of Simulations that Predict Temperatures of an 8x8 Array of Heater Rods within a Vessel Filled with Rarefied Helium Gas

Rachel Green
University of Nevada, Reno
Reno, NV, USA

Ernesto T. Mano
University of Nevada, Reno
Reno, NV, USA

Miles Greiner, Ph.D.
University of Nevada, Reno
Reno, NV, USA
greiner@unr.edu

Jie Li, Ph.D.
Argonne National Laboratory
Argonne, IL, USA

Yung Y. Liu, Sc.D.
Argonne National Laboratory
Argonne, IL, USA

ABSTRACT

A two-dimensional ANSYS/Fluent computational fluid dynamics model is constructed of an existing experiment that consists of a square 8x8 array of heater rods within a square cross section pressure vessel filled with helium. The model includes heat generation and conduction within the rods, conduction and radiation heat transfer across the helium between the rods and enclosure, and the effective thermal resistance at the gas/solid interfaces that is significant at low pressures when the gas is moderately rarified. This configuration is relevant to the vacuum drying process that is used when used nuclear fuel is transferred from underwater to dry storage. Simulations are performed for enclosure temperatures of 27°C and 427°C, and total rod axial heat generation rates between 160 W/m and 820 W/m. Moderately-Rarified simulations, which include an effective thermal resistance between the gas and solid surfaces, are performed for helium pressures of 100 and 400 Pa, thermal accommodation coefficients of 0.25 and 0.4, and a Lennard-Jones collision diameter of 1.9 angstroms. These simulations predict peak heater rod temperatures that are at least 5°C hotter than those predicted by a continuum model, which neglects the rarified gas thermal resistance, when the array heat generation rate is above 330 W/m. Simulations of earlier experiments in the same apparatus, with the helium pressure between 10^5 and $3x10^5$ Pa, predicted peak rod temperatures that were within 5°C of measured values. The current simulation results indicate that the apparatus can be used with a high degree of certainty to benchmark Moderately-Rarified simulation results for rod axial heat generation rates above 330 W/m.

INTRODUCTION

Used light water reactor fuel rods consist primarily of zircaloy cladding tubes that contain highly radioactive fuel pellets as well as high-pressure fission-product and fill gases [1]. The fuel rods are held in a square array by headers, footers and periodic spacer plates. Boiling water

reactor (BWR) assemblies consist of 7x7 to 9x9 rod arrays surrounded by a solid channel. Pressurized water reactor assemblies are 14x14 to 18x18 arrays, but do not have channels.

After being discharged from reactors, used assemblies are stored underwater while their radioactivity and heat generation rate decrease [2]. After sufficient time, typically five years or more, a canister with an internal basket is placed in a transfer cask and lowered into the pool. The canister is then loaded with fuel assemblies, covered, and lifted out of the pool. Helium or another non-oxidizing gas is forced into a port near the top of the canister while water flows out through a tube that reaches to the canister bottom [3]. Small amounts of water may remain at the bottom of the canister and in crevices of the canister and cladding surfaces after draining. Essentially all moisture must be removed from the canister before it is sealed to prevent corrosion of the fuel cladding and cask materials, and/or formation of detonable mixtures of hydrogen and oxygen [4]. After drying, the canister is filled with helium to pressures between 3 and 7 atm (306 to 711 kPa) and sealed either by welding or bolted closure. It is then placed in other packaging for onsite dry cask storage or offsite transport.

With the absence of a defined used-fuel disposal and/or reprocessing path, it is crucial to assure the safety of *long-term* dry cask storage systems [5]. Federal regulations (10CFR72) require that these systems insure that external doses are below certain limits, and that the fuel configuration remains subcritical, confined and contained, and retrievable. The cladding is the primary confinement barrier for the used fuel pellets and fission gas. Its integrity must be protected to assure that, after decades in storage, the assemblies can be safely transferred to other packages, and/or transported to other locations.

Federal regulations (10CFR71) also require that the transport package performance be analyzed under normal conditions of transport (which include a 0.3-m drop) and hypothetical accident conditions (which include a 9-m drop). If the cladding integrity is compromised there is a risk that the fuel will not be in its "as analyzed" configuration after these drop events. Adequate ductility of the cladding must therefore be maintained. Radial hydride formation within the cladding has the potential to radically reduce cladding ductility and its suitability for long term storage or transport [5].

During all post-reactor drying, transfer, storage and transport operations the fuel cladding must be kept below certain temperature limits to avoid (a) dissolution of circumferential hydrides that exist in the cladding and (b) high gas pressures within the tubes, which leads to high cladding hoop stress [6]. If these hydrides dissolve and the hoop stresses become large, then as the heat generation of the used fuel decreases during long-term storage *radial* hydrides may form and cause the cladding to become brittle [7-10]. Drying operations [11] may be the most likely events to cause the fuel temperature to exceed temperature limits. This is because drying is the first operation when the fuel is removed from water and placed in a gas-filled environment, and the fuel heat generation is still relatively high.

Nuclear Regulatory Commission Interim Staff Guidance-11, Revision 3 (ISG-11) [6] specifies conditions that are intended to prevent radial hydride formation. For example, the maximum calculated fuel cladding temperature must remain below 400°C for normal conditions of storage and short term loading conditions (e.g., drying, backfilling with inert gas, and transfer of the cask to the storage pad). For low burnup fuel, a higher short-term temperature limit may be used, provided that the best estimate cladding hoop stress is less than 90 MPa for the temperature limit proposed. During loading operations, repeated temperature cycling is allowed, but is limited to less than 10 cycles with cladding temperature variations of more than 65°C. For off-normal and accident conditions, the maximum cladding temperature should not exceed

570°C, a limit based on creep (stress) rupture consideration. Until further guidance is developed, *high* burnup fuel will be handled on a case-by-case basis [6].

Two methods are currently used by industry for moisture removal from canisters, vacuum drying or forced helium dehydration [3, 6]. In vacuum drying, the canister is evacuated to pressures as low as 67 Pa to promote evaporation and water removal [4]. Several cycles of evacuation and refill may be necessary before operators can demonstrate that the canister is able to meet the drying technical specification of maintaining a low pressure of 400 Pa (3 Torr) for 30 minutes [3, 11].

At the low pressures and gas densities associated with vacuum drying, buoyancy-induced gas motion and natural convection heat transfer from the fuel to the canister surfaces are essentially eliminated. While the gas thermal conductivity is nearly the same at these pressures as it is at atmospheric conditions, the gas is rarefied to the extent that there is a temperature difference (or temperature-jump) between the heated cladding and the gas in contact with it [4, 12-15]. This surface-to-gas temperature-jump is essentially zero at moderate pressures but acts as a thermal resistance between the surfaces and gas at low pressures. These resistances increase the cladding temperature compared to atmospheric pressure conditions. This thermal resistance and the lack of natural convection caused by low pressure may lead to higher cladding temperatures during vacuum drying than during storage conditions for the same fuel heat generation rate.

Forced helium dehydration is used for drying canisters containing high-burnup fuel [3]. In that process, helium is forced into the canister through a port near its top and withdrawn though a tube that reaches to the canister bottom. Moisture is removed from the helium by condensing, demoisturizing, and preheating the gas outside the canister. In some cases cooling water is also circulated in the gap between the canister and transfer cask. The gas pressure during helium dehydration is maintained at roughly the same level as that used during storage. As a result the same natural convection and minimal temperature-jump thermal resistance are expected as in storage. However, gas demoisturizing and cooling equipment are required for forced helium dehydration, which are not needed for vacuum drying.

At the current time, package vendors predict cladding temperatures and hoop stresses during drying using experimentally-benchmark whole-package computational fluid mechanics (CFD) simulations [3, 16]. In these models, the fuel and basket are replaced by a region with an effective thermal conductivity and porosity. This allows prediction of the maximum fuel heat generation rate that can be transferred without exceeding the temperature and hoop stress limits. It also helps determine which fuel may be vacuum-dried, and for which fuel the more complex forced helium dehydration process must be used.

The whole-package computational methods been validated [17] against measurements performed in an actual evacuated storage package [18]. Currently, these effective properties are calculated without regard to the rarefied-gas temperature-jump thermal resistance. However, the fuel heat generation in the tests used to validate the current methods was moderately low. The effect of the rarified-gas thermal resistance on peak cladding temperatures increases with generation rate.

Current Work The long term objective of the current research program is to develop and experimentally-benchmark CFD models of the vacuum drying process that includes the effect of the rarefied-gas thermal resistance. This work will eventually employ an existing experimental apparatus that consists of an 8x8 array of heater rods within an aluminum pressure vessel (Fig. 1). This apparatus simulates a region of a BWR assembly within its channel and between consecutive spacer plates. Experiments will be performed to acquire rod temperatures for a

range of rod heat generation rates, wall temperatures and helium gas pressures. Low pressures relevant to the vacuum drying process will be examined.

In the current paper two-dimensional CFD simulations are performed to model the apparatus filled with helium at 100 and 400 Pa. The simulations include heat generation and conduction within the rods, conduction and radiation heat transfer across the helium-filled region between the rods and enclosure, and the rarified gas thermal resistance at the solid/gas interfaces. The objective is to quantify how much this thermal resistance increases the maximum or peak rod temperature compared to simulations that do not include that effect. These results will be used to determine the experimental conditions under which this effect is sufficiently large that it can be differentiated from random variations in the experimental temperature measurements. In the future the test facility will be used under these conditions to benchmark simulations of drying operations.

EXPERIMENTAL APPARATUS

Figure 1 shows the disassembled test facility that models the region of a used BWR fuel assembly between consecutive spacer plates and within its channel. It was originally constructed to model the thermal conditions during used fuel transport and storage [19, 20]. On the left side of Fig. 1 is an 8x8 square array of rods held by spacer plates at both ends. The rods contain electric heaters and internal thermocouples. The array is placed in a square cross-section anodized-aluminum pressure vessel (right side of Fig. 1). The spacer plates and vessel walls also contain thermocouples. Stainless steel endplates (not shown) are bolted to both ends of the enclosure, and sealed using high-temperature O-rings. The heater power cables and thermocouple lead wires are connected to high-temperature feedthroughs in the endplates. A computer data acquisition system and a power supply are connected to the outer terminals of the feedthroughs to record temperatures and power the heaters.

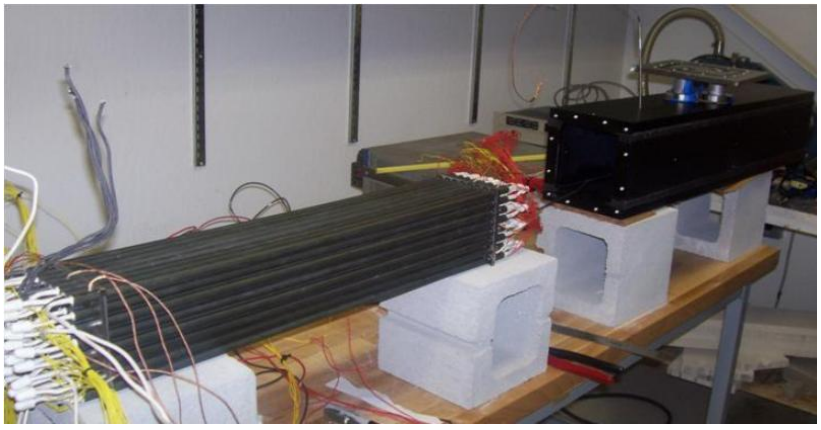

Figure 1. Disassembled view of an experiment apparatus consisting of an 8x8 array of heater rods within a square cross-section aluminum pressure vessel [20]

Each heater rod is 1.1 cm in diameter and has a L = 60.9-cm heated length. Individual heater rods are made up of compressed MgO core surrounded by a 0.7-mm-thick Incoloy sheath. The heaters are arranged in a square pattern with center-to-center pitch spacing of 1.46 cm. The enclosure interior surface is a square, 12 ± 0.25 cm on each side. The array is centered within

the aluminum vacuum chamber. As a result the minimum spacing between the rods and the wall is 3.35 mm, while the minimum spacing between adjacent rods is 3.6 mm.

The heated rod length is shorter than the typical 3.6-m active length of a fuel assembly. As mentioned before, the apparatus is intended to be representative of a region between consecutive grid spacers [1]. The surface emissivity of the rods and chamber walls are 0.8 (specified by the manufacturer) and 0.5 for the anodized aluminum walls [21].

Steady-state rod and surface temperature measurements were made in seventy-two experiments under the following conditions: (a) helium or nitrogen fill gases at pressures of 1 to 3 atm, (b) rods in the vertical (storage) and horizontal (transport) orientation, (c) array heat generation rates of 100 to 500 W, and (d) different thicknesses of insulation surrounding the system (to increase the aluminum enclosure temperature to up to 280°C).

Figure 2a shows the apparatus wrapped in insulation in the vertical orientation. Figure 2b shows heater surface temperature contours calculated from a three-dimensional CFD simulation of the experimental apparatus in the vertical orientation [20]. Half of the heaters are removed to show the hottest rods. This calculation was performed using the ANSYS/Fluent CFD package with the enclosure filled with nitrogen gas at 3 atm. The simulations include heat generation and conduction within the rods, and natural convection and radiation heat transfer across the gas. Figure 2b shows buoyancy-induced gas motion causes the highest temperatures to be above the array center. Simulations with helium (not shown), which has a higher thermal conductivity than nitrogen and so are not as affected by buoyancy, show the maximum temperature is closer to the rod mid-height.

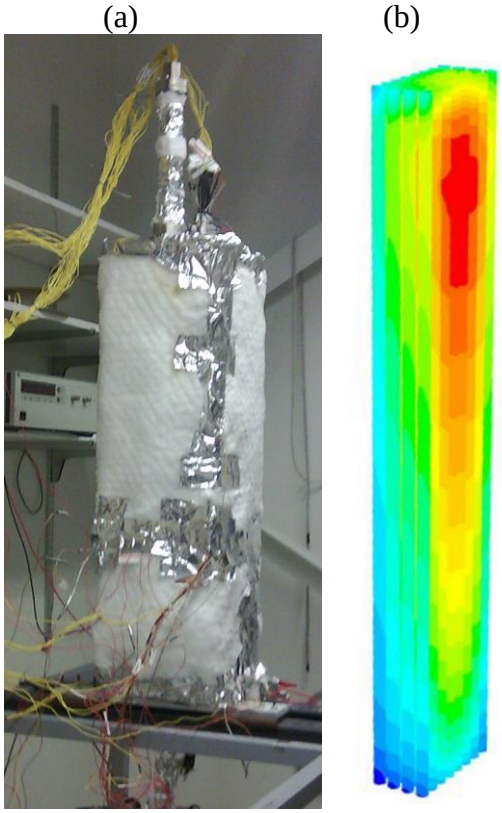

Figure 2. (a) Experimental apparatus in the vertical orientation and wrapped in insulation. (b) Heater surface temperature contours from ANSYS/Fluent simulations. Half of the heaters are removed to show the hottest locations. [20]

Figure 3 shows simulated versus measured results for the temperature difference between the hottest measured rod location and the wall [20]. The results from experiments and simulations are included, for different wall temperatures, heat generation rates, gas pressures, for both helium and nitrogen fill gases. The figure shows that 95% of the simulated temperature differences were within 5°C of the measured data.

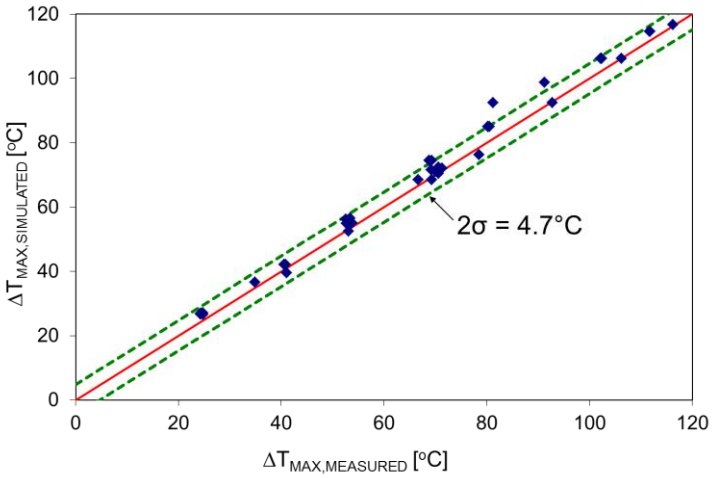

Figure 3. Simulated versus measured results for the difference between the hottest rod and wall temperatures. Results are presented for 42 experiments with different rod heat generation rates, wall temperatures, gas pressures, for both He and N_2 gases. [20]

In the current work we wish to determine if the apparatus described in this section can be used to benchmark rarified-gas simulations under conditions that are relevant to vacuum drying. In order to do that with a high degree of certainty, the experiment must be operated under conditions that cause the maximum temperature predicted by rarified gas simulations to be at least 5°C hotter than simulations that do not include this effect.

RARIFIED GAS HEAT TRANSFER

Under normal atmospheric conditions, gas molecules confined within a moderate-sized volume experience many collisions with each other between interactions with the walls (4, 12-15). The mean free path between molecular collisions is:

$$\lambda = \frac{kT}{\sqrt{2}\pi P d^2}\ , \qquad (1)$$

where k is the Boltzmann constant, T is the local temperature, P is the local pressure, and d is the Lennard-Jones collision diameter of the molecules.

Knudsen Number (Kn) is the ratio of the mean free path to the characteristic length L_C of the region occupied by the gas:

$$Kn = \frac{\lambda}{L_C} \qquad (2)$$

We note that L_C is easily defined in simple enclosures such as parallel plates, spheres and cylinders. However, in complex geometries such the enclosed heater rod array in Figs. 1 and 2, the characteristic length is not easily determined.

If $\lambda << L_C$, a molecule will experience "many" molecular collisions between interactions with the walls, and the molecules at any location reach equilibrium with each other. As a result when Kn << 1, the gas may be treated as a continuum. When Kn < 0.01, the Navier-Stokes and Convective Energy equations accurately model momentum and energy transport within a gas [13]. Moreover, at the interface between the gas and solid surfaces, the gas and wall temperatures and their velocities are effectively the same, that is $T_G = T_W$, and $V_G = V_W$ (no-slip boundary condition).

Equations (1) and (2) show that the molecular mean free path and the Knudson number increase as the gas pressure decreases and/or temperature increases. If Kn is sufficiently large then a molecule experiences only a few molecular interaction between wall collisions. Under those conditions, the system exhibits characteristics of a coarse molecular structure, and the gas is considered rarified. When Kn > 0.1 the Boltzmann kinetic equation must be applied to accurately model the gas, and its numerical solution is computationally intensive [13].

For 0.01< Kn < 0.1 the gas is considered to be at a level of slight rarefaction [14]. In such cases the gas tends to behave as a continuum in regions away from the walls. However, a molecule that comes into contact with a wall does not meet other molecules enough times to reach equilibrium with them in the vicinity of the wall [15]. Therefore there can be an abrupt change of temperature and speed from the surface to the gas, that is $T_G \neq T_W$, and $V_G \neq V_W$. This is known as temperature-jump or slip-flow. As a result, for 0.01< Kn < 0.1, the Navier-Stokes and Convective Energy equations accurately model momentum and energy transport away from the walls, but gas rarefaction must be taken into account at the walls using "temperature-jump" and "velocity-slip" boundary condition [13, 14]. Due to the difference in the gas and surface velocity, this condition is known as the slip-flow regime.

Under moderately rarefied conditions, Sharipov [22] indicates that the local temperature-difference or temperature-jump between the gas and wall is determined using a resistance model,

$$T_G - T_W = R_{TJ} Q \; . \qquad (3)$$

In this model, Q is the portion of the heat transfer rate directed to the solid surface transported by conduction within the surrounding gas and does not include the component transported by radiation to other surfaces. The temperature-jump thermal-resistance is

$$R_{TJ} = \frac{\mu}{P}\left(\frac{2kT_W}{m}\right)^{1/2} \frac{\zeta_T}{A\kappa} \; . \qquad (4)$$

In this expression μ is the gas dynamic viscosity, m is the mass of a gas molecule, κ is the thermal conductivity of the gas, and A is the surface area. The Temperature Jump Coefficient ζ_T

in Equation (4) is determined by applying the Boltzmann Equation to the Knudsen Layer [13], and is calculated as

$$\zeta_T = \frac{2-\alpha}{\alpha}\frac{\sqrt{\pi}\gamma}{(\gamma+1)\mathrm{Pr}}, \text{ where } \mathrm{Pr} = \frac{\mu}{\kappa}c_P . \qquad (5)$$

In these expressions α is the gas/surface accommodation coefficient γ is the gas specific heat ratio, Pr is the gas Prandtl number, and c_P is the gas specific heat at constant pressure.

SIMPLE CONCENTRIC CYLINDER MODEL PROBLEM

Figure 4a shows a two-dimensional ANSYS/Fluent computational mesh of a helium-filled annular-space with inner and outer surface temperatures and radii of, respectively, T_{Wi} = 400°C and r_i = 1 cm, and T_{Wo} = 350°C and r_o = 3 cm. Its height normal to the plane of Fig. 4a is lL = 1 m. The choice of the dimensions and temperatures of this model problem are somewhat arbitrary.

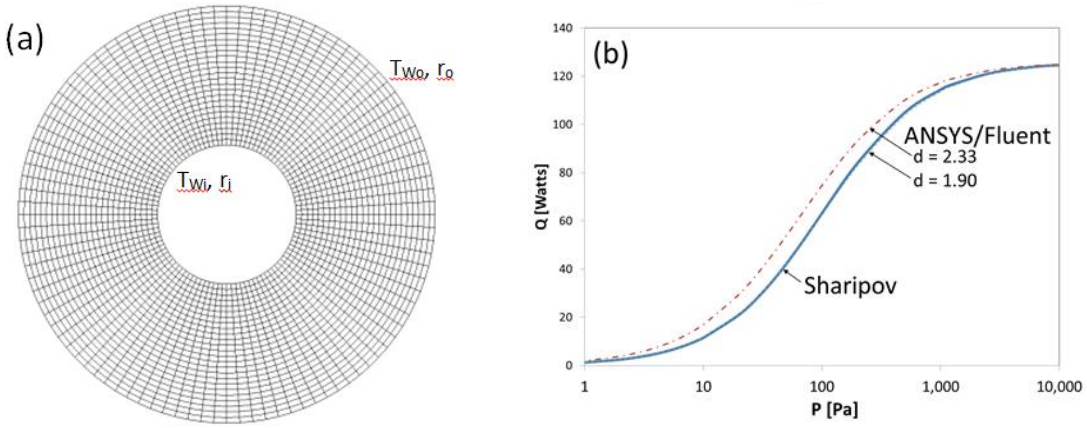

Figure 4. Simple heater rod centered in a cylindrical vessel configuration used to compare ANSYS/Fluent and Sharipov results. (a) Concentric circle computational domain. (b) Heat flux versus helium pressure results from ANSYS/Fluent simulations and Sharpov calculations.

The Sharopov model may be used to predict conduction heat transfer across this region for a range of helium pressures. The heat must flow through a thermal resistances associated with conduction within the helium,

$$R_{COND} = \frac{Ln(r_o/r_i)}{2\pi kL} . \qquad (6)$$

It must also pass through temperature-jump thermal resistances at the inner and outer surfaces, which are respectively

$$R_{TJi} = \frac{\mu}{P}\left(\frac{2kT_{Wi}}{m}\right)^{1/2}\frac{\zeta_T}{2\pi r_i L\kappa} \text{ and } \qquad (7)$$

$$R_{TJo} = \frac{\mu}{P}\left(\frac{2kT_{Wo}}{m}\right)^{1/2}\frac{\zeta_T}{2\pi r_o L\kappa} \quad . \qquad (8)$$

This heat transfer is driven by the temperature difference between the inner and outer surfaces of the annular space. The resulting conduction heat transfer is calculated using a circuit analogy, as

$$Q = \frac{T_{Wi} - T_{Wo}}{R_{TJi} + R_{COND} + R_{TJo}} \quad . \qquad (9)$$

At the average wall temperature of 350°C, the relevant helium properties are γ = 1.666, m = 6.642×10^{-27} kg, Pr = 0.68, κ = 0.17 W/mK, $\mu = 221 \times 10^{-7}$ Ns/m^2 [23]. When helium is in contact with an "engineering surface" at 27°C and 427°C, the accommodation coefficient is approximately α = 0.4 and 0.25, respectively [24].

In Fig. 4b, the solid line marked Sharipov shows the resulting conduction heat transfer versus pressure. For pressures above 10,000 Pa, the heat transfer is essentially the value expected based on conduction in the helium, and the effect of the temperature-jump is negligible. As the pressure decreases below this value, the temperature-jump thermal resistances on the inner and outer surfaces increase, and the heat transfer rate decreases.

ANSYS/Fluent has an option to impose temperature jumps at surfaces due to moderately rarefied gas effects. That model requires specification of Helium's Lennard-Jones collision diameter d. Values of d = 1.9 and 2.33 angstroms are found in the literature [25]. In Fig. 4b, the dashed lines marked ANSYS/Fluent d = 1.9 and d= 2.33 shows heat transfer rate versus pressure for those collision diameters. Like the Sharipov calculation, these heat transfer rates is essentially not affected by gas rarification for P > 10,000 Pa, and decreases due to the increased importance of the temperature jump at lower pressures. The rates predicted with d = 1.9 angstroms are in much better agreement with the Sharipov model than the other value. This value is used in the rest of the simulations presented in this paper.

COMPUTATIONAL MODEL OF EXPERIMENTAL APPARATUS

This section describes the computational methods used to predict the experimental heater rod and helium gas temperatures within the experimental apparatus in Figs. 1 and 2 for a range of isothermal enclosure temperatures T_E, gas pressures P, and rod array heat generation rates Q. Results from Continuum simulations, which do not include temperature jumps between the solid and gas, are compared to those obtained for Moderately Rarified simulations which include the temperature jump. Figure 5 shows a two-dimensional ANSYS/Fluent finite volume grid of the experiment cross section. It includes 64 heater rods, the interior boundary of the enclosure, and the helium gas in-between. Each rod consists of a D = 9.5-mm-diameter magnesium oxide (MgO) core surrounded by a 0.71 mm thick Incoloy sheath. The rod center-to-center pitch is 14.35 mm, and the minimum distance between the rod surface and the enclosure is 1.72 mm. The length of the enclosure walls is 114.83 mm (this is slightly shorter than the experimental apparatus dimension).

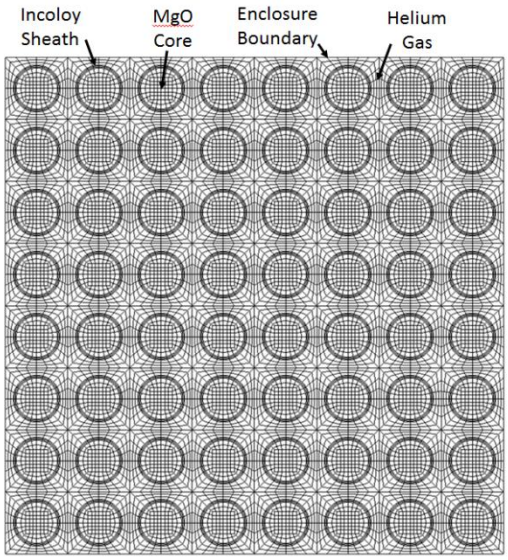

Figure 5. Two-dimensional computational mesh of the experiment cross section composed of 46,592 elements.

The mesh consists of 46,592 elements. The current authors used the same meshing scheme to create a two-dimensional CFD mesh of a 7x7 array with nitrogen at atmospheric pressure, and showed the results were independent of further mesh refinements [26]. Future simulations with the current geometry at low pressures will be performed with different grid refinements to confirm grid independence.

Steady-state thermal simulations were performed using the ANSYS/Fluent package. These simulations included heat generation within the MgO rod cores, conduction within the solids and helium, and surface-to-surface radiation across the helium filled region. These simulations do not include buoyancy-induced gas motion or natural convection in the helium because they are negligible at the low pressures considered in this work. Appropriate temperature-dependent thermal conductivities were applied to each material region.

Simulations are performed with enclosure temperatures of 27°C and 427°C to cover conditions between room temperature and situations that cause the cladding to reaches it limit temperature. Simulations were performed for array heat generation rates between Q = 100 and 500 W. In this work a uniform volumetric heat generation rate applied to the MgO cores that is equal to the total array heat generation rate divided by the MgO volume, $q = Q/(64\pi(D/2)^2L)$. For array heat generation rates between 100 and 500 W and a heated length of L = 60.9 cm, the axial heat generation rates are between 164 W/m and 820 W/m. For a typical BWR with a length of 3.6 m and a peaking factor of 1.25 [1], these axial heat generation rates correspond to assembly heat generation rates between 470 and 2300 W.

Three different heat transfer models are used in this work. The first is the Continuum Model, which does not include temperature jumps between the solid surfaces and the gas. The second is the Moderately-Rarefied Model, which includes the temperature jump thermal resistance described in Equations 4 and 5. Simulations for this model are performed for pressures of P = 100 and 400 Pa, and thermal accommodation coefficients of α = 0.25 and 0.4. The last model was for a Hard Vacuum, which neglects all conduction in the helium gas, and assumes all heat transfer between the rods and enclosure is by radiation.

The ANSYS/Fluent package employs a second-order upwind scheme to solve the energy equations. Radiative heat transfer was solved for gray diffuse surfaces using the discrete ordinates method with a second-order upwind scheme. The governing equations were solved using double precision.

RESULTS AND DISCUSSION

Figure 6 shows temperature contours from a Continuum Model simulation with T_E = 27°C (300 K), and Q = 500 W. There is a central high temperature region. The contours exhibit symmetry about horizontal, vertical and diagonal lines, which reflects the symmetry of the geometry and boundary conditions. The maximum or peak temperature in the domain is T_P = 133°C (406 K). Due to symmetry, it appears within all four of the rods closest to the domain center, along the diagonal symmetry lines. The maximum temperature difference within the domain is $T_P - T_E$ = 106°C. Figure 6 shows the s-axis whose origin is at the domain center. It lies on a diagonal symmetry line and passes through four heater rods and a domain corner.

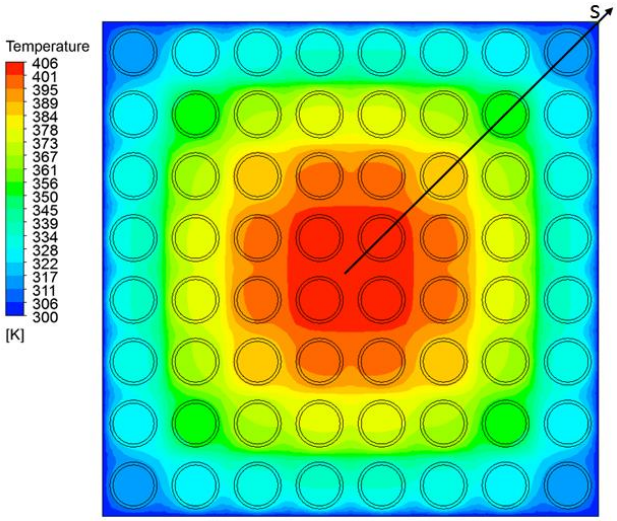

Figure 6. Temperature contours calculated for Q = 500 W, T_E = 27°C, P = 100 Pa and helium gas. The s-coordinate system, whose origin is at the domain center and passes through one corner, is shown.

Figure 7 shows rod and gas temperature minus the enclosure temperature $T - T_W$, versus distance from the domain center along the s-axis for T_E = 27°C and Q = 500 W. Results from Continuum and Moderately-Rarefied simulations are included. The line marked Continuum shows temperatures from the contours in Fig. 6. The temperatures within the four heater rods are relatively uniform compared to the gradients in the gas. Since this model does not include temperature jumps, the gas temperature is the same as the heater rod and enclosure surfaces they it are in contact with.

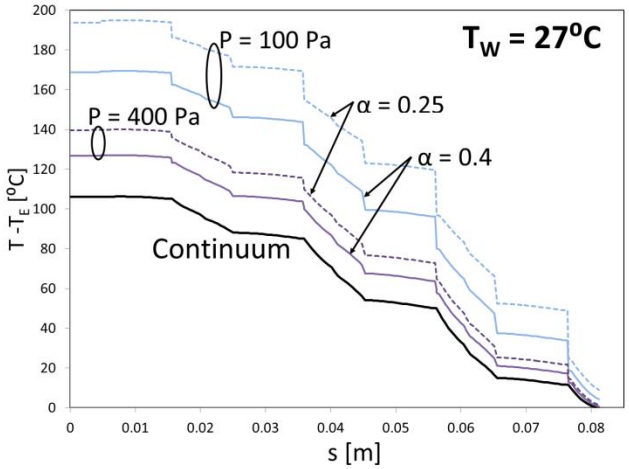

Figure 7. Temperature minus wall temperature along the s-axis shown in Fig. 6, calculated for Q = 500 W, T = 27°C, and helium gas. Results are given for a continuum models (at roughly atmospheric pressure) and low pressured (P = 100 Pa) models with thermal accommodation coefficients of α = 0.25 and 0.4.

Moderately Rarified simulations results are also in Fig. 7, for pressures of P = 100 and 400 Pa, and thermal accommodation coefficients of α = 0.25 and 0.4. These temperature profiles include thermal resistances between the gas and solid surfaces, which make them hotter than those from the Continuum Model. Equations 3 and 4 show that these resistances increase as P and α decrease. Figure 7 shows that the rod and gas temperature increase as the thermal resistance increase.

The Moderately-Rarified simulation temperature profiles in Fig. 7 exhibit jumps or discontinuities at the interface between the gas and the solid rod and enclosure surfaces. The jumps on the outer surfaces of each rod (the surfaces further from the domain center) increase with distance from the domain surface. This is because the heat flux leaving the rod outer surfaces increases with distance from the center. The effect of the individual temperature jumps accumulate as the distance from the enclosure surface increases. As a result, the differences between the Moderately Rarified and Continuum simulation temperatures are larger at the domain center than they are near the enclosure wall. In each simulation, the peak temperature in the domain, T_P, is located near s = 0.01 m.

Figure 8 shows the maximum temperature difference in the domain, $T_P - T_E$ versus heat generation rate. Results are shown for the Continuum, Moderately-Rarified, and Hard Vacuum simulations. Figures 8a and 8b show results for T = 27 and 427°C, respectively. The peak temperature difference increases with assembly heat generation rate. The Moderately-Rarified results are consistently hotter than the continuum temperatures, and the Hard Vacuum temperatures are hotter still. The temperature differences in Fig. 8b, for the higher enclosure temperature, are smaller than those in Fig. 8a, because the effects of radiation increase with temperature.

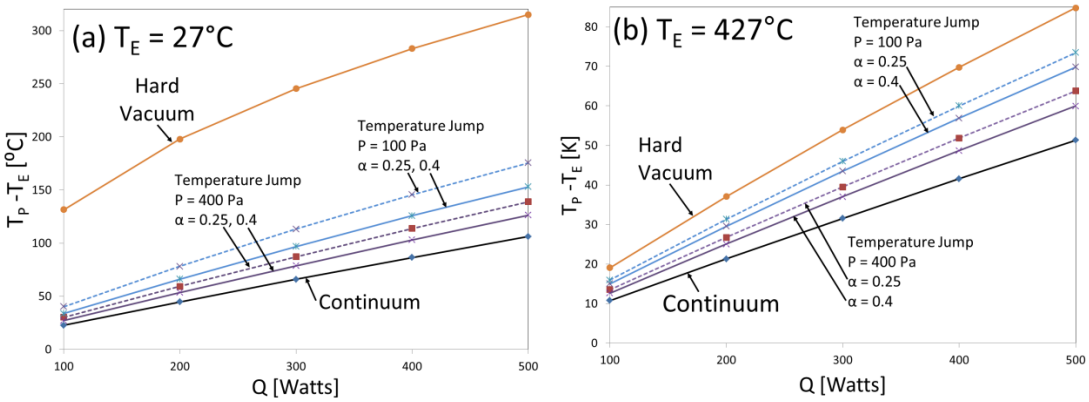

Figure 8. Peak fuel temperature minus wall temperature versus heat generation rate from Continuum, Moderately Rarified (P = 100 and 400 Pa, and α = 0.25 and 0.4), and Hard Vacuum simulation models. (a) T_W = 27°C, (b) T_W = 427°C.

The objective of the current paper is to determine the minimum rod array heat generation rate for which the maximum rod temperatures from the Moderately-Rarified simulations are at least 5°C hotter than those from Continuum calculations. Figure 8 shows that this condition is met if the array heat generation rate is greater than Q = 200 W (axial heat generation rate Q/L = 330 W/m).

SUMMARY

Evacuating helium gas from used nuclear fuel canisters during vacuum drying, to pressures as low as 100 or 400 Pa, has the potential to increase cladding temperatures compared to atmospheric pressure conditions. This is because, at these low pressures, natural convection becomes ineffective at enhancing heat transfer beyond the levels from pure conduction, and the gas become moderately rarified, which effectively increases the thermal resistance between the remaining gas and the solid surface. The overall objective of this research program is to develop and experimentally-benchmark computational models that can be used to predict cladding temperatures during vacuum drying.

In this paper, the Sharipov temperature-jump thermal-resistance model [22] was used to predict the heat transfer across a simple helium-fill annular region as a function of pressure. ANSYS/Fluent simulations of the same configuration were performed with two different Lennard-Jones collision diameters, d = 1.9 and 2.33 angstroms. The simulation with d = 1.9 angstroms exhibited good agreement with the Sharipov calculation. It was therefore used to simulate heat transfer in a square array of heaters rods within an isothermal enclosure. This configuration is relevant to used nuclear fuel assemblies within a canister basket opening. It also models an existing experimental apparatus that has been used to benchmark computational models of used nuclear fuel under storage conditions, in which the helium pressure is between 1 to 3 atm. ANSYS/Fluent simulations of those experiments predicted peak rod temperatures that were within 5°C of the measured value. The objective of the current paper is to determine the heater array heat generation rate for which causes the peak temperature from rarified gas simulations to be at least 5°C hotter than those from continuum calculations.

Two-dimensional ANSYS/Fluent simulations of the experiment cross section were performed for a range of array heat generation rates and enclosure temperatures. Results from

Continuum simulations (which did not include the rarified gas temperature jump) were compared to Moderately-Rarified simulations with at 100 and 400 Pa. When the array heat generation rate was above 200 W, the difference between the peak rod temperatures predicted by the continuum and Moderately-Rarified simulations was greater than 5°C. This indicates that the existing experimental apparatus can be used to benchmark the rarified gas computational models that are being developed to predict used nuclear fuel cladding temperatures under vacuum drying conditions.

FUTURE WORK

The existing experimental apparatus will be used to measure rod temperatures for a range of enclosure temperatures, rod array heat generation rates, and low helium pressures. These data will be compared to results from three-dimensional simulations of the experimental conditions. This comparison will be used to benchmark and/or adjust the computational methods. Computational models of whole transfer packages, in which nuclear fuel is vacuum dried, will be constructed. The effects of gas rarification will be implemented in these models. Steady-state and transient simulations using these models will be performed to predict the peak cladding temperatures. These simulations will be used to develop effective methods for vacuum drying used fuel without causing cladding temperatures that lead to radial hydride formation.

Forced helium dehydration is used to remove moisture from packages containing high burnup and other high-heat-generating fuel assemblies. Vacuum drying these assemblies may cause their cladding temperature to exceed limits that lead to radial hydride formation unless those assemblies spend a very long time in underwater storage pools. In forced helium dehydration, helium is circulated through the canister, and moisture is removed from it by condensing, demoisturizing, and preheating the gas outside the canister. The gas pressure is roughly the same as that used during storage (3–7 atm) so natural convection cooling effects are active, and the gas is not rarified. Future work should consider developing and experimentally benchmarking advanced computational models of forced helium dehydration. To perform that work an enclosed, vertical heater array test facility, whose length is the same as that of a fuel assembly (~3.6 m), with an external circulation system, would need to be constructed. That facility would exhibit the mixed natural/forced convection heat transfer phenomena relevant during forced helium dehydration. These data would be used to experimentally benchmark computational fluid dynamics simulations that can be used to calculate heat and moisture transport during drying operations, and to design efficient drying methods.

After an advanced computational model of natural and forced convection within a canister has been developed and benchmarked for forced helium dehydration, it may be used to solve another difficult problem related to long-term storage of used nuclear fuel. That is, developing a nondestructive method to determine if high-conductivity helium has leaked out of the canister and been replaced by lower-conductivity air [27]. In pressurized vertical storage canisters, buoyancy effects cause the gas in the relatively warm center region to flow upward, and then flow downward near its periphery, i.e., thermal siphoning. Since helium has a relatively high thermal conductivity, the temperatures within the canister and on its external surfaces are relatively uniform. However, if the helium were replaced by air, and since air has a much lower thermal conductivity, the interior and exterior of the canister will exhibit higher temperatures near its top compared to those at its bottom. The advanced computation model of canister convection can be used to calculate the interior and exterior temperatures when helium and air

are within the canister. These results can be used to determine how the external temperature changes if helium were to leak out of the canister, and design method to determine if this has happened by measuring the canister's external temperature.

ACKNOWLEDGMENTS

This work was supported by the US Department of Energy Office of Nuclear Energy's Nuclear Energy University Program.

NOMENCLATURE

BWR	Boiling Water Reactor
CFD	Computational Fluid Dynamics
c_P	Specific Heat [J/kgK]
d	Diameter of the molecules of cover gas [m]
Kn	Knudsen Number [-]
k	Boltzmann constant, 1.38×10^{-23} [m^2kg/s^2K]
L_C	Characteristic Length [m]
m	molecular mass of the gas [kg]
P	Local pressure [Pa]
Pr	Prandtl Number ($C_p\mu/\kappa$)
PWR	Pressurized Water Reactor
Q	Total array heat load [W]
q	Volumemetric heat generation rate [W/m^3]
T_G	Temperature of the gas near the wall [°C]
T_P	Peak or Maximum temperature within domain [°C]
T_W	Temperature of the wall [°C]
T	Local temperature [°C]
α	Thermal accommodation coefficient [-]
ε	Surface emissivity [-]
γ	Specific heat ratio [-]
κ	Thermal conductivity of the gas [W/mK]
λ	Mean free path [m]
μ	Stress viscosity of the gas [kg/ms]
ζ_T	Temperature Jump Coefficient (TJC) [-]

REFERENCES

1. U.S. Dept. of Energy, Office of Civilian Radioactive Waste Management (OCRWM), 1987, "Characteristics of Spent Nuclear Fuel, High-Level Waste, and Other Radioactive Wastes Which May Require Long-Term Isolation", DOE/RW-0184, December.
2. Saling, J.H., and Fentiman, A.W., 2002, *Radioactive Waste Management*, 2nd Edition, Taylor and Francis, New York.
3. Holtec International, "HI-STORM 100 FSAR," Revision 8, Report HI-2002444, 2010.

4. Colmont, D. and Roblin, P., 2008, “Improved thermal modeling of SNF shipping cask drying process using analytical and statistical approaches”, Packaging, Transport, Storage & Security of Radioactive Material, Vol. 19, No. 3, pp. 160-164.
5. Hanson, B., Alsaed, H., Stockman, C., Enos, D., Meyer, R., and Sorenson, K., 2012, “Gap Analysis to Support Extended Storage of Used Nuclear Fuel,” FCRD-USED-2011-000136 Rev. 0, U.S. Department of Energy Used Fuel Disposition Campaign.
6. “Cladding Considerations for the Transportation and Storage of Spent Fuel,” ISG-11 R3, Interim Staff Guidance Report for the Spent Fuel Project Office of the U.S. NRC, 2003.
7. Daum, R.S., Majumdar, S., Liu, Y.Y., and Billone M.C., 2006. “Radial-hydride Embrittlement of High-burnup Zircaloy-4 Fuel Cladding.” J. Nucl. Sci. Tech., Vol. 43, No. 9, Paper 43090, pp. 1-14.
8. Daum, R.S. Majumdar, S., and Billone, M.C. 2008, “Experimental and Analytical Investigation of the Mechanical Behavior of High-Burnup Zircaloy-4 Fuel Cladding.” J. ASTM Intern., Vol. 5, No. 5, Paper ID JAI101209, available online at www.astm.org.
9. Billone, M.C., Burtseva, T.A., and Einziger, R.E., “Ductile-to-brittle transition temperature for high-burnup cladding alloys exposed to simulated drying-storage conditions,” J. Nucl. Mater. 433, 431-448 (2013).
10. Billone, M.C., Burtseva, T.A., and Liu, Y.Y., “Baseline Properties and DBTT of High-Burnup PWR Cladding Alloys,” Proc. PATRAM 2013, San Francisco, CA, August 18-23, 2013.
11. Large, W.S. and Sindelar, R.L., 1997, “Review of Drying Methods for Spent Nuclear Fuel” Westinghouse Savannah River Company, Savannah River Site, Aiken, SC, report number WSRC-TR-0075
12. Pan, L.S., Ng, T.Y., Xu, D., Liu, G.R., and Lam, K.Y, 2002, “Determination of Temperature Jump Coefficient Using the Direct Simulation Monte Carlo Method”, *Journal of Micromechanics and Microengineering*, Vol. 12, pp. 41-52
13. Sharipov, F. and Kalempa, D., 2005, “Velocity Slip and Temperature Jump Coefficients for Gaseous Mixtures. IV. Temperature jump coefficient” *International Journal of Heat and Mass Transfer* 48, pp. 1076-1083
14. Schaaf, S.A. and Chambre, P.L, 1961, *Flow of Rarefied Gases*, Princeton University Press, New Jersey.
15. Loeb, L.B., 1934, *Kinetic Theory of Gases*, 2nd Edition, McGraw-Hill Book Company Inc.
16. Tseng, Y.S, Wang, J.R., Tsai, F.P., Cheng, Y.H., and Shih, C., 2011, “Thermal design investigation of a new tube-type dry-storage system through CFD simulations,” *Annals of Nuclear Energy*, 38, 1088-1097.
17. Holtec International, 2000, “Topical Report on the HI-STAR/HI-STORM Thermal Model and its Benchmarking with Full-Scale Cask Test Data,” Holtec Report No. HI-992252.
18. Pacific Northwest Laboratory, et al., 1987, "The TN-24P PWR Spent Fuel Storage Cask: Testing and Analyses", EPRI NP-5128.
19. Chalasani, N.R., Araya, P., and Greiner, M., 2009, "Benchmark of Computational Fluid Dynamics Simulations using Temperatures Measured within Enclosed Vertical and Horizontal Arrays of Heated Rods," Nuclear Technology., Vol. 167, No. 3, pp. 371-383.
20. Chalasani, N.R and Greiner, M., 2010, “Benchmark of Computational Fluid Dynamics Simulations Using Temperatures Measured Within Enclosed Vertical and Horizontal Arrays of Heated Rods,” PVP2010-25803, Proceedings of the ASME 2010 Pressure Vessels and

Piping Division/K-PVP Conference, PVP2010, July 18-22, 2010, Bellevue, Washington, USA
21. Modest, M.F., 2003, *Radiative Heat Transfer*, 2nd Edition, Academic Press, New York.
22. Sharipov, F., 2004, "Data on the velocity slip and temperature jump coefficients," *Thermal and Mechanical Simulation and Experiments in Micro-Electronics and Micro-Systems*. Proc. 5th Int. Conf. EuroSimE, Belgium, pp. 243-249.
23. Incropera, F.P. and DeWitt, D.P., 1996, *Introduction to Heat Transfer*, 3rd Edition, J. Wiley & Sons, New York.
24. Song, S., and Yovanovich, M. M., "Correlation of thermal accommodation coefficient for 'engineering' surfaces," *Fundamentals of conduction and recent developments in contact resistance*, Proceedings of the Twenty-fourth ASME National Heat Transfer Conference and Exhibition, Pittsburgh, PA, Aug. 9-12, pp. 107-116.
25. Hirschfelder, J.O., Curtis, C.F., and Bird, R., 1954, *Molecular Theory of Gases and Liquids*, John Wiley & Sons, Inc., p. 552.
26. Araya, P.E. and Greiner, M., 2007, "Two-Dimensional Simulations of Natural Convection/Radiation Heat Transfer for BWR Assembly within Isothermal Enclosure," *Packaging, Transport, Storage and Security of Radioactive Material*, Vol. 18, No 3, pp. 171-179.
27. Tsai, H.C., Liu, Y.Y. and Shuler, J.M., "Monitoring Critical Facilities by using Advanced RF Devices," Proc 15th Intl. Conf. on Environmental Remediation and Radioactive Waste Management, ICEM2013, September 8–12, 2013, Brussels, Belgium.

Proceedings of the PVP2014
ASME 2014 Pressure Vessels & Piping Division Conference
July 20-24, 2014, Anaheim, California, USA

PVP2014-29018

DESIGN OF AN EXPERIMENTAL APPARATUS TO MEASURE THE THERMAL ACCOMMODATION COEFFICIENT BETWEEN STAINLESS STEEL SURFACES AND RAREFIED HELIUM.

Rachel Green
University of Nevada, Reno
Reno, NV, USA

ErnestoT. Manzo
University of Nevada, Reno
Reno, NV, USA

Mustafa Hadj Nacer
University of Nevada, Reno
Reno, NV, USA

Miles Greiner
University of Nevada, Reno
Reno, NV, USA
greiner@unr.edu

ABSTRACT

The objective of this work is to design an experimental apparatus that can acquire data to benchmark rarefied gas heat transfer simulations, and determine the thermal accommodation coefficient at the interface between the solid surfaces and the gas. The design consists of an aluminum cylinder with an electric heater at its centerline, and within a stainless-steel sheath, centered inside a cylindrical pressure vessel whose temperature is controlled using an external water jacket. There is 0.47-cm-wide helium-filled gap between the inner cylinder and vessel wall. For a given heat generation rate, the temperature difference across this gap will increase as the gas pressure decreases due to ratification. Thermocouples will be bonded to the vessel's outer surface, and the inner surface of the sheath that surrounds the heated aluminum cylinder. Two, two-dimensional computational meshes of the apparatus (one cross sectional and the other cross sectional is offset) and one three-dimensional computational mesh are constructed. These models include heat generation within the electric heater, conduction within the solid and gas-filled regions, and radiation heat transfer across the gas, and rarefied gas thermal resistances at the solid/gas interfaces. These simulations show that the difference between the thermocouple temperatures and the surfaces of the helium filled gap are small compared to the temperature across the gap. This will allow this apparatus design to be used to effectively benchmark the ANSYS/Fluent simulations, and determine the thermal accommodation coefficient.

NOMENCLATURE

a	Slope of the temperature difference variation with the inverse of the pressure
d	Diameter of the molecules of cover gas [m]
Kn	Knudsen Number [-]
k_B	Boltzmann constant, 1.38×10^{-23} [m^2kg/s^2K]
L	Cylinder length [m]
L_C	Characteristic Length [m]
m	Molecular mass of the gas [kg]
P	Local pressure [Pa]
Q	Total heat load [W]
Q'	Heat Flux [W/m]
Q_r	Radial heat flux [W]
R_{TJ}	Temperature jump thermal resistance [K/W]
T	Temperature [K]
T_i	Temperature of the incident molecules [K]
T_r	Temperature of the reflected molecules [K]
T_w	Temperature of the wall [K]

Greek symbols

α	Thermal accommodation coefficient [-]
ε	Surface emissivity [-]
γ	Specific heat ratio [-]
κ	Thermal conductivity of the gas [W/mK]
λ_d	Mean free path based on the molecular diameter [m]
λ_μ	Mean free path based on the viscosity [m]
μ_0	Reference viscosity [kg/ms]
μ	Stress viscosity of the gas [kg/ms]
λ_d	Mean free path based on the molecular diameter [m]
ζ_T	Temperature Jump Coefficient (TJC) [-]

Acronyms

CFD	Computational Fluid Dynamics
DSMC	Direct Simulation Monte Carlo
LJ	Lennard-Jones
TAC	Thermal Accommodation Coefficient

INTRODUCTION

Spent nuclear fuel transportation casks are made of thick walled containers so that they can survive potentially severe accidents while being transported by rail and truck [1, 2]. The fuel assemblies are placed in canister at the center of the cask where they are supported horizontally within square cross-section basket openings inside the package containment region.

During the transportation the generation of heat from the fuel along with the solar heating, cause the transportation container to have a higher temperature than its surroundings. The Nuclear Regulatory Commission Interim Staff Guidance-11, Revision 3 (ISG-11) [3] requires that the Zircaloy cladding temperature must exceed 400°C during the drying, transport and storage to prevent the radial hydride formation. This temperature

restriction limits the heat generation rate by the fuel and so the number and age of the fuel assemblies inside the packages.

Heat transfer processes inside the fuel assembly/backfill gas region have not yet been fully characterized. This uncertainty significantly contributes to the prediction of the maximum cladding temperature for a specified fuel heat load, and the maximum fuel heat load.

To address this uncertainty package designers have reduced the number and the heat generation rate of the assemblies that are loaded into the packages. It is this reduction that ensures that the maximum cladding temperatures are not exceeded. However, this reduction increases the number of shipments and the associated risk to the public. More accurate models for fuel cladding temperature predictions are needed and could have potential public safety consequences.

Package temperatures are determined for typical ambient conditions of a hot day of 38°C described in federal regulations [4]. The temperature difference between the cylindrical zircaloy tubes in the fuel assemblies and the ambient are directly affected by fuel heat generation rate. The radial and axial temperature profiles of the cylindrical zircaloy tubes are also affected by the fuel heat generation rate.

Before transportation and after being discharged from the reactors, the fuel assemblies are stored underwater to decrease their heat generation and radioactivity [5]. After an appropriate time, they are placed in canister and loaded out of the pool. The water in the canister is evacuated by forcing helium gas through the canister. Small amount of water may remain at the bottom of the canister [6]. Essentially all the water and moisture remaining must be removed to prevent the corrosion of the fuel cladding and cask material during the transport and storage. After drying the canister is backfilled with a non-oxidizing gas to pressure between 3 to 7 atm, then placed in other packaging for onsite interim storage or offsite transport.

Currently there are two methods that are used by industry for this process, forced helium dehydration and vacuum drying. Both of these methods must meet the drying technical specification of maintaining the specified pressure of 400 Pa for 30 minutes to be considered dry [6, 7].

Canisters with high heat generation fuel are subjected to forced helium dehydration for drying. At the top of the canister is a port that helium is forced into and at the bottom of the canister it is withdrawn through a tube. It is also common in some cases for cooling water to be circulated in the gap between the canister and its transfer cask during this process. The pressures during the forced helium dehydration is roughly maintained the same as during the storage. The shortcoming of this method is equipment (gas demoisturizing and cooling) required for accomplishing this process.

The vacuum drying method requires less equipment compared to the forced helium dehydration. During this method the pressure in the canister is decreased as low as 67 Pa to promote evaporation and removal of the water [8]. This is accomplished by performing several cycles of evacuation and refill until the operator is able to demonstrate that the canister meets the technical specifications.

At these low pressures and densities, buoyancy-induced gas motion and natural convection heat transfer from the fuel to the solid surfaces of the canister can be neglected; while the thermal conductivity of the gas is almost the same as at atmospheric pressure conditions.

The shortcoming of the drying vacuum method is the increasing of the cladding temperature due to the rarefaction (at low pressure). When the gas is rarefied there is a notable temperature difference (temperature jump) between the fuel cladding wall and the gas that is interacting with it [9-12]. As the pressure increases this temperature jump becomes negligible, but the more rarefied the gas is the more important this jump is and may contribute to higher cladding temperatures during the vacuum drying process and storage.

The temperature jump is characterized by the Thermal Accommodation Coefficient (TAC). At low pressure the collisions between gas molecules and the surfaces dominate the molecules-molecules collisions. In these conditions the equilibrium and the continuity of the macroscopic parameters (velocity and temperature) near the walls are not reached. Maxwell [13] postulated that when molecules enter in collision with the wall there are a range possible results bounded by two extremes: (i) the molecules can be reflected specularly, without transferring any of their momentum or energy to the surface (the molecule's temperature and velocity component parallel to the wall remain unchanged, but its velocity normal to the wall is reversed), and (ii) the molecules can be reflected diffusely: a molecule leaving the surface "forgets" all information about upon collision and it leaves accommodating the surface properties (i.e., their average bulk velocity is equal to the surface velocity and the temperature is equal to the temperature of the surface). Based on this definition, the thermal accommodation coefficient (α) can be related to the temperature of incident T_i and reflected T_r molecules as

$$\alpha = \frac{T_i - T_r}{T_i - T_w} \tag{1}$$

where T_w is the wall temperature. The value of TAC varies from 0 to 1. In the case of α=0, the reflection is perfectly specular. For α=1, the incident molecule is reflected diffusely after complete accommodation to the wall temperature. A lower value of α will leads to higher temperature jump between the wall and gas molecules interacting with it.

Because of the low-pressure levels during the vacuum drying the gas natural convection in the fuel package is negligible comparing to the conduction and radiative heat transfer process. Due to multiple fuel assemblies within the packages finite element analysis of the package is used with an

appropriate effective thermal conductivities and materials emissivity to determine the temperature and heat flux distribution throughout the package fuel regions [6, 14]. These simulations are utilized because of the complex geometries and heat transfer characteristics of the packages and fuel assemblies. These simulations do not include the temperature jump thermal resistance that is associated with rarefied-gas environment. The effects of the rarified-gas thermal resistance become more important for the increasing cladding temperature with heat generation rate.

Chalasani and Greiner [15] performed experimental and computational fluid dynamics/radiation heat transfer simulations of an 8×8 array of heated rods within an aluminum enclosure in both horizontal and vertical orientations. The results showed that the simulation under estimate the hotter rod temperature but accurately predict the cooler ones.

Current Work The goal of the current research is to develop and experimentally benchmark computational models that predict the temperature difference between the cladding and basket walls during vacuum drying processes. The computational models will include the temperature jump thermal resistance at the gas/surface interfaces. To achieve this goal, the first step is the experimental measurement of the thermal accommodation coefficient between stainless-steel surface and helium gas. The experimental design consists of coaxial cylinders' geometry filled with helium gas. The temperature and heat flux from the inner cylinder (hotter) to the outer cylinder (colder) will be measured and the thermal accommodation coefficient will be obtained from the comparison between the measurement and the analytical model in the slip regime ($10^{-3} \leq Kn \leq 10^{-1}$) and the DSMC calculations in the transitional regime. The objective of the current paper is to validate the design of the experimental apparatus that will be used to measure the value of the thermal accommodation coefficient. Two and three dimensional models are performed using ANSYS/Fluent package that represent the experimental apparatus. Conduction and radiation heat transfer simulations are performed with helium gas filling the gap region between the stainless-steel cylinders. The temperature of the outer cylinder is set to a constant value of 27°C and the pressure is varied from 10^5 to 10 Pa to cover the continuum to transitional regimes.

RAREFIED GAS CONDITIONS AND HEAT TRANSFER

At low pressure conditions the collisions between gas molecules and surfaces dominate the molecules-molecules collisions. The continuity of the macroscopic parameters of temperature and velocity near the wall is not achieved. In these conditions the gas flow may be characterized by the Knudsen number, which is defined as the ratio of the mean distance traveled by molecules between successive collisions (known also as the mean free path λ [16]) to a macroscopic characteristic length L_C. Typically the characteristic length is the smallest dimension of the system which is in this case the gap between the coaxial cylinders. The Knudsen number (Kn) is named after Danish physicist Martin Knudsen (1971 -1949) and is defined as

$$Kn = \frac{\lambda}{L_C} \tag{2}$$

When the Knudsen number increases (due to the increase of λ or the decreases of L_C) the gas flow becomes more rarefied. Using the Knudsen number different regimes of gas flow rarefaction (see Fig. 1) can be identified as [11]

- Continuum flow regime ($Kn \leq 10^{-3}$), where the number of collisions between molecules and molecules-surface are enough big to reach the equilibrium. In this regime the classical Navier-Stokes equation and the Convective Energy equation, with the conditions of non-slip and continuity of temperature on the wall, is enough precise to model the flow.
- Slip flow regime ($10^{-3} \leq Kn \leq 10^{-1}$), where the number of collisions molecules-surface are not enough to reach the equilibrium near the wall, but far from the wall the equilibrium is reached. In this regime the Navier-Stokes equations are still appropriate but they should be subjected to the conditions of velocity-slip and temperature-jump at the wall.
- Transitional flow regime ($10^{-1} \leq Kn \leq 10$), it is the most difficult regime for modeling. In this regime the mean free path is comparable to the characteristic length scale, therefore, the collisions between molecules and surfaces dominate the collisions between molecules. To model the flow in this regime the Boltzmann equation should be solved using the discrete velocity method [17, 18] or Direct Simulation Monte Carlo (DSMC) method [19].
- Free molecular regime ($10 \leq Kn$), where the gas is highly rarefied and the flow is driven by the collisions between molecules and surface. In this regime the flow is modeled using the collisional kinetic Boltzmann equation or the DSMC method.

This classification is not strict. The limits between the regimes have to be taken as an order of magnitude, because the transition between regimes is progressive. It should be noted also that all the regimes defined above can be accurately modeled using the kinetic theory, by solving the Boltzmann equation. However, for the continuum and slip regimes will require significant computational effort to reach this solution.

Definition of the mean free path

As cited above the mean free path λ is defined as the averaged distance traveled by molecules between two successive collisions [16]. Two definitions of the mean free path that are found in the literature [20] will be used in this paper, (a) macroscopic fluid viscosity and (b) the microscopic Lennard-Jones collision diameter.

(a) The first definition is based on the macroscopic fluid viscosity as

$$\lambda_\mu = \frac{\mu}{P}\sqrt{\frac{2k_BT}{m}} \tag{3}$$

where P is the pressure, T is the temperature, k_B is the Boltzmann's constant, m is the mass of the gas molecule, and μ is the dynamic viscosity, whose dependence on temperature is obtained from the Hard Sphere (HS) model as

$$\mu = \mu_0\left(\frac{T}{T_0}\right)^{1/2} \tag{4}$$

where T_0 is the reference temperature equal to 273.15K and μ_0 is the reference viscosity that depends on the gas, equal to $1.865\text{x}10^{-5}$Pa·s for helium.

(b) The second definition is based on the microscopic Lennard-Jones collision diameter as

$$\lambda_d = \frac{k_BT}{\pi\sqrt{2}Pd^2} \tag{5}$$

where d is the diameter of the gas molecule, for helium two values are retained in this paper d=2.33 Å [19] and d = 1.90 Å [21]. These values were found from the VHS (Variable Hard Sphere) method and the square well potential method respectively.

Thermal analysis in slip flow regime

In the slip regime the gas flow is considered to be moderately rarefied [22]. In such case the interaction between molecules is not sufficient to reach the equilibrium near the wall, *i. e.* there is a discontinuity of temperature and velocity near the wall ($T_g \neq T_w$, and $V_g \neq V_w$), called a temperature jump or a velocity slip. As the pressure decreases the effect of the temperature jump and the velocity slip on the flow becomes more important and taking them into account in the boundary conditions of the problem becomes crucial for accurate description of the flow. For such moderate conditions of rarefaction ($Kn \leq 0.1$), the Navier-Stokes and Convective Energy equations can accurately model the flow with the temperature jump and velocity slip boundary condition [13].

Sharipov [22] suggested that in the case of moderate rarefied gas, for small temperature difference $\Delta T << T_0$ between two concentric cylinders, where T_0 is the average temperature, and without considering the radiative heat flux, the radial heat flux across the gas can be expressed as

$$Q_r = 2\pi L\kappa\Delta T\left[\ln\frac{R_B}{R_A} + \zeta_T\lambda\left(\frac{1}{R_A}+\frac{1}{R_B}\right)\right]^{-1} \tag{6}$$

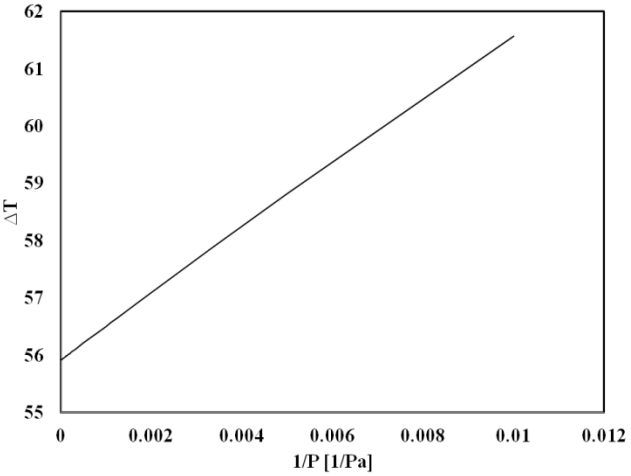

Figure 1 Temperature difference increase with inverse of Pressure

where R_A and R_B are the radii of the inner and outer cylinders respectively. L and κ are the length of the cylinders and thermal conductivity of the gas, which is approximately constant for small temperature difference ΔT, respectively. In equation (6) ζ_T is the temperature jump coefficient. Kennard [21] proposed an expression for this coefficient by assuming that the incident molecules on surface have the same distribution function as the molecules in the midst of the gas. The expression of temperature jump coefficient ζ_T proposed by Kennard is

$$\zeta_T = \frac{\sqrt{\pi}\gamma}{(\gamma+1)\Pr}\frac{2-\alpha}{\alpha} \tag{7}$$

For Helium the ratio of specific heat at constant pressure to that at constant volume is γ=5/3 and Prandtl number is Pr = 2/3. Replacing the expression of the Knudsen number (2) and the mean free path (3) in equation (6), the temperature difference ΔT can be written as function of the inverse of the pressure as

$$\Delta T = \frac{Q_r}{2\pi L\kappa}\mu\zeta_T\left(\frac{1}{R_A}+\frac{1}{R_B}\right)\sqrt{2\frac{k_B}{m}T_A}\frac{1}{P} + \frac{Q_r}{2\pi L\kappa}\ln\frac{R_B}{R_A} \tag{8}$$

It is clear from this last expression that the temperature difference ΔT is linear function of the inverse of the pressure. The expression (8) will be used for comparison with experimental data to extract the value of the thermal accommodation coefficient α. The experimental measurements of the temperature difference ΔT will be carried out for a constant value of the heat flux Q_r and the different values of the pressure P. The measured data of ΔT as function of the inverse of the pressure will be plotted and fitted with first order polynomial form using the least square method as

$$\Delta T = a\frac{1}{P} + b \tag{9}$$

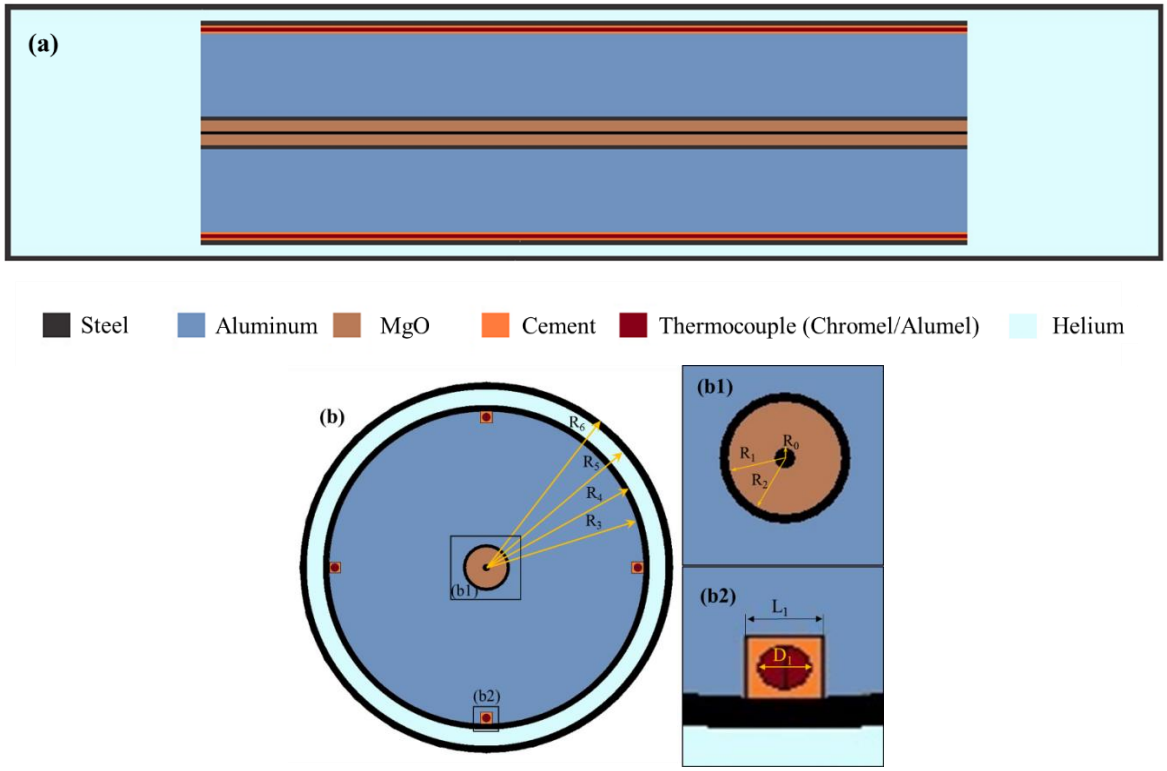

Figure 2 Regional material details of computational domain. (a) Color coded material list for model containing stainless-steel, Aluminum, Magnesium-Dioxide, Cement, Thermocouple and gas backfill. (b) Cross section view with detailed region of (b1) the heat rod and (b2) the thermocouple.

where a is the slop of the function $\Delta T(1/P)$. The comparison between the expression of the measured ΔT (Eq. 9) and the analytical expression of ΔT (Eq. 8) gives

$$a = \frac{Q_r}{2\pi L\kappa}\mu\zeta_T\left(\frac{1}{R_A}+\frac{1}{R_B}\right)\sqrt{2\frac{k_B}{m}T_A} \qquad (10)$$

From this expression (10) the value of the temperature jump coefficient ζ_T can be obtained, and using the expression (7), the value of the thermal accommodation coefficient α can be calculated.

VALIDATION OF THE EXPERIMENTAL DESIGN

As stated earlier, the objective of this paper is to validate the experimental design and procedure that will be used to calculate the value of the thermal accommodation coefficient α. In order to achieve this objective, the experimental model was simulated using ANSYS/Fluent computational fluid dynamics (CFD). Two and three dimension simulations are carried out for the heat transfer across concentric cylinders at different level of rarefaction (from continuum to near transitional regime). The simulations included the radiative heat flux and the temperature jump at the surface.

To calculate the temperature jump at the interface between gas and solid walls ANSYS/Fluent model employs the following expression of the temperature jump coefficient ζ_T

$$\zeta_{T,F} = 2\left(\frac{2-\alpha}{\alpha}\right) \qquad (11)$$

This expression differ from the Kennard expression (7) by the factor $\sqrt{\pi}\gamma/((\gamma+1)\mathrm{Pr})$ which is assumed in equation (11) o be equal to 2. Also Fluent's model uses different expression of the mean free path, based on the Lennard-Jones (LJ) molecular diameter (5). Two different values of the LJ molecular diameter $d = 2.33$ Å [19] and $d = 1.90$ Å [21] and two values of the thermal accommodation coefficients α=1 and 0.4 are considered for the simulations.

Figure 1 shows the linear increase of the temperature difference ΔT with the inverse of the pressure (Eq. 9) obtained from the Fluent simulations for α=1 and $d = 2.33$ Å. This result confirms the ability of Fluent model to model the temperature jump effect on the cylinders wall.

Experimental design

The concentric cylinders design consists of a main inner cylinder and an outer vessel whose temperature is controlled by the use of an external water jacket. The main inner cylinder is composed of an electrical heating rod that is centered inside a thick walled aluminum cylinder that is then surrounded by a stainless-steel sheath. By using aluminum for the thicker walled cylinder a nearly uniform temperature and heat flux profile can

be ensured. It is between this aluminum cylinder and the stainless-steel sheath that thermocouples are strategically placed inside profiled grooves that minimize any possible air gaps and are secured with highly thermal conductive cement. This main inner cylinder is then centered inside the outer vessel so that a roughly 0.47 cm-wide gas filled gap is created to enable a thermal-temperature jump resistance from rarefied conditions to be evaluated.

Table 1 Dimensions for experiment setup and corresponding surfaces

Dimension	Measurement [cm]	Corresponding Surfaces (Inner/Outer)
R_0	0.094	Heating Element/MgO
R_1	0.56	MgO/Stainless Steel
R_2	0.64	Stainless Steel/Aluminum
R_3	4.28	Aluminum/Stainless Steel
R_4	4.45	Stainless Steel/Helium
R_5	4.92	Helium/Stainless Steel
R_6	5.08	Stainless Steel/Ambient
L_1	0.22	Cement/Aluminum
D_1	0.16	Cement/Thermocouple

The two-dimensional computational models only differ in that the second model's inner cylinder is offset from the center of the outer vessel. The three-dimensional model has all of the same dimensions as the two-dimensional model with the addition of being extruded so as to represent the length of the proposed experiment.

Conduction and Radiation heat transfer simulations where performed with helium gas filling the gap region between the stainless-steel sheath and the vessel with a constant ambient vessel exterior temperature of 300K (27^oC) and varying pressure from 10^5 to 10 Pa. By using this range of pressures both continuum model (P=1atm), and rarefied gas model (P<500Pa) are evaluated. By using a constant heat generation rate of Q=500W the temperatures of each wall inside the vessel can be used to determine the thermal-temperature jump resistance in order to calculate the thermal accommodation coefficient. Radial temperature profiles are reported along with the effects of the thermocouple placement on temperature measurements. The dimensions in Figures 2a and 2b are given in Table 1 along with the corresponding temperature measurement naming convention used for the results discussion.

RESULTS AND DISCUSSIONS

Figure 3 shows the two and three dimensional computational domain model of the concentric cylinders used in the current work to validate the experimental model. The mesh consists of 20158 elements in the 2D-model and 558191 elements in the 3D-model. This computational model

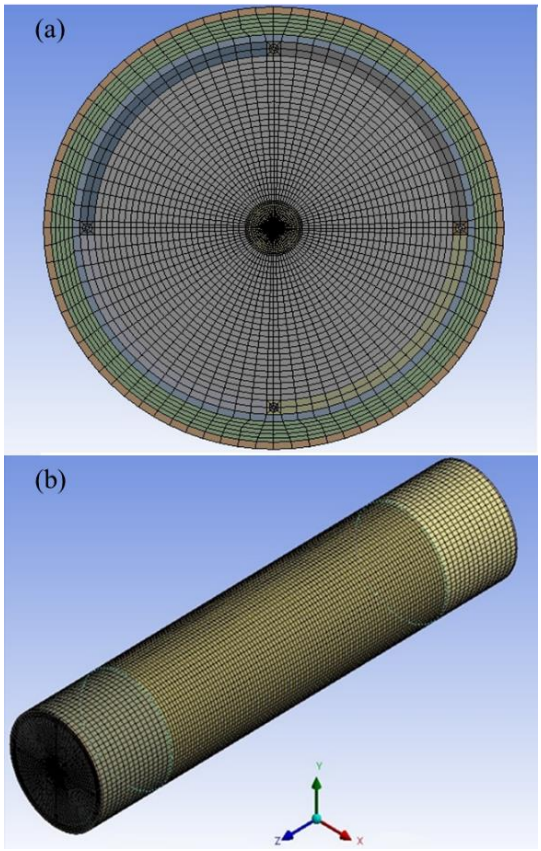

Figure 3 (a) Computational domain for the two-dimensional model with 20158 number of elements (b) Computational domain for the three-dimensional model with 558191 number of elements.

reproduced the dimensions that will be used in the experimental model. In order to determine if the designed model will be suitable for the experimental apparatus the radial (r-axis) and axial (z-axis) temperature and heat flux profiles are drawn for two values of the accommodation coefficient α=1 and 0.4 and two different values of the LJ molecular diameters d=2.33 Å and d=1.90 Å. Figure 4 shows the typical temperature contour obtained for all the simulated cases considered in this paper. Radial axes at θ=0° and θ=45° are also shown. From this figure one can see that the maximum temperature is obtained in the center of the cylinders. The temperature is nearly uniform across aluminum and stainless-steel sheath. A steep decrease of the temperature is observed across the helium gas.

Figure 5 shows the radial temperature profile along the axes at θ=0° (cross the thermocouple) and 45° (see Figure 4) for Q=300W and atmospheric pressure condition P=1atm. It can be seen that the temperature profile along the two axes are very similar and that the only difference is obtained at the thermocouple, where the thermocouple experience slightly smaller temperature by less than 0.3K difference. This difference is maintained when changing the generated heat flux,

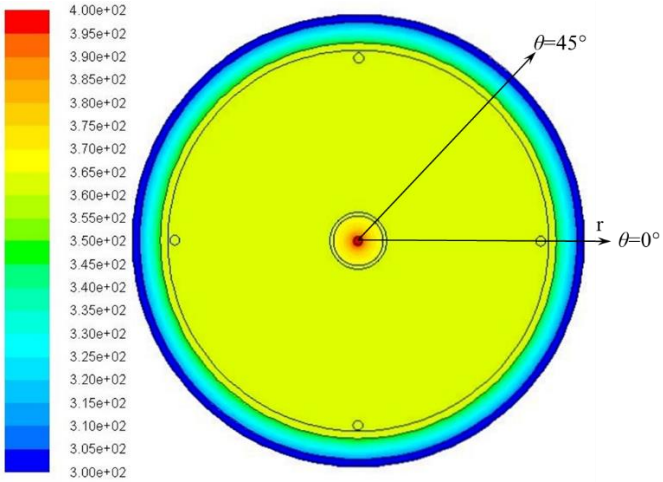

Figure 4 Typical temperature profile for all simulated cases.

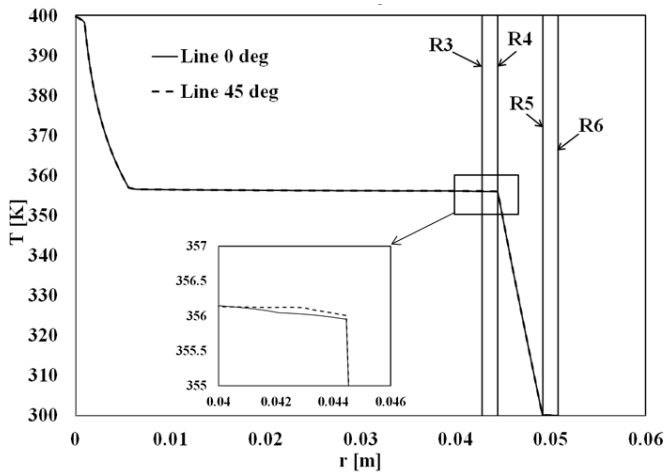

Figure 5 Temperature profile along the r-axis shown in Figure 4 for atmospheric pressure (continuum model).

thermal accommodation coefficient α, LJ molecular diameter d and the pressure.

Figure 6a shows the difference obtained in the temperature profile between the 2D and 3D models for atmospheric pressure and the same heat generation Q=300W. Both models have a similar temperature profiles, however, the temperature is lower in the case of 3D model. This difference of temperature is due to the heat loses from the two ends of the inner cylinder. In order to accurately calculate the thermal accommodation coefficient using Equation (8) the heat loses from the sides should be reduced as much as possible. This can be achieved by insulating the two ends of the inner cylinders. Further investigation on the insulation performance will be performed in future work.

Figure 6b and 6c show the effect of the rarefaction model compared to the continuum model. These results are obtained using the 3D model. The results of the rarefaction model are obtained for P=100Pa, α=1 and 0.4 and d=2.33 Å and d=1.90 Å. From Figure 6b and 6c one can observe that the rarefaction

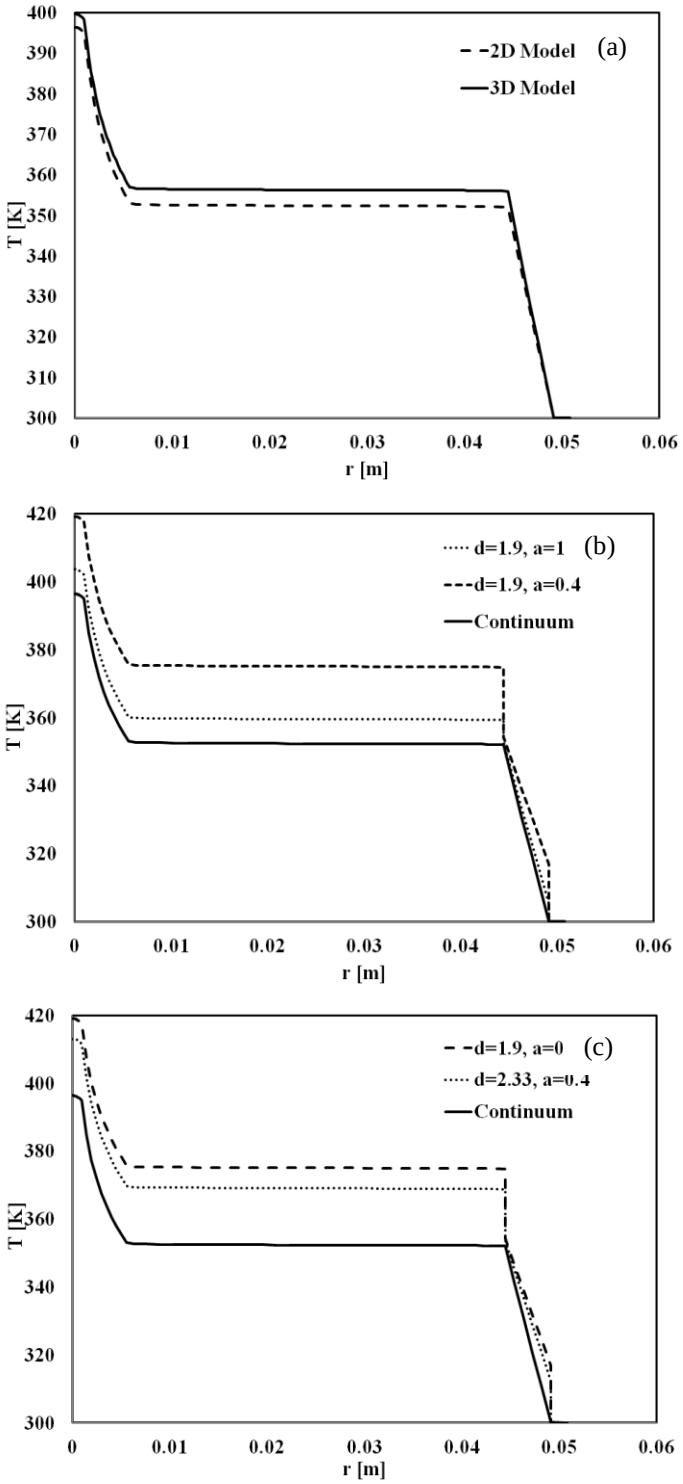

Figure 6 (a) Comparison of temperature profiles along the y-axis between the two-dimensional and three-dimensional model along the θ=0^0 and θ=45^0 lines (b) Comparison between continuum and rarefaction model for different values of TAC (c) Comparison between the continuum model and rarefaction model for different values of d.

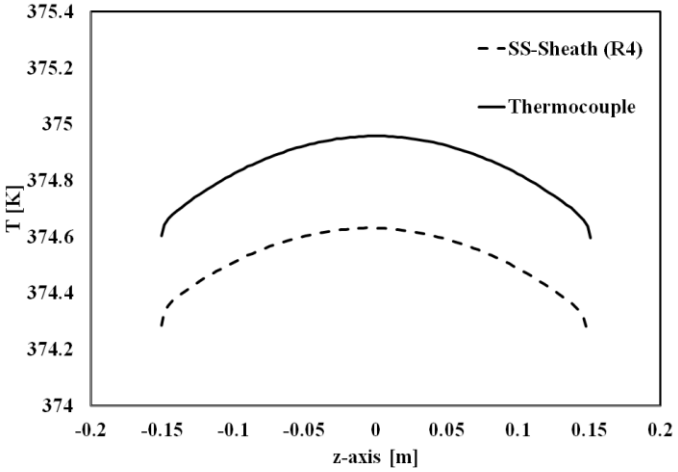

Figure 7 Axial temperature profiles for the inner and outer surfaces of the stainless-steel sheath and the thermocouple region.

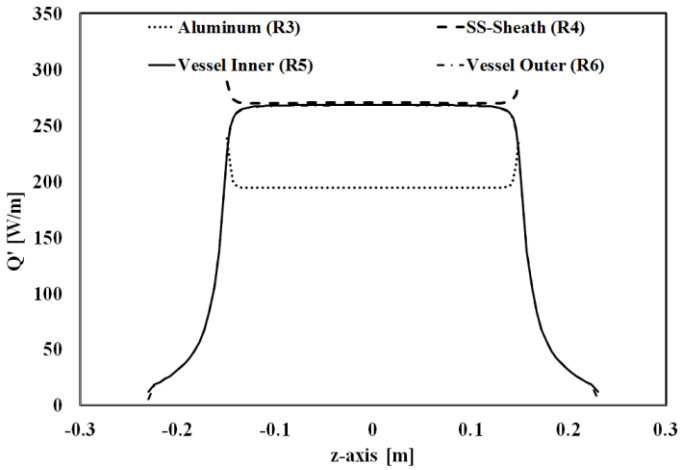

Figure 8 Axial heat flux loss to the side walls

model predicts higher temperature than the continuum model, which is due to the temperature jump resistance induced by the low pressure (rarefaction). This difference varies with the variation of thermal accommodation coefficient α and the LJ molecular diameter d. Figure 6b shows the effect of the thermal accommodation coefficient variation on increasing the temperature, as α decreases the temperature increases. The effect of variation of the LJ molecular diameter is shown in Figure 6c and seems to be less important than the effect of the thermal accommodation coefficient in increasing the temperature.

Temperature profiles along the axial axis (z-axis, see Figure 3) is shown in Figure 7. The temperature is essentially uniform along the z-axis with maximum obtained in the center of the cylinder. The maximum temperature difference between the thermocouple center (solid line) and the stainless-steel sheath surface (dashed line) is less than 0.3K, which justifies the implementation of the thermocouples to measure the stainless-steel sheath surface.

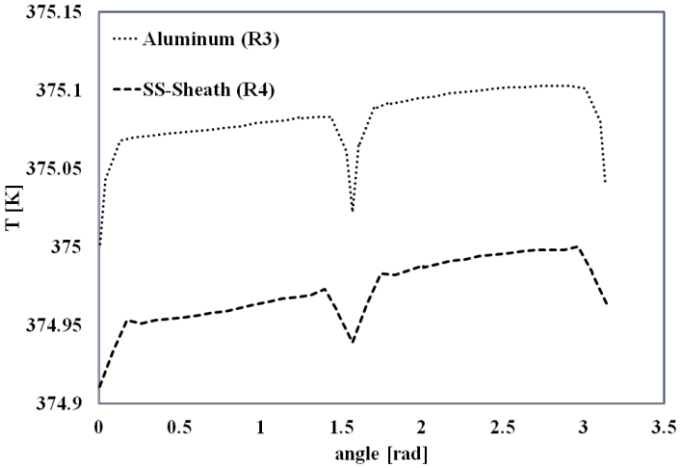

Figure 9 Circumferential temperature profile for the stainless – steel sheath

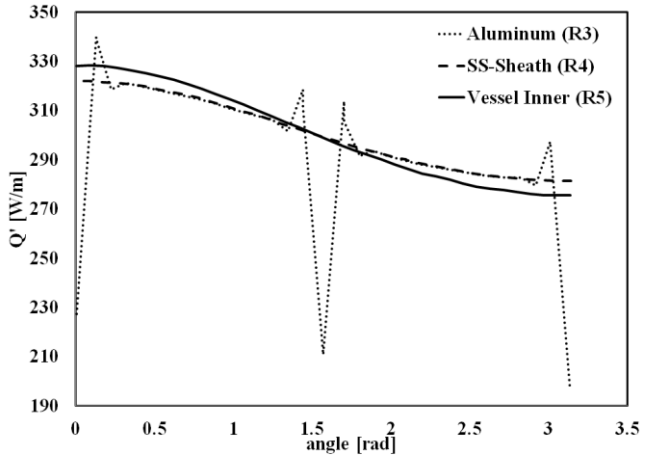

Figure 10 Circumferential radial heat flux Q'[W/m] for P=100 Pa, α=0.4 and d=2.33.

The radial heat flux leaving the side walls of the cylinders is given in Figure 8. It is clear from this figure that the heat flux leaving the outer surface of the stainless-steel sheath and entering the inner surface of the vessel, which are in contact with helium, are almost the same and uniform along the axial axis. The uniformity and equality of the heat flux leaving the surfaces in contact with helium confirms the validity of the actual experimental design to be used for the calculation of the value of the thermal accommodation coefficient from Equation (8). In Figure 8 one can see that the heat flux leaving the Aluminum surface (R3) is much less than the others. This is due to the presence of the thermocouple and the surrounded cement (see Figure 2b), which has lower thermal conductivity than the Aluminum, so most of the heat goes around the thermocouple.

One of the parameters influencing the uniformity of the temperature and heat flux leaving the cylinder sides is the concentricity of the two cylinders. An offset of the cylinders from the center can cause the temperature and heat flux to be

non-uniform. Simulations are carried out for the eccentric cylinders with an offset of 1 mm in the x-direction (see Figure 3b), which represents around 21% of the initial gap between cylinders. Figure 9 shows the circumferential temperature profile for the eccentric cylinders. From this figure it appears that the eccentricity has a weak effect on the temperature variation. The difference with the concentric cylinders is less than 0.05K. The decrease of the temperature shown in Figure 8 is due to the thermocouple, which has lower thermal conductivity than Aluminum.

Contrarily to the temperature results the eccentricity has an important effect on the radial heat flux (see Figure 10) leaving the side walls. The 1mm offset caused a variation of the radial heat flux of about 16% between the smallest and largest gaps, with a higher heat flux leaving from the smallest gap. In order to calculate the thermal accommodation coefficient with a good accuracy the eccentricity of the cylinders should be minimized.

Another parameter that could affect the calculation of the thermal accommodation coefficient is the amount of the heat flux leaving the side walls of the inner cylinder. Equation (8) assumes that all the heat flux is leaving the side walls of the inner cylinder. In Table 2 the percentage of the heat flux leaving the end walls of the inner cylinder to the side wall is given.

Table 2 Percentage of heat flux Loss from both sides of the inner cylinder

			Side-Walls	End-Walls
	α	LJ	Percentage of wall heat Flux [%]	
Continuum			93	7
P=100Pa	1	2.33	92.3	7.7
	1	1.9	92	8
	0.4	2.33	90.8	9.2
	0.4	1.9	90	10

From Table 2 it is clear that the heat losses from the inner cylinder sides are affected by the rarefaction. The heat losses from the ends is more important at low pressure (P=100Pa) and it is even more important when α and d are smaller. The maximum heat losses from the sides are estimated to be 10% of the total heat generated by the heating rod. A good insulation of the inner cylinder sides should decrease this heat loss.

SUMMARY

The rarefied gas condition during vacuum drying can have an important effect on used nuclear fuel cladding temperature. As the pressure decreases, the temperature of the cladding increases. This increase in temperature is due to the temperature jump thermal resistance between the gas and the solid surfaces induced by the gas rarefaction. The thermal resistance is a function of the thermal accommodation coefficient. The main objective of this paper is to validate the design of the experimental apparatus that will be used to measure the thermal accommodation coefficient.

ANSYS/Fluent simulations representing the proposed experimental apparatus design with different Lennard-Jones molecular diameters, d = 2.33 Å [19] and d = 1.90 Å [21], and two values of the thermal accommodation coefficient, α=1 and 0.4 are performed. Three computational models were used for this paper, two two-dimensional and one three-dimensional model. The simulations were carried out for a wide range of pressure (~10^5 Pa to 100 Pa) that covers gas flow regimes from continuum to near transitional regimes. The results for the continuum simulations (no temperature jump) were compared with results from the moderately rarified conditions (temperature jump). When rarified gas theory was applied the temperature was 20K greater than the resulting temperatures from the continuum model. The temperature was higher when the thermal accommodation coefficient was decreased from 1 to 0.4 in the rarified theory model. The results showed also that the Fluent's model was able to reproduce the linear increases of the temperature difference between the cylinders surface with the inverse of the pressure.

The Fluent simulations showed also that the implantation of the thermocouple in the design was justified. The temperature difference between the thermocouple and the stainless-steel sheath surface in contact with helium was less than 0.3K regardless of the pressure, thermal accommodation coefficient, and LJ molecular diameter. The axial and circumferential heat flux profiles of the outer stainless-steel sheath where uniform.

The experimental apparatus described in this paper will be constructed and used to measure the thermal accommodation coefficient for helium on the stainless-steel surface.

REFERENCES

[1] OCRWM, 1993, Multi-Purpose Canister (MPC) Implementation Program Conceptual Design Phase Report, U.S. DoE Office of Civilian Radioactive Waste Management, Final Draft, Sept. 30,

[2] Meyer, R. and Greiner, R., 1994, GA-9 Legal Weight Truck From-Reactor Spent Fuel Shipping Cask. Safety Analysis Report for Packaging (SARP). Prepared by General Atomics for the Office of Civilian Radioactive Waste Management of the U.S. DoE.

[3] NRC, 2005 "Cladding Considerations for the Transportation and Storage of Spent Fuel", Interim Staff Guidance Report for the Spent Fuel Project Office of the U.S. NRC, ISG-11 R3; available at www.nrc.gov.

[4] NRC, 2006, Title 10 Code of Federal Regulations, Part 71 available at www.nrc.gov/reading-rm/doc-collections/cfr/, published by the U. S. Nuclear Regulatory Commission, 10 CFR – 71

[5] Saling, J.H., and Fentiman, A.W., 2002, Radioactive Waste Management, 2nd Edition, Taylor and Francis, New York.

[6] Holtec International, "HI-STORM 100 FSAR," Revision 8, Report HI-2002444, 2010.

[7] Large, W.S. and Sindelar, R.L., 1997, "Review of Drying Methods for Spent Nuclear Fuel" Westinghouse Savannah

River Company, Savannah River Site, Aiken, SC, report number WSRC-TR-0075
[8] Colmont, D. and Roblin, P., 2008, “Improved thermal modeling of SNF shipping cask drying process using analytical and statistical approaches”, Packaging, Transport, Storage & Security of Radioactive Material, Vol. 19, No. 3, pp. 160-164.
[9] Pan, L.S., Ng, T.Y., Xu, D., Liu, G.R., and Lam, K.Y, 2002, “Determination of Temperature Jump Coefficient Using the Direct Simulation Monte Carlo Method”, Journal of Micromechanics and Microengineering, Vol. 12, pp. 41-52
[10] Sharipov, F. and Kalempa, D., 2005, “Velocity Slip and Temperature Jump Coefficients for Gaseous Mixtures. IV. Temperature jump coefficient” International Journal of Heat and Mass Transfer 48, pp. 1076-1083
[11] Schaaf, S.A. and Chambre, P.L, 1961, Flow of Rarefied Gases, Princeton University Press, New Jersey.
[12] Loeb, L.B., 1934, Kinetic Theory of Gases, 2nd Edition, McGraw-Hill Book Company Inc.
[13] Sharipov, F., 2004, “Data on the velocity slip and temperature jump coefficients,” Thermal and Mechanical Simulation and Experiments in Micro-Electronics and Micro-Systems. Proc. 5th Int. Conf. EuroSimE, Belgium, pp. 243-249.
[14] Tseng, Y.S, Wang, J.R., Tsai, F.P., Cheng, Y.H., and Shih, C., 2011, “Thermal design investigation of a new tube-type dry-storage system through CFD simulations,” Annals of Nuclear Energy, 38, 1088-1097.
[15] Chalasani, N.R and Greiner, M., 2010, “Benchmark of Computational Fluid Dynamics Simulations Using Temperatures Measured Within Enclosed Vertical and Horizontal Arrays of Heated Rods,” PVP2010-25803, Proceedings of the ASME 2010 Pressure Vessels and Piping Division/K-PVP Conference, PVP2010, July 18-22, 2010, Bellevue, Washington, USA
[16] Bird, G. A. “Definition of mean free path for real gases”. Phys. Fluids, 26, 11 1983.
[17] Pantazis, S. and Valougeorgis, D. 2010, “Heat transfer through rarefied gases between coaxial cylindrical surfaces with arbitrary temperature difference” European Journal of Mechanics B/Fluids 29 (2010) 494-509.
[18] Sharipov, F. Cumin, L. Kalempa, D. 2006, “Heat flux between parallel plates through a binary gaseous mixture over the whole range of the Knudsen number” Physica A 378 (2007) 183–193.
[19] Bird, G. A. “Molecular Gas Dynamics and the Direct Simulation of Gas Flows”. Oxford Science Publications, 1994.
[20] Sharipov, F. and Seleznev, V. 1998, Data on internal rarefied gas flows. J. Phys. Chem. Ref. Data 27, 657.
[21] Kennard, E. H. “Kinetic Theory of Gases” McGraw-Hill Book Company, Inc., New York, 1938.
[22] Sharipov, F. 2011, Data on the Velocity Slip and Temperature Jump on a Gas-Solid Interface. J. Phys. Chem. Ref. Data, Vol. 40, No. 2.

Proceedings of PVP2014
2014 ASME Pressure Vessels and Piping Conference
July 20-24, 2014, Anaheim, CA, USA

PVP2014-29048

PREDICTION OF CLADDING TEMPERATURES WITHIN A USED NUCLEAR FUEL TRANSFER CASK FILLED WITH RAREFIED HELIUM

Ernesto T. Mano
University of Nevada, Reno
Reno, NV, USA

Rachel Green
University of Nevada, Reno
Reno, NV, USA

Mustafa Hadj Nacer
University of Nevada, Reno
Reno, NV, USA

Miles Greiner, Ph.D.
University of Nevada, Reno
Reno, NV, USA
greiner@unr.edu

Jie Li, Ph.D.
Argonne National Laboratory
Argonne, IL, USA

Yung Y. Liu, Sc.D.
Argonne National Laboratory
Argonne, IL, USA

ABSTRACT

During the used nuclear fuel vacuum drying process, helium is evacuated to pressures as low as 70 Pa, to promote water vaporization and removal. At these low pressures the gas is rarefied to the extent that there is a temperature jump thermal resistance between the surface and gas. This occurs when the mean free path of a molecule becomes a comparable to the characteristic length of a system. In order to correctly apply this jump model to a nuclear transfer cask, a two dimensional model of parallel plates and concentric cylinders were created using ANSYS/Fluent package. Heat generation was plotted against a variety of relevant pressures. The results in these simple geometries are compared to kinetic model calculations, performed by other investigators, to determine the appropriate collision diameters to use in rarefied helium gas simulations within complex geometries. A two dimensional mesh of a transfer cask containing 24 pressurized water reactor used fuel assemblies is then constructed, and the rarefied gas model was implemented in the helium-filled regions between the fuel and basket support structures. Steady state simulations with a fuel heat generation rate of 710 W/m/assemble shows that the cladding is measurably hotter when the helium gas pressure is reduced from atmospheric conditions ~10^5 Pa to 500 Pa. The heat generation rate that brings the peak cladding temperature to a hydride dissolution temperature of 400°C is as much as 10% lower when the gas is at 500 Pa than under atmospheric conditions.

NOMENCLATURE

A	Boundary surface area [m^2]
c_P	Specific Heat [J/kgK]
d	Diameter of the molecules of cover gas [m]
Kn	Knudsen Number [-]
k_B	Boltzmann constant, 1.38×10^{-23} [m^2kg/s^2K]
L_C	Characteristic Length [m]
M	Molecular mass of the gas [kg]
P	Local pressure [Pa]
Pr	Prandtl Number ($C_p\mu/\kappa$)
Q	Total array heat load [W]
R_{TJ}	Temperature jump thermal resistance [K/W]
T_0	Reference temperature [K]
T_{cask}	Temperature of the outer boundary of the transfer cask [°C]
T_g	Temperature of the gas near the wall [°C]
T_i	Temperature of the incident molecules [K]
T_P	Peak or Maximum temperature within domain [°C]
T_r	Temperature of the reflected molecules [K]
T_w	Temperature of the wall [°C]

Greek symbols

α	Thermal accommodation coefficient [-]
ε	Surface emissivity [-]
γ	Specific heat ratio [-]
κ	Thermal conductivity of the gas [W/mK]
λ_d	Mean free path based on the molecular diameter [m]
λ_μ	Mean free path based on the viscosity [m]
μ_0	Reference viscosity [kg/ms]
μ	Stress viscosity of the gas [kg/ms]
ζ_T	Temperature Jump Coefficient (TJC) [-]

Subscripts

K	Kennard model
F	Fluent model

Acronyms

BWR	Boiling Water Reactor

CFD	Computational Fluid Dynamics
DSMC	Direct Simulation Monte Carlo
LJ	Lennard-Jones
PWR	Pressurized Water Reactor
TAC	Thermal Accommodation Coefficient

INTRODUCTION

Used light water reactor fuel rods consist primarily of Zircaloy cladding tubes that contain highly radioactive fuel pellets as well as high-pressure fission-product and fill gases [1]. The fuel rods are held in a square array by headers, footers and periodic spacer plates. Boiling water reactor (BWR) assemblies consist of 7x7 to 9x9 rod arrays surrounded by a Zircaloy channel. Pressurized water reactor assemblies are 14x14 to 18x18 arrays, but do not have channels.

After being discharged from reactors, used assemblies are stored underwater while their radioactivity and heat generation rate decrease [2]. After sufficient time, typically five years or more, a canister with an internal basket is placed in a transfer cask and lowered into the pool. The canister is then loaded with fuel assemblies, covered, and lifted out of the pool. Helium or another non-oxidizing gas is forced into a port near the top of the canister while water flows out through a tube that reaches to the canister bottom [3]. Small amounts of water may remain at the bottom of the canister and in crevices of the canister and cladding surfaces after draining. Essentially all moisture must be removed from the canister before it is sealed to prevent corrosion of the fuel cladding and cask materials, and/or formation of combustible mixtures of hydrogen and oxygen [4]. After drying, the canister is filled with helium to pressures between 3 and 7 atm (306 to 711 kPa) and sealed either by welding or bolted closure. It is then placed in other packaging for onsite dry cask storage or offsite transport.

With the absence of a defined used-fuel disposal and/or reprocessing path, it is crucial to assure the safety of *long-term* dry cask storage systems [5]. Federal regulations (10CFR72) require that these systems insure that external doses are below certain limits, and that the fuel configuration remains subcritical, confined and contained, and retrievable. The cladding is the primary confinement barrier for the used fuel pellets and fission gas. Its integrity must be protected to assure that, after decades in storage, the assemblies can be safely transferred to other packages, and/or transported to other locations.

Federal regulations (10CFR71) also require that the transport package performance be analyzed under normal conditions of transport (which include a 0.3-m drop) and hypothetical accident conditions (which include a 9-m drop). If the cladding integrity is compromised there is a risk that the fuel will not be in its "as analyzed" configuration after these drop events. Adequate ductility of the cladding must therefore be maintained. Radial hydride formation within the cladding has the potential to radically reduce cladding ductility and its suitability for long term storage or transport [5].

During all post-reactor drying, transfer, storage and transport operations the fuel cladding must be kept below certain temperature limits to avoid (a) dissolution of circumferential hydrides that exist in the cladding and (b) high gas pressures within the tubes, which leads to high cladding hoop stress [6]. If these hydrides dissolve and the hoop stresses become large, then as the heat generation of the used fuel decreases during long-term storage *radial* hydrides may form and cause the cladding to become brittle [7-10]. Drying operations [11] may be the most likely events to cause the fuel temperature to exceed temperature limits. This is because drying is the first operation when the fuel is removed from water and placed in a gas-filled environment, and the fuel heat generation is still relatively high.

Nuclear Regulatory Commission Interim Staff Guidance-11, Revision 3 (ISG-11) [6] specifies conditions that are intended to prevent radial hydride formation. For example, the maximum calculated fuel cladding temperature must remain below 400°C for normal conditions of storage and short term loading conditions (e.g., drying, backfilling with inert gas, and transfer of the cask to the storage pad). For low burnup fuel, a higher short-term temperature limit may be used, provided that the best estimate cladding hoop stress is less than 90 MPa for the temperature limit proposed. During loading operations, repeated temperature cycling is allowed, but is limited to less than 10 cycles with cladding temperature variations of more than 65°C. For off-normal and accident conditions, the maximum cladding temperature should not exceed 570°C, a limit based on creep (stress) rupture consideration. Until further guidance is developed, *high* burnup fuel will be handled on a case-by-case basis [6]. In other countries like Germany the maximum cladding temperature is 370°C [12] for both storage and drying operations.

Two methods are currently used by industry for moisture removal from canisters, vacuum drying or forced helium dehydration [3, 6]. In vacuum drying, the canister is evacuated to pressures as low as 67 Pa to promote evaporation and water removal [4]. Several cycles of evacuation and refill may be necessary before operators can demonstrate that the canister is able to meet the drying technical specification of maintaining a low pressure of 400 Pa (3 Torr) for 30 minutes [3, 11].

At the low pressures and gas densities associated with vacuum drying, buoyancy-induced gas motion and natural convection heat transfer from the fuel to the canister surfaces are essentially eliminated. While the gas thermal conductivity is nearly the same at these pressures as it is at atmospheric conditions, the gas is rarefied to the extent that there is a temperature difference (or temperature-jump) between the heated cladding and the gas in contact with it [4, 13-16]. This surface-to-gas temperature-jump is essentially zero at high pressures but acts as a thermal resistance between the surfaces and gas at low pressures. These resistances increase the cladding temperature compared to atmospheric pressure conditions. This thermal resistance and the lack of natural convection caused by low pressure may lead to higher cladding

temperatures during vacuum drying than during storage conditions for the same fuel heat generation rate.

Forced helium dehydration is used for drying canisters containing high-burnup and other high heat generating fuel [3]. In that process, helium is forced into the canister through a port near its top and withdrawn though a tube that reaches to the canister bottom. Moisture is removed from the helium by condensing, demoisturizing, and preheating the gas outside the canister. In some cases cooling water is also circulated in the gap between the canister and transfer cask. The gas pressure during helium dehydration is maintained at roughly the same level as that used during storage. As a result the same natural convection and minimal temperature-jump thermal resistance are expected as in storage. However, gas demoisturizing and cooling equipment are required for forced helium dehydration, which are not needed for vacuum drying.

Currently, package vendors predict cladding temperatures and the resulting hoop stresses during drying using experimentally-benchmark whole-package computational fluid mechanics (CFD) simulations [3, 17]. In these models, the fuel and basket are replaced by a region with an effective thermal conductivity and porosity. Other models used the accurate geometry model where the fuel rods and the baskets are modeled [18, 19]. This allows prediction of the maximum fuel heat generation rate that can be transferred without exceeding the temperature and hoop stress limits. It also helps determine which fuel may be vacuum-dried, and for which fuel the more complex forced helium dehydration process must be used.

The whole-package computational methods have been validated [20] against measurements performed in an actual evacuated storage package [21]. Currently, these effective properties are calculated without regard to the rarefied-gas temperature-jump thermal resistance. However, the fuel heat generation in the tests used to validate the current methods was moderately low. The effect of the rarified-gas thermal resistance on peak cladding temperatures increases with generation rate.

Current Work The long term objective of the current research program is to develop and experimentally-benchmark CFD models of the vacuum drying process that includes the effect of the rarefied-gas thermal resistance. The current work employs ANSYS/Fluent computational fluid dynamics (CFD) simulations that include a model for the temperature-jump and thermal-resistance at the interfaces between rarefied gases and solid surfaces. Conduction heat transfer simulations through helium gas in a flat region between parallel plates, and an annular region between concentric cylinders, are performed for a solid surface temperature difference of 30°C and gas pressures from 10^5 to 10 Pa. These results are compared gas kinetic model simulations in the same configuration in order to benchmark the ANSYS/Fluent simulation technique. The benchmarked ANSYS/Fluent simulations are then used to predict the cladding temperature within a loaded transfer cask for a range of fuel heat generation rates. Simulations are performed using a continuum model for a helium pressure of 1 atm (10^5 Pa), and a rarefied gas model for the helium at 500 Pa. The fuel heat generation rates that bring the cladding temperature to ISG-11 limit temperature of 400°C, and a reduced limit of 370°C used in Germany [12], are reported.

RARIFIED GAS HEAT TRANSFER

Under normal atmospheric conditions, gas molecules confined within a moderate-sized volume experience many collisions with each other and with the walls [4, 13-16]. In this case the flow can be defined as a continuum and the Navier-Stokes and convective heat transfer equations are sufficiently precise to describe the flow. When the pressure decreases or the container's scale decreases, some phenomena related to the rarefaction of gas can be observed and they possess some special characteristics. In such situations the gas flow can be characterized by the Knudsen number which is defined as the ratio of the mean distance traveled by molecules between two successive collisions (known as mean free path λ [22]) to a representative physical length scale L_c. This length scale is generally the smallest dimension of an enclosure. The Knudsen number (Kn) is defined as:

$$Kn = \frac{\lambda}{L_C} \tag{1}$$

The Knudsen number is the parameter used to describe the degree of gas rarefaction. When the Knudsen number increases the gas becomes more rarefied. That happens when the mean free path λ increases (i.e. in case of pressure decreasing) or when the characteristic length L_c decreases (for example, in micro or nano-channels).

Schaaf and Chambre [15] suggested to use the Knudsen number as guidelines for identifying different rarefied gas regimes. Usually, the following classification is used:

- The continuum flow regime ($Kn \leq 10^{-3}$), where the flow and heat transfer can be accurately modelled by the Navier-Stokes and Convective Energy equations with classical no-slip boundary conditions (fluid and gas temperature and velocity at the wall are the same as those of the wall).
- The slip regime ($10^{-3} \leq Kn \leq 10^{-1}$), where the continuum model (Navier-Stokes equations) is still appropriate away from the wall, but it is subjected to the conditions of velocity slip and temperature jump on the wall.
- The transitional regime ($10^{-1} \leq Kn \leq 10$), where the continuum models (Navier-Stokes and Convective Energy equations) are not valid. For simulations in this regime, the Boltzmann equation should be resolved using the discrete velocity method [23, 24] or the Direct Simulation Monte Carlo (DSMC) technique [25].
- The free molecular regime ($Kn \leq 10$), where the gas flow is highly rarefied. In this regime the number of molecule-molecule collisions are smaller than the numbers of molecule-surface collisions. Therefore, the flow is driven by the interaction between gas and wall. The flow in this case is modeled using numerical solution of collisionless kinetic Boltzmann equation or DSMC method.

It should be pointed out that all the regimes cited above can be accurately modelled using the kinetic theory, by solving the Boltzmann equation. Nevertheless, it is inefficient to implement this equation or other kinetic equations for gas flow simulation in the hydrodynamic and slip regimes because of the large computational efforts needed for their solution.

Definition of the mean free path

The mean free path λ is defined as the average distance traveled by molecules between successive collisions. Several definition for the mean free path can be found in the literature [26]. In this paper we will retain only two definition that are used below. The first is based on macroscopic fluid viscosity:

$$\lambda_\mu = \frac{\mu}{P}\sqrt{\frac{2k_BT}{m}} \tag{2}$$

where P is the pressure, T is the temperature, k_B is Boltzmann's constant, m is the mass of the gas molecule, and μ is the dynamic viscosity, whose temperature dependence is determined using the Hard Sphere (HS) model as

$$\mu = \mu_0\left(\frac{T}{T_0}\right)^{1/2} \tag{3}$$

The reference temperature T_0 is equal to 273.15K, while the reference values of the viscosity μ_0 depends on the gas and it is equal to 1.865×10^{-5} Pa·s for helium.

The second definition is based on the microscopic Lennard-Jones collision diameter of the gas molecule d, as

$$\lambda_d = \frac{k_BT}{\pi\sqrt{2}Pd^2} \tag{4}$$

for helium there are two values of the Lennard-Jones diameter in the literature d=2.33 Å [25] and d=1.9 Å [27]. The first value was obtained from the VHS (Variable Hard Sphere) method and the second value is obtained from the square well potential method.

Accommodation coefficient

At low-pressure conditions the collisions that occur between gas molecules and surface dominate the molecules-molecules collisions. Under these conditions the local thermodynamic equilibrium and the continuity of the macroscopic parameters (tangential velocity and temperature) at the wall is not achieved, which is known as the velocity slip and temperature jump conditions.

In the middle of nineteenth century Maxwell introduced the concept of the accommodation coefficient [26]. He postulated that when molecules collide with a surface, a range of possible interaction can take place. Moreover, there are two extremes of this range: (i) the molecules can be reflected specularly, without transferring any of their momentum or energy to the surface (the molecule's temperature and velocity component parallel to the wall remain unchanged, but its velocity normal to the wall is reversed), and (ii) the molecules can be reflected diffusely: a molecule leaving the surface "forgets" all information about upon collision and it leaves accommodating the surface properties (i.e., their average bulk velocity is equal to the surface velocity and the temperature is equal to the temperature of the surface). So the concept of reflection can be related to the temperature incident molecules T_i and the reflected molecules T_r as [28]

$$\alpha = \frac{T_i - T_r}{T_i - T_w} \tag{5}$$

where T_w is the wall temperature. This ratio is known as the Thermal Accommodation Coefficient (TAC). The value of TAC varies in the range from 0 to 1. In the case of α=0, the reflection is perfectly specular. For α=1, the incident molecule is reflected diffusely after complete accommodation to the wall temperature.

The value of TAC was determined experimentally for a wide range of surface and gas molecules. Authors [29, 30] reported that the value of α =1 can be used for most of the engineering surfaces. Other reported the value of α=0.4 for the pair helium-stainless steel [23]. These two values will be used in the current work for all the calculations.

Thermal model for slip regime

As discussed above, in the slip regime the gas is considered to be at a level of moderate rarefaction [15]. In such cases the gas tends to behave as a continuum in regions away from the walls. However, a molecule that comes into contact with a wall does not meet other molecules enough times to reach equilibrium with them in the vicinity of the wall [16]. Therefore there can be an abrupt change of temperature and speed from the surface to the gas, that is $T_g \neq T_w$, and $V_g \neq V_w$. This is known as temperature-jump or slip-flow. As a result, for regime ($0.001 \leq Kn \leq 0.1$), the Navier-Stokes and Convective Energy equations accurately model momentum and energy transport away from the walls, but gas rarefaction must be taken into account at the walls using "temperature-jump" and "velocity-slip" boundary condition [14, 15].

Simple analytical model

Under moderately rarefied conditions, Sharipov [26] indicates that the local temperature-difference or temperature-jump between the gas and wall is determined using a resistance model,

$$T_g - T_w = R_{TJ}Q \tag{6}$$

In this model, Q is the portion of the heat transfer rate directed to the solid surface transported by conduction within the surrounding gas and does not include the component transported by radiation to other surfaces. The temperature-jump thermal-resistance is

$$R_{TJ} = \frac{\lambda_\mu\zeta_T}{A\kappa} \tag{7}$$

In this expression A is the boundary surface area, and κ is the gas thermal conductivity that is related to the viscosity μ (Eq.

3), the gas specific heat at constant pressure c_P and Prandtl number Pr as

$$\kappa = \frac{c_P}{\Pr}\mu \tag{8}$$

For helium, the specific heat at constant pressure is c_p = 5193 J/Kg.K, and its Prandtl number is Pr = 2/3, both values are independent of temperature. In equation (7) ζ_T is the Temperature Jump Coefficient. Kennard [27] proposed an expression for this coefficient by assuming that the incident molecules on surface have the same distribution function as the molecules in the midst of the gas. The expression of temperature jump coefficient ζ_T proposed by Kennard is

$$\zeta_{T,K} = \frac{\sqrt{\pi}\gamma}{(\gamma+1)\Pr}\frac{2-\alpha}{\alpha} \tag{9}$$

where the ratio of specific heat at constant pressure to that at constant volume is γ=5/3 for helium. In this expression the subscript "*K*" refer to Kennard model [27].

Using a circuit analogy the conduction heat transfer Q across the gas can be calculated as

$$Q = \frac{T_A - T_B}{R_{TJ_A} + R_C + R_{TJ_B}} \tag{10}$$

where R_C is the thermal resistances associated with conduction within the helium R_{TJ_A} and R_{TJ_B} (see Eq. 7) are the temperature-jump thermal resistances for the hot and cold surface, respectively.

Numerical Fluent model

The ANSYS/Fluent computational fluid dynamics (CFD) package employs a simplified model to predict temperature-jump thermal-resistance at the interfaces between rarefied gases and solid surfaces. This model is similar to the one given by equations (6) and (7). However, it employs the collision-diameter-based definition of the mean free path λ_d (Eq. 4, instead of the viscosity based on in eq. 2) and different expression of the temperature jump coefficient ζ_T given by

$$\zeta_{T,F} = 2\left(\frac{2-\alpha}{\alpha}\right) \tag{11}$$

This model essentially assumes that the term $\sqrt{\pi}\gamma/\left((\gamma+1)\Pr\right)$ in the Kennard expression (Eq. 9) is in the Fluent model the thermal resistance is affected by the Lennard-Jones diameter of the gas molecules. For simulations with helium gas, two values of this diameter are used, d=2.33 Å [25] and d=1.9 Å [27].

BENCHMARK SIMULATIONS

Figure 1 shows the two-dimensional planar and annual regions used in the current work to benchmark ANSYS/Fluent simulations of conduction through rarefied gases. For the planar region (Fig. 1a) the gap H between the parallel plates is equal to 1 cm and the length L was set to 100 times the hight H in order

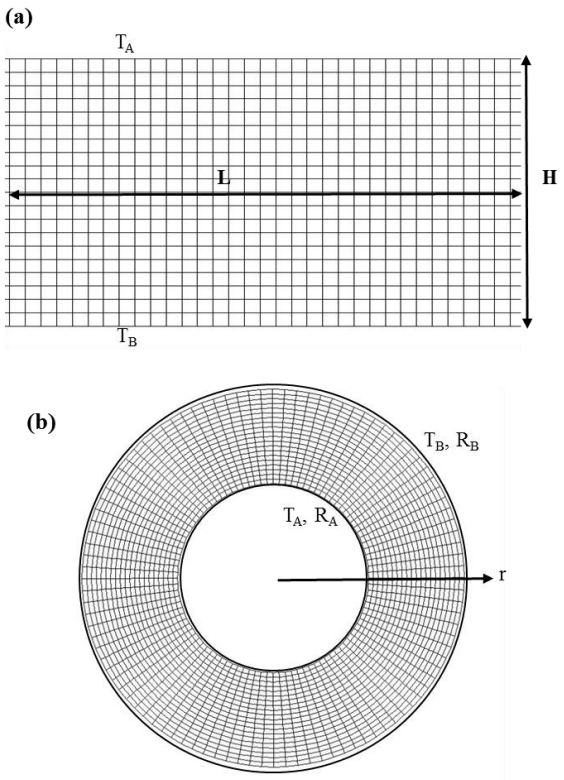

Figure 1 Benchmark Computational Domains (a) Planar Region between Parallel Plates, domain composed of 42,000 nodes and 40000 element (b) Annular Region between Concentric Cylinders, domain composed of 2100 nodes and 2000 elements.

to neglect the lateral walls effect. For the annular region (Fig. 1b) the radii of the inner and outer cylinders are R_A=0.5 cm and R_B=1 cm. The hot and cold temperature of the surfaces for both geometries are respectively, T_A=330 ºC and T_B=300 ºC (see Fig. 1). These spacing and temperature differences were chosen because they are similar to those between rods within used fuel assemblies.

In order to benchmark the ANSYS/Fluent simulations comparisons with (a) the accurate kinetic models based on the Boltzmann equation and (b) the simple analytical model (Eq. 10) based on the Kennard temperature jump model and are performed.

Sharipov et *al* [23] used the McCormack kinetic model equation to solve the Boltzmann equation between parallel plates (Fig. 1a) using the discrete velocity method subjected to the diffuse Maxwell boundary condition α=1 (5). They used the hard sphere (HS) intermolecular interaction model for the viscosity calculation (3) and they assumed a constant thermal conductivity of gas. The heat flux was calculated for several gas types and temperature difference. For the concentric cylinders (Fig. 1b) Pantazis and Valougeorgis [24] used the nonlinear Shakhov kinetic model (also known as the S-model) subjected to the Cercignani-Lampis boundary condition with diffuse

reflection (α=1) in order to solve the Boltzmann equation and to obtain the radial heat flux.

Figure 2 shows the conduction heat transfer reduction ratio $(Q_{cont}-Q)/Q_{cont}$ versus pressure, where Q is the heat flux obtained as function of the pressure using different models and Q_{cont} is the heat flux limit in the continuum regime. From Figures 2 one can observe that the conduction heat transfer reduction ratio obtained by the kinetic models of Sharipov and Pantazis for α=1 (thicker solid line) in both geometries increases with the decrease of the pressure. The results obtained by the analytical Kennard model (thinner solid line) show the same behavior. However, the values obtained are lower than the kinetic models in both geometries. Figures 2 shows also that when the thermal accommodation coefficient α changes from 1 to 0.4, the Kennard model predicts that the conduction heat transfer reduction ratio increases.

The comparison of the ANSYS/Fluent simulations with the kinetic and the analytical models for both geometries are also shown in Figures 2. Two values of the thermal accommodation coefficients α=1 and 0.4 and different values of the LJ molecular diameter d are considered. The Fluent results are marked with dashed lines.

From Figures 2, for α=1 one can see that results obtained from the kinetic models, in both geometries, are between the two results obtained from the Fluent model for values of LJ molecular diameters d=1.9 Å and 2.33 Å. The results for the LJ diameter d=1.9 Å are closer. However, the results obtained with LJ diameter d=2.33 Å are very close to the analytical Kennard models in both geometry.

The LJ molecular diameters that make the Fluent model match the kinetic models are estimated for both geometries and found to be 2.07 Å for parallel plates and 2.09 Å for concentric cylinders. Those values are drawn in Figure 2 with dash dotted lines, it appears from this results that a value of LJ diameter of 2.08 Å may be a good estimation for more complex geometries.

From Figures 2 it is clear that the Fluent model was able to predict with a good accuracy the conduction heat transfer at moderate low pressure. In the next section, the Fluent model will be implemented to calculate the peak cladding temperature in a whole package model.

TRANSFER CASK MODEL

This section describes the computational model used to predict the peak cladding temperatures in the presence of helium with and without a rarefied model. Figure 3 shows the computational domain of the canister modeled in ANSYS/Fluent along with a detailed view of the mesh. The domain pictured contains a total of 131,202 elements and uses symmetry to simplify the complete package into a one-eighth model. It includes a square array of 15x15 fuel rods with an UO_2 core surrounded by a Zircaloy sheath. Instrumentation rods are included in the model and are assumed similar size to the fuel rods. The outer diameter of each rod measures 10.92 mm with a 0.67 mm Zircaloy sheath.

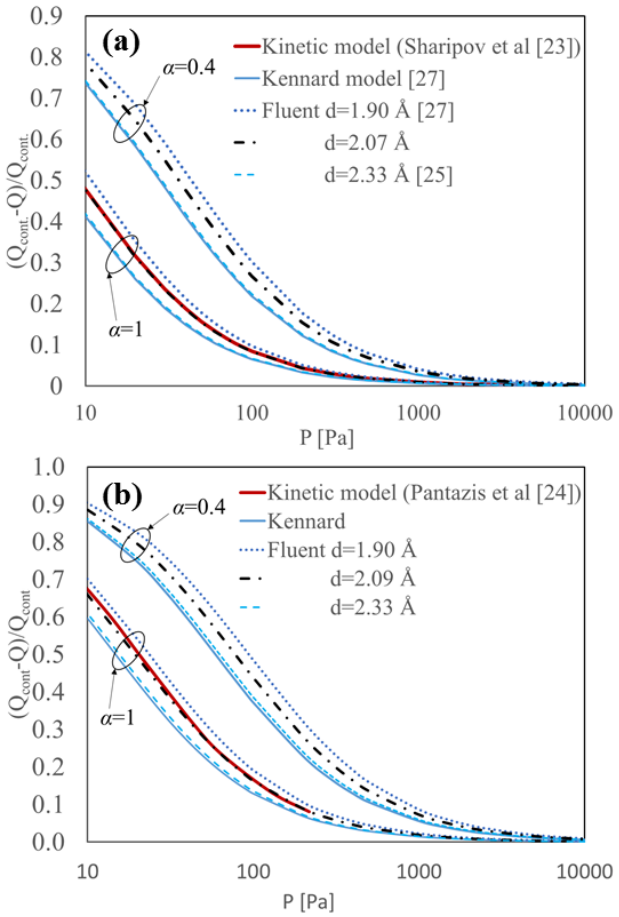

Figure 2 Reduced heat transfer ratio gas pressure (a) Planar Region between Parallel Plates (b) Annular Region between Concentric Cylinders.

The rod center-to-center pitch is 14.43 mm and the shortest distance from the fuel rod cladding to the stainless steel basket is centered at 6.58 mm. The 2D reference depth used in the model is 3.66 m.

Figure 4 shows the material regionals of the computational domain. The square fuel rod assembly is centered inside a stainless steel basket. The stainless steel basket rests inside the aluminum supports along with the neutron poison; thermal properties for BORAL® were used for the neutron poison. The neutron poison is placed in selected spots inside the aluminum support geometry. In Figure 4b, a detailed view of the fuel rod array showing the gas filled regions of the instrumentation rods between the Aluminum support and the Stainless Steel which is in a symmetrical pattern. Figure 4c shows the gap enclosure which is gas filled and represents the smallest dimension in the canister with size of 2.286 mm.

Steady-state thermal simulations were performed using ANSYS/Fluent 14.5. These simulations assume uniform heat generation in all the UO_2 regions, and they included conduction within the solids and helium, and surface-to-surface radiation

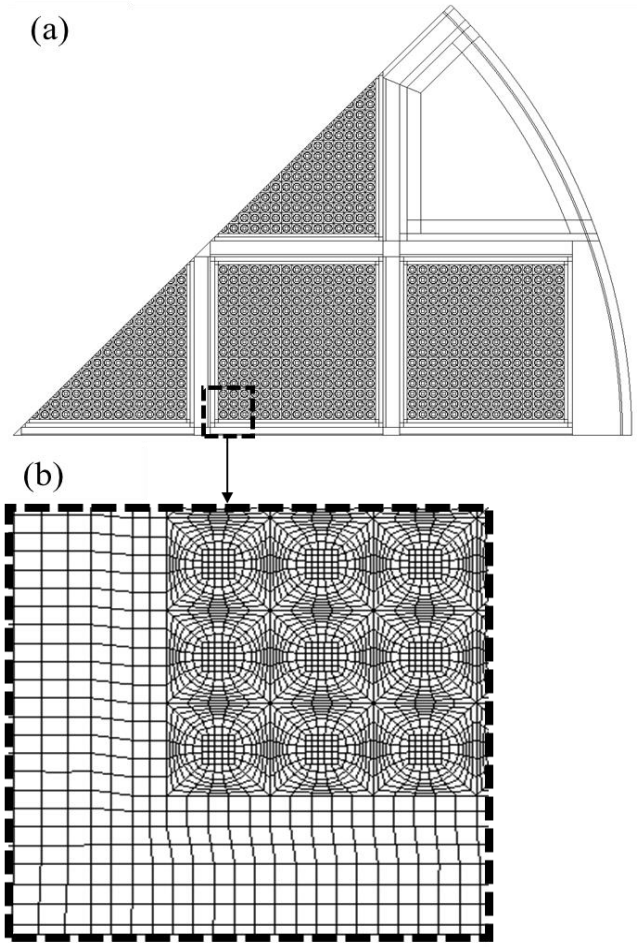

Figure 3 Two-dimensional computational domain of the packaged model. (a) Two dimensional quarter model of the model used containing a total of 131,202 elements. (b) Detailed section of heated fuel rod region shown.

across the helium filled region with surface emissivity of 0.46 for the stainless steel and 0.8 for the Aluminum and Zircaloy [30]. These simulations do not include buoyancy-induced gas motion or natural convection in the helium because they are negligible at the low pressures considered in this work. The outer boundary condition of the transfer cask is assumed to be underwater at a constant temperature of 101.7 °C. The heat input for each fuel rod region is 270 – 800 W/m/assembly, calculated as

$$Q_A^{'} = P_f \frac{Q}{L} \tag{12}$$

where P_f and L are the peaking factor and the length of the fuel rods. Q is the total heat generated per fuel assemblies.

Two different heat transfer models are used in this work. The first is the Continuum Model, which does not include temperature jumps between the solid surfaces and the helium.

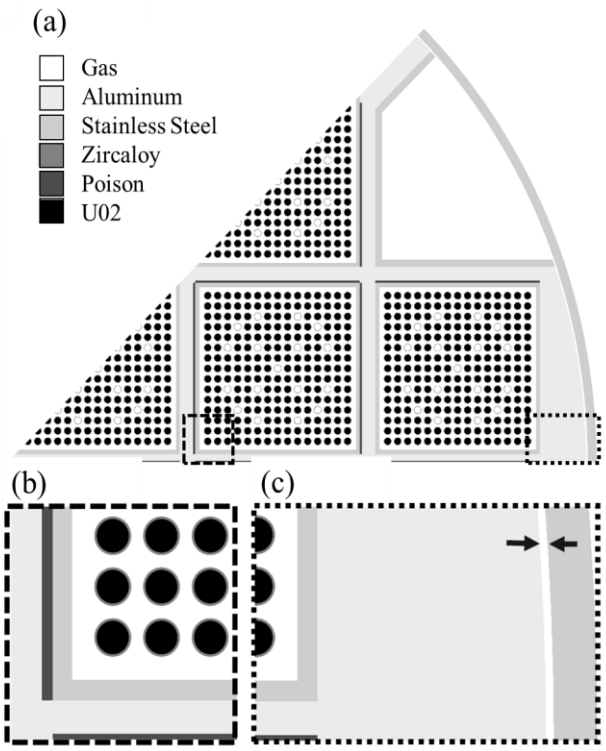

Figure 4 Regional material details of computational domain. (a) Color coded material list for model containing UO2, Stainless Steel, Zircaloy, Aluminum, Neutron poison, and gas backfill. (b) Detailed region of the fuel rod array in the stainless steel basket. (c) Detailed view of the 2.286 mm annular gap that wraps around the entire canister

The second is the Moderately-Rarefied Model, which includes the temperature jump thermal resistance described in equations (7) and (11). Simulations for this model are performed for pressure of P=500 Pa, and thermal accommodation coefficients of α=0.4 and 1 with LJ molecular diameters d=1.9 Å and 2.33 Å.

The ANSYS/Fluent package employs a second-order upwind scheme to solve the energy equations. Radiative heat transfer was solved for gray diffuse surfaces using the discrete ordinates method with a second-order upwind scheme. The governing equations were solved using double precision. For the rarefied gas condition Fluent's low-pressure boundary slip is used.

RESULTS AND DISSCUSSION

Figure 5 shows temperature contours from a Continuum Model simulation with outer boundary temperature T_{cask} =101.7°C (374.7 K) and heat generation of 710 W/m/assembly.

The maximum or peak temperature in the domain is T_P = 353.4 °C (626.5 K). This peak temperature is located near the

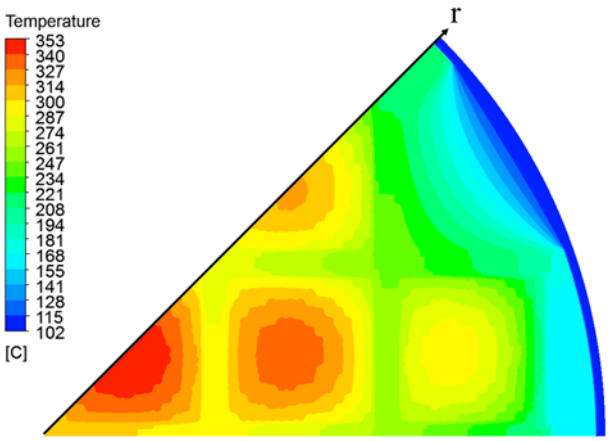

Figure 5 Temperature Contour Plots (helium at atmospheric pressure with Q = 710 W/m/assembly)

center of the innermost fuel assembly. This temperature is less than the allowable maximum cladding temperature T_{RH}=400°C. The maximum difference within the domain is T_p-T_{cask}=251.7°C. In Figure 5 also the radial r-axis across the transfer cask model is drawn.

Figure 6 shows the rod and gas temperature along the radial r-axis for heat generation of 710 W/m/assembly and helium-filled pressure of 500 Pa. The thick solid line marked Continuum shows the temperature profile from the contour of Figure 5 without temperature jump. The dotted line marked Continuum (no gap) shows the temperature profile along the r-axis where the gap in Figure 4c is then filled with Stainless-Steel instead of helium. Since the conductivity of Stainless-Steel is much higher than helium, the resulting maximum temperature for the same heat generation rate is 90°C higher when the gap is filled with helium. Since the temperature in the gap is relatively small the effect of radiation heat transfer is weak. The no-gap model was simulated to show the importance of the gap to the peak clad temperature.

The maximum temperature is recorded within the rods of the internal assembly region, and the outer assembly regions experience lower temperatures. The temperature within the rods are relatively uniform comparing to the gradient in the gas. Since the continuum model do not include the temperature jump, the temperature of the gas at the rods surface is the same as the temperature of the rods surface.

Figure 6 also includes the results for the moderate low pressure model for pressure of P=500 Pa marked with thin solid and dashed lines for d=1.9 Å and 2.33 Å, respectively with α=1 and α=0.4. Considering the temperature jump resistance between the gas and solid surfaces in this model the temperatures of gas and rods are hotter those predicted by the continuum model. As the pressure of the gas decreases the mean free path λ increases (see Eq. 4) which results in the increase of the resistance between gas and solid (see Eq. 7). The same behavior of the thermal resistance increasing happen when the

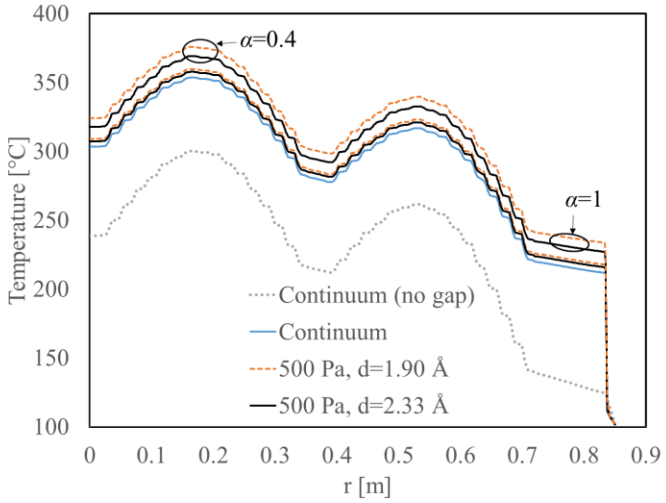

Figure 6 Radial temperature profile along the radial axis shown in Figure 5, calculated for Q'=710 W/m/assembly and for atmospheric pressure (continuum model) with gas filled gap (thick solid line) and Stainless-Steel filled gap (dotted line), moderately-rarified

thermal accommodation coefficient decreases (see Eq. 7 and 11).

Figure 7 shows the peak cladding temperature versus the assembly heat generation rate per meter. Results are shown for the Continuum model (atmospheric pressure) and moderately-rarefied model with pressure P=500 Pa and two thermal accommodation coefficient values α=1 and 0.4, and two values of the LJ molecular diameter d=1.9 Å and 2.33 Å. In the figure also two maximum allowable cladding temperatures that cause the radial hydride formation are drawn by horizontal lines at T=370°C [12] and 400°C [6].

The peak temperature increases with the increase of the assembly heat generation rate. The moderately-rarified results are consistently hotter than the continuum temperatures, and the temperatures for the smaller values of the accommodation coefficient (α=0.4) and the LJ molecular diameter (d=1.9 Å) are hotter still. For a given value of heat generation the maximum temperature predicted by the moderately-rarefied model can be more than 20°C higher.

Table 1 gives the maximum assembly heat generation rate for which the peak rod temperatures are equal to the maximum allowed temperature that causes the radial hydride (RH) formation $T_{RH,R}$=370°C and T_{RH}=400°C. Table 1 shows that the heat generation rate predicted by the continuum model is higher than that predicted by the moderately rarefied model. The moderately-rarefied model with thermal accommodation coefficient α=0.4 and LJ diameter d=1.9 Å gives the lowest heat generation rate. The heat generation rate that brings the peak cladding temperature to a radial hydride formation temperature of 400°C is 10% lower when the moderately rarefied model is used than continuum model.

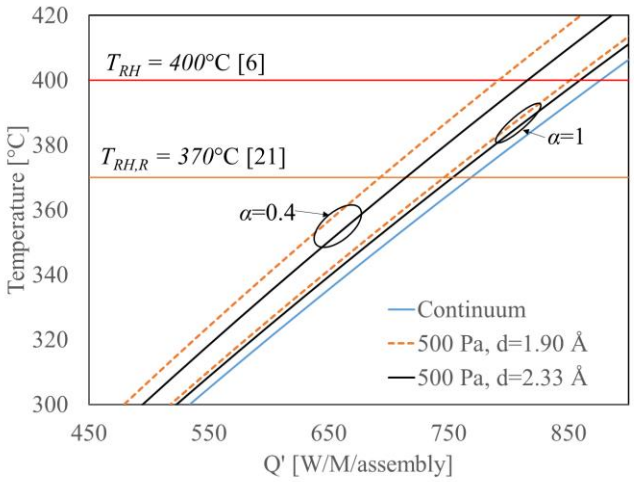

Figure 7 Peak cladding temperature versus fuel heat Generation rate for atmospheric pressure (Continuum model) and *P*=500 Pa (moderate low pressure model) with two values of the thermal accommodation coefficient α=1 and 0.4, and two values of the LJ molecular diameter *d*=1.9 Å and 2.33 Å.

SUMMARY

Evacuating helium gas from used nuclear fuel canisters during vacuum drying, to pressures as low as 500 Pa, has the potential to increase cladding temperatures compared to atmospheric pressure conditions. This is because, at these low pressures, natural convection becomes ineffective at enhancing heat transfer beyond the levels from pure conduction, and the gas become moderately rarified, which effectively increases the thermal resistance between the remaining gas and the solid surface. The overall objective of this research program is to develop and experimentally-benchmark computational models that can be used to predict cladding temperatures during vacuum drying.

In this paper, the kinetic model [23, 24] based on the Boltzmann equation was used to predict the heat transfer across simple helium-fill planar and annular regions as a function of pressure. ANSYS/Fluent simulations of the same configuration were performed with three different Lennard-Jones molecular diameters, *d* = 1.9 Å and 2.33 Å. The simulation exhibited good agreement with the kinetic models for LJ molecular diameter around 2.08 Å in both configurations (circular and annular).

Two-dimensional ANSYS/Fluent simulations of the 24 basket transfer cask were performed for a range of array heat generation rates, accommodation coefficient, and LJ molecular diameters with a constant outer wall temperature. Results from Continuum simulations (which did not include the temperature jump effect) were compared to Moderately-Rarified simulations at 500 Pa. When the rarefied gas theory was applied the temperature was 20°C greater when compared to the continuum model. When the thermal accommodation coefficient was changed from 1 to 0.4 in the moderately-rarefied gas model the temperature was higher for the lower value of the thermal accommodation coefficient. This slight temperature change indicates the accommodation coefficient has a damped effect when applied to the whole packaged model due to other modes of heat transfer. The heat generation rate that causes the circumferential hydride dissolution predicted by the moderately-rarefied model was 11% less than that predicted by the continuum model. Future work includes performing steady-state calculations for the current package model with water instead of helium as the backfill fluid. This steady state condition will be used as a starting point for transient calculations with helium as the backfill gas. The time to reach maximum temperature will be recorded for relevant heat loads and temperature slip conditions. These transient simulations will better represent vacuum drying conditions. Future work also includes building an experimental apparatus of concentric cylinders and an 8x8 heater rod arrays that will be benchmarked against Fluent's temperature slip solver.

Table 1 Maximum allowable heat generation per assembly *Q'* for the continuum and moderately rarefied models at the radial hydride formation temperature T_{RH}=400°C and the reduced temperature $T_{RH,R}$=370°C.

	Continuum model (Q'[W/m/assembly])	Rarefied model (Q'_c [W/m/assembly])			
		α=1		α=0.4	
		1.9 Å	2.33 Å	1.9 Å	2.33 Å
T_{RH} = 400°C	877	851	860	791	816
$T_{RH,R}$ = 370°C	769	719	753	692	714

ACKNOWLEDGMENTS

This work was supported by the US Department of Energy Office of Nuclear Energy's Nuclear Energy University Program.

REFERENCES

[1] U.S. Dept. of Energy, Office of Civilian Radioactive Waste Management (OCRWM), 1987, "Characteristics of Spent Nuclear Fuel, High-Level Waste, and Other Radioactive Wastes Which May Require Long-Term Isolation", DOE/RW-0184, December.

[2] Saling, J.H., and Fentiman, A.W., 2002, *Radioactive Waste Management*, 2nd Edition, Taylor and Francis, New York.

[3] Holtec International, "HI-STORM 100 FSAR," Revision 8, Report HI-2002444, 2010.

[4] Colmont, D. and Roblin, P., 2008, "Improved thermal modeling of SNF shipping cask drying process using analytical and statistical approaches", Packaging, Transport, Storage & Security of Radioactive Material, Vol. 19, No. 3, pp. 160-164.

[5] Hanson, B., Alsaed, H., Stockman, C., Enos, D., Meyer, R., and Sorenson, K., 2012, "Gap Analysis to Support Extended Storage of Used Nuclear Fuel," FCRD-USED-2011-000136 Rev. 0, U.S. Department of Energy Used Fuel Disposition Campaign.

[6] "Cladding Considerations for the Transportation and Storage of Spent Fuel," ISG-11 R3, Interim Staff Guidance Report for the Spent Fuel Project Office of the U.S. NRC, 2003.
[7] Daum, R.S., Majumdar, S., Liu, Y.Y., and Billone M.C., 2006. "Radial-hydride Embrittlement of High-burnup Zircaloy-4 Fuel Cladding." J. Nucl. Sci. Tech., Vol. 43, No. 9, Paper 43090, pp. 1-14.
[8] Daum, R.S. Majumdar, S., and Billone, M.C. 2008, "Experimental and Analytical Investigation of the Mechanical Behavior of High-Burnup Zircaloy-4 Fuel Cladding." J. ASTM Intern., Vol. 5, No. 5, Paper ID JAI101209, available online at www.astm.org.
[9] Billone, M.C., Burtseva, T.A., and Einziger, R.E., "Ductile-to-brittle transition temperature for high-burnup cladding alloys exposed to simulated drying-storage conditions," J. Nucl. Mater. 433, 431-448 (2013).
[10] Billone, M.C., Burtseva, T.A., and Liu, Y.Y., "Baseline Properties and DBTT of High-Burnup PWR Cladding Alloys," Proc. PATRAM 2013, San Francisco, CA, August 18-23, 2013.
[11] Large, W.S. and Sindelar, R.L., 1997, "Review of Drying Methods for Spent Nuclear Fuel" Westinghouse Savannah River Company, Savannah River Site, Aiken, SC, report number WSRC-TR-0075
[12] Kim, H. G. Jeong, Y. H. and Kim, K. T. 2010, "The effects of creep and hydride on spent fuel integrity during interim dry storage" Nuclear Engineering and Technology, vol.42 no.3.
[13] Pan, L.S., Ng, T.Y., Xu, D., Liu, G.R., and Lam, K.Y, 2002, "Determination of Temperature Jump Coefficient Using the Direct Simulation Monte Carlo Method", *Journal of Micromechanics and Microengineering*, Vol. 12, pp. 41-52
[14] Sharipov, F. and Kalempa, D., 2005, "Velocity Slip and Temperature Jump Coefficients for Gaseous Mixtures. IV. Temperature jump coefficient" *International Journal of Heat and Mass Transfer* 48, pp. 1076-1083
[15] Schaaf, S.A. and Chambre, P.L, 1961, *Flow of Rarefied Gases*, Princeton University Press, New Jersey.
[16] Loeb, L.B., 1934, *Kinetic Theory of Gases*, 2nd Edition, McGraw-Hill Book Company Inc.
[17] Tseng, Y.S, Wang, J.R., Tsai, F.P., Cheng, Y.H., and Shih, C., 2011, "Thermal design investigation of a new tube-type dry-storage system through CFD simulations," *Annals of Nuclear Energy*, 38, 1088-1097.
[18] Chalasani, N.R., Araya, P., and Greiner, M., 2009, "Benchmark of Computational Fluid Dynamics Simulations using Temperatures Measured within Enclosed Vertical and Horizontal Arrays of Heated Rods," Nuclear Technology., Vol. 167, No. 3, pp. 371-383.
[19] Chalasani, N.R and Greiner, M., 2010, "Benchmark of Computational Fluid Dynamics Simulations Using Temperatures Measured Within Enclosed Vertical and Horizontal Arrays of Heated Rods," PVP2010-25803, Proceedings of the ASME 2010 Pressure Vessels and Piping Division/K-PVP Conference, PVP2010, July 18-22, 2010, Bellevue, Washington, USA
[20] Holtec International, 2000, "Topical Report on the HI-STAR/HI-STORM Thermal Model and its Benchmarking with Full-Scale Cask Test Data," Holtec Report No. HI-992252.
[21] Pacific Northwest Laboratory, et al., 1987, "The TN-24P PWR Spent Fuel Storage Cask: Testing and Analyses", EPRI NP-5128.
[22] Bird, G. A. "Definition of mean free path for real gases". Phys. Fluids, 26, 11 1983.
[23] Pantazis, S. and Valougeorgis, D. 2010, "Heat transfer through rarefied gases between coaxial cylindrical surfaces with arbitrary temperature difference" European Journal of Mechanics B/Fluids 29 (2010) 494-509.
[24] Sharipov, F. Cumin, L. Kalempa, D. 2006, "Heat flux between parallel plates through a binary gaseous mixture over the whole range of the Knudsen number" Physica A 378 (2007) 183–193
[25] Bird, G. A. "Molecular Gas Dynamics and the Direct Simulation of Gas Flows". Oxford Science Publications, 1994.
[26] Sharipov, F., 2004, "Data on the velocity slip and temperature jump coefficients," *Thermal and Mechanical Simulation and Experiments in Micro-Electronics and Micro-Systems*. Proc. 5th Int. Conf. EuroSimE, Belgium, pp. 243-249.
[27] Kennard, E. H. "Kinetic Theory of Gases" McGraw-Hill Book Company, Inc., New York, 1938.
[28] Goodman, F. O. 1980. "Thermal accommodation coefficients",J. Phys. Chem. 84, 1431-144.
[29] Song, S., and Yovanovich, M. M., "Correlation of thermal accommodation coefficient for 'engineering' surfaces," *Fundamentals of conduction and recent developments in contact resistance*, Proceedings of the Twenty-fourth ASME National Heat Transfer Conference and Exhibition, Pittsburgh, PA, Aug. 9-12, pp. 107-116.
[30] Trott, W. M. Castañeda, J. N. Torczynski, J. R. Gallis, M. A. and Rader, D. J. 2011, "An experimental assembly for precise measurement of thermal accommodation", Review of scientific instruments 82, 035120.
[31] Modest, M.F., 2003, *Radiative Heat Transfer*, 2nd Edition, Academic Press, New York

PHENOMENA AFFECTING USED NUCLEAR FUEL CLADDING TEMPERATURES DURING VACUUM DRYING OPERATIONS

Hadj-Nacer M. [*1], Manzo T.[1], Ho M. [2], Graur I. [2] and Greiner M. [1]
[1] *University of Nevada Reno, 1664 N. Virginia St. Reno, 89557 Nevada, USA.*
[2] *Aix-Marseille Université, Polytech Marseille, UMR CNRS 7343, 5 rue Enrico Fermi, 13453 Marseille Cedex 13, France*
[*] *mhadjnacer@unr.edu*

A two-dimensional computational model of a loaded used nuclear fuel canister filled with helium gas was constructed to predict the cladding temperature during vacuum drying conditions. It includes distinct regions for the fuel pellets, cladding and helium within each basket opening. Symmetry boundary conditions are employed so that only one-eighth of the package cross-section is included, and temperature boundary conditions on the canister exterior surface in contact with water is used. Thermal modeling includes heat generation within the fuel pellets, conduction heat transfer within all solid components, and conduction and surface-to-surface radiation across the gas filled regions. The peak clad temperature is determined as a function of fuel heat generation rate, assuming atmospheric pressure helium. The allowable fuel heat generation rate, which brings the peak clad temperature to its limit is determined. The Willis solid/gas interfaces thermal-resistance model is verified against discrete-velocity-method slip-region rarefied-gas heat transfer calculated across planar and cylindrical helium filled-gaps for a range of thermal accommodation coefficients, α. The Willis model is then implemented at the solid/gas interfaces within the canister model. Simulations with a helium pressure of 100 Pa and α = 1, 0.4 and 0.2 are preformed to determine how much hotter the fuel cladding is under vacuum drying conditions compared to atmospheric pressure. The results showed that the allowed fuel heat generation rate is reduced by up to 34% for α = 0.2. Transient simulations are performed, and show that the fuel cladding temperature rises for roughly 50 hours after the loaded canister is removed from the water pool.

I. INTRODUCTION

Following discharge from the reactor, used nuclear fuel is stored in a water-filled pool for many years, where decay heat is transported by the water [1]. After appropriate time, typically five years or more, the used fuel is loaded from the storage pool into a canister that was earlier placed in a transfer cask and both lowered into the pool. The lid is then installed and the transfer cask is lifted out of the pool and drained [2]. Small amounts of water may remain at the bottom and in the crevices of the canister or adsorbed to the cladding surfaces [3]. The presence of residual water within a sealed dry-storage cask may result in container pressurization, fuel retrievability issues, container and fuel cladding corrosion and/or formation of combustible mixtures of hydrogen and oxygen during transport and long-term storage [4]. After drying, the canister is backfilled with helium nitrogen to a pressure between 3 and 7 atm, then is sealed and the final cover lid is bolted or welded in place.

With the absence of a defined used-fuel disposal and/or reprocessing path, it is crucial to assure the safety of long-term dry cask storage systems [5]. Federal regulations (10CFR72) requires that "spent fuel cladding must be protected during storage against degradation that leads to gross ruptures or the fuel must be otherwise confined such that degradation of the fuel during storage will not pose operational safety problems with respect to its removal from storage." The cladding is the primary confinement barrier for the used fuel pellets and fission gas. Its integrity must be protected to assure that, after decades in storage, the assemblies can be safely transferred to other packages, and/or transported to other locations. Radial hydride formation within the cladding has the potential to radically reduce cladding ductility and its suitability for transport or long term storage [5].

During all post-reactor drying, transfer, storage and transport operations the fuel cladding must be kept below the temperature limit of 400°C (673K), specified by the Nuclear Regulatory Commission Interim Staff Guidance-11, Revision 3 (ISG-11) [6], to avoid (a) dissolution of circumferential hydrides that exist in the cladding and (b) high gas pressures within the tubes, which leads to high cladding hoop stress [6]. If these hydrides dissolve and the hoop stresses become large, then as the heat generation of the used fuel decreases during long-term storage radial hydrides may form and cause the cladding to become brittle [7-10]. Drying operations [11] may be the most likely event to cause the fuel temperature to exceed the temperature limit. This is because drying is the first operation when the fuel is removed from water and placed in a gas-filled environment, while the fuel heat generation is still relatively high.

Currently, two methods are used by industry to remove moisture and residual water from the canister, forced helium dehydration and vacuum drying.

Forced helium dehydration is used for high burnup or other high heat generation fuels. Dry helium is forced through a port near the top of the canister and withdrawn through a tube that reaches its bottom. Moisture is removed from the helium by condensing, demoisturizing, and preheating the gas outside the canister. The process continues until the technical specification, for the temperature of helium exiting the system demoisturizer is

maintained below 21°F (-6°C) for a minimum 30 minutes, [1, 11] is reached to consider that the canister is dry. This method requires several pieces of equipment (gas demoisturizing and cooling system) to accomplish the process.

Vacuum drying method requires less equipment compared to the forced helium dehydration. During this method a vacuum drying system is connected to the canister and the pressure in the canister is decreased as low as 70 Pa to promote evaporation and removal of water. Several cycles of evacuation and refill are accomplished until the technical specifications of maintaining a low pressure of 400 Pa (3 Torr) for 30 minutes are fulfilled [2, 11]. Because of the low pressures and densities associated with vacuum drying, buoyancy-induced gas motion and natural convection heat transfer from the fuel to the solid surfaces of the canister is small and can be neglected. The gas thermal conductivity is almost same as it is at atmospheric pressure conditions. Moreover, the rarefaction condition (low pressure) induces a notable temperature difference (temperature jump) between the fuel cladding wall and the gas that is interacting with it [12-14]. As the pressure increases this temperature jump becomes negligible, but the more rarefied the gas is the more important this temperature jump is and may contribute to higher cladding temperatures during the vacuum drying process compared to atmospheric pressure conditions.

Currently, package vendors predict cladding temperatures and the resulting hoop stresses during drying operation using experimentally-benchmarked whole-package CFD simulations [1, 15-17]. In these models, the fuel and basket are replaced by a region with an effective thermal conductivity and porosity, which are calculated without regard to the rarefied-gas temperature-jump thermal resistance. However, the fuel heat generation in the tests used to validate the current methods was moderately low. The effect of the rarified-gas thermal resistance on peak cladding temperatures increases with heat generation rate.

Current Work: The objective of this work is to develop CFD simulations that accurately predict used nuclear fuel peak cladding temperatures during the vacuum drying operations. The ANSYS/Fluent CFD package is used to model heat transfer across the fuel package. The simulations are performed using the temperature jump condition at the interfaces between rarefied gases and solid surfaces. In order to benchmark the ANSYS/Fluent simulation technique, conduction heat transfer simulations through rarefied helium gas in a gap between parallel plates and concentric cylinders are performed for a solid surface temperature difference of 30°C and gas pressures from 10^5 to 10 Pa. These results are compared to the gas kinetic model calculations. The benchmarked ANSYS/Fluent simulations are then used to predict the cladding temperature within a loaded transfer cask for a range of fuel heat generation rates. Simulations are performed using a continuum model for helium at pressure of 1 atm (~10^5 Pa), and temperature jump model for helium at 100 Pa. The fuel heat generation rates that bring the cladding temperature to ISG-11 limit temperature of 400°C [6], and a reduced limit of 370°C [18] used in Germany, are reported. The transient response of the fuel package subjected to vacuum drying operation is also examined. The time required to reach the ISG limit is reported.

II. RARIFIED GAS HEAT TRANSFER

At low pressure conditions the number of collisions between gas molecules and solid surfaces is low comparing to the normal atmospheric conditions. The continuity of the macroscopic parameters of temperature and velocity near the wall is not achieved. At these pressures some special characteristics related to the gas rarefaction can be observed. The principal parameter characterizing rarefied gas is the Knudsen number (Kn), which is defined as

$$Kn = \frac{\lambda}{Lc} \tag{1}$$

where, λ is the mean free path defined as the distance travelled by molecules between two successive collisions [19] and Lc is a representative physical length scale. Typically the characteristic length Lc is the smallest dimension of the system. The mean free path λ is defined as

$$\lambda = \frac{\mu}{P}\sqrt{\frac{2k_B T}{m}} \tag{2}$$

where, P and T are the pressure and the temperature, respectively. k_B is the Boltzmann's constant, m is the mass of the gas molecule, and μ is the dynamic viscosity, whose temperature dependence is determined using the Hard Sphere (HS) model as

$$\mu = \mu_0\left(\frac{T}{T_0}\right)^{1/2} \tag{3}$$

where, T_0 is the reference temperature equal to 273.15 K and μ_0 is the reference viscosity that depends on the gas, equal to 1.865×10^{-5} Pa·s for helium.

The Knudsen number is used as a parameter to describe the gas rarefaction level. Using this parameter we can distinguish four regimes of rarefaction; (i) The continuum regime ($Kn\leq10^{-3}$), where the flow and heat transfer can be accurately modeled using the classical Navier-Stokes and Convective Energy equations. The number of collisions is big enough to reach the continuity of parameters at the wall. (ii) The slip regime ($10^{-3}\leq Kn\leq10^{-1}$), where the number of collisions molecules-surface are not enough to reach equilibrium near the wall, but far from the wall equilibrium is reached. In this regime the Navier-Stokes and Convective Energy equations are still appropriate but they should be subjected to the conditions of velocity-slip and temperature-jump at the wall. (iii) Transitional regime ($10^{-1}<Kn<10$), it is the most

difficult regime for modeling. In this regime the mean free path is comparable to the characteristic length scale, therefore, the collisions between molecules and surfaces dominate the collisions between molecules. To model the flow in this regime the Boltzmann equation should be solved using the Discrete Velocity Method (DVM) [20] or Direct Simulation Monte Carlo (DSMC) method [21]. (iv) The free molecular regime ($10 \leq Kn$), where the gas is highly rarefied and the flow is driven by the collisions between molecules and surface. In this regime the flow is modeled using the collisional kinetic Boltzmann equation.

It should be pointed out that all the regimes cited above can be accurately modelled using the kinetic theory, by solving the Boltzmann equation. Nevertheless, it is inefficient to implement this equation or other kinetic equations for gas flow simulation in the hydrodynamic and slip regimes because of the large computational efforts needed for their solution.

II.A. Thermal accommodation coefficient

Under rarefied conditions, the collisions between gas molecules and surfaces dominate the molecules-molecules collisions. Maxwell [22] postulated that when molecules enter in collision with the wall there are two possibilities: (i) the molecules can be reflected specularly, without transferring any of their momentum or energy to the surface (the molecule's temperature and tangential velocity remain unchanged, but its velocity normal to the wall is reversed), and (ii) the molecules can be reflected diffusely: a molecule leaving the surface "forgets" all information about upon collision and it leaves accommodating the surface properties (i.e., their average bulk velocity is equal to the surface velocity and the temperature is equal to the temperature of the surface). Based on this definition, the Thermal Accommodation Coefficient (TAC), denoted here by α, can be related to the temperature of incident T_i and reflected T_r molecules as [23]

$$\alpha = \frac{T_i - T_r}{T_i - T_w} \tag{4}$$

where T_w is the wall temperature. The value of TAC is in the range from 0 to 1. In the case of α=0, the reflection is perfectly specular. For α=1, the incident molecule is reflected diffusely after complete accommodation to the wall temperature. When α is between 0 and 1, the fraction of molecules equal to (1-α) is reflected specularly and the fraction of molecules equal to α is reflected diffusely.

The values of TAC were determined experimentally for a wide range of surfaces and gas molecules, using different methods [23-24]. Its value depends on a number of parameters, such as the type of gas, surface material, its cleanliness and its roughness. Song and Yovanovich [24] reported values of α close to 1 for heaviest molecules and values close to 0 for lighter molecules. The value of TAC reported for the pair helium-stainless steel [24] is in the range [0.2, 0.4] depending on temperature. The values α=1, 0.4 and 0.2 will be used in the current work for all the calculations.

II.B. Temperature jump model

In slip regime ($10^{-3} \leq Kn \leq 10^{-1}$), the interaction between molecules and wall is not sufficient to reach the equilibrium of temperature near the wall, *i.e.* $T_g \neq T_w$. The local temperature-difference or temperature-jump between the gas and wall can be determined using a resistance model [25],

$$T_g - T_w = \zeta_T \lambda \frac{\partial T_g}{\partial r} = R_{TJ} Q \tag{5}$$

In this model, Q is the portion of the heat transfer rate transported by conduction within the surrounding gas and does not include the component transported by radiation to other surfaces. The temperature-jump thermal-resistance is

$$R_{TJ} = \frac{\lambda \zeta_T}{A\kappa} \tag{6}$$

In this expression A is the boundary surface area, and κ is the gas thermal conductivity that is related to the viscosity μ (Eq. 3), the gas specific heat at constant pressure c_P and Prandtl number Pr as

$$\kappa = \frac{c_P}{\Pr} \mu \tag{7}$$

In equation (6) ζ_T is the temperature jump coefficient. Lin and Willis, 1972 [26] proposed an expression for this coefficient using the Bhatnagar-Gross-Krook (BGK) kinetic model. This expression reads

$$\zeta_T = \frac{\sqrt{\pi}\gamma}{(\gamma+1)\Pr}\left(\frac{2-\alpha}{\alpha} + 0.17\right) \tag{8}$$

where γ is the ratio of specific heat at constant pressure to that at constant volume. The temperature jump coefficient in Equation (8) is a function of TAC (α). A lower value of α will lead to a higher temperature jump between the wall and gas molecules interacting with it.

III. BENCHAMRK SIMULATIONS

Figure 1 shows the two-dimensional computational domain of the planar and annual regions used in the current work to benchmark ANSYS/Fluent simulations of conduction through rarefied gases. The planar region (Fig. 1a) consists of two parallel plates spaced by gap H=10 mm. The length L of the plates was set to 100 times the gap H to neglect the lateral walls effect. For the annular region (Fig. 1b) the inner and outer cylinders radii are R_A=5 mm and R_B=10 mm, respectively. The hot and cold temperature of the surfaces for both geometries are respectively, T_A=330K and T_B=300K. These spacings and temperature differences were chosen because they are similar to those between the fuel rods within used fuel assemblies.

Graur et al [20] used the kinetic Shakhov model (S-model) equations to solve the Boltzmann equation in

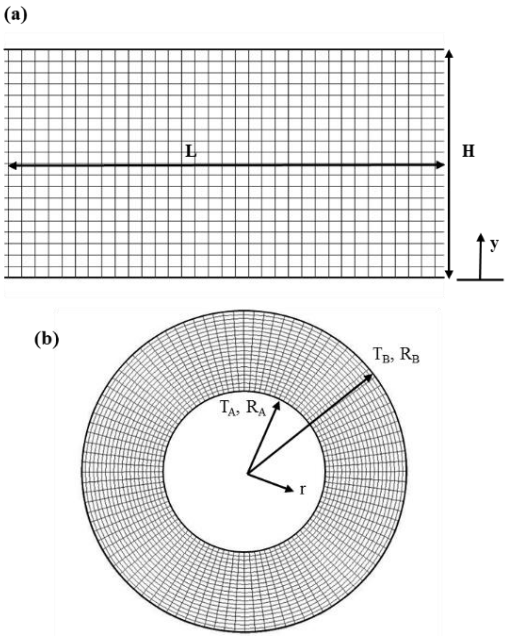

Fig. 1. Benchmark computational domains (a) Planar region between parallel plates (b) Annular region between concentric cylinders.

plannar and annular regions using the DVM subjected to the Maxwellian specular-diffuse boundary conditions. The Hard Sphere (HS) intermolecular interaction model was used for viscosity calculation (Eq. 3). The heat flux across the planar and annular gaps was calculated for different values of the accommodation coefficients.

Figures 2a and 2b show the comparison between the heat transfer reduction ratio $(Q_C\text{-}Q)/Q_C$, where Q_C is the heat flux limit in the continuum regime, obtained from Fluent simulations using the Willis temperature jump model (Eq. 9) and from the S-model kinetic equation for different values of the thermal accommodation coefficient α.

From these figures (2a and 2b) one can see that the ANSYS/Fluent simulations are in good agreement with the DVM kinetic calculations for both configurations (parallel plates and concentric cylinders) and for all the values of the thermal accommodation coefficient (α=1, 0.4 and 0.2). The maximum deviation of the Fluent model from the kinetic calculations is less than 1.1% for the concentric cylinders configuration. For the parallel plate configuration the maximum deviation of 2.4% is observed for pressure of 22 Pa (corresponding to the limit of the slip regime) and thermal accommodation coefficient of 0.2. For the other values of the thermal accommodation coefficient the deviation was smaller than 1.26%.

From Figures 2 it is clear that the Fluent model was able to predict with a good accuracy the conduction heat transfer in the slip regime. In the next section, ANSYS/Fluent simulations with the Willis temperature jump model will be performed to calculate the peak cladding temperature in a whole package model.

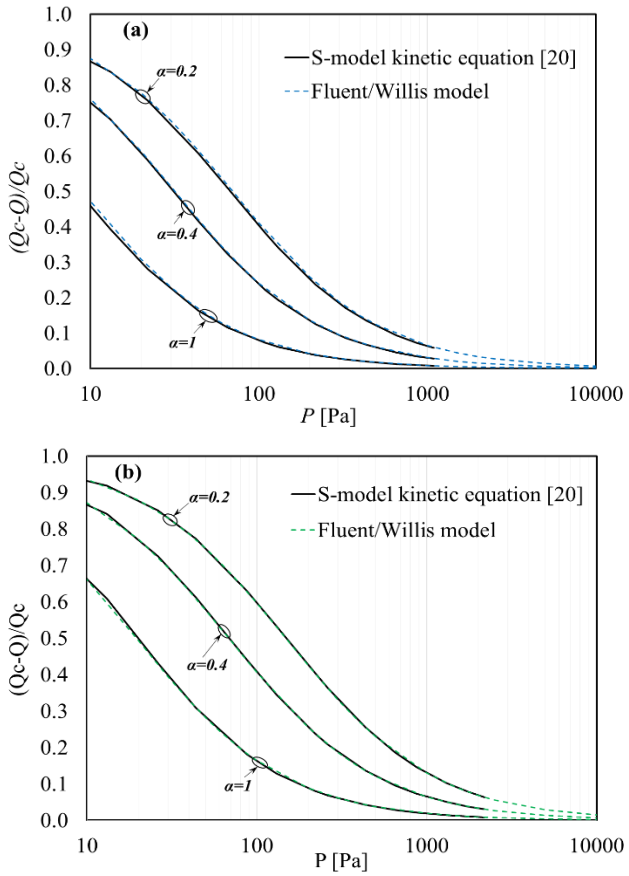

Fig. 2. Heat transfer reduction ratio as function of gas pressure and thermal accommodation coefficient (a) Planar region between parallel plates (b) Annular Region between concentric cylinders.

IV. TRANSFER CASK MODEL

Figure 3 shows the computational-domain-material-regionals of the canister used in ANSYS/Fluent simulations. The model presented in Figure 3 is similar to the Transnuclear TN-24 canister that contains 24 PWR Westinghouse fuel assemblies. This model uses symmetry to simplify the complete package into a one-eighth model.

The domain shown in Figures 3a, 3b and 3c includes a square array of 15x15 fuel rods with an UO_2 core surrounded by a Zircaloy sheath. Instrumentation rods are included in the model and are assumed similar size to the fuel rods. The square fuel rod assembly is centered inside a stainless steel basket. The stainless steel basket rests inside the aluminum supports along with the neutron poison; thermal properties for BORAL® were used for the neutron poison. The neutron poison is placed in selected spots inside the aluminum support geometry. In Figure 3b, a detailed view of the fuel rod array showing the gas filled regions of the instrumentation rods between the aluminum support and the stainless steel which is in a symmetrical pattern. Figure 3c shows the gap between the aluminum support and the stainless-steel-enclosure which is gas filled

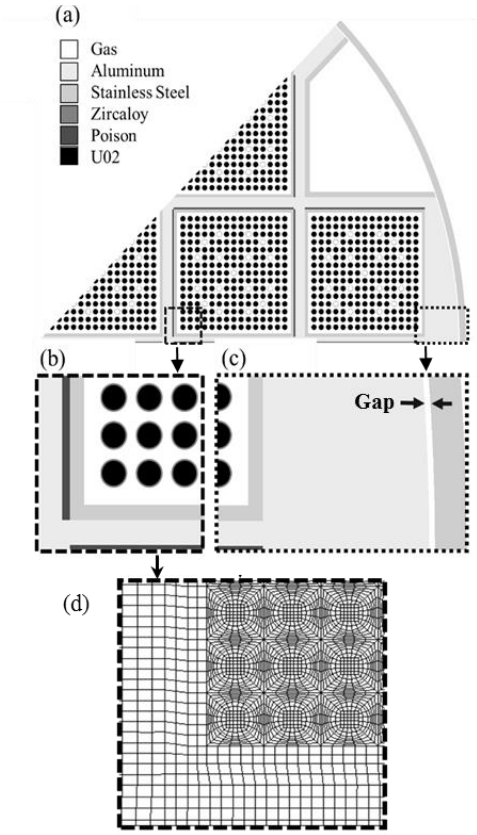

Fig. 3. Regional materials and mesh details of computational domain. (a) Grey scale coded material list for the model. (b) Detailed region of the fuel rod array in the stainless steel basket. (c) Detailed view of the 2.29 mm annular gap that surrounds the entire canister. (d) Mesh detail of the region (b).

and represents the smallest dimension in the canister with size of 2.29 mm.

The outer diameter of each rod measures 10.92 mm with a 0.67 mm Zircaloy sheath. The rod center-to-center pitch is 14.43 mm. The 2D reference depth used in the model is 3.66 m. The domain shown in Figure 3 with the detailed view of the region (b) (Figure 3d) contains a total of 131,202 elements.

Steady-state and transient thermal simulations were performed using ANSYS/Fluent 15. These simulations assume uniform heat generation in all the UO_2 regions at given axial location, and they included conduction within the solids and gas regions, and surface-to-surface radiation across the gas regions with surface emissivity of 0.46 for the stainless steel and 0.8 for the aluminum and zircaloy [27]. These simulations do not include buoyancy-induced gas motion or natural convection in the backfilled regions because they are negligible at the pressures considered in this work. The outer boundary condition of the transfer cask is assumed to be underwater at a constant temperature of 101.7°C. This boundary condition is used for all the simulations (steady-state and transient simulations)

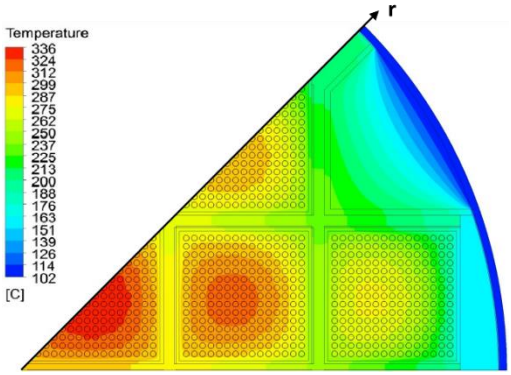

Fig. 4. Temperature contour plots (helium at atmospheric pressure with Q=2291 W/m/assembly)

reported in this paper. The heat input for each fuel rod region is 270 to 1000 W/m/assembly, calculated as

$$Q' = P_f \frac{Q}{L} \tag{12}$$

where P_f and L are the axial peaking factor and the length of the fuel rods. The value of 1.1351 for the peaking factor is used [28]. Q is the total heat generated per fuel assemblies.

V. RESULTS AND DISCUSSION

Two different heat transfer models are used in this work. The first is the continuum model, which does not include temperature jumps at the interface between solid surfaces and helium. The second is the temperature jump model, which includes the Willis-temperature-jump-thermal-resistance model described in equations (5) and (8). Simulations for this model are performed for pressure P=100 Pa, and thermal accommodation coefficients α=0.2, 0.4 and 1.

Figure 4 shows temperature contours from the continuum model (P=1 atm) with outer enclosure wall temperature at 101.7°C and heat generation of 2291 W/assembly. The maximum peak cladding temperature in the domain is located in the center of the innermost fuel assembly. The maximum peak temperature obtained is T_P=336.3°C which below the allowable maximum clading temperature T_{RH}=400°C.

Figure 5 shows the profile of the temperature along the r-axis shown in Figure 4 for the continuum and temperature jump models. The highest temperatures in the domain are located at the center of the assemblies and the minimum temperatures are located at the outer assembly regions. The temperatures within the fuel rods are relatively uniform compared to the gas region between solids. For the continuum model (solid line) sudden increase of temperature occurred at the gap between the aluminum support and stainless-steel-enclosure (see Figure 3). This is due to the low thermal conductivity of helium when compared to aluminum and stainless steel, and also to the accumulation of heat generated by the fuel rods in this gap. The effect of radiation heat transfer is weak since the

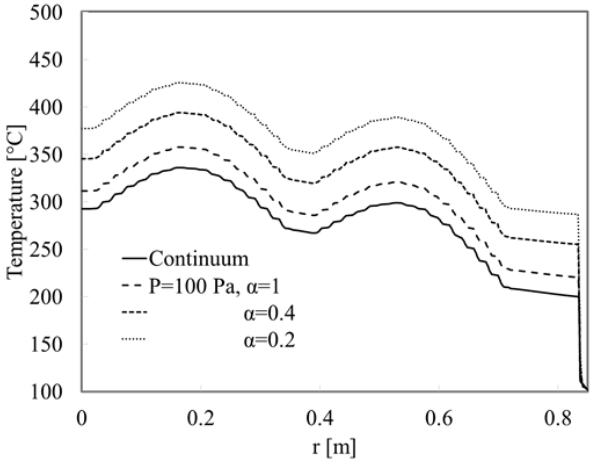

Fig. 5. Radial temperature profile along the radial axis shown in Figure 5, calculated for Q=2291 W/ assembly and for continuum model (atmospheric pressure) and temperature jump model (P=100 Pa) for different values of the thermal accommodation coefficient.

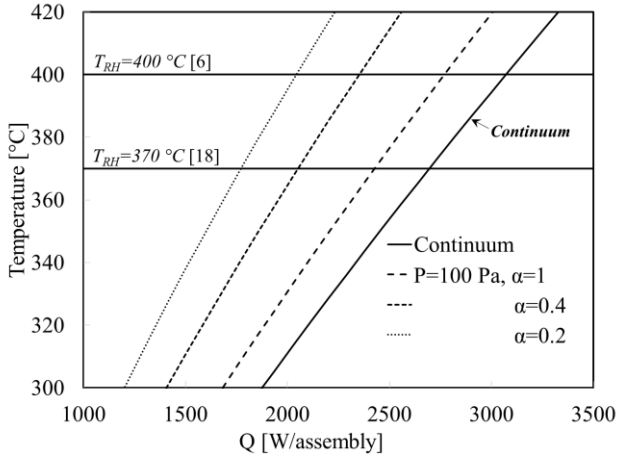

Fig. 6. Peak cladding temperature versus fuel heat generation rate for helium at atmospheric pressure (continuum model) and P=100 Pa (temperature jump model) with three values of the thermal accommodation coefficient α=1, 0.4 and 0.2.

temperatures in the gap are relatively small. The maximum temperature reached for the continuum model is less than the limit temperature of 400°C. The continuum model is valid down to the pressure of 13,345 Pa, which represents the limit between the continuum and slip regime (Kn=10^{-3}). Below this pressure the effects of gas rarefaction start to be visible.

Figure 5 shows also the results for the temperature jump model (P=100 Pa). When the pressure in the domain decreases from atmospheric pressure to P=100 Pa the maximum temperature in the domain increases. The same behavior is observed when the thermal accommodation coefficient (α) decreases while the pressure is kept constant at P=100 Pa. The maximum temperature jump is induced at the gap between the aluminum support and stainless-steel-enclosure. The participation of the fuel cladding surfaces in the increase of the temperature due to temperature jump resistance is small. For the case P=100Pa and α=0.2 the maximum peak cladding temperature is T_P=425.8°C, which is higher by 89.5°C comparing to the continuum model and exceed the allowable limit T_{RH}=400°C. This shows the importance of taking into account the effects of rarefied gases for the estimation of the peak cladding temperature during vacuum drying operations. It should be noted that the pressures during vacuum drying operations may be less than 100 Pa (around 70 Pa), which has the potential to further increase the cladding's temperature.

Figure 6 shows the maximum peak cladding temperature as function of the fuel heat generation per assembly. The results are reported for atmospheric pressure conditions (continuum model) and for P=100 Pa (temperature jump model) with three values of the thermal accommodation coefficient α=1, 0.4 and 0.2. The temperature limit that leads to the formation of radial hydride considered in the United States (T_{RH}=400°C) and in Germany ($T_{RH,R}$=370°C) are shown by two horizontal lines.

The temperature differences between the temperature jump and continuum models increase as the heat generation increases. For a given heat generation this difference can be higher than 80°C. The temperatures experienced with the temperature jump model are always higher than those with the continuum model. Smaller value of thermal accommodation coefficient α leads to higher temperature.

From Figure 6 the maximum allowable heat generation that brings the peak cladding temperature to the radial hydride formation temperature T_{RH}=400°C and the reduced one $T_{RH,R}$=370°C are obtained and the values are given in Table I.

TABLE I. Maximum allowable heat generation per assembly Q for continuum model (P=1 atm) and temperature jump model (P=100 Pa) at the radial hydride formation temperature T_{RH}=400°C and the reduced temperature $T_{RH,R}$=370°C.

Temperature of radial hydride formation	Maximum heat generation [W/assembly]			
	Continuum model	Temperature jump model		
		α=1	α=0.4	α=0.2
T_{RH} = 400°C	3070	2769	2351	2043
$T_{RH,R}$ = 370°C	2695	2426	2051	1772

Table I shows that the maximum allowable heat generations predicted by the continuum model are higher than those predicted by the temperature jump model. For the case of temperature jump model (P=100 Pa) with α=0.2 the maximum allowable heat generation that brings the peak cladding temperature to the limit of 400°C is 34% less than that predicted by the continuum model.

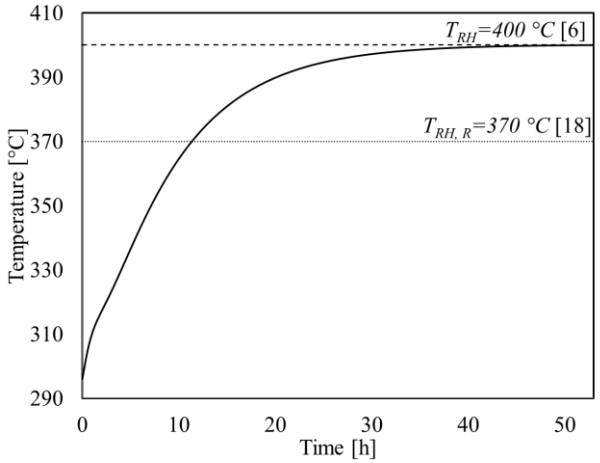

Fig. 7. Transient response of the fuel assemblies under vacuum drying condition. Peak cladding temperature as function of time.

Figure 7 shows the transient response of the fuel assemblies subjected to vacuum drying. The maximum peak cladding temperature in the domain is plotted versus the time in hours. The fuel assembly heat generation Q=2351 W/assembly that brings the peak cladding temperature to the limit of 400 °C is used (see Table I).

The transient simulation is performed in two steps. First, steady state simulation is performed with canister/cask filled with water, which simulate the condition of loading the fuel assemblies into the canister while it is underwater. Second, the transient simulation is started by using the temperature field from the steady state simulation as an initial condition. The pressure during the transient simulation is set to the vacuum pressure P=100 Pa and the value of thermal accommodation coefficient α=0.4 is used.

At the beginning of transient simulation the maximum cladding temperature in the domain is T_P=297.4°C. The maximum cladding temperature increases with time and reaches the limit of 400°C within 53 hours. This time is less than the typical time for vacuum drying of a canister with BORAL® neutron poison, more than 60 hours [29]. The time needed to reach the limit temperature of 370°C, used in Germany, is 11.5 hours. For fuel assemblies with heat generation 10 % higher than Q=2351 W/assembly the time to reach the limit temperature of 400°C decreases significantly, t=13.75 hours, for the same conditions of pressure and thermal accommodation coefficient. It should be noted here that the value of the accommodation coefficient is kept constant for the transient simulation. However, its value varies with temperature, as temperature increases the value of the thermal accommodation coefficient decreases [24]. This has the potential to further increase the temperature and reduce the time to reach the limit temperature.

Figure 7 shows also that at the beginning of the simulation, below 5 hours, there is a bump in the profile of temperature. At the starting of the simulation the temperatures in the domain are low and the heat is mainly transferred by conduction through solid and gas. As the temperature increases the portion of heat transferred by radiation becomes more important, which results in the changing of the temperature slope. Another reason could be the change of location of the maximum temperature within the innermost fuel assembly.

VI. CONCLUSIONS

Geometrically-accurate-two-dimensional simulations of heat transfer in used nuclear transfer cask containing 24 assemblies of 15×15 fuel rods array have been performed using ANSYS/Fluent code. Steady state and transient simulations were performed to calculate the peak cladding temperatures during vacuum drying conditions of the transfer cask filled with helium at atmospheric pressure (continuum model) and P=100 Pa (temperature jump model).

ANSYS/Fluent simulations in simple geometries (parallel plate and concentric cylinders) were compared to the accurate DVM kinetic model based on the Boltzmann equation [20] for different values of the thermal accommodation coefficient in order to assess the accuracy of ANSYS/Fluent to model the conditions of gas rarefaction. The simulation results showed that the Willis model for temperature jump applied in ANSYS/Fluent was in good agreement with the DVM kinetic calculations. This model was applied for the transfer cask simulations.

For the steady state simulations of the transfer cask, the continuum model (which did not include the temperature jump effect) was compared to the temperature jump model at P=100 Pa. The results showed that the peak cladding temperature in the domain is located in the center of the innermost fuel assembly. When the temperature jump model was applied, with thermal accommodation coefficient α=1, the peak cladding temperature increased by 21.5°C comparing to the continuum model. The change of the thermal accommodation coefficient from 1 to 0.2 caused an increase of temperature of 89.5°C when compared to the continuum model. The results showed also the gap between the aluminum support and stainless-steel-enclosure plays the more important role in temperature increase. The heat generation rate that causes the radial hydride formation predicted by the temperature jump model was 34% less than that predicted by the continuum model.

The transient simulation results showed that the required time to reach the maximum peak cladding temperature T_{RH}=400°C is 53 hours for the vacuum conditions of P=100 Pa and α=0.4. A slight increase of the fuel assembly's heat load could significantly reduce this time. A change of thermal accommodation coefficient α from 0.4 to 0.2 also has the potential to significantly reduce this time.

This paper showed that taking into account of the effect of gas rarefaction in the simulations of the vacuum drying operations is crucial to accurately model this process, as it results in significant increase of temperature, which is not considered in the continuum model.

ACKNOWLEDGMENTS

This work was supported by the US Department of Energy Office of Nuclear Energy University Program.

REFERENCES

1. Holtec International, "HI-STORM 100 FSAR", Revision 8, Report HI-2002444, (2010).
2. D. Colmont and P. Roblin, "Improved thermal modeling of SNF shipping cask drying process using analytical and statistical approaches," *Packaging, Transport, Storage & Security of Radioactive Material*, vol. 19, no. 3, pp. 160-164, (2008).
3. P. Loscoe, "Transitioning metallic uranium spent nuclear fuel", *WM'00 Conference*, Tucson, AZ, (2000).
4. R. Wittman, "Radiolysis model sensitivity analysis for a used fuel storage canister", U.S Department of Energy. PNNL-22773, (2013).
5. B. Hanson, H. Alsaed, C. Stockman, D. Enos, R. Meyer and K. Sorenson, "Gap Analysis to Support Extended Storage of Used Nuclear Fuel", FCRD-USED-2011-000136 Rev. 0, U.S. Department of Energy Used Fuel Disposition Campaign, (2012).
6. "Cladding Considerations for the Transportation and Storage of Spent Fuel", ISG-11 R3, Interim Staff Guidance Report for the Spent Fuel Project Office of the U.S. NRC, (2003).
7. R. S. Daum, S. Majumdar and M. Billone, "Experimental and Analytical Investigation of the Mechanical Behavior of High-Burnup Zircaloy-4 Fuel Cladding", J. ASTM Intern., vol. 5, no. 5, (2008).
8. R. S. Daum, S. Majumdar, Y. Liu and B. M.C., "Radial-hydride Embrittlement of High-burnup Zircaloy-4 Fuel Cladding", J. Nucl. Sci. Tech., vol. 43, no. 9, pp. 1-14, (2006).
9. M. C. Billone, T. Burtseva and R. Einziger, "Ductile-to-brittle transition temperature for high-burnup cladding alloys exposed to simulated drying-storage conditions", J. Nucl. Mater, vol. 433, pp. 431-448, (2013).
10. M. C. Billone, T. Burtseva and Y. Liu, "Baseline Properties and DBTT of High-Burnup PWR Cladding Alloys," in Proc. PATRAM, San Francisco, CA, (2013).
11. W.S. Large, and R.L. Sindelar, "Review of Drying Methods for Spent Nuclear Fuel", Westinghouse Savannah River Company, Savannah River Site, Aiken, SC, report number WSRC-TR-0075, (1997).
12. L. Loeb, Kinetic Theory of Gases, 2nd Edition, McGraw-Hill Book Company Inc., (1934).
13. E. H. Kennard, Kinetic Theory of Gases, McGraw-Hill Book Company, Inc., New York, (1938).
14. S. A. Schaaf and P. L. Chambre, Flow of Rarefied Gases, Princeton University Press, (1961).
15. Y.S. Tseng, J.R. Wang, F.P. Tsai, Y.H. Cheng and C. Shih, "Thermal design investigation of a new tube-type dry-storage system through CFD simulations", Annals of Nuclear Energy, 38, 1088-1097, (2011).
16. Holtec International, "Topical Report on the HI-STAR/HI-STORM Thermal Model and its Benchmarking with Full-Scale Cask Test Data", Holtec Report No. HI-992252, (2000).
17. Pacific Northwest Laboratory, "The TN-24P PWR Spent Fuel Storage Cask: Testing and Analyses", EPRI NP-5128, (1987).
18. H. G. Kim, Y. H. Jeong, and K. T. Kim, "The effects of creep and hydride on spent fuel integrity during interim dry storage", Nuclear Engineering and Technology, vol.42 no.3, (2010).
19. G. A. Bird, "Definition of mean free path for real gases", Phys. Fluids, 26, 11, (1983).
20. I. Graur, M. T. Ho and M. Wuest, "Simulation of the transient heat transfer between two coaxial cylinders", J. Vac. Sci. Technol. A 31(6) (2013).
21. G. A. Bird, Molecular Gas Dynamics and the Direct Simulation of Gas Flows. Oxford Science Publications, (1994).
22. J. C. Maxwell, "On stress in rarefied gases arising from inequalities of temperature," Phil.Trans. R. Soc. Lond., vol. 170, p. 231–256, (1878).
23. F. O. Goodman, "Thermal accommodation coefficients", J. Phys. Chem. 84, 1431-144, (1980).
24. S. Song, and M. M. Yovanovich, "Correlation of thermal accommodation coefficient for 'engineering' surfaces", Proceedings of the 24th ASME National Heat Transfer Conference and Exhibition, Pittsburgh, PA, pp. 107-116, (1987).
25. F. Sharipov, "Data on the velocity slip and temperature jump coefficients", Thermal and Mechanical Simulation and Experiments in Micro-Electronics and Micro-Systems. Proc. 5th Int. Conf. EuroSimE, Belgium, pp. 243-249, (2004).
26. J. T. Lin and D. R. Willis, "Kinetic Theory Analysis of Temperature Jump in a Polyatomic Gas," *Phys. Fluids*, vol. 15, p. 31 (1972).
27. M. F. Modest, Radiative Heat Transfer, 2nd Edition, Academic Press, New York (2003).
28. R. H. Bahney, and T. L. Lotz, Spent Nuclear Fuel Effective Thermal Conductivity Report, Prepared for the U.S. DOE, Yucca Mountain Site Characterization Project Office by TRW Environmental Safety Systems, Inc., (1996).
29. W. Bracey and P. Smith, "Transnuclear Drying Experience and Lessons Learned," ASTM Workshop, Atlanta, GA, (2012).

Proceedings of the ASME 2015 Pressure Vessels & Piping Division Conference
PVP2015
July 19-23, 2015, Boston, Massachusetts, USA

PVP2015-45852

DESIGN OF AN EXPERIMENT TO MEASURE THE THERMAL ACCOMMODATION COEFFICIENT BETWEEN HELIUM AND STAINLESS-STEEL IN CONCENTRIC CYLINDERS

Rachel Green
University of Nevada, Reno
Reno, NV, USA

Mustafa Hadj-Nacer*
University of Nevada, Reno
Reno, NV, USA
mhadjnacer@unr.edu

Miles Greiner
University of Nevada, Reno
Reno, NV, USA

ABSTRACT

Heat transfer through a 1 mm gap between two concentric cylinders representing the gap between a fuel support basket and a canister is experimentally and numerically investigated. The objective of this work is to study rarefied gas heat transfer in a simple geometry, and to measure the thermal accommodation coefficient at the interface between stainless steel and rarefied helium. The thermal accommodation coefficient is used to characterize the interaction between gas molecules and wall at the molecular level. It is important to determine its value with precision for better determination of heat transfer at low pressure. The experimental procedure consists of measuring the temperature difference between the inner and outer cylinders as the pressure is decreased in the gap. By knowing the heat flux across the gap the thermal accommodation coefficient can be extracted from the theoretical expression relating the temperature difference to the radial heat flux. Three-dimensional simulations using the ANSYS/Fluent commercial code are conducted to assess on the design of the experimental apparatus. These simulations confirmed that the apparatus design is effective to study the heat transfer across rarefied gas and to determine the thermal accommodation coefficient for helium on stainless steel surface.

NOMENCLATURE

a	Slope of the temperature difference variation with the inverse of the pressure
Kn	Knudsen Number
k	Boltzmann constant, 1.38×10^{-23} [m^2kg/s^2K]
L	Length [m]
m	Molecular mass of gas [kg]
P	Pressure [Pa]
Pr	Prandtl number
Q_r	Radial heat flux [W]
T	Temperature [K]
R	Radius of the cylinders [m]

Greek symbols

α	Thermal accommodation coefficient
γ	Specific heat ratio
κ	Thermal conductivity of the gas [W/mK]
λ	Mean free path [m]
μ	Stress viscosity of the gas [kg/ms]
ζ_T	Temperature Jump Coefficient

Subscript

0	Reference
A	Inner cylinder
B	Outer cylinder
g	Gas
w	Wall

Acronyms

CFD	Computational Fluid Dynamics
DSMC	Direct Simulation Monte Carlo
DVM	Discrete Velocity Method
TAC	Thermal Accommodation Coefficient

INTRODUCTION

Nuclear fuel assemblies consist of fuel rods containing high radioactive fuel pellets and fission product gases, held in square arrays by a header, a footer and periodic spacer plates [1].

Following their discharge from the reactor, used fuel assemblies are stored underwater while their heat generation rate and radioactivity decrease. After five or more years, [2] a canister is lowered into the pool and the fuel assemblies are placed inside it. The canister is closed, lifted out of the pool and drained. Before the canister is sent for storage it is subjected to a vacuum drying operation to remove the remaining water and moisture. It is important that all the water and moisture be removed to prevent corrosion of the fuel cladding and internal structures, and the creation of a flammable mixture of oxygen and hydrogen within the canister [3]. After drying, the canister

*Address all correspondence to this author.

is filled with helium to pressures between 3 and 7 atm (306 to 711 kPa), sealed, and the final cover lid is bolted or welded in place.

With the absence of a defined used-fuel disposal and/or reprocessing path, it is crucial to assure the safety of long-term dry cask storage systems [4]. Federal regulations (10CFR72) requires that "spent fuel cladding must be protected during storage against degradation that leads to gross ruptures or the fuel must be otherwise confined such that degradation of the fuel during storage will not pose operational safety problems with respect to its removal from storage." The cladding is the primary confinement barrier for the used fuel pellets and fission gas. Its integrity must be protected to assure that, after decades in storage, the assemblies can be safely transferred to other packages, and/or transported to other locations. Radial hydride formation within the cladding has the potential to radically reduce cladding ductility and its suitability for transport or long term storage [4].

During all post-reactor drying, transfer, storage and transport operations the fuel cladding must be kept below the temperature limit of 400°C (673K), specified by the Nuclear Regulatory Commission (NRC) Interim Staff Guidance-11, Revision 3 (ISG-11) [5], to avoid (a) dissolution of circumferential hydrides that exist in the cladding and (b) high gas pressures within the tubes, which leads to high cladding hoop stress [5]. If these hydrides dissolve and the hoop stresses become large, then as the heat generation of the used fuel decreases during long-term storage radial hydrides may form and cause the cladding to become brittle [6-9]. Vacuum drying operation [10] may be the most likely event to cause the fuel temperature to exceed the temperature limit. This is because it is the first operation when the fuel is removed from water and placed in a gas-filled environment, while the fuel heat generation is still relatively high.

During the vacuum drying operation the pressure in the canister is decreased to as low as 67 Pa to promote evaporation and removal of remaining water [3]. Several cycles of evacuation and refill are required before the operator can demonstrate that the canister satisfies the technical specifications of maintaining pressure of 400 Pa (3 Torr) for 30 minutes [10, 11]. Because of the low pressures and densities associated with vacuum drying, buoyancy-induced gas motion and natural convection heat transfer within the helium gas can be neglected. The thermal conductivity of the gas is almost the same as it is at atmospheric conditions. Moreover, the rarefaction condition (low pressure) induces a notable temperature difference (temperature jump) at the interface between wall surfaces and gas [3, 12-15]. As the pressure decreases this temperature jump increases and causes the cladding temperature to increase.

The temperature jump is characterized by the thermal accommodation coefficient [16, 17]. At low pressure the collisions between gas molecules and the surfaces dominate the molecules-molecules collisions. In these conditions the continuity of the macroscopic parameters (velocity and temperature) near the walls are not achieved. The concept of the accommodation coefficient was introduced by Maxwell during the mid-nineteenth century [18]. The thermal accommodation coefficient (α) is related to the temperature of incident T_i and reflected T_r molecules as

$$\alpha = \frac{T_i - T_r}{T_i - T_w} \tag{1}$$

where T_w is the wall temperature. The value of α varies from 0 to 1. In the case α=0, the molecules are reflected specularly, without transferring any of their momentum or energy to the surface (the molecule's temperature and velocity component parallel to the wall remain unchanged, but its velocity normal to the wall is reversed). For α=1, the molecules are reflected diffusely: a molecule leaving the surface "forgets" all information upon collision and it leaves accommodating the surface properties (i.e., their average bulk velocity is equal to the surface velocity and the temperature is equal to the temperature of the surface). A lower value of α leads to a higher temperature jump between the wall and gas molecules interacting with it.

The values of α were determined experimentally for a wide range of surfaces and gas molecules, using different methods [19-21]. Its value depends on a number of parameters, such as the type of gas, surface material, its cleanliness and its roughness. Authors [19, 20] reported values of α close to 1 for heaviest molecules and smaller values for lighter molecules. The value of α reported for the pair helium-stainless steel [20] is in the range [0.2, 0.4] for T=700 K to 300 K. The values α=1, 0.4 and 0.2 will be used in the current work for all the calculations.

Current Work The long term objective of the current research is to develop and experimentally benchmark computational models that predict the temperature difference between the cladding and basket walls during vacuum drying operation. An experimental apparatus that consists of 8×8 array of heated rods enclosed in square-cross-section-pressure-vessel subjected to vacuum condition will be constructed. The measurements will be compared to the computational model that will include the temperature jump boundary condition at the gas/surface interfaces. To achieve this objective experimental measurements of the thermal accommodation coefficient between stainless-steel surface and helium gas is conducted. The experimental design consists of coaxial cylinders' geometry filled with helium gas. The temperature and heat flux from the inner cylinder (hotter) to the outer cylinder (colder) will be measured and the thermal accommodation coefficient will be obtained from the comparison between the measurements and an analytical model. The aim of the current paper is to discuss the results obtained from the simulated model of the experimental apparatus that will be used to measure the value of the thermal accommodation coefficient. Three dimensional simulations are performed using ANSYS/Fluent package that accurately represent the experimental apparatus. Conduction and radiation heat transfer simulations are performed with rarefied helium gas filling the gap region between the stainless-steel cylinders. The temperature of the outer cylinder is maintained at a constant value of 300K and the pressure is varied from 10^5 to 100 Pa.

Experiments will be performed with matching heat generation rates and pressure ranges to that of the ANSYS/Fluent models, while maintaining the constant outer temperature using a water jacket.

RAREFIED GAS CONDITIONS AND HEAT TRANSFER

At low pressure conditions the number of collisions between gas molecules and solid surfaces is low compared to the normal atmospheric conditions. The continuity of the macroscopic parameters of temperature and velocity near the wall is not achieved. At these pressures some special characteristics related to the gas rarefaction can be observed. The principal parameter characterizing rarefied gas is the Knudsen number (*Kn*), which is calculated as

$$Kn = \frac{\lambda}{Lc}, \tag{2}$$

where λ is the mean free path defined as the distance travelled by molecules between two successive collisions [22] and *Lc* is a representative physical length scale. Typically the characteristic length *Lc* is the smallest dimension in the system. The mean free path λ is defined as

$$\lambda = \frac{\mu}{P}\sqrt{\frac{2kT}{m}}, \tag{3}$$

where *P* and *T* are the pressure and the temperature, respectively. *k* is the Boltzmann's constant, *m* is the mass of the gas molecule, μ is the dynamic viscosity, whose temperature dependence is determined using the intermolecular interaction Hard Sphere (HS) model [23] as

$$\mu = \mu_0\left(\frac{T}{T_0}\right)^{1/2}, \tag{4}$$

where T_0 is the reference temperature equal to 273.15 K and μ_0 is the reference viscosity, which depends on the gas. It is equal to 1.865×10-5 Pa·s for helium.

The Knudsen number is used as a parameter to describe the gas rarefaction level. Using this parameter four regimes of rarefaction can distinguish; (i) The continuum regime ($Kn \leq 10^{-3}$), where the flow and heat transfer can be accurately modeled using the classical Navier-Stokes and Convective Energy equations. The number of collisions is large enough to reach the continuity of parameters at the wall. (ii) The slip regime ($10^{-3} \leq Kn \leq 10^{-1}$), where the number of molecule-surface collisions are not enough to reach equilibrium near the wall, but far from the wall equilibrium is reached. In this regime the Navier-Stokes and Convective Energy equations are appropriate but they must be subjected to the conditions of velocity-slip and temperature-jump at the wall. (iii) Transitional regime ($10^{-1} < Kn < 10$), it is the most difficult regime for modeling. In this regime the mean free path is comparable to the characteristic length scale, therefore, the collisions between molecules and surfaces dominate the collisions between molecules. To model the flow in this regime the Boltzmann equation should be solved using the Discrete Velocity Method (DVM) [24, 25] or Direct Simulation Monte Carlo (DSMC) method [23]. (iv) The free molecular regime ($10 \leq Kn$), where the gas is highly rarefied and the flow is driven by the collisions between molecules and surface. In this regime the flow is modeled using the collisional kinetic Boltzmann equation.

It should be pointed out that all the regimes cited above can be accurately modelled using the kinetic theory, by solving the Boltzmann equation. Nevertheless, it is inefficient to implement this equation or other kinetic equations for gas flow simulation in the hydrodynamic and slip regimes because of the large computational efforts needed for their solution.

EXTRACTION OF THE THERMAL ACCOMMODATION COEFFICIENT

The measurement of the accommodation coefficient can be either performed in the slip or free molecular regimes. In these two regimes the analytical expression relating the thermal accommodation coefficient to the temperatures of inner and outer walls can be obtained. For the pressures experienced during vacuum drying operation of fuel canister the gas is in the slip regime. For this reason only the slip regime is considered in this paper.

In the slip regime the interaction between molecules and the wall does not allow equilibrium near the wall to be reached, meaning that there is a discontinuity of temperature and velocity near the wall ($T_g \neq T_w$, and $V_g \neq V_w$), which is called as temperature jump or velocity slip boundary conditions. In order to obtain the analytical expression of temperature difference between the inner and outer cylinders as function of pressure, heat flux and accommodation coefficient the Navier-Stokes and Convective Energy equations are used and subjected to the temperature jump boundary condition.

Sharipov [26] suggested that when gas is in the slip regime with the assumption of the temperature difference between two concentric cylinders ΔT is smaller than the average temperature T_m ($\Delta T << T_m$) and without considering the radiative heat flux, the radial heat flux across the gas may be expressed as

$$Q_r = 2\pi L\kappa\Delta T\left[\ln\frac{R_B}{R_A} + \zeta_T\lambda\left(\frac{1}{R_A}+\frac{1}{R_B}\right)\right]^{-1} \tag{5}$$

where R_A and R_B are the radii of the inner and outer cylinders, respectively. *L* and κ are the length of the cylinders and thermal conductivity of the gas, which is assumed to be constant for the small temperature difference $\Delta T = T_A - T_B$, where T_A and T_B are the temperature of the inner and outer cylinders, respectively. In equation (5) ζ_T is the temperature jump coefficient. It was demonstrated in previous work [27] that the expression of

temperature jump coefficient provided by Lin and Willis [28] is in very good agreement with the kinetic simulations carried out using the Shakhov model (S-model) kinetic equation. This expression is

$$\zeta_T = \frac{\sqrt{\pi}\gamma}{(\gamma+1)\,\mathrm{Pr}}\left(\frac{2-\alpha}{\alpha}+0.17\right). \quad (6)$$

For helium the ratio of specific heat at constant pressure to that at constant volume is γ=5/3 and the Prandtl number is Pr=2/3. Substituting equation (3) into (5), the temperature difference ΔT between the inner and outer cylinders can be written as function of the inverse of the pressure,

$$\Delta T = \frac{Q_r}{2\pi L\kappa}\mu\zeta_T\left(\frac{1}{R_A}+\frac{1}{R_B}\right)\sqrt{2\frac{k}{m}T_B}\,\frac{1}{P}+\frac{Q_r}{2\pi L\kappa}\ln\frac{R_B}{R_A}. \quad (7)$$

This expression shows that the temperature difference ΔT is a linear function of the inverse of the pressure. The expression (8) is used for comparison with experimental data to extract the value of the thermal accommodation coefficient α.

The experimental measurements of the temperature difference will be performed for a fixed value of the radial heat flux Q_r and for a range of pressure P. The measured temperature differences ΔT_{exp} will be plotted as function of the inverse of the pressure and fitted with first order polynomial form using the least square method as

$$\Delta T_{\mathrm{exp}} = a\frac{1}{P}+b, \quad (8)$$

where a is the slop of the function $\Delta T(1/P)$. By substituting Eq. (6) into Eq. (7) and using the expression of the Prandtl number $\mathrm{Pr}=c_p\mu/\kappa$, and comparing it to the expression of the measured ΔT_{exp} (Eq. 8) the slope a can be expressed as function of the thermal accommodation coefficient as

$$a = \frac{Q_r}{2c_p}\frac{\gamma}{\gamma+1}\left(\frac{2-\alpha}{\alpha}+0.17\right)\left(\frac{1}{R_A}+\frac{1}{R_B}\right)\sqrt{\frac{2}{\pi}\frac{k}{m}T_B}. \quad (9)$$

From this equation the value of the thermal accommodation coefficient can be calculated. It is clear from Eq. (9) that the slope a depends only on the cylinder's dimensions, radial heat flux and gas nature but does not depend on the thermal conductivity or viscosity of the gas.

The uncertainty for the extraction of the thermal accommodation coefficient is calculated using the root square sum (RSS) method as

$$\frac{\Delta\alpha}{\alpha} = \left[\left(\frac{\Delta a}{a}\right)^2+\left(\frac{\Delta L}{L}\right)^2+\left(\frac{\Delta Q_r}{Q_r}\right)^2+\left(\frac{\Delta R_A}{R_A}\right)^2+\left(\frac{\Delta R_B}{R_B}\right)^2+\frac{1}{4}\left(\frac{\Delta T_B}{T_B}\right)^2\right]^{\frac{1}{2}} \quad (11)$$

The total uncertainty on the value of α calculated using expression (11) is 5.2%.

EXPERIMENTAL DESIGN

Figure 1 shows drawing of the experimental setup, which consists of a main inner cylinder system centered inside an outer cylindrical vessel. The inner cylinder system has an outer diameter of 43.51 mm and the vessel cylinder has an inner diameter of 45.49 mm, which leaves a gap of about ~1 mm between the two cylinders. The length of the inner cylinder system is 1.032 m, however the length of the vessel cylinder is 1.132 m. In order to keep a constant gap between the cylinders the experiment is oriented vertically to avoid the problem of inner cylinder system bowing.

The main inner cylinder system is composed of an electrical heating cartridge that is centered inside a thick walled aluminum cylinder. Twelve thermocouples were strategically placed inside precision 0.15 mm deep grooved channels machined on the outer surface of the aluminum cylinder and secured with highly thermal conductive cement so that any potential gaps are minimized. The shrink fit process was used to insert the aluminum cylinder inside 1 mm thickness stainless-steel-sheath, which comprises the outer surface of the inner cylinder system. This process was used to ensure an intimate contact between the outer aluminum surface and inner stainless-steel-sheath surface. Figure 2a shows a picture of the end of the inner cylinder system with the centered heating cartridge, aluminum cylinder and stainless-steel sheath along with the thermocouples channels. The aluminum cylinder has a thick wall to allow uniform temperature profile on the outer surface of the inner cylinder system. The heating cartridge is secured in place with highly-conductive epoxy.

Low thermal conductivity (κ = 0.06 W/mK) alumina insulation material, with a thickness of 50 mm, is placed on both ends of the inner cylinder system, then the assembly (inner cylinder system + insulations) is centered inside the outer vessel cylinder with the aid of stainless-steel supports and spacer plates. This low thermal conductivity insulation is employed to minimize the heat losses from the ends of the cylinder system. The supports provide rigidity and ability to hold the inner system concentric to the vessel so that a 1 mm-wide gap is created between the two.

The temperature of the outer vessel is controlled using an external water jacket. Twelve thermocouples are placed inside small grooves machined on the outer surface of the vessel to monitor the vessel temperatures. The thermocouples where secured inside the grooves with epoxy and aluminum straps to ensure their ability to withstand the turbulence of the water flow. Figure 2b shows the water jacket that surrounds the main vessel with the thermocouple and water inlet ports.

Conflat flanges on both ends of the vessel are used to seal and maintain the pressure inside the vessel. One of the flanges contains thermocouple and power feedthroughs (not shown) to allow the connection of the thermocouples and power leads from the vacuum chamber to the outside. The other flange contains a vacuum tree (not shown) that connects the vacuum chamber to the vacuum pump through an open/close valve. To the vacuum tree is also connected a high pressure helium tank through a

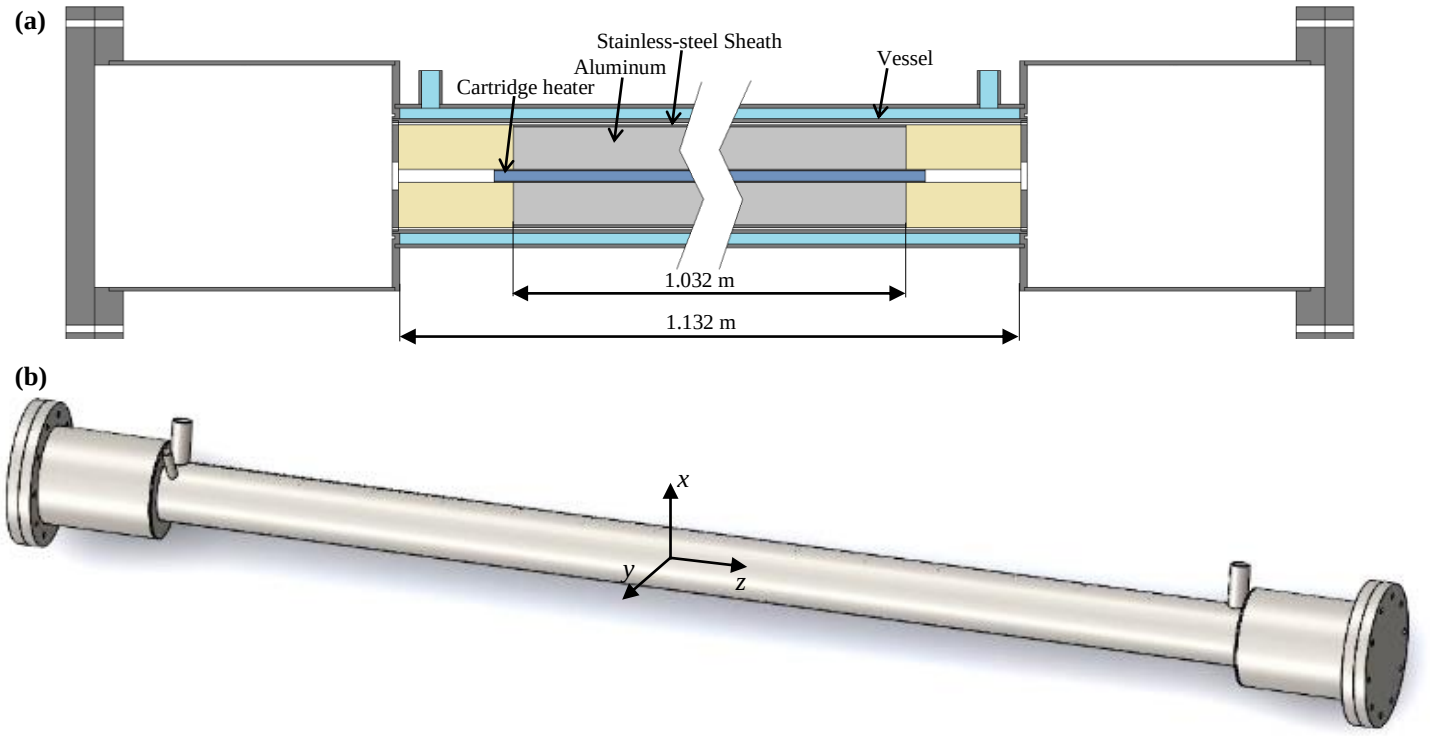

FIGURE 1 COLOR CODED MATERIAL LIST OF THE REGIONAL MATERIAL DETAILS OF COMPUTATIONAL DOMAIN: (DARK GREY) STAINLESS-STEEL, (LIGHT GREY) ALUMINUM, (DARK BLUE) MAGNESIUM-OXIDE, (YELLOW) ALUMINA INSULATION, (LIGHT BLUE) WATER, (WHITE) GAS BACKFILL. (b) PICTURE OF THE THREE DIMENSIONAL MODEL CONSTRUCTED USING SOLIDWORKS SOFTWARE.

variable valve that allows to set the pressure inside the vacuum chamber.

The emissivities of the vessel inner surface and stainless-steel sheath outer surface are measured, and are 0.152 and 0.149, respectively.

VALIDATION OF THE EXPERIMENTAL DESIGN

A geometrically accurate three-dimensional model of the experimental apparatus is created and meshed using ANSYS/Fluent Computational Fluid Dynamics (CFD) commercial code. Simulations that include conduction and radiation heat transfer, and temperature-jump at the interface between solid surfaces and gas are performed. The outer surface of the vessel was maintained at constant temperature of 300K and the pressure in the gap was varied from atmospheric pressure to P = 200 Pa. This range of pressures covers both continuum and slip regimes. Three values of the thermal accommodation coefficient, α = 1, 0.4 and 0.2, and a constant heat generation within the cartridge heater (Q=150W) are considered for all the simulations. The expression of temperature jump coefficient proposed by Lin and Willis [28] (see Eq. (6)) is implemented in ANSYS/Fluent simulations.

These simulations are used to check the ability of the apparatus to measure α with high confidence. The effect of heat losses from the cylinder's ends on the extraction of the thermal accommodation coefficient is investigated. The assumptions of constant temperature and heat flux profiles along the z-axis is verified.

RESULTS AND DISCUSSION

Figure 3 shows a typical cross-section-temperature-contour for all of the simulated cases considered in this paper. The maximum temperature is located at the center of the inner cylinder assembly with nearly uniform temperature through the aluminum cylinder and stainless-steel sheath surrounding the aluminum cylinder. A steep decrease in temperature is observed across the helium gas gap.

Figure 4 shows the profiles of the temperature along the r-axes shown in Fig. 3 for θ = 0° (across the thermocouple) and θ=45°, for Q = 150 W, and a continuum condition (P=1 atm). The temperature profiles along the two axes are very similar and the only difference is obtained at the thermocouples location, where the thermocouples experience slightly lower temperatures difference of the order of 0.1 K. Even when varying the heat generation rate Q from 150W to 300W the temperature difference across the thermocouple remains small (less than 0.15K). This systematic error in thermocouple temperature reading is included in the calculation of the thermal accommodation coefficient uncertainty (Eq. (11)).

In Fig. 5 the effect of rarefaction on the increase in temperature, compared to the continuum model, is shown. The rarefaction simulations are performed for P=300 Pa and α=1, 0.4 and 0.2. From Figure 5 it can be seen clearly that the rarefaction

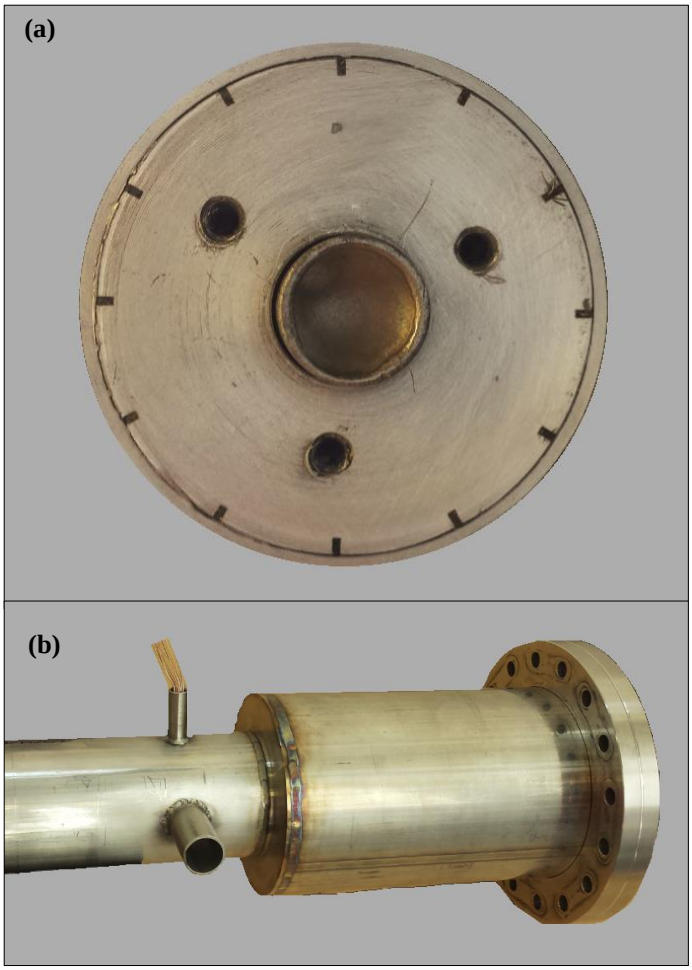

FIGURE 2 (a) INNER CYLINDER SYSTEM; ALUMINUM AND STAINLESS-STEEL SHEATH WITH THERMOCOUPLES AND CENTERED HEATING CARTRIDGE, (b) WATER JACKET WITH THERMOCOUPLES WIRES AND WATER INLET PORT.

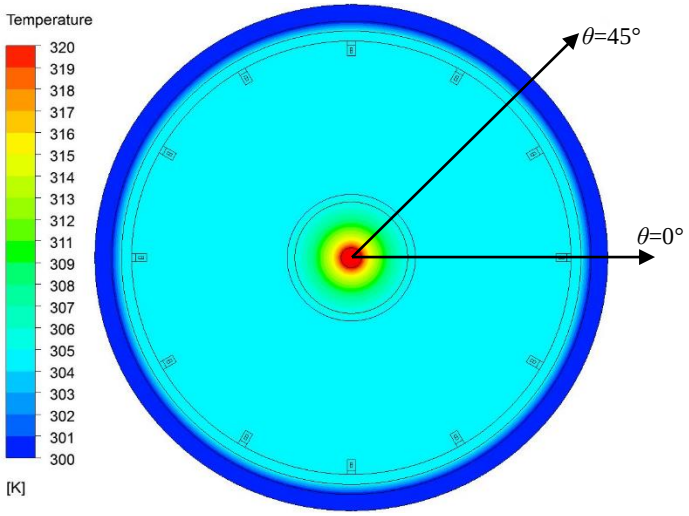

FIGURE 3 TYPICAL TEMPERATURE CONTOUR FOR ALL SIMULATED CASES.

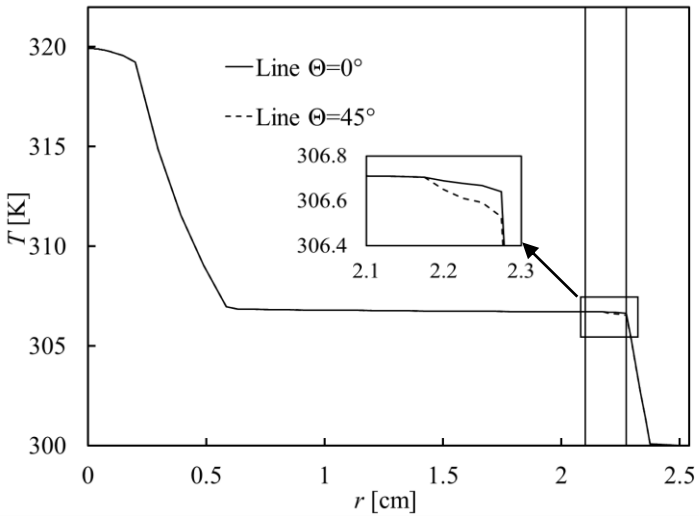

FIGURE 4 TEMPERATURE PROFILE ALONG THE *r*-AXIS SHOWN IN FIG. 3 FOR ATMOSPHERIC PRESSURE (CONTINUUM MODEL).

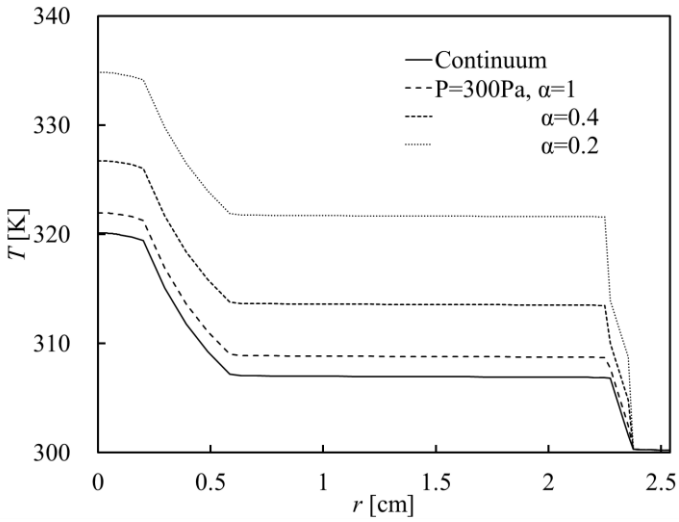

FIGURE 5 COMPARISON BETWEEN CONTINUUM (*P*=1 atm) AND RAREFIED MODELS (*P*=300 Pa) FOR DIFFERENT VALUES OF α.

model predicts higher temperature in comparison to the continuum model, which is due to the temperature-jump at the interface between solid surfaces and gas. This temperature increases as the thermal accommodation coefficient decreases (see Fig. 5).

Temperature profiles along the cylinder axis (*z*-axis, see Fig. 1) are shown in Figure 6 for outer surface of the stainless-steel sheath and thermocouples region. These profiles are obtained using the continuum model. A nearly uniform temperature along the stainless-sheath-surface is obtained. The maximum variation of temperature along this surface is less than 0.1 K with the maximum value obtained at the midplane.

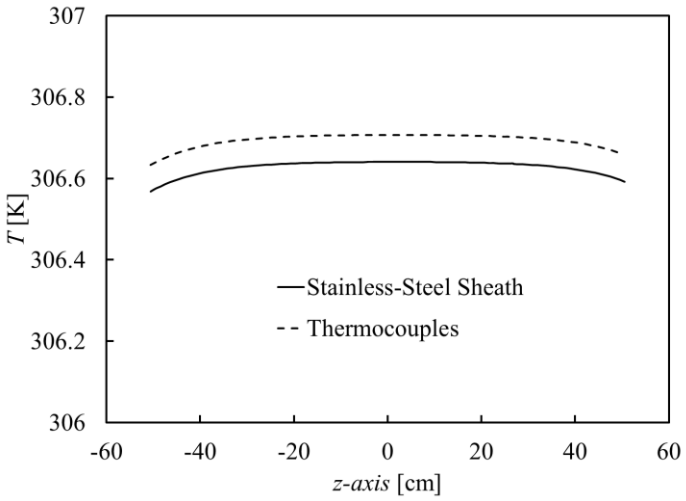

FIGURE 6 AXIAL TEMPERATURE PROFILES FOR THE OUTER SURFACE OF THE STAINLESS-STEEL SHEATH AND THE THERMOCOUPLE REGION.

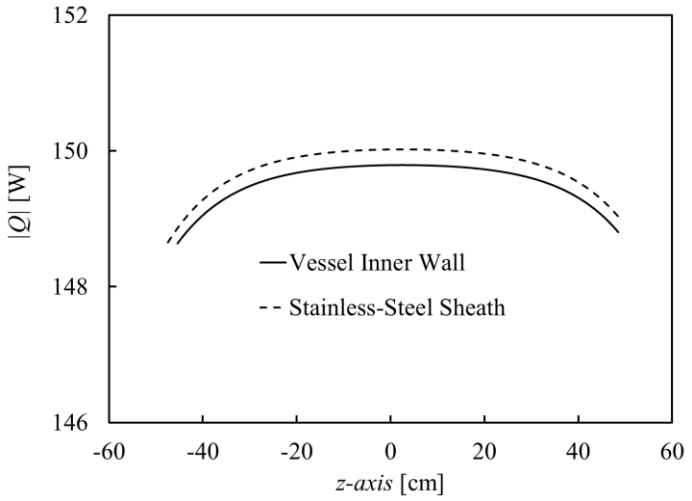

FIGURE 7 HEAT FLUX ALONG THE VESSEL INNER SURFACE AND OUTER STAINLESS-STEEL-SHEATH SURFACE.

Axial heat flux profiles along the side surfaces of the stainless-steel-sheath and vessel are shown in Figure 7. It is clear from this figure that the heat flux leaving the outer surface of the stainless-steel-sheath and delivered to the inner surface of the vessel, which are in contact with helium, are nearly identical and uniform along the axial axis direction. The maximum variation of the heat flux along the axial axis is less than 1%.

Heat losses from both ends of the inner cylinders system are minimized by choosing a cylinder with small aspect ratio R_i/L=0.02, where R_i and L are the radius and length of the inner cylinders system, respectively, and by placing low thermal conductivity alumina insulation material (κ=0.06 W/m.K) with 50 mm thickness on both ends of the inner cylinders system. In Eq. (7) it is assumed that all the heat generated by the cartridge heater leaves from the side surface of the inner cylinders system. Table 1 shows the percentage of the estimated heat leaving from the side and ends surface of the inner cylinders system for continuum and rarefied models with three different values of thermal accommodation coefficient. The heat leaving the end surfaces is affected by the rarefaction; as the pressure or α decrease the heat loss from the end surfaces is higher, however it is small and therefore Eq. (7) can be utilized to extract the value of α with considering this heat loss in the calculation of the uncertainty on α.

The uniformity of the temperature and heat flux leaving the surfaces in contact with helium, shown in Figs 6 and 7 confirms the validity of the actual experimental design to be used for the calculation of the value of the thermal accommodation coefficient α from Equation (7).

CONCLUSION

The rarefied gas condition during vacuum drying of nuclear canister could potentially have a significant effect on used nuclear fuel cladding temperature. The cladding temperature increases as the pressure decreases. This increase in temperature is a result of the temperature jump that is induced between the gas and the solid surfaces. The temperature jump is dependent of the thermal accommodation coefficient. The objective of this paper is to verify the design of an experimental apparatus that will be used to determine the thermal accommodation coefficient at the interface between stainless steel and rarefied helium.

TABLE 1 PERCENTAGE OF HEAT LOSS FROM THE SIDE AND ENDS OF THE INNER CYLINDER SYSTEM.

		Percentage of wall heat flux [%]	
	α	Side-Walls	End-Walls
Continuum	-	99.66	0.34
P = 300Pa	1	99.13	0.87
	0.4	98.97	1.03
	0.2	98.88	1.12

Three-dimensional simulations using the ANSYS/Fluent code were used with thermal accommodation coefficient values of α=1, 0.4 and 0.2, P=1 atm (continuum model) and 300 Pa (temperature jump model) with Q_r = 150W. The results for the temperature jump model were 15 K higher than the continuum model results (no temperature jump, Fig. 5) when the thermal accommodation coefficient was decreased from 1 to 0.2.

The Fluent simulations showed also that the implantation of the thermocouple in the design did not significantly change this temperature. The temperature difference between the thermocouple and the stainless-steel-sheath surface in contact with helium was less than 0.1K.

The total uncertainty on the determination of the thermal accommodation coefficient was estimated to be less than 5.2%. Currently the experimental apparatus is being constructed.

ACKNOWLEDGMENTS

This work was supported by the US Department of Energy Office of Nuclear Energy University Program.

REFERENCES

[1] U.S. Dept. of Energy, Office of Civilian Radioactive Waste Management (OCRWM), 1987. "Characteristics of Spent Nuclear Fuel, High-Level Waste, and Other Radioactive Wastes Which May Require Long-Term Isolation," DOE/RW-0184, December.

[2] Saling, J.H., and Fentiman, A.W., 2002. *Radioactive Waste Management*, 2nd Edition, Taylor and Francis, New York.

[3] Colmont, D. and Roblin, P., 2008. "Improved thermal modeling of SNF shipping cask drying process using analytical and statistical approaches," *Packaging, Transport, Storage & Security of Radioactive Material*, Vol. 19, No. 3, pp. 160-164.

[4] Hanson, B., Alsaed, H., Stockman, C., Enos, D., Meyer, R., and Sorenson, K., 2012. "Gap Analysis to Support Extended Storage of Used Nuclear Fuel," FCRD-USED-2011-000136 Rev. 0, U.S. Department of Energy Used Fuel Disposition Campaign.

[5] NRC, 2003. "Cladding Considerations for the Transportation and Storage of Spent Fuel," ISG-11 R3, Interim Staff Guidance Report for the Spent Fuel Project Office of the U.S. NRC.

[6] Daum, R.S., Majumdar, S., Liu, Y.Y., and Billone M.C., 2006. "Radial-hydride Embrittlement of High-burnup Zircaloy-4 Fuel Cladding." *J. Nucl. Sci. Tech*., Vol. 43, No. 9, Paper 43090, pp. 1-14.

[7] Daum, R.S. Majumdar, S., and Billone, M.C., 2008. "Experimental and Analytical Investigation of the Mechanical Behavior of High-Burnup Zircaloy-4 Fuel Cladding." *J. ASTM Intern*., Vol. 5, No. 5, Paper ID JAI101209, available online at www.astm.org.

[8] Billone, M.C., Burtseva, T.A., and Einziger, R.E., 2013. "Ductile-to-brittle transition temperature for high-burnup cladding alloys exposed to simulated drying-storage conditions," *J. Nucl. Mater*. 433, 431-448.

[9] Billone, M.C., Burtseva, T.A., and Liu, Y.Y., 2013. "Baseline Properties and DBTT of High-Burnup PWR Cladding Alloys," Proc. PATRAM, San Francisco, CA.

[10] Large, W.S. and Sindelar, R.L., 1997. "Review of Drying Methods for Spent Nuclear Fuel", Westinghouse Savannah River Company, Savannah River Site, Aiken, SC, report number WSRC-TR-0075

[11] Holtec International, 2010. "HI-STORM 100 FSAR," Revision 8, Report HI-2002444.

[12] Pan, L.S., Ng, T.Y., Xu, D., Liu, G.R., and Lam, K.Y, 2002. "Determination of Temperature Jump Coefficient Using the Direct Simulation Monte Carlo Method," *Journal of Micromechanics and Microengineering*, Vol. 12, pp. 41-52

[13] Sharipov, F. and Kalempa, D., 2005. "Velocity Slip and Temperature Jump Coefficients for Gaseous Mixtures. IV. Temperature jump coefficient," *International Journal of Heat and Mass Transfer* 48, pp. 1076-1083

[14] Schaaf, S.A. and Chambre, P.L, 1961. *Flow of Rarefied Gases*, Princeton University Press, New Jersey.

[15] Loeb, L.B., 1934. *Kinetic Theory of Gases*, 2nd Edition, McGraw-Hill Book Company Inc.

[16] Goodman, F.O., 1980. "Thermal accommodation coefficients", *J. Phys. Chem.* 84, 1431-144.

[17] Wachman, H.Y., 1962. "The Thermal Accommodation Coefficient: A Critical Survey," *ARS Journal*, vol. 32, no. 1, pp. 2-12.

[18] Maxwell, J.C., 1878. "On stress in rarefied gases arising from inequalities of temperature," *Phil.Trans. R. Soc. Lond*., vol. 170, p. 231–256.

[19] Song, S., and Yovanovich, M.M., 1987. "Correlation of thermal accommodation coefficient for 'engineering' surfaces," Fundamentals of conduction and recent developments in contact resistance, Proceedings of the Twenty-fourth ASME National Heat Transfer Conference and Exhibition, Pittsburgh, PA, pp. 107-116, Aug. 9-12.

[20] Trott, W.M., Castañeda, J.N., Torczynski, J.R., Gallis, M.A., and Rader, D.J., 2011. "An experimental assembly for precise measurement of thermal accommodation," *Review of scientific instruments* 82, 035120.

[21] Yamaguchi, H., Kanazawa, K., Matsuda, Y., Niimi, T., Polikarpov, A., and Graur, I., 2012. "Investigation on heat transfer between two coaxial cylinders for measurement of thermal accommodation coefficient," *Physics of Fluids*, vol. 24, no. 062002.

[22] Bird, G. A., 1983, "Definition of mean free path for real gases," *Physics of Fluids*, 26, 11.

[23] Bird, G. A., 1994. *Molecular Gas Dynamics and the Direct Simulation of Gas Flows*. Oxford Science Publications.

[24] Graur, I. A. and Polikarpov, A.P., 2009. "Comparison of different kinetic models for the heat transfer problem," *Heat and Mass Transfer* 46 (2), 237-244.

[25] Graur, I., Ho, M.T., and Wüest, M., 2013. "Simulation of the transient heat transfer between two coaxial cylinders," *J. Vac. Sci. Technol. A* 31(6).

[26] Sharipov, F., 2004. "Data on the velocity slip and temperature jump coefficients," Thermal and Mechanical Simulation and Experiments in Micro-Electronics and Micro-Systems. Proc. 5th Int. Conf. EuroSimE, Belgium, pp. 243-249.

[27] Manzo, E. T., Green, R., Hadj-Nacer, M., Greiner, M., Li, J., and Liu, Y. Y., 2014. "Prediction of cladding temperatures within a used nuclear fuel transfer cask filled with rarefied helium," In Proceedings of ASME Pressure Vessels and Piping Conference.

[28] Lin, J. T., and Willis, D. R., 1972. "Kinetic Theory Analysis of Temperature Jump in a Polyatomic Gas," *Physics of Fluids*, vol. 15, p. 31.

Proceedings of the ASME 2015 Pressure Vessels & Piping Conference
PVP2015
July 19-23, 2015, Boston, Massachusetts, USA

PVP2015-45851

GEOMETRICALLY-ACCURATE-THREE-DIMENSIONAL SIMULATIONS OF A USED NUCLEAR FUEL CANISTER FILLED WITH HELIUM

Triton Manzo
University of Nevada, Reno
Reno, NV, USA

Mustafa-Hadj Nacer*
University of Nevada, Reno
Reno, NV, USA
mhadjnacer@unr.edu

Miles Greiner
University of Nevada, Reno
Reno, NV, USA

ABSTRACT

This paper presents preliminary results of heat transfer simulations performed in geometrically-accurate-three-dimensional model of nuclear fuel canister filled with helium. The numerical model represents a vertical canister, which relies on natural convection as its primary heat transfer mechanism, containing 24 PWR fuel assemblies. The model includes distinct regions for the fuel pellets, cladding and gas regions within each basket opening. Symmetry boundary conditions are employed so that only one-eighth of the package cross-section is included. The canister is assumed to be filled with helium at atmospheric pressure. A constant temperature of 101.7°C is employed on the canister outer surfaces, assuming the canister to be surrounded with water. These conditions of pressure and temperature were considered, in this paper, for comparison purpose with previous work. The effects of buoyancy-induced gas motion and natural convection, along with radiation and conduction through gas regions and solid are considered. Steady state simulations using ANSYS/Fluent were performed for different heat generation rates in the fuel regions. Simulations that include the effect of natural convection and others that do not include this effect are conducted. The peak cladding temperature and its radial and axial locations are reported. The maximum allowable heat generation that brings the cladding temperatures to the radial hydride formation limit (T_{RH}=400°C) is also reported. The results of the three dimensional model simulations were compared to two dimensional model simulations for the same heat generation rate. The results showed that the two-dimensional simulations overestimate the temperature in the canister by almost 70°C.

INTRODUCTION

Used Nuclear Fuel (UNF) assemblies consist primarily of fuel rods containing high radioactive UO_2 pellets within tubular shaped zircaloy cladding, held in square arrays by header, footer and periodic spacer plates [1]. Different Boiling Water Reactor (BWR) assemblies consist of 6×6 to 11×11 rod arrays inside zircaloy channels. Pressurized Water Reactor (PWR) assemblies are composed of 14×14 to 17×17 arrays but do not have channels.

Following discharge from the reactor, fuel assemblies are stored underwater, while their radioactivity and heat generation decrease [2]. After appropriate time, the fuel assemblies are loaded from the storage pool into a canister that was earlier placed in a transfer cask and both lowered into the pool. The lid is then installed and the transfer cask is lifted out of the pool, drained and dried [3]. After drying, the canister is backfilled with a non-oxidizing gas, such as helium or nitrogen to a pressure between 3 and 7 atm, then is sealed and the final cover lid is bolted or welded in place. The non-oxidizing gas is used to ensure adequate heat transfer during storage and transport, and provides an inert atmosphere for long-term fuel integrity. The loaded canister is then moved to the dry storage facility on the reactor site for interim storage.

While in storage the UO_2 pellets continue to generate heat. The amount of heat generated depends on the UO_2's initial enrichment, reactor burn-up, and time spent in the water pool. During all the operations after the used fuel assemblies are removed from water the temperature of the fuel cladding must remain below the temperature limit of 400°C, specified by the Nuclear Regulatory Commission Interim Stuff Guidance 11, revision 3 [4], for normal conditions of storage, to prevent the formation of radial hydride in the zircaloy claddings and high hoop stress, which may affect the cladding's ductility and suitability for transport and storage [5, 6]. This can limit the heat generation rate of the fuel assemblies that can be stored in a canister. The heat transfer processes inside the fuel assembly/backfill gas regions must be fully understood to accurately predict the maximum cladding temperature for a specified fuel heat load, and the maximum safe fuel heat load.

*Address all correspondence to this author.

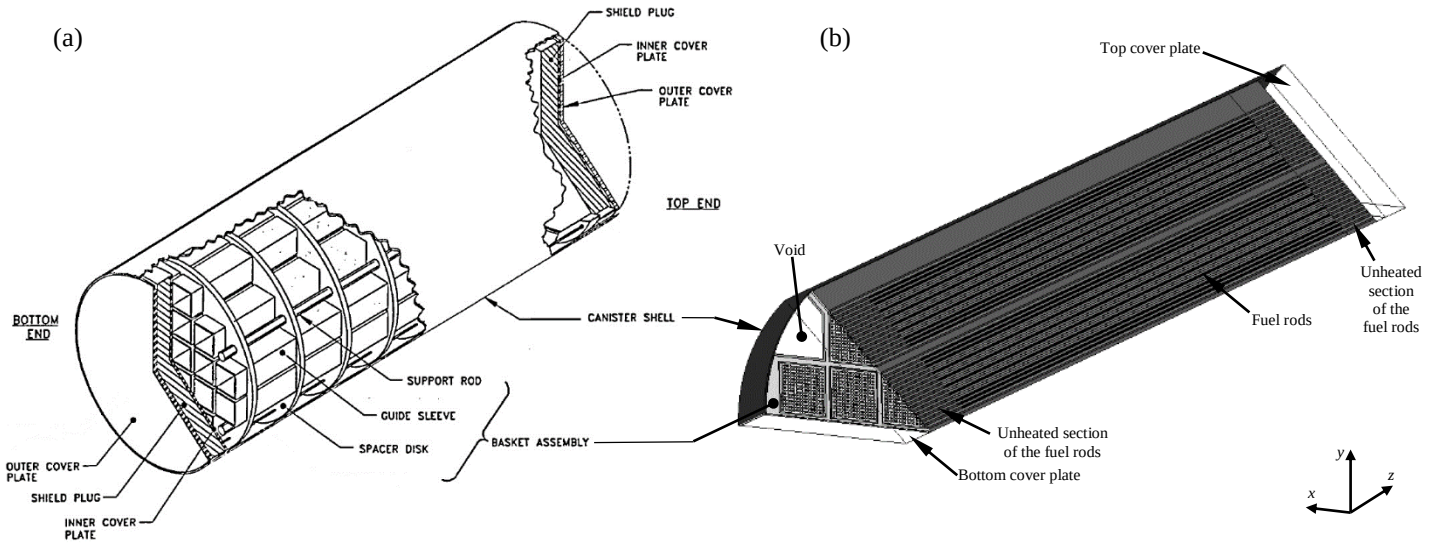

FIGURE 1 SCHEMATIC OF THE CANISTER. (a) CUTAWAY VIEW OF THE TRANSNUCLEAR TN24 SRORAGE CANITER (COURTESY OF AREVA). (b) 3D COMPUTATIONAL MODEL OF THE CANISTER ONE-EIGHTH MODEL CONSTRUCTED IN ANSYS/FLUENT.

Finite element thermal models of casks have been used to predict the cladding temperature for different fuel heat generation rates [7]. Multiple simulations are performed to determine the cask thermal capacity, which is the fuel heat generation rate that causes the cladding to reach its temperature limit. In some models, the fuel and basket are replaced by a smeared region with an Effective Thermal Conductivity (ETC) and an effective porosity [8-14]. Other models use an accurate-geometry computational domain where the fuel rods, gas and the baskets are modeled separately [15-25]. These models are used to predict the peak cladding temperature for a given fuel heat generation rate, and the fuel heat generation rate that causes the clad temperature to reach their allowed limits.

Effective thermal conductivities are simplified models that neglect natural convection and some other heat transfer effects such as corner effects. ETC models assume that the heat flux at a location depends only on the temperature and its gradient at that point. For natural convection, however, transport is affected by local velocity, which is affected by temperatures at other locations. Radiation heat transfer at a location is also affected by temperatures at a distance. In general, different ETCs must be used for different fuel assemblies.

The geometrically-accurate models overcome the shortcomings of the ETC models but are difficult to construct and require significant computational efforts. Most of the geometrically-accurate models for the simulation of fuel assemblies loaded in a canister in the literature are two dimensional models [15-17] or represents only one fuel assembly with an isothermal enclosure [18-25]. Only few works have considered the three dimensional-geometrically-accurate simulations of transfer cask [26, 27]. Current computational resources allow the use of three-dimensional (3D) models that accurately include the many fuel rods and unheated assembly components within a cask.

This paper presents one of the efforts to build a geometrically-accurate-three-dimensional model of a canister. This model represents a canister loaded with 24 Westinghouse PWR used fuel assemblies. It accurately represents 15x15 arrays of fuel rods and helium gas within each basket opening, and the helium-filled gap between basket and canister surface. Our objective is to develop a three-dimensional canister model capable of modeling conduction, radiation, mixed natural and forced convections in forced helium dehydration and temperature jump in vacuum drying. The current objective of this paper is construct and verify the model.

Steady-state simulations are performed for a range of fuel heat generation rates with helium at atmospheric pressure and with an isothermal canister outer surface temperature of 101.7°C, which assumes that the canister is under water. Even though this temperature condition is for a conservative condition for the drying process, it was used here to verify the 3D model by comparing it to a previous 2D model [28]. Buoyancy-induced gas motion and natural convective, and radiation heat transfer within the gas-filled regions, as well as conduction in the solid regions, are modeled using the ANSYS/Fluent Computational Fluid Dynamic (CFD) package. Those simulations are compared to stagnant-gas CFD simulations, in the same geometrically-accurate 3D model to determine the effect of the gas motion. A comparison to the 2D model simulations performed in previous work [28] is also presented. The peak cladding temperatures, their axial locations and the maximum allowable heat generation that brings the cladding temperature to its limit are reported.

CANISTER NUMERICAL MODEL

Figure 1a and 1b show a cutaway view of the TN24 Transnuclear canister and corresponding 3D computational-domain of the canister, respectively. The model represents a canister and basket loaded with 24 Westinghouse 15×15 PWR assemblies. The model takes advantage of the canister symmetry

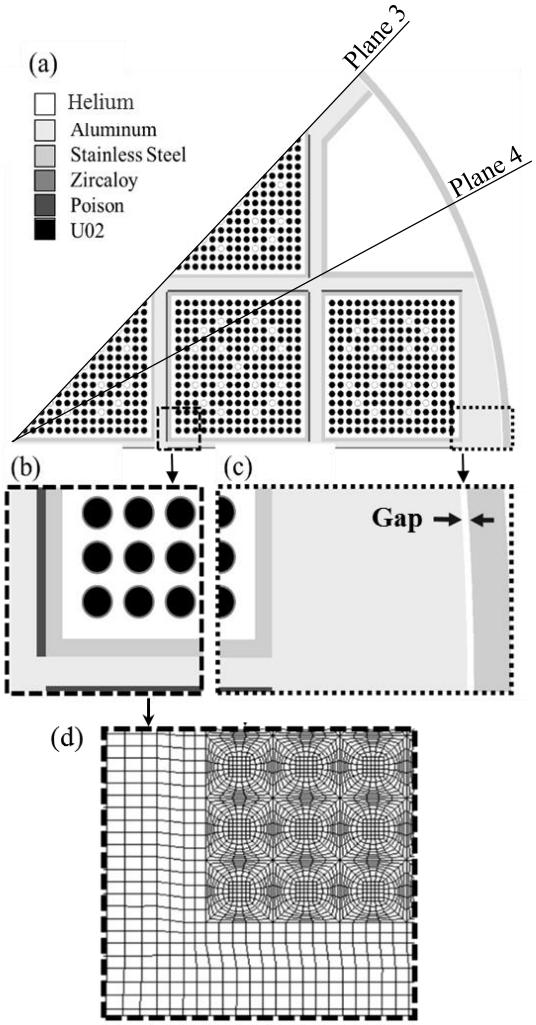

FIGURE 2 CROSS-SECTION-CUT OF THE CANISTER 3D MODEL SHOWED IN FIG. 1. (a) GRAY-SCALE CODED MATERIAL-REGION MODEL. (b) DETAILED REGION OF FUEL ROD ARRAY. (c) DETAILED REGION INCLUDING ANNULAR GAP BETWEEN BASKET AND CANISTER. (d) COMPUTATIONAL MESH FOR THE REGION IN PART (b).

along the radial axis, so that only one-eighth of the canister cross-section is included. Figure 1b shows the major components of the canister model, which include the fuel rods, aluminum basket, top and bottom cover plates, and heated and unheated sections of the fuel rods. For simplification the support rods and the spacer disks shown in Fig. 1a were not included in the model mesh.

In Fig. 1b the region marked by "void" is an open space that extends across the entire length of the canister. The header and footer of the fuel assemblies are replaced in this model with unheated sections of the fuel rods, however the gaps between the rods are kept as gas regions. There is gaps between the unheated fuel rods sections, and the top cover and bottom cover plates of 16.51 mm and 88.09 mm, respectively. All these gas regions are used to enhance the natural convection through the axial direction in the canister. Both top and bottom cover plates are represented with a single solid piece.

The canister outer diameter is 1.70 m and its length is 4.80m. The heated section of the fuel rods represents 76% of the canister total length. The total number of finite volume mesh cells in the one-eighth model is ~57 million. Gas regions where the natural convection occurs are represented by no less than 5 mesh elements in the radial direction. The mesh sensitivity study showed that 4 elements in the radial direction of the gas regions are sufficient. It was not possible to conduct mesh sensitivity study in the axial direction because of the limitation in the number of mesh elements that could be simulated.

Figure 2a shows a cross-section-cut of the 3D model material regions along with a detailed view of the mesh. Each assembly consists of a 15x15 array of 10.92-mm outer-diameter rods. Each fuel rod consists of d = 9.58-mm-diameter UO_2 pellets surrounded by 0.67-mm thick zircaloy cladding. There are also thirteen hollow zircaloy instrument tubes. The rod center-to-center pitch is 14.43 mm. The square cross-section basket tubes are constructed from stainless steel, and some surfaces are backed by BORAL® neutron poison plates. The tubes are supported by an aluminum structure. The basket and assemblies are enclosed within a stainless steel canister, and there is a large void space in the upper right of the domain.

Figure 2b is a detailed view of one corner of an assembly within a stainless steel basket opening, a BORAL® plate, and the aluminum support. Figure 1c shows a region at the periphery of the canister, including a 2.29-mm-wide gap between the basket and canister wall. Figure 3d shows the computational mesh within the region shown in Fig. 2b.

NUMERICAL SIMULATIONS AND BOUNDARY CONDITIONS

Steady state simulations were performed using ANSYS/Fluent 15 for different heat loads. These simulations assume uniform heat generation along the axial direction of all UO_2 pellets regions, and include conduction within solid and gas regions, and surface-to-surface radiation across all gas regions with surface emissivities of 0.46 for stainless steel and 0.80 for aluminum and zircaloy [29]. Helium at atmospheric pressure is considered as the working gas and a temperature boundary condition is employed on the canister outer surface with T_C=101.7°C. These conditions of pressure and temperature represent the conditions of drying, and they were considered in this work for the purpose of comparison with previous 2D simulations [28] performed in the same cross section geometry with these temperature and pressure conditions. This comparison will allow to verify the performances of the 3D model.

In order to investigate the effects of buoyancy induced gas motion and natural convection on heat transfer inside the canister, a comparison between the simulations that include this effect (natural convection simulations) and others that do not include it (conduction simulations) is performed. For natural convection simulations the incompressible ideal gas law is used to calculate density as $\rho=PM/RT$, where P is the pressure, T is the temperature, and R and M are the universal gas constant and

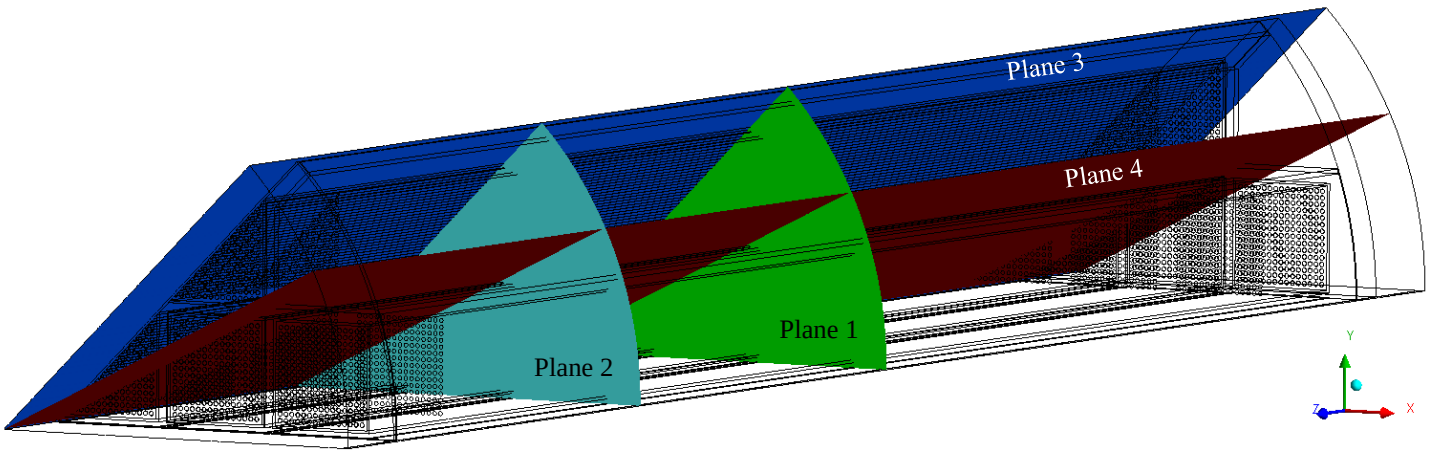

FIGURE 3 ILLUSTRATION OF THE DIFFERENT PLANES USED TO PRESENT THE RESULTS.

gas molecular weight of helium, respectively. The conduction simulations (not including natural convection) are compared to the 2D simulations.

Other 3D conduction simulations are conducted where the end surfaces of the top and bottom cover plates (see Fig. 1) are insulated and the results are compared to the conduction simulations with temperature boundary condition on all outer surfaces. These simulations are performed to examine the amount of heat losses from the canister ends.

RESULTS AND DISCUSSION

In this section the results of the 3 dimensional model are presented. Different planes through the model are considered to illustrate the results. Figure 2a and 3 show these different planes:

- Plane1 is the axial-cross-section plane located at the axial-center of the fuel assemblies, z/L_F=0.5, where L_F is the fuel rods length.
- Plane 2 is the axial-cross-section plane located where the maximum temperature is calculated.
- Plane 3 is the radial plane located on the upper boundary of the one-eighth model. It cross the most inner fuel assembly, an outer assembly and the aluminum basket.
- Plane 4 is the radial plane that cross the an inner fuel assembly, a neighboring one and the void (see Fig. 1).

Plane 2 and 3 will be used only for the natural convection simulations.

Figures 4a and 5a show the temperature contours from Plane 1 and Plane 3, respectively, obtained from the 3D conduction simulation (no natural convection) for fuel assembly heat generation rate Q_F=2291 W/assembly and temperature boundary condition on all the canister outer surfaces of T_C=101.7°C. The temperature contour from the 2D conduction model with the same temperature boundary and heat generation rate is very similar to that shown in Fig. 4a but with different scale. Figure 4a shows that there are maximum temperatures within each fuel assembly, but the global maximum is located near the center of the innermost fuel assembly. Figure 5a shows that the maximum temperature is located at the axial center of the innermost fuel assembly, z/L_F=0.5.

The solid line in Fig. 6 shows the temperature profile along the *r*-axis, shown in Fig. 4a, for the 2D model with the same conditions used in that figure. The maximum temperature or peak clad temperature obtained for the 2D model is T_{PC}=336°C, which is lower than the temperature of radial hydride formation considered in the US, T_{RH}=400°C [4], or the reduced temperature considered in Germany, $T_{RH,R}$=370°C [30]. The peak temperature of the inner assembly are ~37°C hotter than that of the outer assembly through which the *r*-axis passes. The temperature within the fuel rods and the solid regions are almost uniform however there are steep gradients in the helium gas regions. The steepest temperature gradient is observed at the peripheral gap between the aluminum basket and the canister inner surface (see Fig. 2c), located at r≈83 cm. This is because the heat flux through that region is relatively high and the contribution of radiation is relatively low due to the low temperatures in the gap. This gap makes a significant contribution to the total temperature difference between the canister outer surface and the hottest cladding.

In Fig. 6 the temperature profile along the *r*-axis of Plane 1 obtained from the 3D conduction model is shown by dashed line for the same heat generation rate Q_F=2291 W/assembly. This profile exhibits the same shape as the 2D conduction model, however they are systematically lower. The temperature gradient at the peripheral gap is smaller than that of the 2D conduction model.

Table I gives the temperature differences ΔT_{PC} and ΔT_{BS}. ΔT_{PC} is defined as the difference between the peak clad temperatures of a 3D model and the 2D conduction model. ΔT_{BS} is defined as the difference between the basket outer surface temperatures of a 3D model and the 2D conduction model. Table I shows that for the 3D conduction model ΔT_{PC} is 4.7 degrees larger than ΔT_{BS}. This indicates that most of the temperature differences between the 3D and 2D conduction models is induced at the peripheral gap. There is less heat crossing the

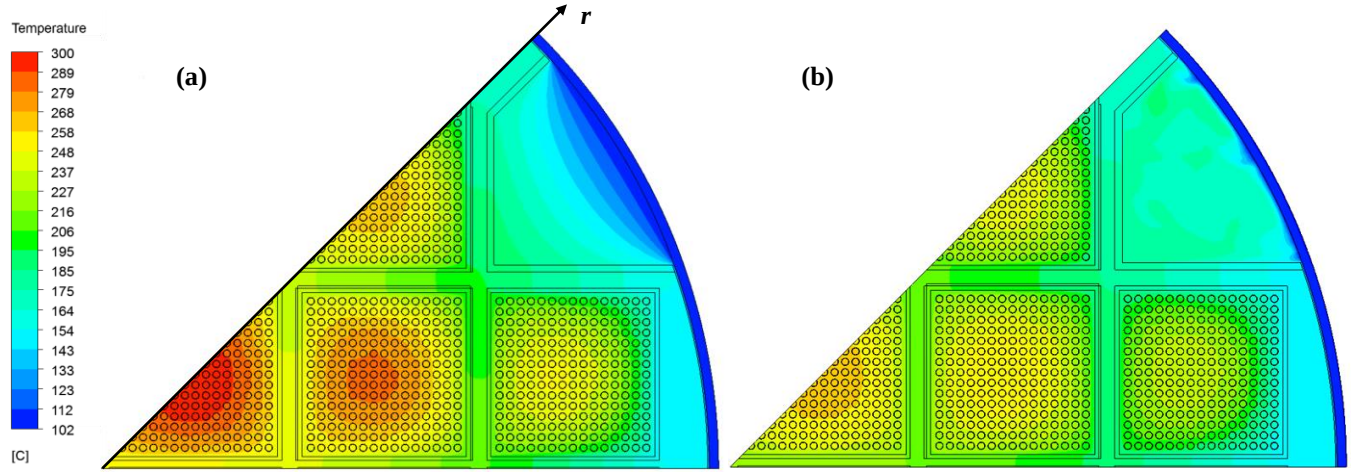

FIGURE 4 CONTOURS OF TEMPERATURE (a) FROM PLANE 1 FOR THE 3D CONDUCTION MODEL AND (b) FROM PLANE 2 FOR THE 3D NATURAL CONVECTION MODEL 4, FOR Q_F=2291 W/ASSEMBLY.

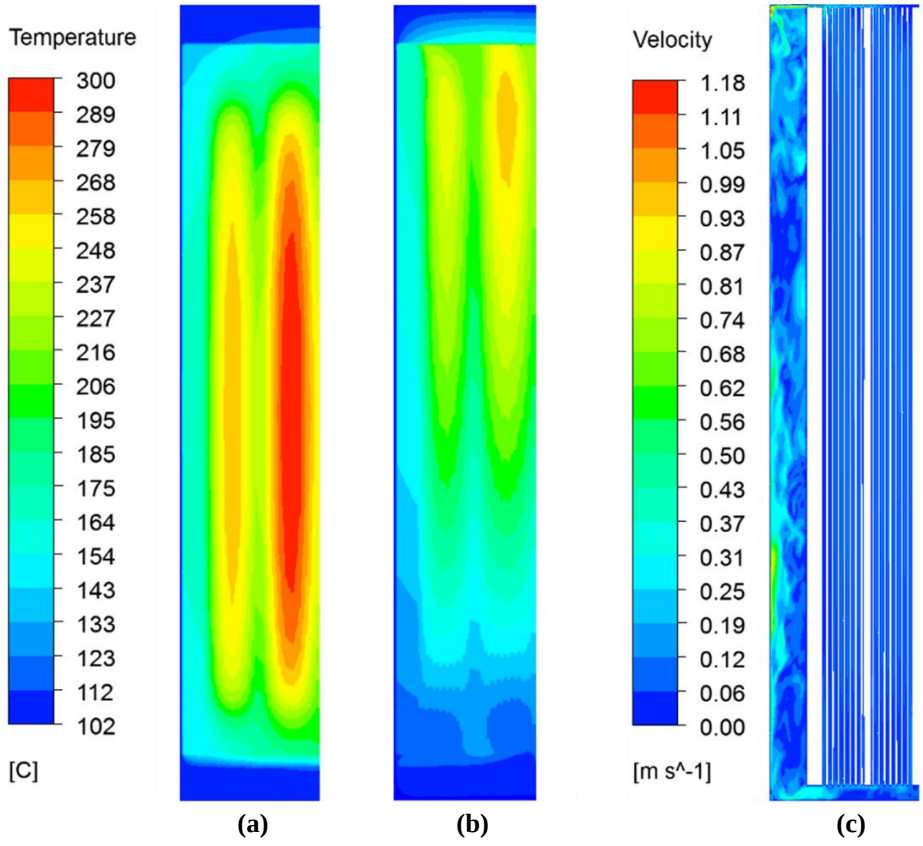

FIGURE 5 TEMPERATURE AND VELOCITY CONTOURS FROM THE RADIAL PLANES 3 AND 4 FOR Q_F=2291 W/ASSEMBLY. (a) TEMPERATURE CONTOUR FROM THE 3D CONDUCTION SIMULATION (PLANE 3). (b) TEMPERATURE CONTOUR FROM THE 3D NATURAL CONVECTION SIMULATION (PLANE 3). (c) VELOCITY CONTOUR FROM THE 3D NATURAL CONVECTION SIMULATION (PLANE 4).

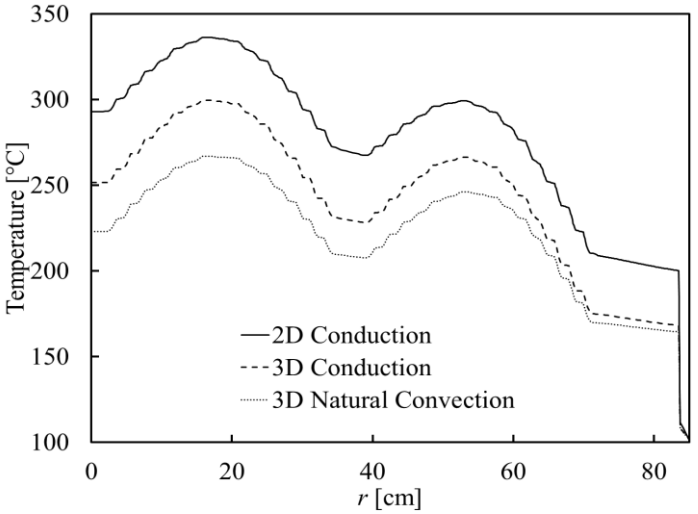

FIGURE 6 RADIAL TEMPERATURE PROFILE ALONG THE RADIAL AXIS SHOWN IN FIGURE 4, CALCULATED FOR Q_F=2291 W/ASSEMBLY, AND FOR THE 2D AND 3D CONDUCTION MODELS AND THE 3D NATURAL CONVECTION MODEL.

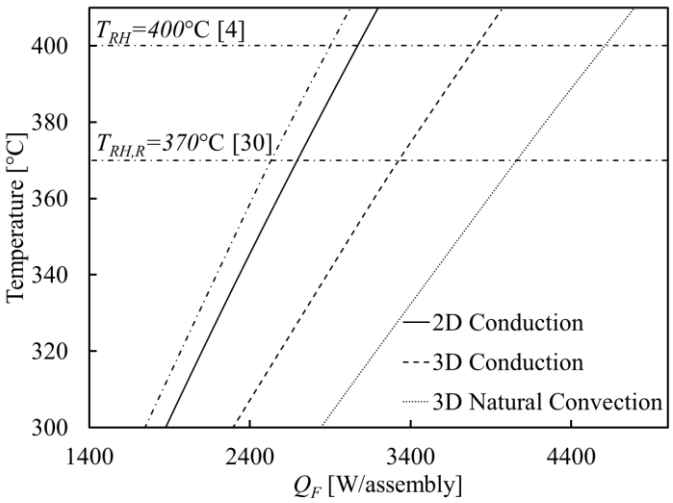

FIGURE 7 PEAK CLADDING TEMPERATURE VERSUS FUEL HEAT GENERATION RATE FOR 2D AND 3D CONDUCTION MODELS AND 3D NATURAL CONVECTION MODEL.

peripheral gap in the 3D model, due to the transport of a portion of the heat in the axial direction.

Figure 7 shows the peak clad temperature versus the assembly heat generation rate. The temperature limits of radial hydride formation T_{RH}=400°C [4] and $T_{RH,R}$=370°C [30] are represented by two horizontal lines, respectively. For all the heat generation rates the peak temperatures experienced with the 3D conduction model are systematical cooler than that of the 2D conduction model. The heat generation rate that brings the clad temperatures to the US limit for the 3D conduction model is 3810.6 W/assembly, which is 19% higher than of the 2D conduction model. These results are summarized in Table II.

TABLE I. DECREASE IN BASKET-END AND PEAK CLAD TEMPERATURES OF THE 3D CONDUCTION AND NATURAL CONVECTION MODELS COMPARED TO THE 2D CONDUCTION MODEL.

Models	Temperature Differences	
	ΔT_{BS} [°C]	ΔT_{PC} [°C]
3D Conduction	-32.0	-36.7
3D Natural Convection	-35.8	-69.3

Simulations on the effect of canister top and bottom boundary conditions were conducted using the 3D conduction model with insulated top and bottom cover plates and temperature boundary condition on the curved surfaces of the canister. These simulation are compared to the 3D conduction model with temperature boundary condition on all canister surfaces for the same heat generations rates. The result of the comparison showed that there is insignificant differences between the two models (less than 1°C). The profiles of temperature, the peak clad temperatures and the maximum allowable heat generation rates were nearly identical. The peak clad temperature differences between the two models for a given heat generation rate were less than 0.8°C, which indicates that essentially all the heat generated by the fuel rods leaves from the canister curved sites.

The dashed dotted line in Fig. 7 represents the same results of the 3D conduction model, but with its heat generation rate values multiplied by 0.76, which represents the ratio of the length of the fuel rods to the total height of the canister. When the heat generation rates were reduced, the peak clad temperatures of the 3D conduction model became higher than those of the 2D conduction model. This indicates that most of the heat generated at the fuel rods leaves the portion of the canister peripheral surface that has the same *z*-coordinates as the fuel rods. It should be noted that the heat generation along the axial direction of the fuel rods is uniform, no peaking factor is used.

TABLE II MAXIMUM ALLOWABLE HEAT GENERATION PER ASSEMBLY Q_F FOR THE 2D AND 3D CONDUCTION MODELS AND THE 3D NATURAL CONVECTION MODEL AT THE RADIAL HYDRIDE FORMATION TEMPERATURE T_{RH}=400°C AND THE REDUCED TEMPERATURE $T_{RH,R}$=370°C.

Temperature of Radial hydride Formation	Maximum allowable heat generation rate [W/assembly]		
	2D Conduction	3D Conduction	3D Natural Convection
T_{RH} = 400°C	3070.0	3810.6 (19.4%)	4611.3 (33.4%)
$T_{RH,R}$ = 370°C	2693.1	3327.4 (19.0%)	4063.5 (33.7%)

3D natural convection simulations are performed in ANSYS/Fluent by activating the gravity and using the non-compressible ideal gas law for the density calculation. Figure 4b shows the temperature contour from Plane 2 where the peak clad

temperature is recorded for the heat generation rate Q_F=2291 W/assembly. The maximum temperature is also located, in this case, in the innermost fuel assembly. The temperatures experienced with the natural convection simulation are systematically lower than those of the conduction simulations for the same heat generation. This is due to the additional transport of heat by natural convection. The maximum or peak cladding temperature for this heat generation is T_{PC}=296°C.

Figures 5b and 5c show the temperature and velocity profiles from radial planes 3 and 4 respectively. The peak clad temperature is located at z/L_F=0.99, which is at the top extremity of the fuel rods. The current model does not include fuel assembly headers, footers or spacer plates. It also does not include basket disks. These components increase conduction in the radial direction and inhibit buoyancy induced flow and natural convection. If these components were included, the peak temperature would be located closed to the middle-height of the rods. Figure 5c shows that there is some perturbations of the velocity field along the void region. The temperatures of the canister inner surface are lower than those of the basket surfaces, which causes the helium near the basket surfaces to flow up and that near the canister inner surface to flow down. The maximum velocity in the domain is 1.18 m/s, located at the top end of the void region close to the gap between the upper unheated rods section and the top cover plate (see Fig. 5c).

Figure 6 shows the profile of temperature along the *r*-axis of Plane 2 for the same condition of Fig. 4. The temperatures of the fuel assemblies from the 3D natural convection simulations are lower than that of 3D continuum simulations, however the temperatures of the basket near the periphery of the canister are close. Table I shows that ΔT_{BS} for both 3D conduction and natural convection models is very close (within 4°C). However ΔT_{PC} is very different. The flow of helium between the fuel rods, due to the buoyancy effect, tends to decrease the temperature of the fuel assemblies, however the heat flux through the peripheral region between the basket and the canister inner surface is almost the same for both models.

The dotted line in Fig. 7 shows the peak clad temperature versus the assembly heat generation rate Q_F from the 3D natural convection model. The peak temperatures are lower than those of the conduction models and the difference increase as the heat generation increases. Form Table II the maximum allowable heat generation rate that brings the cladding temperature to the limit used in the US and Germany for the natural convection simulation are 4611 and 4063 W/assembly, respectively, which are around 19% higher than the 3D conduction model.

CONLUSION AND FUTURE WORK

A geometrical-accurate three-dimensional model of a canister loaded with 24 Westinghouse 15×15 PWR fuel assemblies is constructed in ANSYS/Fluent code. Results of simulations representing the canister filled with helium at atmospheric pressure with isothermal boundary condition on all canister outer surfaces are presented. Steady-state simulations that include natural convection and buoyancy induced gas motion effects, and others that do not include these effect are considered. The results of the 3D models were compared to the 2D model simulations.

The results showed that the temperatures within the 3D conduction model (not includes natural convection) were cooler than the 2D conduction model. Insulating the end surfaces of the top and bottom cover plates did not change the temperatures of the fuel assemblies when compared to the temperature condition on all canister outer surfaces. Most of the heat generated by the fuel rods is conducted through the peripheral surface of the canister. The temperatures experienced with the 3D natural convection model were much cooler than the 3D conduction model. The axial location of the maximum temperature was located at the top extremity of the fuel rods due to the enhanced heat transfer by natural convection in the canister. The maximum allowable heat generation that bring the clad temperature to the radial hydride limit was 19% higher than that predicted by the 3D conduction model.

These preliminary results showed that this geometrically-accurate-three-dimensional model can be employed to accurately simulate the heat transfer in the canister under different conditions.

Future work Helium and nitrogen at pressure between 3 and 7 atm will be considered as working gases. Non-uniform heat generation along the axial direction of the fuel rods will be implemented. Future work will also include spacer disks and supporting rods in the canister. Forced helium dehydration and vacuum drying process will be simulated.

ACKNOWLEDGMENTS

This work was supported by the US Department of Energy Office of Nuclear Energy University Program. References

REFERENCES

1. US Department of Energy, 1987. "Characteristics of spent nuclear fuel, high-level waste, and other radioactive wastes which may require long-term isolation," Office of Civilian Radioactive Waste Management, DOE/RW-0184.
2. Saling, J.H., and Fentiman, A.W., 2002. *Radioactive Waste Management*, 2nd Edition, Taylor and Francis, New York.
3. Colmont, D., and Roblin, P., 2008. "Improved thermal modeling of SNF shipping cask drying process using analytical and statistical approaches," *Packaging, Transport, Storage & Security of Radioactive Material*, vol. 19, no. 3, pp. 160-164.
4. NRC, 2003. "Cladding Considerations for the Transportation and Storage of Spent Fuel," ISG-11 R3, Interim Staff Guidance Report for the Spent Fuel Project Office of the U.S. NRC.
5. Hanson, B., Alsaed, H., Stockman, C., Enos, D., Meyer, R., and Sorenson, K., 2012, "Gap Analysis to Support Extended Storage of Used Nuclear Fuel," FCRD-USED-2011-000136 Rev. 0, U.S. Department of Energy Used Fuel Disposition Campaign.
6. Daum, R.S., Majumdar, S., Liu, Y.Y., and Billone M.C., 2006. "Radial-hydride Embrittlement of High-burnup

Zircaloy-4 Fuel Cladding," *J. Nucl. Sci. Tech*., Vol. 43, No. 9, Paper 43090, pp. 1-14.
7. US. DOE, 1993. "Multi-Purpose Canister (MPC) Implementation Program Conceptual Design Phase Report," DOC ID: A20000000-00811, U.S. Department of Energy, Office of Civilian Radioactive Waste Management.
8. General Atomics (GA), 1998. "GA-4 legal weight truck from-reactor spent fuel shipping cask, safety analysis report for packaging (SARP)," San Diego, CA, USA, 92186-5608, 1998.
9. Unterzuber, R., Milnes, R.D., Marinkovich, B.A., and Kubancsek, G.M., 1982. "Spent-fuel dry-storage testing at E-MAD (March 1978 through March 1982)," prepared for the US DOE Commercial Spent Fuel Management Program Office at the Pacific Northwest Laboratory, B-D3339-A-G.
10. Bahney, R.H., and Lotz, T.L., 1996. "Spent nuclear fuel effective thermal conductivity report," DI: BBA000000-01717-5705-00010 REV 00, US DOE, Yucca Mountain Site Characterization Project Office, Las Vegas, NV, USA.
11. Manteufel, R.D., and Todreas, N.E., 1994. "Effective thermal conductivity and edge conductance model for a spent-fuel assembly," *Nuclear Technology*., 105, 421–440
12. Greiner, M., Gangadharan, K.K., and Gudipati, M., 2007. "Use of Fuel Assembly/Backfill Gas Effective Thermal Conductivity Models to Predict Basket and Fuel Cladding Temperatures within a Rail Package During Normal Transport," *Nuclear Technology*. Vol. 160, pp. 325-336.
13. Li, J., and Liu, Y.Y., 2014. "Thermal performance of vertical dry cask for storage of high-burnup used fuel", INMM 55th Annual Meeting, Atlanta, Georgia, USA.
14. Mittal, K., Han, Z.H., Li, J., Tsai, H.C., and Liu, Y.Y., 2014. "Temperatures of Interest for the TN-32 Cask during Storage of High Burnup Fuel," INMM 55th Annual Meeting, Atlanta, Georgia, USA.
15. Venigalla, V.V.R., and Greiner, M., 2009. "Use of geometrically-accurate fuel models to predict cladding and basket temperatures within a truck cask during normal transport," *Nuclear Technology*. Vol. 167, pp. 313-324.
16. Gudipati, M., and Greiner, M., 2008, "Computational fluid dynamics simulations of fuel cladding and basket surface temperatures in multipurpose canister rail cask during normal transport," *Packaging, Transport, Storage & Security of Radioactive Material*, Vol. 19, No 3, pp 173-179.
17. Bullard, T., Greiner, M., Dennis, M., Bays, S., and Weiner, R., 2010, "Thermal analysis of a proposed transport cask for three advanced burner reactor used fuel assemblies," *Packaging, Transport, Storage & Security of Radioactive Material*, Vol. 21 No. 3, pp. 158-164.
18. Araya, P.E. and Greiner, M., 2007, "Use of regular rod arrays to model heat transfer from BWR fuel assemblies inside transport casks," *Packaging, Transport, Storage and Security of Radioactive Material*, Vol. 18, pp. 171-179.
19. Gomez, P.E.A., and Greiner, M., 2006. "2D natural convection and radiation heat transfer simulations of a PWR fuel assembly within a constant temperature support structure," PVP2006-ICPVT-11- 93332', In Proceeding of the 2006 ASME Pressure Vessels and Piping Conference, Vancouver, BC, Canada.
20. Araya, P.E. and Greiner, M., 2009. "Benchmark natural convection/radiation simulations within an enclosed array of horizontal heat rods," *Nuclear Technology*, Vol. 167, No. 3, pp. 384-394.
21. Wix, S.D., and Koski, J.A., 1993. "Numerically predicting horizontally oriented spent fuel rod surface temperatures," Proc. 4th Ann. Int. Conf. on 'High Level Radioactive Waste Management', Las Vegas, NV, USA, American Society of Civil Engineers (ASCE), 1785–1789.
22. Canaan, R.E., and Klein, D.E., 1998. "A numerical investigation of natural convection heat transfer within horizontal spent-fuel assemblies," *Nuclear Technology*, 123, 193–208.
23. Chalasani, N.R., and Greiner, M., 2009. "Natural convection/radiation heat transfer simulations of an enclosed array of vertical rods," *Packaging, Transport, Storage and Security of Radioactive Material*, Vol. 20, no. 3, pp. 117-125.
24. Chalasani, N.R., Araya, P., and Greiner, M., 2009. "Benchmark of computational fluid dynamics simulations using temperatures measured within enclosed vertical and horizontal arrays of heated rods," *Nuclear Technology*., Vol. 167, No. 3, pp. 371-383.
25. Araya, P.E., Greiner, M., 2007. "Two-dimensional simulations of natural convection/radiation heat transfer for BWR assembly within isothermal enclosure," *Packaging, Transport, Storage and Security of Radioactive Material*, Vol 18, no 3, pp. 171-179
26. Manzo, E. T., Green, R., Hadj-Nacer, M., Greiner, M., Li, J., and Liu, Y. Y., 2014. "Prediction of cladding temperatures within a used nuclear fuel transfer cask filled with rarefied helium," In Proceeding of the 2014 ASME Pressure Vessels and Piping Conference, Anaheim, CA, USA.
27. Yoo, S.H., No, H.C., Kim, H. M., and Lee, E.H., 2010. "Full-scope simulation of a dry storage cask using computational fluid dynamics," Nuclear Engineering and Design, Vol. 240, pp. 4111-4122.
28. Brewster, R.A., Baglietto, E., Volpenhein, E., and Bajwa, C.S., 2012. CFD Analyses of the TN-24P PWR Spent Fuel Storage Cask. Proceeding of the ASME 2012 Pressure Vessels and Piping Conference, Toronto, ON, Canada.
29. Modest, M.F., 2003. *Radiative Heat Transfer*, 2nd Edition, Academic Press, New York.
30. Kim, H.G., Jeong, Y.H. and Kim, K.T., 2010. "The effects of creep and hydride on spent fuel integrity during interim dry storage," Nuclear Engineering and Technology, vol.42 no.3.

Proceedings of the ASME 2016 Pressure Vessels & Piping Division Conference
PVP2016
July 17-21, 2016, Vancouver, British Columbia, Canada

PVP2016-64005

EXPERIMENTALLY-BENCHMARKED COMPUTATIONAL FLUID DYNAMICS SIMULATIONS OF AN ARRAY OF HEATED RODS WITHIN A SQUARE-CROSS-SECTION HELIUM-FILLED PRESSURE VESSEL

Dilesh Maharjan
Graduate Researcher
University of Nevada, Reno
Reno, NV, USA

Mustafa Hadj-Nacer*
Research Scientist
University of Nevada, Reno
Reno, NV, USA
mhadjnacer@unr.edu

Narayana R. Chalasani**
R&D Engineer
Johns Manville
Littleton, CO

Miles Greiner
Professor of Mechanical Engineering
University of Nevada, Reno
Reno, NV, USA

ABSTRACT

An experimental apparatus was constructed, consisting of an 8x8 array of electrically-heated rods held in a square array by stainless-steel spacer plates near their ends. The rod/plate assembly was enclosed within a square-cross-section helium-filled aluminum pressure vessel and the rods were oriented vertically. The apparatus simulates the region between two consecutive spacer plates of a used nuclear fuel assembly within a vertical dry storage canister. Rod, spacer plate, and enclosure wall temperatures were measured using thermocouples in a matrix of nine experiments with total rod heat generation rates of 100, 300, and 500 W, and nominal helium pressures of 1, 2, and 3 atm.

Steady-state simulations representing the experiment were performed, which include heat generation within the rods, conduction within the solid elements, as well as buoyancy-induced motion within, and natural convection and radiation heat transfer across, helium-filled regions. These were compared to the experimental results to assess the accuracy of the computational model for a range of boundary conditions.

The comparison between the simulated and measured data showed that the simulations systematically under predict the hotter rod temperatures and over predict the cooler ones. Linear regression showed that 95% of the simulated temperatures are within 4.26°C of the correlation values.

NOMENCLATURE

2D	Two dimension
3D	Three dimension
BC	Boundary Condition
BWR	Boiling Water Reactor
ETC	Effective Thermal Conductivity
LWR	Light Water Reactor
PWR	Pressurized Water Reactor
Q	Heat generation (in Watts)
S.D.	Standard deviation
$T_{w,Avg}$	Average wall temperature (°C)
$T_{TS,Avg}$	Average temperature of top spacer plate (°C)
$T_{BS,Avg}$	Average bottom spacer plate temperature (°C)
ΔT_{sim}	Simulation minus average wall temperatures (°C)
ΔT_m	Measured minus average wall temperatures (°C)
TC	Thermocouple

* Address all correspondence to this author.
** Dr. Chalasani was Ph.D. student and postdoc at the University of Nevada Reno.

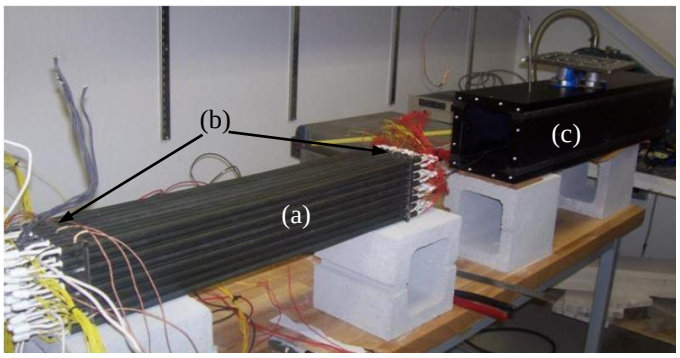

FIGURE 1 (a) HEATER ROD ARRAY WITH (b) SPACER PLATES AND (c) ENCLOSURE.

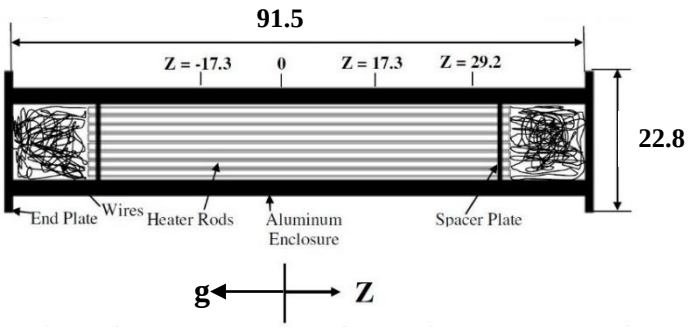

FIGURE 2 AXIAL CROSS SECTION OF THE ASSEMBLY APPARATUS

INTRODUCTION

Light water reactor (LWR) fuel assemblies consist of zircaloy cladding tubes containing stacked uranium dioxide pellets and held in square array by headers, footers and periodic spacer plates [1]. Boiling Water Reactor (BWR) assemblies consist of 7x7 to 9x9 rod array surrounded by zircaloy channel.

Used Nuclear Fuel (UNF) assemblies are highly radioactive and generate heat for long period of time. Therefore, they are placed in water pool for several years to reduce their heat generation and radioactivity [2]. After removal from water pool, fuel assemblies are placed inside cylindrical steel canister filled with non-oxidizing gas like helium to a pressure between 1 to 7 atm. The steel canister is then placed inside concrete cask. These concrete casks are transported to long-term storage sites in horizontal orientation then they are stored in vertical or horizontal orientation [3].

In all these processes, it is very important that the temperature of zircaloy cladding, which is primary confinement of used fuel pellets, does not exceed the limit of 400 °C (673 K), specified by the Nuclear Regulatory Commission (NRC) Interim Staff Guidance-11, Revision 3 (ISG-11) [4], during normal conditions. Beyond this allowable temperature limit, the zircaloy cladding forms radial hydride, which has the potential to radically reduce cladding ductility and its suitability for transport or long-term storage [5, 6]. To keep the temperature of the cladding below the limit, the package designers and operators calculate the maximum cladding temperature in the package for condition of storage and transportation. These calculations are used to determine how many fuel assemblies may be safely loaded into a cask and/or how long the fuel must be aged under water before it is transferred to long-term storage [7, 8].

The accuracy of peak cladding temperature prediction is important to determine the time required for spent fuel to be stored under water before they are transferred to long-term storage. This can play significant role in optimizing waste package design.

Current work: Experimental setup is constructed consisting of 8x8 array of heater rods within square-cross-section-aluminum-enclosure. The setup represents a section of spent BWR assembly between two consecutive spacer plates within assembly channel. The rod diameter, spacing between rods, and distance from the outermost rods to the enclosure are all 10% smaller than the dimensions inside the channel of a GE 8x8 BWR assembly [1]. The assembly is oriented vertically to simulate vertical storage conditions. Helium gas is used as backfill gas. Three pressures and three heat generation rates were employed. The temperature data from the measurements are compared to three-dimensional computational fluid dynamics (CFD) simulations that include conduction, natural convection, and radiation heat transfer within the same domain using ANSYS/FLUENT code. The objective of this work is to develop methods to quantitatively assess the accuracy of the computational method for a range of boundary conditions.

EXPERIMENTAL APPARATUS

The experimental apparatus is shown in Fig. 1. It consists of heater rods (a) arranged in 8x8 array and held by two stainless steel spacer plates (b) inside a square aluminum enclosure (c). Each heater rod is 1.1 cm in diameter and 67.3 cm long. The sheath of each heater is made of 0.7 mm thick Incoloy with compressed Magnesium Oxide (MgO) inside. The heater coil is made of Nichrome (NiCr) wire. The ends of heater coils are connected to metal pins, which are connected to external power leads. The manufacturer specified heat generation is nearly uniform along the length of the heater rods within ±6%, except for 3.2 cm sections on both ends, which are unheated. Sets of eight heater rods are connected in series. The resulting eight sets of heater rods are connected in parallel to a 0-1000W DC power generator.

Stainless steel spacer plates that are 0.635 cm thick with 64 holes of 1.15cm diameter are used to hold the heater rods in position. The center to center pitch between spacer plate holes

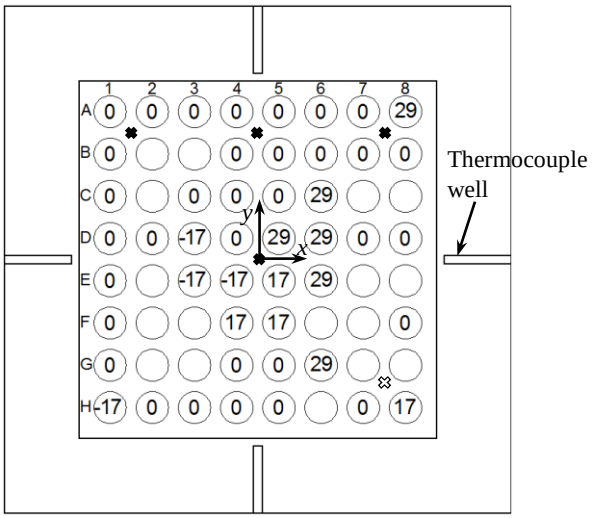

FIGURE 3 ARRAY OF HEATER RODS WITH NOMENCLATURE. NUMERICAL VALUES INDICATE AXIAL LOCATION OF TC FROM MID-PLANE (z=0, 17, and -17 cm). BLANK HEATER RODS DO NOT HAVE TC.

is 1.44 cm. To hold the heater rods in position, an expansion open ring with a bolt was used between set of four heater rods.

Because of this arrangement, the heater rods were not concentric with the holes in spacer plate. All the heater rods were pushed away from the bolt. The inner surface of spacer plate is coplanar with the plane of beginning of heater rod unheated section.

The square enclosure is constructed of four 2.54 cm thick aluminum plates by tungsten inert gas (TIG) welding. The interior dimension is 12 cm with a tolerance of 0.25 cm. The total length of enclosure is 91.4 cm. The heater rod array is placed at the axial center of enclosure, so there is 12 cm gap on each end to house power and thermocouple (TC) wires. Figure 2 shows the axial cross-section of the assembled experiment with the power and TC wires. There is a gap of 0.1 cm between spacer plate and enclosure inner wall. A square endplate with an O-Ring is bolted to each end of the enclosure. The top square endplate has two holes for TC and power feedthroughs. The bottom square endplate has a connector tube that is used to either backfill the enclosure with helium gas to the required pressure or to evacuate the gas. The connector tube is connected to a tree with an atmospheric valve, an evacuation valve, an oil filter, and a tube connected to vacuum pump. The connector tube is instrumented with low pressure and high pressure gages. The leak rate for the experimental setup was determined to be 2×10^{-10} cm^3/s using a leak detector. The direction of z-axis is shown in Fig 2 where origin is at the rod mid-plane. The gravity vector is oriented in the negative z-direction. Fiberfrax insulation blanket of 2.5 cm thickness was used to cover the experimental setup on all four walls and end plates.

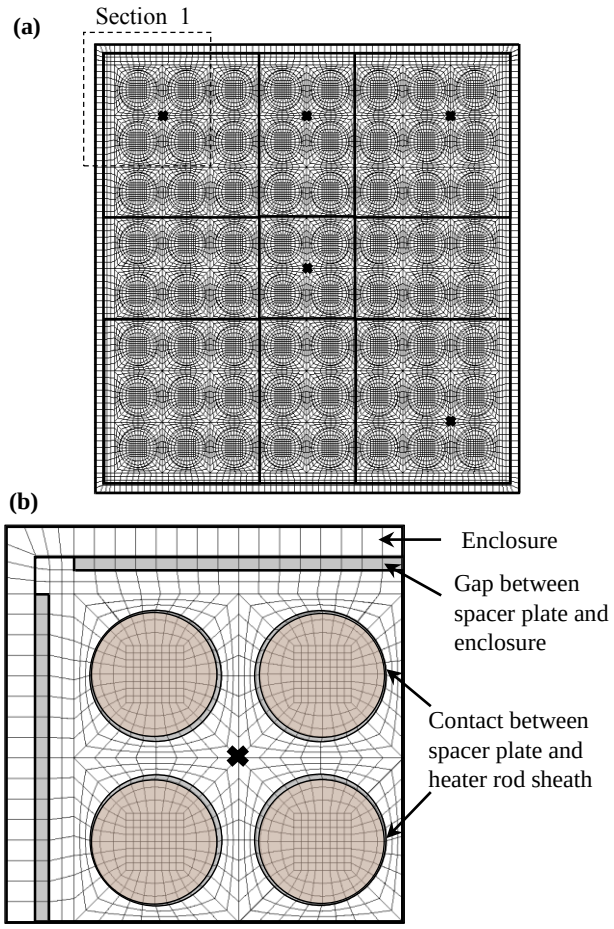

FIGURE 4 (a) END VIEW OF COMPUTATIONAL DOMAIN WITH (b) ENLARGED VIEW OF SECTION 1 SHOWING ECCENTRICITY OF THE HEATER RODS. THE SPACER PLATE IS DIVIDED INTO 9 PARTS. X'S SHOW TC LOCATION ON SPACER PLATE.

Figure 3 is a schematic of the experimental apparatus cross section. Heater rods are named according to their row (A to H) and column (1 to 8) location. The number inside each rod represents the location of TCs in *z*-axis. 33 heater rods have TC in z = 0 cm (mid-plane), 4 have TC in z =17 cm, 6 have TC in z = 29 cm, and 4 have TC in z = -17 cm plane. The ones without any number do not have TC.

The location of the TCs in the enclosure are also shown by four wells on four walls in Fig 3. The black filled X's show the location of TCs on top and bottom spacer plates, whereas open X indicates position of a TC in top spacer plate only. These TCs are located on the outer side of the spacer plates.

Due to symmetry of the geometry, boundary conditions applied (with manufacturing and thermal tolerances), and effect of gravity, we expect near symmetry across *xz*, *yz*, and diagonal planes connecting A1-H8 and H1-A8 heater rods. Hence, a one-

eighth model can represent the complete assembly. Table 1 shows the heaters with symmetric groups α, ß, δ, and γ.

The temperature data from these symmetry groups with TCs at different axial locations can be combined to produce axial temperature profiles, which can be compared with profiles from simulation. For example, group α and γ give temperatures at four different axial locations for central and corner heater rods, respectively. Group ß gives two temperatures for each location (so that consistency can be checked), whereas, group δ gives temperature at only two axial locations.

TABLE 1 GROUPS WITH SYMETRIC HEATED RODS

Group	Heater rods
α	D4, D5, E4, E5
ß	C4, C5, D3, D6, E3 E6, F4, F5
δ	C3, C6
γ	A1, A8, H1, H8

The experiments were conducted for nine different cases. Three different nominal pressure values of 1, 2, and 3 atm and three heat generation rates of 100, 300, and 500 W were applied. Roman numerals in Table 2 are used to name each experiment performed for different pressure and heat input.

TABLE 2 NINE EXPERIMENT CASES PERFORMED FOR DIFFERENT PRESSURE AND HEAT GENERATION

	Total Heat generation, Q [W]		
Pressure [atm]	**100**	**300**	**500**
1	I	IV	VII
2	II	V	VIII
3	III	VI	IX

NUMERICAL MODEL

Computational Domain

Three-dimensional computational meshes representing the experimental apparatus were generated using ANSYS Workbench 15.0. Figure 4 shows a cross-sectional view of the computational mesh model used for simulations. The model consists of 0.25 cm thick aluminum wall and 64 heater rods. The same mesh configuration in Fig 4 is extruded through the length of domain which models region between the two spacer plates within aluminum enclosure. The total number of elements in the domain is 1,834,880. Heat is generated uniformly throughout the heater rods (portion modeled as Magnesium oxide). Two end portions of heater rods equal to thickness of spacer plate are modeled as unheated.

The eccentricity of heater rod within spacer plate holes was modeled with an eccentricity of 0.2 mm. This can be seen in the enlarged view of section 1 in Fig. 4 (b). Four heater rods are pushed away from central expansion ring and are in contact with the spacer plate. The contact region was modeled as 45° arc from center of heater rod. The gaps between spacer plate and heater rod/enclosure are shown as grey portion. To assess the effect of the eccentricity of the heater rods, a computational model with concentric heater rods in spacer plate holes was constructed. Hence, there is uniform gap of 0.25 mm between heater rods and spacer plate.

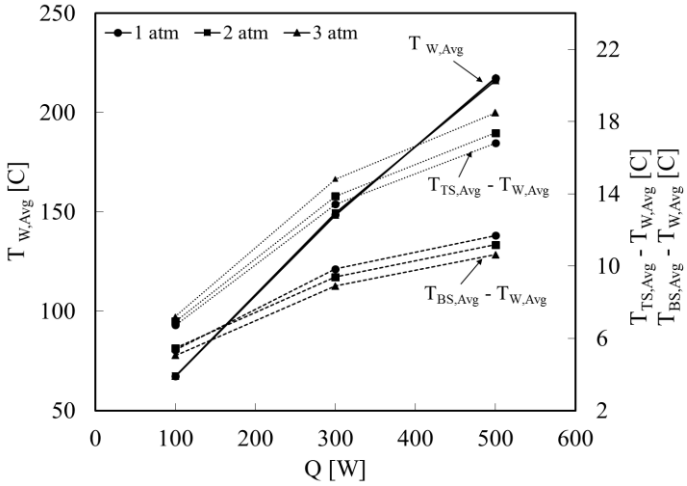

FIGURE 5 AVERAGE WALL TEMPERATURE AND AVERAGE SPACER PLATE TEMPERATURES FOR ALL 9 CASES

Conduction, natural convection, and radiation heat transfer within the domain were simulated using ANSYS/FLUENT commercial CFD package. The steady-state energy equation was solved using a pressure-based solver where the pressure velocity coupling was achieved using the SIMPLE scheme and discretization was done by second order upwind scheme [9].

The discrete ordinate model was used to account for radiation heat transfer. For natural convection, buoyancy induced flow was generated using gravitational acceleration (9.81 m/s^2) in negative *z*-direction. Temperature-based density was applied to helium for the steady-state pressure value measured from experiment for each case.

To check the sensitivity of the mesh, two other finer meshes were constructed. The number of elements in the two meshes were 2,111,992 and 4,730,080. The maximum temperature was used as a tool to check for sensitivity. For two extreme cases (Cases I and IX, see Table 2), the maximum temperature difference between the three meshes were found to be less than 0.3 °C. Hence, the coarse mesh shown in Fig. 4 was selected for all simulations.

Boundary conditions (BC)

All experiments were performed in ambient temperature of roughly 23°C. Initially, all the thermocouples indicated the same temperature. After the power was turned on, it took roughly 25 hours for the temperature to reach steady-state condition. The data acquisition was carried out for 3 hours after

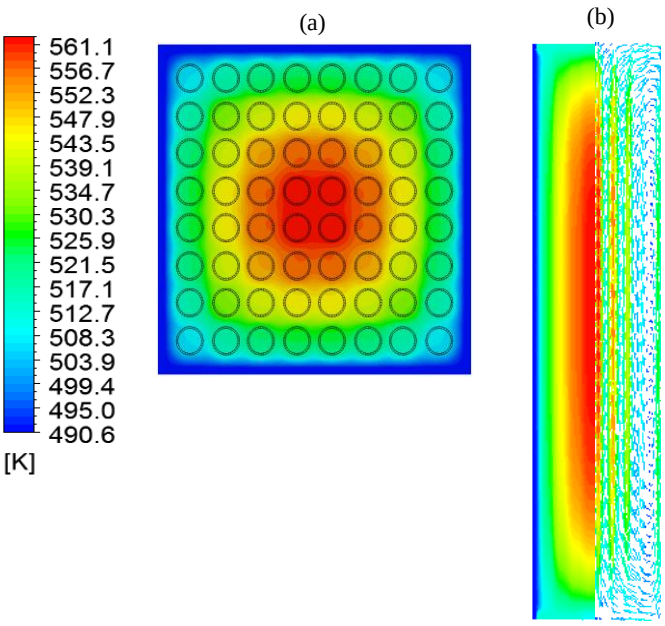

FIGURE 6 TEMPERATURE PROFILE AT MID PLANE (z = 0 cm) (a) AND TEMPERATURE AND VELOCITY PROFILE ALONG VERTICAL (x=0 cm) PLANE (b) FOR CASE IX.

steady state was reached. The temperature values were time-averaged for those 3 hours.

Figure 5 shows average enclosure wall temperature and average top and bottom spacer plate temperatures minus average wall temperature for all cases as a function of heat generation. The largest difference between maximum and minimum values of measured wall temperature was 11.9 °C for case IX. The average wall temperature increases with heat generation rate but is relatively insensitive to gas pressure. The average temperature of the top spacer plate is always higher than the average temperature of the bottom. For each spacer plate, the average temperature increases with heat generation. The difference between average temperature of top and bottom spacer plate was 1.4°C for case I and 7.8°C for case IX. For a given heat generation, the average top spacer plate temperatures increases with pressure, whereas, the average bottom spacer plate temperature decreases with increasing pressure. This is due to the effect of natural convection as pressure increases.

The measured temperatures of the enclosure walls and spacer plates are used as boundary conditions for the CFD simulations. The average value of all measured wall temperatures was applied uniformly on all four aluminum walls as BC. The spacer plates are divided into 9 sections as shown in Fig. 3a with one center section, four side sections, and four corner sections. Uniform temperatures were applied to each of the nine sections. For the center and side sections, uniform temperature measured from the center and side TC were applied respectively. For corner sections, the average of three corner TCs was used. For holes in spacer plates (which contains heater

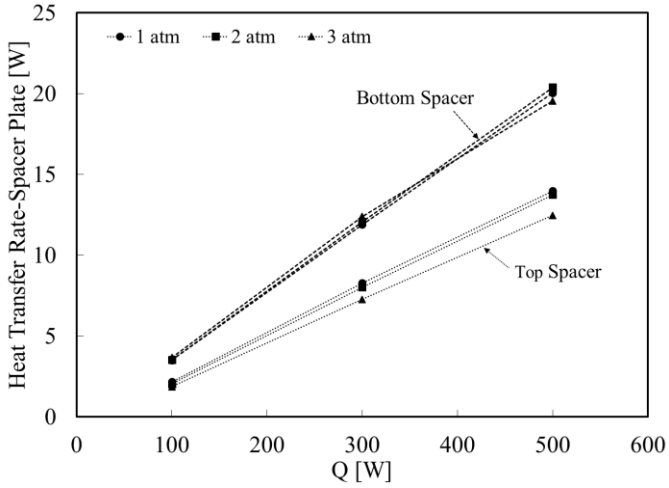

FIGURE 7 HEAT TRANSFER RATE FROM SPACER PLATES FOR ALL CASES.

rods and air gaps) at each end, insulated condition was used. Emissivity values of the aluminum enclosure, incoloy sheath, and stainless steel were initially measured to be 0.75, 0.88, and 0.6, respectively. However because of use of an oil-based vacuum pump, it was observed that all the surfaces were coated with a thin layer of oil. The emissivity of all surfaces inside the enclosure were therefore assigned the value of 1.

RESULTS

Using temperature boundary conditions from the experimental results, CFD simulations were performed for all nine cases. Figure 6 shows the temperature contour and velocity vector field for vertical (x=0 plane) and horizontal (z=0) mid-planes for Case IX. Figure 6a shows that the maximum

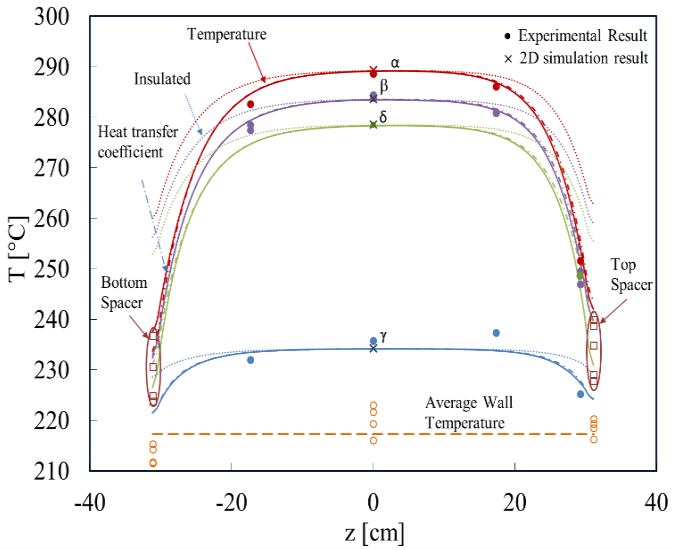

FIGURE 8 COMPARISON OF SIMULATED RESULTS FROM DIFFERENT BOUNDARY CONDITIONS AT SPACER PLATE WITH EXPERIMENTAL RESULTS FOR CASE VII.

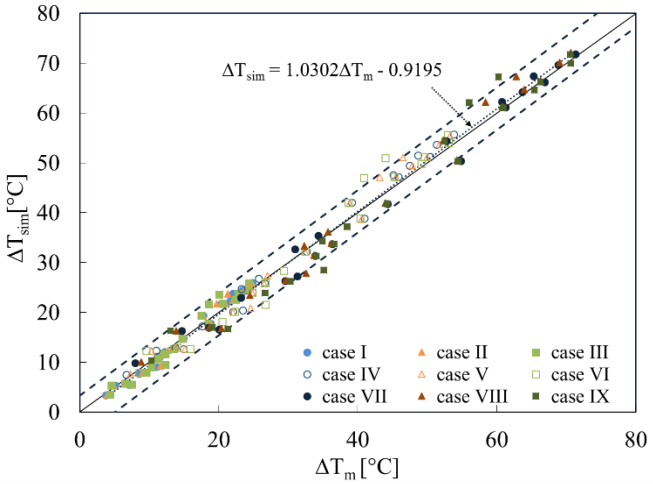

FIGURE 9 SIMULATED VS MEASURED TEMPERATURE COMPARISON FOR ALL CASES

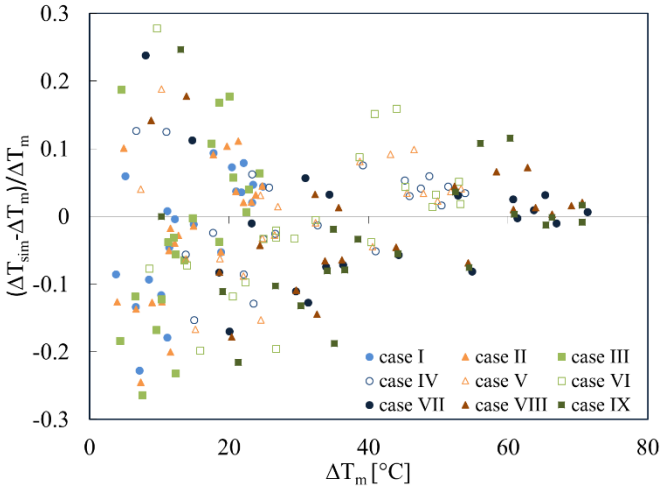

FIGURE 10 PERCENTAGE DEVIATION OF THE SIMULATED TEMPERATURE VALUES FROM THE MEASURED ONES AS FUNCTION OF THE MEASURED TEMPERATURE.

temperature is located within the centermost rods. The velocity vectors along the longitudinal plane (Fig. 6b) indicate the presence of buoyancy induced motion. The vector are upward in the center (hotter region) and downward at the wall (cooler region), which causes the maximum temperature to be at z = 4.4 cm (above the axial center).

From the simulation results, heat losses from the outer surface of the top and bottom spacer plates were computed. Figure 7 shows the heat loss rate for all nine cases. These losses increase with rod heat generation. Bottom spacer plates have a larger heat loss than top spacer plates. The effect of pressure on heat loss is small at low heat generation whereas at higher heat generation, there is a moderate effect. For bottom spacer plate, the effect of pressure on heat loss is not significant. However, for top plate, heat loss decreased with increase in pressure. This indicates small buoyancy effect at high heat generation and pressure. Overall, the heat losses from the spacer plates are less than 7% of total heat generation for all cases.

The square and circular symbols in Fig 8 shows the measured temperatures within the enclosure spacer plates and heater rods for case VII. The wall temperature at three axial locations are plotted as open circles. The dashed horizontal line shows the average wall temperature which is applied uniformly to the walls to simulate this experiment. Open squares show the measured spacer plate temperatures used as boundary condition for this simulation. The filled circles represent temperature of heater rods measured at different axial location.

The lines in Fig 8 represent axial temperature profiles of the four symmetry groups (see Table 1). The temperature profiles close to the center of the heaters are fairly constant, whereas there are steep variation close to the ends. The results show very good agreement between the measured and simulated temperatures at planes z = 0 and 17 cm, except for group γ, where the measured temperature at z= 17 cm is larger. At planes z = -17 and 29 cm, the measured temperatures are lower, except for group δ where the measured temperature is very close to the simulated ones.

Figure 8 also shows that, for group γ, there is a large variation between measured temperatures at z = 17 cm and -17 cm. however, the simulation results show almost the same temperatures. This deviation could be due to the use of average temperature on the walls. The measured wall temperatures at the bottom plane are cooler than central and upper ones.

The symbols in Figure 9 shows the comparison between measured minus average wall temperature and simulated rod temperatures minus average wall temperatures. The solid line indicates equality of measured and simulated temperatures (ΔT_{sim}-ΔT_m). The markers for all 9 cases are distributed closely to the equality line indicating simulated temperatures are close to measured ones. Linear regression gives the dotted line marked ΔT_{sim}=1.0302ΔT_m - 0.9195. For best result, the desired value of slope and intercept of regression line is 1 and 0 respectively. This regression line indicates that simulations over-predict higher temperatures, whereas they slightly under-predict lower temperatures. The standard error of estimate was calculated to be 2.13 °C. Thus, 95% of the simulated temperature fall within 4.26°C of the linear regression line. The two dashed line indicate 4.26°C deviation from regression line.

Figure 10 shows a closer comparison of the simulated and experimental results by comparing the difference between measured and simulated divided by the measured results versus the measured results. The percentage difference between the measured and simulated temperature is of the order of 30% at low temperature region (ΔT_m < 20°C), even though the actual temperature difference is less than 3°C. For the high temperature region, the percentage difference decreased to

10%, however actual temperature differences are as high as 7°C.

The effect of the spacer plate boundary conditions used in the simulations is evaluated in Fig 8. It is difficult to predict appropriate BCs for the spacer plates due to the presence of a large number of power and TC wires. To see the effect of different types of BCs at the outer surface of spacer plate, insulated, average temperature, and convective heat transfer BCs were applied. For insulated conditions, zero heat flux is applied on all the nine sections of the spacer plates (Fig. 3). This condition is very conservative because it suggests that all heat generated by the heaters leaves through the transverse direction. For average temperature condition, area-weighted average of the nine sections of each spacer plate is applied. For convective heat transfer condition, heat transfer coefficient for each plate was calculated from heat losses values shown in Fig. 6 and temperature difference between the spacer plate and enclosure.

The comparison between simulations using the different boundary conditions is shown in Fig. 8 along with the temperature BC results at the spacer plates. The dotted and dashed-dotted lines indicate results for insulated and convective heat transfer BCs, respectively. The convective heat transfer coefficient condition results were very close to temperature condition, with very small difference close to the heater ends. The area-weighted average temperature condition results were also close to temperature condition. Hence, it is not shown in the figure. The insulated condition resulted higher temperatures at the heater ends, which is expected. For all BCs, the temperatures of the heaters at mid-plane (z=0) are roughly same. This suggests that the spacer plate BC has a negligible effect on the maximum temperatures of the rods. To verify this result, a 2D model was generated so that no BCs are required at the spacer plates. The results were plotted in the same figure indicated by "x" symbols. The temperatures from the 2D results match very closely the 3D maximum temperature results, which confirms the conclusion drawn above. It should be noted here that this result was obtained because of the use of helium gas, which induces small buoyancy effect. If another gas with higher density (example: nitrogen) is used, the 2D simulation may not accurately predict the maximum temperature because it does not take into account the buoyancy effect.

Table 3 gives the slope and intercept values of linear regression lines and standard deviation value for 95% confidence level calculated for the different boundary conditions. The result for insulated BC is not presented as the deviation is obviously large. The results from temperature BC and convective heat transfer BC simulation are close. However, average temperature BC simulation results have higher deviation in slope and intercept values.

The numerical model used for all above simulations assumes that the heaters are eccentric to the spacer plates holes (see Fig. 3b) and that there is a 45° arc contact between them. Simulations were conducted for concentric heater rods and spacer plate using temperature BC at spacer plate for all cases. The summary of the results are shown in Table 3.

TABLE 3 SLOPE AND INTERCEPT VALUES OF REGRESSION LINES AND STANDARD DEVIATION VALUES FOR 95% CONFIDENCE LEVEL FOR ALL BOUNDARY CONDITIONS.

Boundary Condition	**Slope**	**Intercept**	**2 S.D.**
Temperature BC	1.030	-0.919	4.26
Convective heat transfer	1.024	- 0.394	4.37
Area weighted average temperature	1.126	-1.688	6.19
Model	**Slope**	**Intercept**	**2 S.D.**
Concentric heater rod model (Temperature BC)	1.027	-0.767	4.15

The effect of eccentricity of heater rod with respect to spacer plate holes is not significant. The slope, intercept and standard deviation from the concentric model are very close to results from eccentric model with same temperature boundary condition.

CONCLUSION

Experiments were performed with 8x8 heated rods inside an aluminum enclosure in vertical orientation with helium as backfill gas for nine different conditions. This setup represents a region inside the channel of a boiling water reactor fuel assembly between two consecutive spacer plates during vertical storage condition. Computational fluid dynamics simulations with radiation heat transfer were conducted for all cases with different models and boundary condition at spacer plate ends. The results show small temperature gradient in central region and high gradient closer to the walls. Heat loss from spacer plates increased with increase in heat generation and changed very little with change in pressure. Linear regression for cases with temperature boundary condition show that the simulation slightly under-predicts the lower temperatures and slightly over-predicts higher temperature values. 95% of simulated data are within 4.26°C of measured values. The effect of eccentricity of heater rods was found to be negligible. The use of other boundary conditions on the spacer plates changed the temperature values at other axial locations but the temperature values in mid-plane remained same. So to predict the highest temperature in a setup without significant buoyancy effect, the 2D model can be used to good accuracy.

The results from this study will be used to design an experiment and CFD simulations to predict temperature of cladding during vacuum drying process.

ACKNOWLEDGEMENT

This work was supported by the US Department of Energy Office of Nuclear Energy University Program.

REFERENCE

[1] Dept. of Energy, Office of Civilian Radioactive Waste Management (OCRWM), U.S., 1987, "Characteristics of Spent Nuclear Fuel, High-Level Waste, and Other Radioactive Wastes which may Require Long-Term Isolation."

[2] Saling, J. H., and Fentiman, A. W., 2002, Radioactive Waste Management, Taylor and Francis, New York.

[3] Rigby, D. B., 2010, " Evaluation of the Technical Basis for Extended Dry Storage and Transportation of Used Nuclear Fuel". United States Nuclear Waste Technical Review Board.

[4] NRC, 2003, "Cladding Considerations for the Transportation and Storage of Spent Fuel," ISG-11 R3, Interim Staff Guidance Report for the Spent Fuel Project Office of the U.S. NRC.

[5] Hanson, B., Alsaed, H., Stockman, C., Enos, D., Meyer, R., and Sorenson, K., 2012, "Gap Analysis to Support Extended Storage of Used Nuclear Fuel," FCRD-USED-2011-000136 Rev. 0, U.S. Department of Energy Used Fuel Disposition Campaign.

[6] Daum, R.S., Majumdar, S., Liu, Y.Y., and Billone M.C., 2006, "Radial-hydride Embrittlement of High-burnup Zircaloy-4 Fuel Cladding," J. Nucl. Sci. Tech., Vol. 43, No. 9, Paper 43090, pp. 1–14.

[7] Holtec International, 2000, "Topical Report on the HI-STAR/HI-STORM Thermal Model and its Benchmarking with Full-Scale Cask Test Data," Holtec Report No. HI-992252.

[8] Pacific Northwest Laboratory, et al., 1987, "The TN-24P PWR Spent Fuel Storage Cask: Testing and Analyses," EPRI NP-5128.

[9] Inc., A., 2015, "ANSYS Fluent User's Guide," www.ansys.com.

EFFECT OF RAREFICATION ON CLADDING TEMPERATURES WITHIN A USED NUCLEAR FUEL CANISTER FILLED WITH DRY HELIUM

Corey Trujillo, Mustafa Hadj-Nacer*, and Miles Greiner
University of Nevada, Reno 1664 N Virginia Street, Reno, NV 89557
**mhadjnacer@unr.edu*

In this paper, the effect of rarefaction on the fuel cladding temperature is investigated. To do this, we apply a temperature-jump thermal-resistance to ANSYS/Fluent CFD simulations of a vacuum drying operation in geometrically-accurate two and three-dimensional models of a loaded nuclear fuel canister. The numerical model represents a vertical canister and basket loaded with 24 Westinghouse 15 × 15 PWR fuel assemblies. The model includes distinct regions for the fuel pellets, cladding and gas regions within each basket opening. Symmetry boundary conditions are employed so that only one-eighth of the package cross section is included. The canister is assumed to be filled with helium. A uniform temperature of 101.7°C is employed on the canister outer surfaces to conservatively model canister surrounded with boiling water.

Steady-state simulations are performed for different fuel heat generation rates and helium pressures, ranging from atmospheric pressure to 100 Pa. These simulations include conduction within solid and gas regions, and surface-to-surface radiation across all gas regions. Constant thermal accommodation coefficients, which characterize the effect of the temperature-jump thermal-resistance at the gas-surface interface are employed. The peak cladding temperature and its radial and axial locations are reported. The maximum allowable heat generation that brings the cladding temperatures to the normal radial hydride formation limit (T_{RH} = 400°C) is also reported. The results of the three-dimensional model simulations are compared to two-dimensional model simulations for the same heat generation rate and pressures.

The results show that the rarefaction condition causes the temperature of the rods to significantly increase compared to the continuum condition (atmospheric pressure). This causes the maximum allowable heat generation for rarefied condition to decrease. The three-dimensional model predicts temperature that are ~15 to 35°C lower than the two-dimensional model.

I. INTRODUCTION

After a period of time in a nuclear reactor, used nuclear fuel (UNF) assemblies are stored underwater (wet storage), in a cooling pool, for several years [1]. The water of the pool shields the radiation produced by the nuclear fuel assemblies while keeping them at a safe temperature. The UNF assemblies are then transitioned into dry storage. A dry storage canister is placed at the bottom of the cooling pool and assemblies are transferred into the canister one at a time. The transfer operation happens under the protective water of the pool to shield the workers from radiation exposure. After the canister has been filled with assemblies, it is sealed, lifted to the surface, drained and then dried [2]. Following drying, the canister is backfilled with non-oxidizing gas, such as helium or nitrogen. The final lid is then installed and the loaded canister is moved to dry storage facility [3].

The canister must be dried to avoid two complications [4]. The first is corrosion – materials inside the canister can corrode if any water is left in the canister. Second, in the radiation and heat environment of the canister, any additional water can dissociate into hydrogen and oxygen, and when the correct ratio forms, the gas mixture can explode.

One of the methods currently used to dry canisters before placing them in long-term storage is vacuum drying, which consists of reducing the pressure in the canister, to pressures as low as 70 Pa, to promote evaporation of the remaining water in the canister [2, 4]. The process continues until the canister can hold a pressure of less than 400 Pa for at least 30 minutes as specified by the Nuclear Regulatory Commission (NRC) Interim Staff Guidance-11, Revision 3 (ISG-11) [4].

Because of the low pressures associated with vacuum drying, there is a temperature difference (temperature-jump) between the solid surfaces and gas in contact with them. This temperature jump acts as thermal-resistance for heat conduction. It causes a significant increase in the temperature of the fuel rods compared to the continuum condition (atmospheric pressure). Vacuum drying is the process in which the fuel cladding may reach its highest temperature, because it is the first operation in which the fuel assemblies are removed from water and placed in a gas environment while their heat generation is still relatively high [4]. It is important to keep the temperature of the fuel cladding bellow the limit of 400°C, as suggested by NRC for normal conditions [4] to avoid the formation of radial hydrides and high gas pressures within the tubes, which may cause them to be brittle [5-8].

Currently, package vendors predict cladding temperatures and the resulting hoop stresses during drying operations using experimentally-benchmarked whole-package CFD simulations [9-12]. In these models, the fuel

and basket are replaced by a region with an effective thermal conductivity and porosity, which is calculated without regard to the rarefied-gas temperature-jump thermal resistance. The fuel heat generation used in the tests to validate the current methods was moderately low.

In this paper, a geometrically-accurate two- and three-dimensional models of a canister is modeled. This model represents a canister loaded with 24 Westinghouse PWR used fuel assemblies. It accurately represents 15×15 arrays of fuel rods, helium gas within each basket opening, and a helium-filled gap between the basket and canister surfaces. Steady-state simulations are performed for a range of fuel heat generation rates and pressures with an isothermal canister outer surface temperature of 101.7°C. Radiation heat transfer within the gas-filled regions and conduction in the solid and gas regions are modeled using the ANSYS/Fluent Computational Fluid Dynamics (CFD) package. A comparison to the 2D model simulations is also presented. The peak cladding temperatures and the maximum allowable heat generation that brings the cladding temperature to the limit of 400°C [4] are reported.

II. RAREFIED GAS HEAT TRANSFER AND TEMPERATURE JUMP

As mentioned earlier, during vacuum drying, the pressure in the canister is lowered to as low as 70 Pa. This causes a temperature-jump thermal-resistance at the interfaces between solid surfaces and gas interacting with them. As the pressure decreases, this temperature-jump becomes more significant and contributes to the increase of the cladding temperatures. However, at relatively high pressure, the effect of temperature-jump is insignificant. The Knudsen number,

$$Kn = \frac{\lambda}{L_C} \tag{1}$$

is defined as the ratio of the mean free path of the gas λ and a characteristic length of the system L_C. The Knudsen number is used to characterize the rarefaction level of a gas. Using this parameter, four regimes of rarefaction may be distinguished. (i) In the continuum regime ($Kn \leq 10^{-3}$), the flow and heat transfer can be accurately modeled using the classical Navier-Stokes and Convective Energy equations. (ii) In the slip regime ($10^{-3} \leq Kn \leq 10^{-1}$), the Navier-Stokes and Convective Energy equations are still appropriate but they should be subjected to the conditions of velocity-slip and temperature-jump at the wall. (iii) In the transitional regime ($10^{-1} < Kn < 10$), the flow needs to be modeled using the collisional Boltzmann equation [28]. (iv) In the free molecular regime ($10 \leq Kn$), the gas is highly rarefied and the flow is modeled using the collisionless kinetic Boltzmann equation [28].

The expression for the mean free path λ is given by

$$\lambda = \frac{\mu}{P}\sqrt{\frac{2k_{BT}}{m}} \tag{2}$$

where μ is the gas viscosity, P is the pressure, k_B is the Boltzmann constant, and m is the gas molecule mass. Considering the smallest dimension of the canister (i.e. 2.29 mm, see Sec III) as a characteristic length, the gas in the canister is in the regimes from continuum ($Kn = 1.17\times10^{-4}$) to the limit of slip ($Kn = 0.17$), for pressure varying from atmospheric to 70 Pa, respectively.

As described in Ref [13], the temperature-jump thermal-resistance at the interface between gas and solid in the slip regime is given by

$$T_g - T_w = R_{TJ}Q \tag{3}$$

where T_g is the temperature of the gas, T_w is the temperature of the wall, and Q is the conduction portion of heat flux. R_{TJ} is the temperature-jump thermal-resistance defined as

$$R_{TJ} = \frac{\lambda\zeta_T}{A\kappa} \tag{4}$$

where ζ_T represents the temperature-jump coefficient, A represents the area of the surface under consideration, and κ represents the gas thermal conductivity. Using the Lin and Willis model [14], the temperature-jump coefficient ζ_T can be written as

$$\zeta_T = \left(\frac{2-\alpha}{\alpha} + 0.17\right)\frac{\gamma\sqrt{\pi}}{(\gamma+1)Pr} \tag{5}$$

where γ is the specific ratio (5/3 for helium) and Pr is the Prandtl Number (2/3 for helium). It was shown in Ref [15-17], that the Lin and Willis temperature jump model accurately predicts the temperature jump at the interface gas/solid in the slip regime.

In this equation, α is the thermal accommodation coefficient (TAC) that characterizes how the molecules of gas interact with the walls, which is defined as

$$\alpha = \frac{T_i - T_r}{T_i - T_w} \tag{6}$$

where T_i is the incident temperature of a molecule, T_r is the reflected temperature of a molecule, and T_w is the temperature of the wall [29]. The TAC is affected by the material, roughness, cleanliness, and overall surface conditions of the wall as well as the properties of the gas itself [20]. The value of α ranges from 0 to 1. As the value of α decreases, there is a larger temperature-jump at the solid-gas interface. Values of α are reported in the literature [15, 18-19]. For helium gas and stainless steel surface, this value was reported between 0.4 and 0.2, for temperature ranging from 25 and 427°C [18]. For helium and zircaloy, a value of α = 0.34 was reported for temperature of 25°C [19].

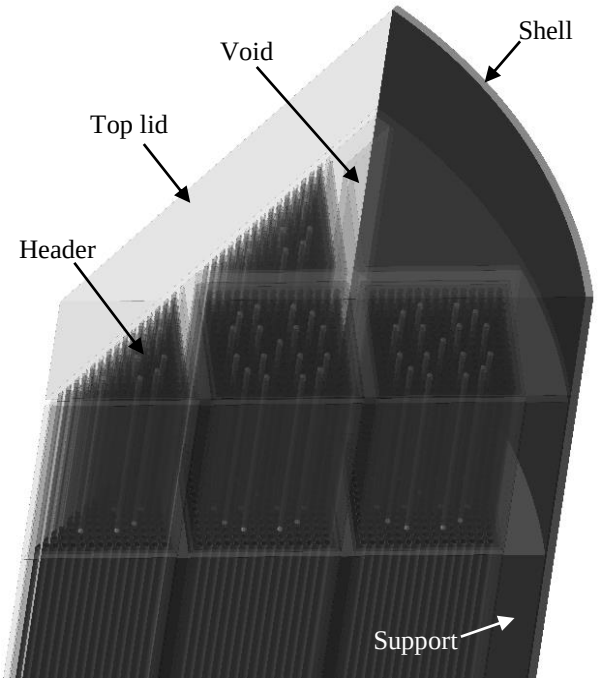

Figure 1: 3D view of the top portion of the one-eighth canister computational model constructed with ANSYS.

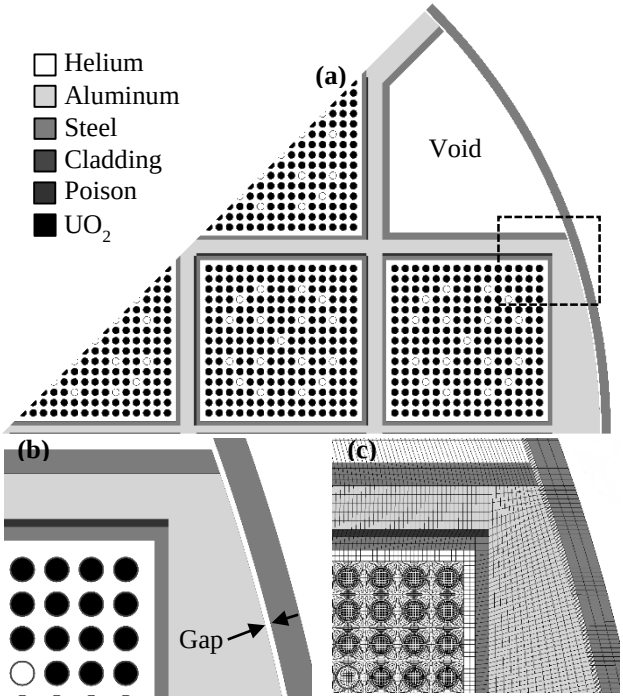

Figure 2: Regional materials and mesh details of computational domain. (a) Grey scale coded material list for the model. (b) Detailed region of the fuel rod array in the stainless steel basket and the 2.29 mm annular gap that surrounds the entire canister. (c) Detailed view of the mesh.

In this paper, three constant values of α = 1, 0.4, and 0.2 are employed. The temperature dependency of α is also implemented.

III. CANISTER NUMERICAL MODEL AND BOUNDARY CONDITIONS

Figure 1 shows a 3D view of the top portion of the computational model of the nuclear fuel canister created in ANSYS FLUENT. The model represents a canister and basket loaded with 24 Westinghouse 15×15 PWR assemblies. This model is relevant to the TN24 Transnuclear storage canister [27]. Figure 1 shows some of the canister's components that include the stainless steel top lid and outer shell, aluminum support, and top nozzle. The nozzles are modeled as unheated extension of the fuel rods and the gaps between the rods are kept as gas regions. There is a gap between the unheated fuel rods sections and the top cover plate and bottom cover plate of 16.51 mm and 88.09 mm, respectively. Both the top and bottom lids are represented with a single solid piece. In Fig. 1, the region marked by "void" is an open space that crosses the entire length of the canister. This region is also showed in Fig. 2a. For simplicity, no spacer disks or spacer grids are considered in this model.

Figure 2a shows a material-coded cross-section view of the 2D computational-domain of the canister. The 3D model is an extrusion of the 2D model into the third dimension. Each fuel rod consists of d = 9.58-mm-diameter UO2 pellets surrounded by 0.67-mm thick zircaloy cladding. There are also thirteen hollow zircaloy instrument tubes that have the same diameter as the fuel rods. The center-to-center pitch between the rods is 14.43 mm. The square fuel rod assembly is centered inside a stainless steel basket. The stainless steel basket rests inside the aluminum supports along with the neutron poison; thermal properties for BORAL® were used for the neutron poison. The neutron poison is placed in selected spots inside the aluminum support geometry. In Fig. 2b, a detailed view of the fuel rod array is shown with the gap between the aluminum support and the stainless-steel-enclosure which is gas-filled and represents the smallest dimension in the canister with size of 2.29 mm.

The canister outer diameter is 1.70 m and its length is 4.80 m. The heated section of the fuel rods represents 76% of the canister total length. Figure 2c shows a detailed view of the mesh. The total number of finite element mesh cells in the 3D one-eighth model is ~54 million.

Steady state simulations were performed using ANSYS/Fluent 17 for different heat loads. These simulations assume a varying heat generation along the axial direction of all UO_2 pellet regions, conduction within solid and gas regions, and surface-to-surface radiation across all gas regions with surface emissivities of 0.46 for stainless steel and 0.80 for aluminum and zircaloy [21]. The simulations do not include buoyancy-induced gas

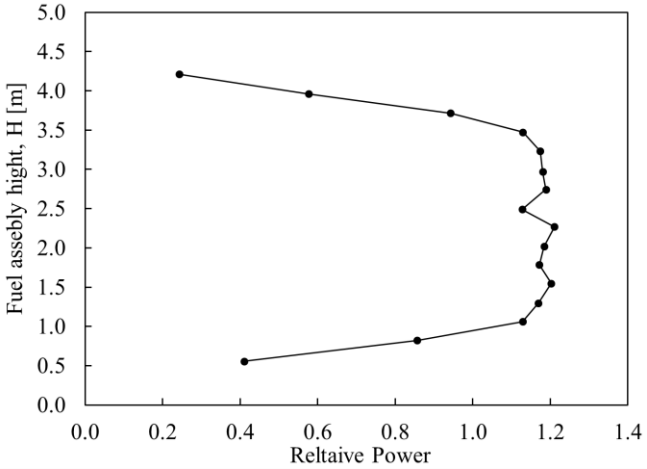

Figure 3: Heat generation profile in the axial direction [24]

motion or natural convection in the backfilled regions because they are negligible at the pressures considered in this work. Helium is considered to be the working gas and an isothermal condition is employed on the canister outer surface with T_C=101.7°C. This condition of temperature assumes that the canister is immersed in boiling water, which allows to conservatively predict the canister temperature [22].

In order to investigate the effects of gas rarefaction on the fuel's peak cladding temperature, simulations with atmospheric pressure, low pressure (100 Pa) and hard vacuum conditions are conducted. For low pressure (rarefied) conditions, three constant values of the thermal accommodation coefficients are considered: α = 1, 0.4, and 0.2.

Even though the NRC ISG 11 R3 report [4] suggests a low pressure of 400 Pa as criteria for canister dryness during vacuum drying, a pressure of 100 Pa is considered for simulations in this paper. This is motivated from the pressures used in industry for vacuum drying operations [4, 23], which are as low as 67 Pa.

The heat generated within each fuel assembly and each fuel rod was assumed to be the same. A non-uniform heat generation rates along the axial length of the fuel assemblies were considered. According to Creer et al [24], heat generated at the ends of the assemblies is significantly lower than in the middle. Figure 3 shows the axial profile of heat load applied to the assemblies [24]. A volumetric heat source was applied to each cell of the fuel pellets to simulate the axial distribution as shown in Fig. 3.

IV. RESULTS AND DISCUSSION

IV.A. Three-Dimensional (3D) Simulations

In this section, simulation results for the 3D canister model are presented for different conditions:

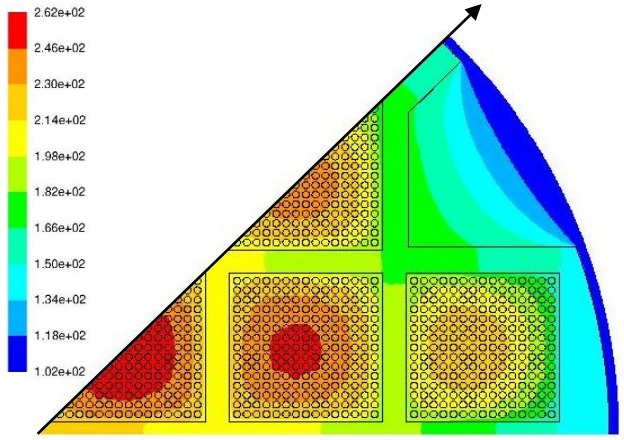

Figure 4: Loaded canister temperature contours for helium at $P \sim 10^5$ Pa and Q_F = 1498 W/assembly.

(i) Continuum ($P \sim 10^5$ Pa), with no temperature-jump boundary condition ($Tg=T_w$);
(ii) Rarefied (P = 100 Pa). For this condition, a temperature-jump boundary condition (3) at the gas-solid interface is taken into account for values of α = 1, 0.4, and 0.2;
(iii) Hard Vacuum (P = 0 Pa). For this condition, only radiation heat transfer across the gas regions and conduction through the solids are activated. Conduction through the gas regions was eliminated using a very low thermal conductivity for helium of 10^{-8} W/mK.

Additionally, an axially varying fuel assembly heat generation of Q_F=1498 W/assembly is used as the base value for all the 3D simulations. This heat load is comparatively higher than those used in the actual fuel canisters. However, average values for PWR fuel assembly heat generation used by industry were reported as high as 1417 W/assembly [23]. The heat load distribution in the canister is not uniform, so single heat assemblies may have higher values than 1417 W/assembly.

Figure 4 shows the cross-sectional temperature contour, where the peak cladding temperature is obtained, for the continuum condition and for fuel assembly heat generation rate, Q_F=1498 W/assembly. There are maximum temperatures within each fuel assembly, but the global maximum is located near the center of the innermost fuel assembly. The temperature contours for rarefied and hard vacuum conditions with the same heat generation rate are very similar to that shown in Fig. 4, but with different scale.

Figure 5 shows the temperature profile along the r-axis shown in Fig. 4 for the continuum, rarefied and hard vacuum conditions. The profiles of temperature are very similar for all conditions, however, the temperatures obtained for the hard vacuum condition are much higher than other conditions. This is because conduction heat

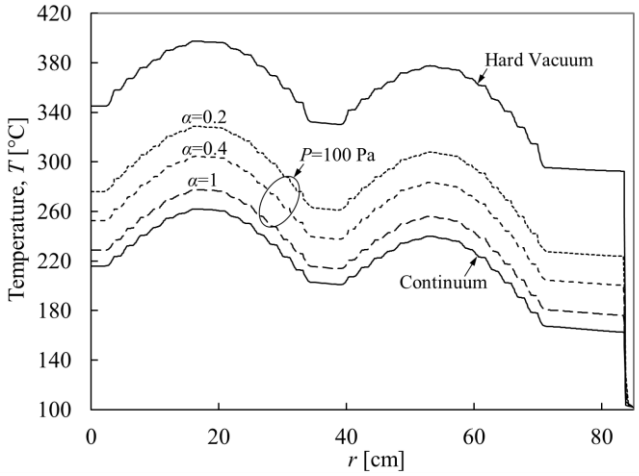

Figure 5: Radial profile of temperature along the *r*-axis shown in Fig. 4 for Q_F=1498 W/assembly. Results are shown for the continuum condition, rarefied condition (P = 100 Pa) with α = 1, 0.4, and 0.2, and the hard vacuum condition.

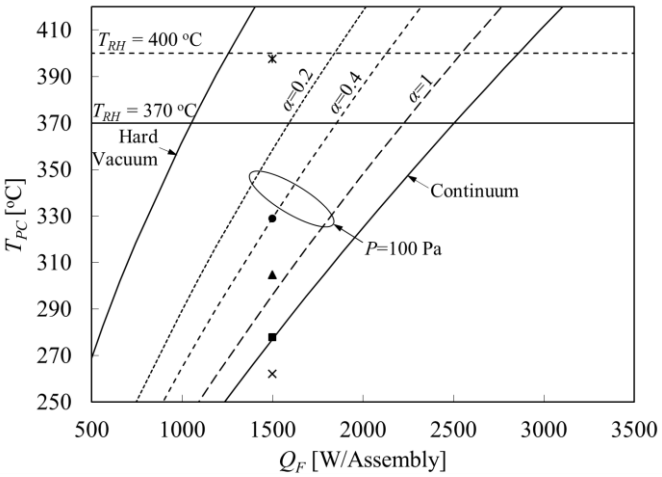

Figure 6: Peak cladding temperature versus assembly heat generation rate. Solid and dashed lines are for 2D results as marked. Symbols are for 3D results: Cross (×) for continuum condition; Square (■), triangle (▲), and circle (●) are for rarefied conditions with α = 1, 0.4, and 0.2, respectively; Star (*) for hard vacuum condition.

transfer through the void regions is eliminated. Moreover, the rarefied condition temperatures are larger than the continuum condition. The low pressure used for the rarefied condition induces a temperature-jump at the wall, which increases the temperature of the fuel assemblies depending on the thermal accommodation coefficient α value. As the value of α decreases, there is a larger temperature-jump, and therefore higher assembly temperatures.

Table 1: Increase in peak cladding and basket-end temperatures of the rarefied and hard vacuum models compared to the continuum model for Q=1498W/assembly

	Rarefied, P=100 Pa			Hard Vacuum
	α=1	α=0.4	α=0.2	
ΔT_{PC} [°C]	16	43	67	136
ΔT_{BC} [°C]	14	38	61	130
$\frac{\Delta T_{PC} - \Delta T_{BC}}{\Delta T_{BC}}$	15%	12%	9%	4%

It can be also observed from Fig. 5 that the temperature within the fuel rods is relatively uniform, however, there is a steep gradient across the gas regions. The steepest gradient is observed in the smallest gap of the canister, between the aluminum support and the stainless-steel-enclosure, at the periphery of the canister (r = 83.5 cm). This gap induces a very large temperature gradient. This is because of the low thermal conductivity of helium compared to stainless steel and aluminum, and the accumulation of heat generated by the fuel assemblies in this gap.

Table 1 gives peak cladding temperature increase ΔT_{PC}, which is defined as the peak cladding temperature at low pressure minus its value for continuum conditions. Its value is as large as 67 °C for rarefied condition with α = 0.2. Table 1 also gives the increase of the basket temperature ΔT_{BC}, which is defined as the outer basket surface temperature (at r = 83.5 cm) at low pressure minus its value under continuum conditions. The difference between ΔT_{PC} and ΔT_{BC} is very small compared to ΔT_{BC}, which indicates that the effect of reducing conduction through the gas for rarefied conditions (temperature-jump thermal-resistance), or eliminating it for the hard vacuum condition in the void spaces within the basket openings is much smaller than it is in the gap between the basket and canister.

IV.B. Comparison with two-Dimensional (2D) Simulations

Figure 6 shows the peak cladding temperature as a function of heat generation from the 2D simulations. The two solid lines are for the continuum and hard vacuum conditions and the dashed lines are for the rarefied condition with α = 1, 0.4, and 0.2. The horizontal lines show the temperature limits used in the United States and Germany, T_L = 400°C [4] and 370°C [25], respectively. The rarefied and hard vacuum lines in Fig. 6 are not parallel to the continuum line, which shows that the difference between the peak cladding temperatures under rarefied or hard vacuum and continuum conditions increases with heat

Table 2: Maximum allowable heat generation per assembly Q_F for 2D model. Results are given for the continuum, rarefied and hard vacuum models at the cladding temperature limits T_L=400°C and 370°C.

T_L [°C]	Maximum allowable heat generation [W/assembly]				
	Continuum P~10^5 Pa	Rarefied, P=100 Pa			Hard Vacuum P = 0 Pa
		α=1	α=0.4	α=0.2	
400	2859	2545 (11.0 %)	2129 (25.5 %)	1841 (35.6 %)	1256 (56.1 %)
370	2504	2226 (11.1 %)	1853 (25.9 %)	1592 (36.4 %)	1051 (58.0 %)

generation. The fuel assembly heat generation rates, Q_{FL}, that bring the peak cladding temperature to its limits are reported in Table 2.

From Table 2, the allowable heat generation rates that bring the cladding temperature to the limits of 400°C and 370°C for the continuum condition are 2859 W/assembly and 2504 W/assembly. For all other conditions, the calculated allowable heat generation rates are 11% to 58% lower than continuum condition. These heat generations are higher than the required average heat generation rates for the TN24 system, <1000 W/assembly for a standard horizontal storage module or 1700 W/assembly for an enhanced module, as specified in the Certificate of Compliance [26, 27]. For the purposes of this paper, we assume that the Certificate of Compliance limit is calculated by the manufacturer to maintain the cladding safely below 400°C during storage, in which the canister is cooled by the natural convection of air.

The calculation of cladding temperatures under dry storage conditions is beyond the scope of this work. However, it is reasonable to assume that the canister surface is hotter in the storage module, where it is cooled by air, than in vacuum drying, where it is submerged in water. If the canister is filled with atmospheric pressure helium in both situations, then it is also reasonable to assume that the cladding temperature may be hotter in the storage module than during vacuum drying. However, including the effects of rarefaction during vacuum drying increases the predicted cladding temperature under that condition.

Table 3: Difference of the peak cladding temperatures between the 2D and 3D models for continuum, rarefied and hard vacuum conditions and for Q_F=1498W/assembly.

	Continuum	Rarefied, P=100 Pa			Hard Vacuum
		α=1	α=0.4	α=0.2	
ΔT [°C]	15	18	24	29	35

Figure 6 also includes the results of the 3D dimensional model for Q_F = 1498 W/assembly. The peak cladding temperatures obtained from the 3D model are systematically lower than the 2D model, which indicates that the 2D model is more conservative. The temperature difference between the 2D and 3D models increases as the gas becomes more rarefied. These results are summarized in Table 3. This difference is a high as 35°C for hard vacuum condition.

It should be noted here that the 2D results presented in this paper are different from those published in Refs [30-33], even though, the same 2D model was used. This is for two reasons. First, the peaking factor used in both papers are different. In Ref [32], a peaking factor of 1.1351 [34] was employed, however, the value of 1.2104 was used in this paper obtained from Fig. 3. Second, in Refs [30-33] results, the emissivity for some stainless steel surfaces was mistakenly set to ε = 1, however, it should be 0.46. This caused the peak cladding temperature in to be underestimated by a few degrees, therefore, the maximum allowable heat generation to be overestimated.

V. CONCLUSION

The objective of this paper was to evaluate the effect of rarefaction on the fuel claddings temperature. Steady-state simulations were performed with a full-length, geometrically-accurate two and three-dimensional models of the TN-24P nuclear fuel canister in ANSYS/Fluent to predict the peak cladding temperature for continuum (P ~ 10^5 Pa), rarefied (P = 100 Pa), and hard vacuum (P = 0 Pa) conditions. For rarefied condition, a thermal-resistance temperature-jump at the interface gas-solid was considered using different values of the thermal accommodation coefficient, α = 1, 0.4, and 0.2. Axially varied heat generation rates for the fuel assemblies were employed

The effect of rarefaction is larger in the smallest gap of the canister, between the aluminum support and stainless-steel-enclosure, than it is in the basket openings. The allowable heat generation rates that bring the cladding temperature to the limit used in the United State, T_L = 400°C for continuum condition is 2859 W/assembly. The allowable heat generation rates decrease with pressure. For hard vacuum condition it is 1256 W/assembly. This represents a reduction by 56.1% from the continuum model.

The peak cladding temperatures calculated for the 3D model are consistently lower than the 2D model. This makes the 2D model more conservative and therefore predicts higher temperatures. This difference ranges from 15 °C for continuum condition to 35 °C for the hard vacuum condition.

ACKNOWLEDGEMENTS

This work was supported by the US Department of Energy Office of Nuclear Energy University Program.

REFERENCES

1. U.S. Department of Energy, Office of Civilian Radioactive Waste Management, "Characteristics of Spent Nuclear Fuel, High-Level Waste, and Other Radioactive Wastes Which May Require Long- Term Isolation," DOE/RW-0184, (1987).
2. D. COLMONT, P. ROBLIN, and C. GUÉRIN, "Improved Thermal Modeling of a SNF Shipping Cask Drying," *International Conference on Mathematics, Computational Methods & Reactor Physics*, Saratoga Springs, New York, 3 - 7 May (2009).
3. D. MAHARJAN, M. HADJ-NACER, N. CHALASANI and M. GREINER, "Experimentally Benchmarked Computational Fluid Dynamics Simulations of an Array of Heated Rods within a Square-Cross-Section Helium-Filled Pressure Vessel," *Proc. ASME PVP Conf.*, Vancouver, BC, 17-27 July (2016).
4. W. LARGE and R. SINDELAR, "Review of Drying Methods for Spent Nuclear Fuel," *Westinghouse Savannah River Company*, report number WSRC-TR-0075, Savannah River Site, Aiken, SC (1997)."Cladding Considerations for the Transportation and Storage of Spent Fuel," ISG-11 R3, Interim Staff Guidance Report of the Spent Fuel Project Office of the U.S. NRC (2003).
5. R. S. DAUM, S. MAJUMDAR and M. BILLONE, "Experimental and Analytical Investigation of the Mechanical Behavior of High-Burnup Zircaloy-4 Fuel Cladding," *J. ASTM Intl*., vol. 5, no. 5, (2009).
6. R. S. DAUM, S. MAJUMDAR, Y. LIU and M. C. BILLONE, "Radial-hydride Embrittlement of High-burnup Zircaloy-4 Fuel Cladding," *J. Nucl. Sci. Tech*., vol. 43, no. 9, pp. 1-14, (2006).
7. M. C. BILLONE, T. BURTSEVA and R. EINZIGER, "Ductile-to-brittle transition temperature for high-burnup cladding alloys exposed to simulated drying-storage conditions," *J. Nucl. Mater*, vol. 433, pp. 431-448, (2013).
8. M. C. BILLONE, T. BURTSEVA and Y. LIU, "Baseline Properties and DBTT of High-Burnup PWR Cladding Alloys," *Proc. PATRAM*, San Francisco, CA, (2013).
9. Holtec International, "HI-STORM 100 FSAR," Revision 8, Report HI-2002444, (2010).
10. Y.S. TSENG, J.R. WANG, F.P. TSAI, Y.H. CHENG and C. SHIH, "Thermal design investigation of a new tube-type dry-storage system through CFD simulations," *Annals of Nuclear Energy*, 38, 1088-1097, (2011).
11. Holtec International, "Topical Report on the HI-STAR/HI-STORM Thermal Model and its Benchmarking with Full-Scale Cask Test Data," Holtec Report No. HI-992252, (2000).
12. Pacific Northwest Laboratory, "The TN-24P PWR Spent Fuel Storage Cask: Testing and Analyses," EPRI NP-5128, (1987).
13. F. SHARIPOV, "Data on the velocity slip and temperature jump coefficients," *Thermal and Mechanical Simulation and Experiments in Micro-Electronics and Micro-Systems Proc. 5th Int. Conf. EuroSimE*, Belgium, pp. 243-249, (2004).
14. J. T. LIN and D. R. WILLIS, "Kinetic Theory Analysis of Temperature Jump in a Polyatomic Gas," Phys. Fluids, vol. 15, p. 31 (1972).
15. R. GREEN, M. HADJ-NACER, and M. GREINER, "Design of an Experiment to Measure the Thermal Accommodation Coefficient between Helium and Stainless-Steel in Concentric Cylinders," *Proc. Of ASME PVP Conf.*, Boston, MA, 19-23 July, (2015).
16. M. HADJ-NACER, D. MAHARJAN, M. HO, S. STEVANOV, I. GRAUR, and M. GREINER, "Continuum and Kinetic Simulations of Heat Transfer through Rarefied Gas in Annular and Planar Geometries in the Slip Regime," *ASME J. Heat Transfer*. In press (2016).
17. D. MAHARJAN, M. HADJ-NACER, M. HO, S. STEFANOV, I. GRAUR, and M. GREINER, "Simulation of Heat Transfer across Rarefied Gas in Annular and Planar Geometries: Comparison of Navier-Stokes, S-Model and DSMC Methods Results," *ASME Proc. Int. Conf. Nanochannels, Microchannels, and Minichannels* (InterPACK/ICNMM2015), San Francisco, CA, July 6–9, (2015).
18. S. SONG and M. YOVANOVICH, "Correlation of Thermal Accommodation Coefficient for 'Engineering' Surfaces," (1987).
19. L. THOMAS and S. LOYALKA, "Determination of Thermal Accommodation Coefficeints of Helium, Argon, and Xenon on a Surface of Zircaloy-2 at about 25ºC," *Nuclear Technology*, **57**, 213, (1982).
20. F. GOODMAN, "Thermal Accommodation Coefficients," *J. Phys. Chem.*, **84**, 1431, (1980).
21. M. F. MODEST, *Radiative Heat Transfer*, 2nd Ed., Academic Press, New York (2003).
22. "NUHOMS®-24PTH DSC Thermal Evaluation for Storage and Transfer Conditions," Project No. NUH24PTH Transnuclear, Inc.
23. W. BRACEY and P. SMITH, "Transnuclear Drying Experience and Lessons Learned," ASTM Workshop, Atlanta, GA, (2012).
24. J. M. CEER et al, "The TN-24 PWR Spent-Fuel Storage Cask: Testing and Analyses" (1987).

25. H. G. Kim, Y. H. Jeong, and K. T. Kim, " The Effects of Creep and Hydride on Spent Fuel Integrity During Interim Dry Storage," *Nucl. Eng. Technol.*, **42**, 249 (2010).
26. "Certificate of Compliance for Spent Fuel Storage Casks, NUHOMS®-24P," Certificate Number 1004, Docket Number 72-1004, *U.S. Nuclear Regulatory Commission* (1995).
27. "Standardized Advanced NUHOMS® Horizontal Modular Storage System for Irradiated Nuclear Fuel," *Transnuclear, Inc.*, NUH-003, Rev. 8 (2004).
28. S. A. SCHAAF and P. L. CHAMBRE, *Flow of Rarefied Gases*, Princeton University Press, New Jersey (1961).
29. J. C. MAXWELL, "On Stress of Rarefied Gases arising from Inequalities of Temperature," *Philisophical Transactions R. Soc. Lond.*, Vol. 170, pp. 231-256 (1878).
30. M. HADJ-NACER, T. MANZO, M. HO, I. GRAUR, and M. GREINER, "Phenomena Affecting Used Nuclear Fuel Cladding Temperatures during Vacuum Drying Operations," *International High Level Radioactive Waste Management Conference* (2015).
31. T. MANZO, R. GREEN, M. HADJ-NACER, M. GREINER, J. LI, AND Y. LIU, "Prediction of Cladding Temperatures within a used Nuclear Fuel Transfer Cask Filled with Rarefied Helium" *Proc. ASME PVP Conf.*, Anaheim, CA, 20-24 July (2014).
32. M. HADJ-NACER, T. MANZO, M. HO, I. GRAUR, and M. GREINER, "Effects of Gas Rarefaction on Used Nuclear Fuel Cladding Temperatures during Vacuum Drying," *Nuclear Technology*, **20**, 1-13 (2016).
33. T. MANZO, M. HADJ-NACER, and M. GREINER, "Geometrically-Accurate Three-Dimensional Simulations of a used Nuclear Fuel Canister Filled with Helium," *Proc. ASME PVP Conf.*, Boston MA, 19-23 July (2015).
34. R. H. BAHNEY and T. L. LOTZ, "Spent Nuclear Fuel Effective Thermal Conductivity Report," *U.S. Department of Energy*, TRW Environmental Safety Systems, Inc. (1996).

Proceedings of the ASME 2017 Pressure Vessels & Piping Division Conference
PVP2017
July 16-20, 2017, Waikoloa Village, HI, USA

PVP2017-66001

[DRAFT] TEMPERATURE MEASUREMENT OF AN ARRAY OF HEATED RODS SUBJECTED TO VACUUM DRYING CONDITIONS

Dilesh Maharjan
Graduate Researcher
University of Nevada, Reno
Reno, NV, USA

Mustafa Hadj-Nacer
Research Scientist
University of Nevada, Reno
Reno, NV, USA
mhadjnacer@unr.edu

Miles Greiner
Professor of Mechanical Engineering
University of Nevada, Reno
Reno, NV, USA

ABSTRACT

During vacuum drying of used nuclear fuel canister, helium pressure is decreased to as low as 67 Pa to promote evaporation and removal of water remaining in the canister following draining operation. At low pressures associated with vacuum drying, there is a temperature jump (thermal resistance) between the solid surfaces and helium in contact with them. This temperature jump increases as the pressure decreases (rarefied condition), which contributes to the fuel assembly's temperature increase. It is important to keep the temperature of the fuel assemblies below 400°C during vacuum drying to ensure their safety for transport and storage.

In this work, an experimental apparatus consisting of a 7×7 array of electrically heated rods maintained between two spacer plates and enclosed inside a square cross-section stainless steel pressure vessel is constructed to evaluate the temperature of the heater rods at different pressures. This geometry is relevant to a BWR fuel assembly between two consecutive spacer plates. Thermocouples are installed in each of the 49 heater rods, spacer plates and enclosure walls. They provide a complete temperature profile of the experiment. Different pressures and heat generation relevant to vacuum drying conditions are tested. The results showed that the maximum temperature of the heater rods increases as the pressure decreases. The results from these experiments will be compared to computational fluid dynamics simulations in separate work.

INTRODUCTION

Nuclear fuel assemblies consist primarily of 7×7 to 17×17 arrays of fuel rods held in place by spacer plates[1, 2]. Each rod consists of zircaloy cladding tubes that contain highly radioactive fuel pellets and high pressure fission-product and fill gases. After being discharged from reactor, these assemblies are stored underwater while their radioactivity and heat generation rate decrease. After sufficient time, a canister with an internal basket is placed in a transfer cask and lowered into the pool. The canister is then loaded with the fuel assemblies, sealed, lifted out of the pool, and drained while an inert gas (He or N_2) flows in. Small amounts of water may remain at the bottom of the canister and in crevices of the canister and cladding surfaces after draining. All moisture must be removed from the canister before it is filled with helium (3-7 atm) and sealed for onsite storage or offsite transport. This reduces possible corrosion and/or formation of combustible oxygen/hydrogen mixtures.

Vacuum drying is commonly used to remove moisture for low burnup fuels [3]. During this process, the canister is evacuated to pressures as low as 67 Pa to promote evaporation and removal of water [4, 5]. The fuel claddings may experience their highest temperature during vacuum drying because it is the first time they are removed from water to gas environments. Additionally, due to the low pressure condition (rarefaction), there is a temperature jump at the gas/solid interfaces [6-13],

which increases resistance to heat transfer and causes the temperature of fuel claddings to increase.

It is important to keep the temperature of the cladding below certain limit [14] to avoid re-orientation of the hydride present in the cladding in the radial direction. The hydrides present in the cladding are typically oriented in circumferential direction. This orientation does not significantly affect the cladding ductility. But if the temperature of cladding exceeds 400 °C, formation of radial hydride may occur during the slow cooling of fuel cladding [15-17]. The formation of radial hydride is not desired as it can cause cladding embrittlement and increases the likelihood of brittle failure under drop accidents during handling and transportation.

Currently, numerical predictions of the temperatures during the vacuum drying operation does not include the effect of rarefaction (low pressure). An accurate estimation of cladding temperatures during drying operations is important to determine the maximum allowable fuel assembly heat generation rate at time-of-transfer. Storing the assemblies in cooling pool for longer period of time decreases their heat generation, however, over-conservatism in estimating canister temperatures during drying operations can lead to unnecessarily long storage times, especially for high-burnup fuel.

The long-term objective of this research is to develop and experimentally-benchmark CFD models of the vacuum drying process that includes the effect of rarefaction. The main objective of this work is to construct an experimental apparatus relevant to a nuclear fuel assembly, subjected to vacuum drying conditions, to quantify the effect of rarefaction. An experiment consisting of an array of 7×7 electrically heated rods held between two spacer plates and enclosed in a stainless steel square cross-section pressure vessel is constructed. Various pressures, ranging from 50 to ~10^5 Pa, relevant to vacuum drying conditions are tested for two heat generations, Q = 50 and 100 W.

DESCRIPTION OF EXPERIMENT

The experiment was designed to represent a central portion of a 7×7 fuel assembly between two consecutive spacer plates inside a nuclear canister oriented vertically and subjected to vacuum drying conditions. The experimental apparatus consists of a stainless steel enclosure containing heater rods bundled in a 7×7 configuration and held by two spacer plates. Figure 1a shows the drawing of the experiment created in SolidWorks. The enclosure is made transparent to show the inner parts of the experiment. The most important parts of the experiment are described below.

Heater Rods: Electrically powered heater rods are used to simulate fuel rods of a nuclear assembly. Each rod consists of a heating coil surround by magnesium oxide (MgO) and covered with a thin stainless steel sheath of 0.72 mm thickness. They have a diameter of 1.25 ± 0.003 cm and a total length of 65 ± 0.5 cm long. These rods generates throughout the length of the rod except for unheated sections at both ends. Solid pins are attached to both ends where the electric wires are connected. The unheated length was designed by the manufacturer to be

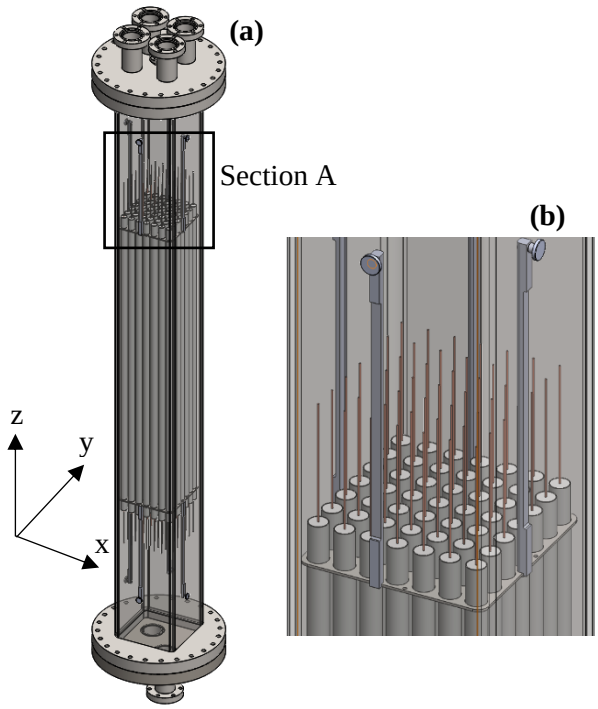

Figure 1: (a) Assembled model of experiment, (b) Enlarged view of Section A

2.2 cm long. However, by taking X-rays of 10 random heater rods, the unheated length was found to be 3 cm on average. Because of the way the rods were bundled together (7×7), seven rods in each of the seven rows are connected in series. These seven groups are then connected in parallel. Each heater rod is rated to be 20W ± 1W. All the heater rods have one type K thermocouple installed at one of five different axial locations. Installation of more than one thermocouple in a heater rod was not feasible due to the small diameter of the heater rods. There are 21 heater rods with thermocouple at center, 13 thermocouple at 25 cm above the axial center, 11 thermocouple at 25 cm below the axial center, 2 thermocouple at 10 cm above and 2 thermocouple at 10 cm below the axial center.

The thermocouple locations in the heater rods provided by the manufacturer were found to significantly vary, within ± 5 cm. This is due to the swaging process used in fabrication of these rods. To check the location of the thermocouples in the heater rods, a test setup was constructed using flat heaters and an aluminum block. Figure 2 shows the setup used to test the thermocouple locations. .An array of semi-circular grooves were cut on one side to fit the heater rods and a flat heater was attached to other side. Three thermocouples were installed in the aluminum block to monitor its temperature. The width of the block where it is in contact with the heater rod is 6 mm.

Constant power was supplied to the heater. Once the temperature of the block is steady, it is placed on heater rods in specific locations (marked every 6mm) for 30 seconds making sure there is proper contact. The temperature increase indicated

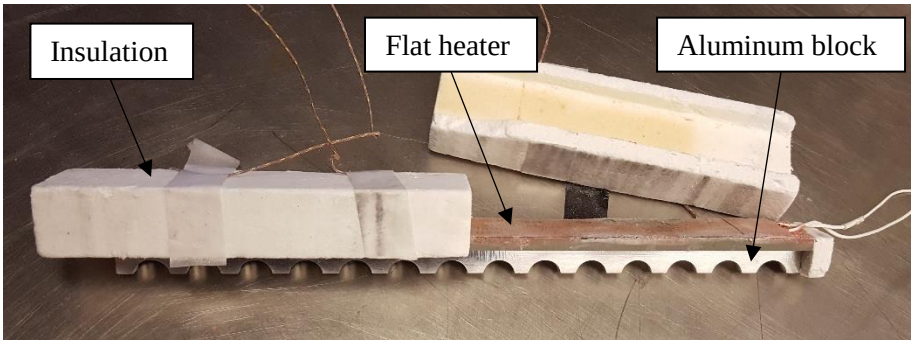

Figure 2: Setup used to determine the location of thermocouples in heater rods

by the thermocouple inside the heater rod was measured. The aluminum block was then removed and both the aluminum block and the heater rods were allowed to get to a steady temperature. Once in steady temperature, the process was repeated again for next location. Figure 3 shows the results obtained for six heater rods represented by six different colors. The location of the thermocouples in the rod is determined as the location where the peak of temperature is measured. These locations are predicted to a tolerance of ± 3 mm.

Spacer plate: Two square stainless steel plates of 1.5 mm thickness and 11.5 cm length were used as spacer plates. Each plate has 49 holes of 1.27 cm diameter with pitch of 1.625 cm. The corners of spacer plate were rounded to accommodate the inner shape of the enclosure and to leave a constant circumferential gap between the plates and enclosure inner wall. As shown in Fig. 1b, on four edges of the plate small slots were created to bolt the spacer plate to the supporting rods. Small holes of 1 mm diameter and 0.5 mm depth were drilled in specific locations on the plates to host 14 thermocouples. The thermocouples were welded to these holes and used to obtain a complete profile of the spacer plates.

Supporting rods: Supporting rods were used to secure the spacer plates and heater rods in place. Figure 1b shows two supporting rods bolted to the top spacer plate and enclosure. The length, width and thickness of each rod is 21.5 cm, 6.5 mm and 6 mm. The top of each rod has a threaded hole to bolt the spacer plate to the rod. A step is machined on the end of the supporting rod connected to the spacer plate with a depth equal to thickness of the spacer plate. The thickness of the step is equal to the gap between the spacer plate and enclosure wall. On the other end, a slot was machined to bolt the supporting rod to the enclosure wall. Eight of these rods are used, four on each spacer plate.

Enclosure: The enclosure consists of a square stainless steel tube with 12.7 cm outside dimension and a wall thickness of 4.75 mm. The total length of the tube is 122 cm. The dimension of two sides is slightly different. Since, the tube is constructed by folding a stainless steel plate, the corners are rounded. On the outer surface of enclosure body, grooves of 1.2 mm depth and 1 mm wide were machined to host 13 thermocouples on each wall. These thermocouples provides a complete axial and longitudinal temperature profiles of the four outer walls of the enclosure.

Ultra-high vacuum flanges were welded to both ends of the enclosure to hold vacuum inside the chamber. The top flange hosts four thermocouple feedthroughs and one power feedthrough, which are used to connect the heater rod and spacer plate thermocouples, and heater rod power wires from the inside of the vacuum chamber to the air side. The bottom flange houses a thermocouple/power feedthrough and a vacuum tree. The vacuum tree consists a stainless steel tube to which is attached a vacuum pump, pressure gage, and helium tank through an open/close and leaking valves. Figure 4 shows a picture of the experimental apparatus fully assembled.

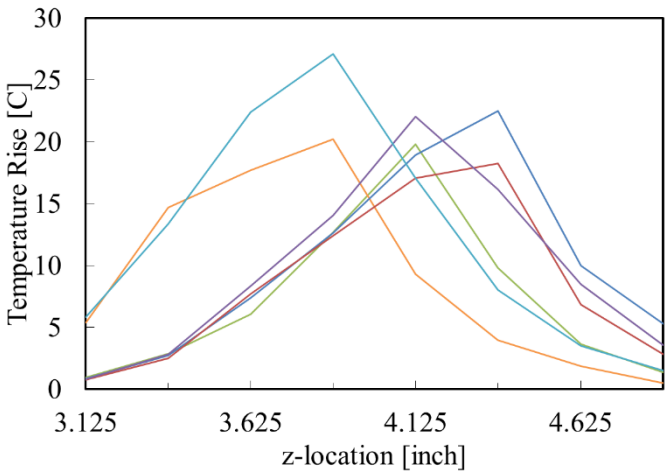

Figure 3: Plot of thermocouple response in thermocouple location test

Insulation: The outside of the enclosure was covered with 2.54 cm (1 inch) thick LD Duraboard Unifrax insulation to minimize the effect of ambient condition on the experimental results. An additional insulation layer of 2.54 cm Unifrax blanket was used on top of the insulation board.

EXPERIMENT DESIGN

To adequately design the experiment and determine tolerances associated with each part of the experiment, CFD

Figure 4: Picture of the experimental apparatus fully assembled.

simulations were carried out beforehand. These simulations were necessary to quantify the errors associated with the fabrication process and dimensional tolerances of the components, which may lead to asymmetry of the experimental apparatus. As the asymmetry and geometric tolerances, which occur during fabrication cannot be quantified, they cannot be represented in the original simulations. Since, these simulations are conducted for finalizing the experimental design, the geometry used for these simulations does not exactly match the final experimental apparatus. Some of the major simulations carried out are mentioned here.

Effect of the heater rod's position

A recent study [18, 19] by the authors suggested that the knowledge of exact location of the heater rods in the *x*-*y* plane is extremely important. The movement of the heater rods in *x* and/or *y* directions is caused mainly by tolerances in diameter of the spacer plate holes and heater rods. Another important cause is the deformation (bowing) of the heater rods resulted from their elongation when temperature increases. The temperatures measured from the heater rods closer to the enclosure wall are mainly sensitive to the rod's location in *x*-*y* plane. Test simulations were conducted in ANSYS/Fluent to

-0.38	-1.68 ↑	-0.34	-0.30	-0.61	-1.80 ↑	-1.12 ↑
← -1.77	-0.52	→ 0.00	← -0.28	0.19 ↓	-0.62	-0.38
-0.68	→ 0.06	→ 0.01	-0.24	← -0.18	-0.42 ↓	-0.54
-0.55	-0.70	→ 0.01	← -0.35	-0.54	-0.58	→ -2.34
← -2.03	-0.79 ↓	-0.47	-0.50	-0.60	← 0.07	→ -2.51
-0.44	0.22 ↑	-0.50	-1.33 ↓	-0.60	-0.55	-1.91
← -1.04	-0.61	-2.15 ↓	-2.04 ↓	-0.45	-0.34	-0.31

Figure 5: Temperature difference for randomly moved and arranged heater rods for Q = 500 W and P = 1atm.

quantify this effect for different pressures. Approximately half of the heater rods were randomly moved by 0.5 mm and 0.1 mm in either *x* or *y* directions. Keeping all other conditions (rod heat generations, pressure and boundary conditions) the same, the comparison of the heater rod temperatures at the axial center was done for properly arranged condition and randomly moved condition. The effect of movement of 0.1 mm was observed to be negligible. However, the movement of 0.5 mm resulted in some significant temperature variations. The variation at low pressures was smaller than atmospheric pressure.

In Fig. 5, the arrows shows the 0.5 mm movement of the heater rods in the positive or negative *x* or *y* directions, and the numerical values show the temperature of randomly arranged minus perfectly arranged conditions for Q = 500W and P = 1 atm. As observed in the recent study [18, 19], the difference is significantly high at the heater rods closer to the enclosure wall than those at the center. Hence, for this experiment, tighter tolerance for the diameter of the heater rod and spacer plate holes was maintained. In addition, the experiment was designed to allow the heater rods to increase in length without deformation when temperature increases.

Symmetry groups

The objective of installing a thermocouple in every heater rod is to get as much information about temperature profile as possible. For this, it is necessary to have thermocouples in such locations that we can take advantage of the geometrical symmetry. If all the enclosure walls have same temperature profile, then there is symmetry across *xz* and *yz* planes and planes passing through opposite corners of the square enclosure in Fig. 6. Hence, only $1/8^{th}$ portion can represent the complete temperature profile of the experiment. Figure 6 shows the location of thermocouple in each heater rod. The position of the rod thermocouples in the axial direction are represented by

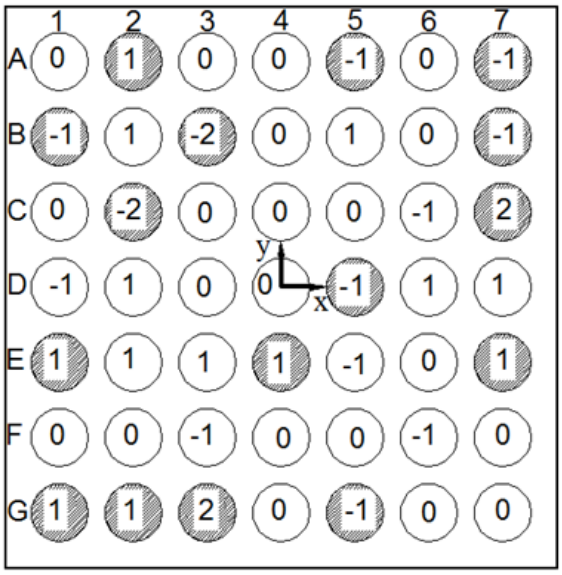

Figure 6: Configuration showing axial locations of thermocouples in each heater rod and heater rod pairs used to check symmetry across z = 0 cm plane.

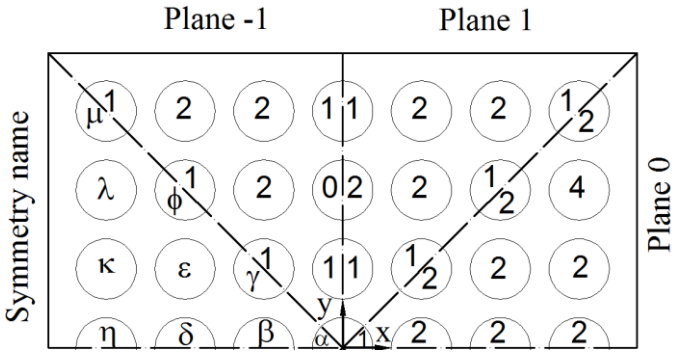

Figure 7: Symmetry groups and number of heater rods with thermocouples in three different axial planes (-1, 0, and 1).

numeric values. The 0 value represents thermocouples located at the axial center (z = 0 cm), 1 represents thermocouples at 25 cm above the axial center, -1 represents thermocouples at 25 cm below the axial center, 2 represents thermocouples at 10 cm above the axial center and -2 represents thermocouples at 10 cm below axial center. The rows are represented by alphabets from A to G whereas the columns are represented by numbers from 1 to 7. The combination of alphabets and numbers can be used to name the heater rods in any position if required.

Figure 7 shows 10 different symmetry groups and their names represented by Greek symbols from α to μ. The dashed line shows the plane of symmetry at three different axial locations shown by planes 0, 1 and -1. The numerical value inside the circle represents number of heater rods with thermocouple at that axial location and symmetry group. Except for α and δ symmetry group, there are thermocouples available for all other symmetry groups at 3 axial locations. Hence, an

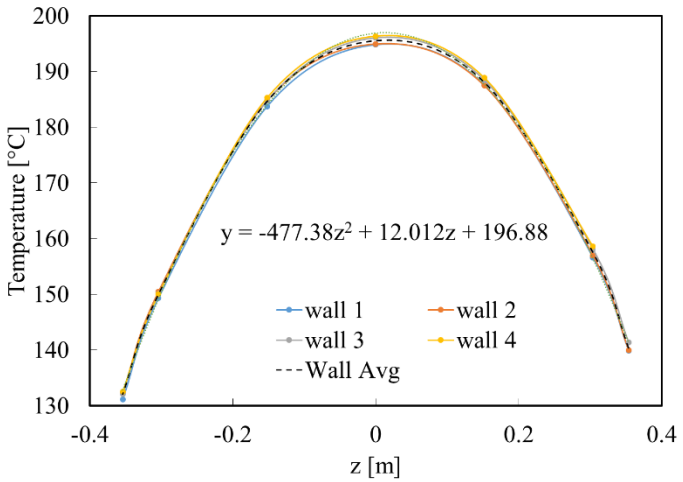

Figure 8: Temperature profile of all four enclosure walls for P= 77 Pa and Q = 100 W

axial temperature profile can be drawn from the experiment for these symmetric locations.

The symmetry group with more than one thermocouple in any plane can be used to check symmetry of the experiment. A combination of the heater rods in different symmetric groups will be used to check the complete symmetry across all the planes.

Ideally, there should be an axial symmetry across z = 0 cm plane. The heater rods in symmetry are shown in Fig 6 by hatched heater rods. The total of eight pairs of heater rods with thermocouple at four different locations can be used to check symmetry across mid plane.

EXPERIMENTAL RESULTS

Experiments are carried out for two heat generation rates, Q = 50 and 100 W, and a total of nine pressure values ranging from 50 to 10^5 Pa. Helium is used as the working fluid. Initially, the experimental apparatus was outgassed for a few days with an applied heat generation rate of 50 W to assist in the outgassing process.

Each experiment takes about 72 hours to get to steady state for low pressure cases, whereas it takes about 48 hours for higher pressures. The experiments are then run for few additional hours past steady state to collect data.

Temperature profile of the enclosure walls

As mentioned earlier, 13 thermocouples are used in each wall to get the complete temperature profile of the enclosure outer walls. Figure 8 shows the temperature variation along z-axis of the four walls for P = 77 Pa and Q = 100 W. The axial variation of temperature, along the z-axis, is significant. However, its variation in the longitudinal direction (not shown) is insignificant. The difference of temperature for all four walls at same z-value is less than 2°C. The wall temperature profiles are not symmetric in respect to the z = 0 cm plane. The

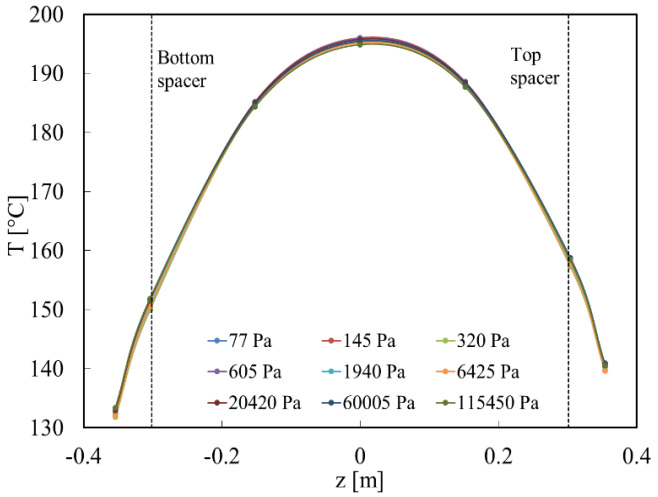

Figure 9: Average enclosure temperature along *z*–axis for all pressure and for Q = 100 W.

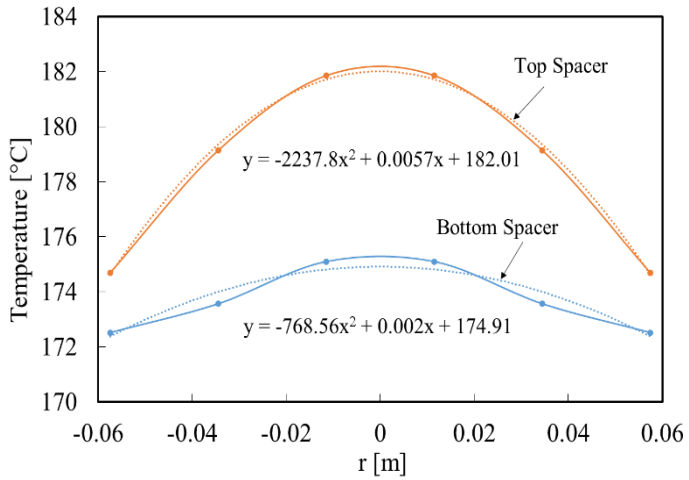

Figure 10: Top and bottom spacer plates temperature profiles as function of distance from plates' center for P = 77 Pa and Q = 100 W.

temperatures above the mid-plane (positive *z*) are larger than those below it (negative *z*). The dashed line in Fig. 8 shows the average temperature of the four walls.

The temperature variation of the walls with respect to the pressure variation for heat input of 100 W is shown in Fig. 9. The average temperature profile of the four walls is shown for each pressure. The variation in the wall temperature profile is insignificant with change in pressure. The two vertical dashed line show the location of the top and bottom spacer plates.

Temperature of the spacer plate

It is expected that the temperature profile of the spacer plates to be circular with highest temperature at the center, with temperature decreasing as the radial distance from the center increases. The six thermocouples along the diagonal of the space plate were used to generate the circular temperature profile as a function of radius. Figure 10 shows the temperature

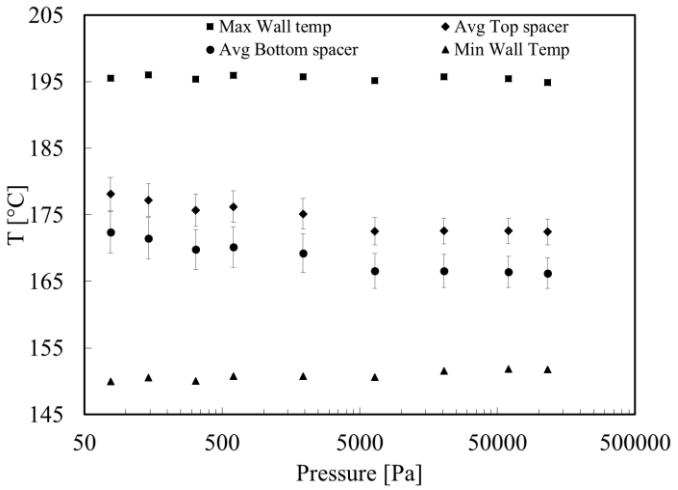

Figure 11: Average top and bottom spacer temperatures and, maximum and minimum wall temperatures as function of pressure for Q = 100 W.

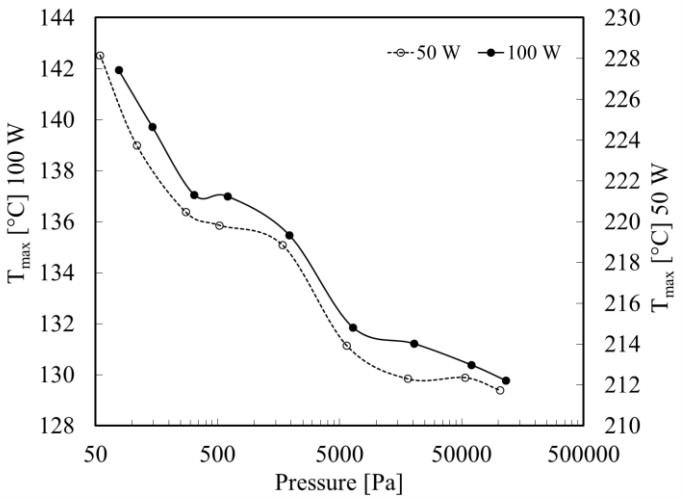

Figure 12: Maximum temperature of heater rod as function of pressure.

profile for the top and bottom spacer plate for P = 77 Pa and Q = 100 W. The temperatures of the top spacer plate are higher than the bottom spacer plate. This variation is observed for all cases, which suggests that more heat is being conducted through the bottom than the top of the experimental apparatus. This is due to the presence of vacuum tree connected to the bottom of the experimental apparatus. In addition, the experiment rests on a table creating an additional path for heat conduction.

Figure 11 shows the average top and bottom spacer plate temperatures as function of pressure for Q = 100 W. For both the top and bottom spacer plates, the average temperature increases with decrease in pressure. This is due to the effect of rarefaction, which causes the heater rods temperature to increase (as described below), and subsequently the spacer plate's temperature.

Temperature of the heater rods

Figure 12 shows the maximum heater rod temperature, obtained from the centermost rod, as function of pressure for Q = 50 and 100 W indicated by solid and dashed lines, respectively. For both heat generations, the profiles of temperature follow similar trend. The temperature of the rods increases as the pressure decreases. There is an increase by 13.1°C for Q = 50 W when pressure decreases from ~10^5 to 50 Pa. However, this increase is of 15.2°C for Q = 100 W for the same pressure range. This increase of temperature is caused by the rarefaction effect. A temperature jump at the interface between solid surfaces (cladding and enclosure walls) and helium is created as the pressure decreases, which acts as resistance for heat transfer. This temperature jump is larger for higher heat generation.

In Fig. 12, a slight 'bump' in the profile of temperature at pressure between 500 and 5000 Pa is observed for both heat generations. The cause of this irregularity in the temperature profile is not well understood. The experiments were repeated for these pressure values but the obtained results were nearly the same. Further investigation needs to be performed to explain this phenomenon.

CONCLUSION

An experimental setup representing a central portion of a BWR 7×7 fuel assembly between two consecutive spacer plates inside a canister is designed and constructed. This experiment was used to study the effect of rarefaction during vacuum drying process applied to nuclear fuel assemblies. It consists of a stainless steel enclosure containing heater rods bundled in a 7×7 configuration and held by two spacer plates. Heat generation rates of 50 and 100 W was applied for nine different pressures ranging from ~ 50 to 10^5 Pa. Thermocouples were installed on the enclosure outer walls and spacer plates to obtain their profiles. For same heat generation rate, enclosure wall temperatures were not significantly affected by pressure change. However, the temperature of the spacer plates slightly increased when the pressure was decreased.

Furthermore, as the pressure decreased, temperature of the centermost heater rods increased by 13.1 °C and 15.2 °C for 50 and 100 W heat generations, respectively. This was due to the effect of rarefaction at the solid/gas interfaces developed at low pressure.

The experimental results presented in this paper are compared to CFD simulations carried out using ANSYS/Fluent in separate work published in the same conference in order to benchmark the numerical model.

ACKNOWLEDGEMENT

This work was supported by the US Department of Energy Office of Nuclear Energy University Program.

REFERENCE

[1] Office of Civilian Radioactive Waste Management (OCRWM), U. S. D. o. E., 1987, "Characteristics of Spent Nuclear Fuel, High-Level Waste, and Other Radioactive Wastes which may Require Long-Term Isolation."

[2] Saling, J. H., and Fentiman, A. W., 2002, Radioactive Waste Management, Taylor and Francis, New York.

[3] International, H., 2010, "HI-STORM 100 FSAR."

[4] Large, W. S., and Sindelar, R. L., 1997, "Review of Drying Methods for Spent Nuclear Fuel," Westinghouse Savannah River Company, report number WSRC-TR-0075, Savannah River Site, Aiken, SC.

[5] Bracey, W., and Smith, P., "Transnuclear drying experience and lessons learned," Proc. ASTM Workshop.

[6] Colmont, D., and Roblin, P., 2008, "Improved thermal modeling of SNF shipping cask drying process using analytical and statistical approaches," Packaging, Transport, Storage & Security of Radioactive Material, 19(3), pp. 160-164.

[7] Hadj-Nacer, M., 2012, "Tangential momentum accommodation coefficient in microchannels with differebt surface materials (measurement and simulations)," PH.D Thesis, University of Aix-Marseille.

[8] Schaaf, S. A., and Chambre, P. L., 1961, Flow of Rarefied Gases, Princeton University Press, New Jersey.

[9] Hadj-Nacer, M., Manzo, T., Ho, M., Graur, I., and Greiner, M., 2016, "Effects of Gas Rarefaction on Used Nuclear Fuel Cladding Temperatures during Vacuum Drying," Nuclear Technology, 20, pp. 1-13.

[10] Hadj-Nacer, M., Manzo, T., Ho, M., Graur, I., and Greiner, M., 2015, "Phenomena Affecting Used Nuclear Fuel Cladding Temperatures during Vacuum Drying Operations," International High Level Radioactive Waste Management Conference.

[11] Manzo, T., Green, R., Hadj-Nacer, M., Greiner, M., Li, J., and Liu, Y., 2014, "Prediction of Cladding Temperatures within a used Nuclear Fuel Transfer Cask Filled with Rarefied Helium," ASME PVPAnaheim, CA.

[12] Manzo, T., Hadj-Nacer, M., and Greiner, M., 2015, "Geometrically Accurate Three-Dimensional Simulations of a used Nuclear Fuel Canister Filled with Helium," ASME PVPBoston, MA.

[13] Hadj-Nacer, M., Maharjan, D., Ho, M., Stefanov, S., Graur, I., and Greiner, M., 2016, "Continuum and Kinetic Simulations of Heat Transfer through Rarefied Gas in Annular and Planar Geometries in the Slip Regime," ASME Journal of Heat Transfer.

[14] NRC, 2005, "Cladding Considerations for the Transportation and Storage of Spent Fuel."

[15] Daum, R. S., Majumdar, S., Liu, Y. Y., and M.C., B., 2006, "Radial-hydride Embrittlement of High-burnup Zircaloy-4 Fuel Cladding," J. Nucl. Sci. Tech., 43(9), pp. 1-14.

[16] Daum, R. S., Majumdar, S., and Billone, M. C., 2008, "Experimental and Analytical Investigation of the

Mechanical Behavior of High-Burnup Zircaloy-4 Fuel Cladding," J. ASTM Intern., 5(5).
[17] Hanson B, R. S., C Lavender, P MacFarlan, P Eslinger., 2013, "Hydride Rim Formation in Unirradiated Zircaloy," PNNL-22438. Prepared for the U.S. Department of Energy Used Fuel Disposition Campaign, Washington, D.C.
[18] Maharjan, D., Hadj-Nacer, M., Chalasani, N., and Greiner, M., 2016, "Experimentally Benchmarked Computational Fluid Dynamics Simulations of an Array of Heated Rods within a Square-Cross-Section Helium-Filled Pressure Vessel," ASME PVP ConferenceVancouver, BC.
[19] Maharjan, D., Hadj-Nacer, M., Chalasani, N., and Greiner, M., 2017 (Submitted), "Experimental Validation of Heat Transfer Simulations for a Vertical Heated Rod Array within a Square-Cross-Section, Helium-Filled Isothermal Enclosure," ASME Journal of Thermal Science and Engineering Applications.

Proceedings of the ASME 2017 Conference on Pressure Vessels and Piping

PVP2017

July 16-20, 2017, Waikoloa Village, HI, USA

PVP2017-66002

[DRAFT] EXPERIMENTALLY BENCHMARKED COMPUTATIONAL FLUID DYNAMICS SIMULATIONS OF A 7×7 ARRAY OF HEATED RODS WITHIN A SQUARE-CROSS-SECTION ENCLOSURE FILLED WITH RAREFIED HELIUM

Dilesh Maharjan
Graduate Researcher
University of Nevada, Reno
Reno, NV, USA

Mustafa Hadj-Nacer
Research Scientist
University of Nevada, Reno
Reno, NV, USA
mhadjnacer@unr.edu

Miles Greiner
Professor of Mechanical Engineering
University of Nevada, Reno
Reno, NV, USA

ABSTRACT

Computational fluid dynamics simulations of a 7×7 array of heated rods within a square-cross-section enclosure filled with rarefied helium are performed for heat generation rates of 50 W and 100 W and various helium pressures ranging from 10^5 to 50 Pa. The model represents a section of nuclear fuel assembly between two consecutive spacer plates inside a nuclear canister subjected to during vacuum drying process. A temperature jump model is applied at the solid-gas interface to incorporate the effects of gas rarefaction at low pressures. The temperature prediction from simulations are compared to measured temperatures. The results showed that when helium pressure was decrease from 10^5 to 50 Pa, the maximum temperature of the heater rod array increased by about 14 °C. The temperatures of hottest rod predicted by simulations are within 4°C of the measured values for all pressure. The random difference of simulated rod temperatures from the measured temperatures are 3.33 °C and 2.62 °C for 100 W and 50 W heat generation rate.

INTRODUCTION

Used nuclear fuel assemblies are stored underwater, in a water pool, for few years while their radioactivity and heat generation rate decrease [1, 2]. A canister with an internal basket is placed in a transfer cask and lowered into the water pool. The canister is then loaded with the fuel assemblies, sealed, lifted out of the pool and drained. Small amount of water may remain at the bottom of the canister and in crevices of the canister and cladding surfaces after draining. All the remaining moisture must be removed before the canister is filled with helium (or nitrogen) and transported to long-term storage facility to avoid any corrosion or formation of combustible mixture of hydrogen and oxygen. Vacuum drying process is widely used to remove moisture from the fuel canisters before placing them in long-term storage [3]. During this process, the pressure is reduced to as low as 67 Pa [4, 5] to promote evaporation and removal of water. The process continues until the canister can hold a pressure of less than 400 Pa for at least 30 minutes as specified by the Nuclear Regulatory Commission (NRC) Interim Staff Guidance-11, Revision 3 (ISG-11) [6]. The fuel assemblies may experience their highest temperature during vacuum drying process because it is the first operation when the fuel assemblies are removed from water to helium environment, which has relatively lower thermal conductivity compared to water and the heat generation of fuel assemblies is still relatively high. The other main factor contributing to the increase of temperature during the process is the low pressure conditions applied to the canister. Because of this low pressure, the gas inside the canister is in rarefied condition [7].

At rarefied condition, the average distance travelled by gas molecules between successive collisions, defined as the mean free path, λ [8], is comparable or larger than the characteristic

length (L) of the system. Therefore, at low pressure, the continuum fluid approximation breaks down and the particle nature of fluid must be taken into account [9]. The ratio of the mean free path and the characteristic length is called Knudsen number, $Kn = \lambda/L$. The Knudsen number is used to characterize the rarefaction level of a gas. Using this parameter, four regimes of rarefaction may be distinguished. (i) The continuum regime ($Kn \leq 10^{-3}$), where the flow and heat transfer can be accurately modeled using the classical Navier-Stokes and Convective Energy equations. (ii) The slip regime ($10^{-3} \leq Kn \leq 10^{-1}$), where the Navier-Stokes and Convective Energy equations are still appropriate but conditions of velocity-slip and temperature-jump at the wall must be used. (iii) The transitional regime ($10^{-1} < Kn < 10$), where the flow needs to be modeled using the collisional Boltzmann equation. (iv) The free molecular regime ($10 \leq Kn$), where the gas is highly rarefied and the flow can modeled using the collisionless kinetic Boltzmann equation.

Because of the low pressures associated with vacuum drying and inner dimensions of the canister, helium is the slip regime. There is a temperature-jump between the solid surfaces and gas in contact with them. This jump acts like a thermal-resistance for heat conduction [7, 10-12]. Hence, the temperature inside the canister is higher during low pressure condition than at normal or atmospheric pressure[13-15].

To model the thermal behavior of the canister during vacuum drying process, the Navier-Stokes equation can be employed subjected to the temperature-jump boundary condition given by [16]

$$T_g' = T_w' + \xi_T \lambda \left.\frac{dT'}{dr'}\right|_w \quad (1)$$

where T_g' is the gas temperature at gas-wall interface, T_w' is the wall temperature, and ξ_T is the temperature jump coefficient [17]. The coefficient ξ_T depends on the gas nature and surface state. Using the Lin and Willis model [**Error! Reference source not found.**], the temperature-jump coefficient ζ_T can be written as

$$\zeta_T = \left(\frac{2-\alpha}{\alpha} + 0.17\right)\frac{\gamma\sqrt{\pi}}{(\gamma+1)Pr} \quad (2)$$

where γ is the specific ratio (5/3 for helium) and Pr is the Prandtl Number (2/3 for helium). It was shown in Ref [18, 19], that the Lin and Willis temperature jump model accurately predicts the temperature jump at the interface gas/solid in the slip regime.

In above equation, α is the thermal accommodation coefficient (TAC) that characterizes how the molecules of gas interact with the walls, and is defined as

$$\alpha = \frac{T_i - T_r}{T_i - T_w} \quad (3)$$

where T_i is the incident temperature of a molecule, T_r is the reflected temperature of a molecule, and T_w is the temperature of the wall [20]. The TAC is affected by the material, roughness, cleanliness, and overall surface conditions of the wall as well as the properties of the gas itself. The value of α ranges from 0 to 1. As the value of α decreases, there is a larger temperature-jump at the solid-gas interface. Values of α are reported in the literature [21, 22]. For helium gas and stainless steel surface, this value was reported between 0.4 and 0.2, for temperature ranging from 25 and 427°C [23]. For helium and zircaloy, a value of α = 0.34 was reported for temperature of 25°C [24]. Recent attempts have been made to predict α for stainless steel and helium[25].

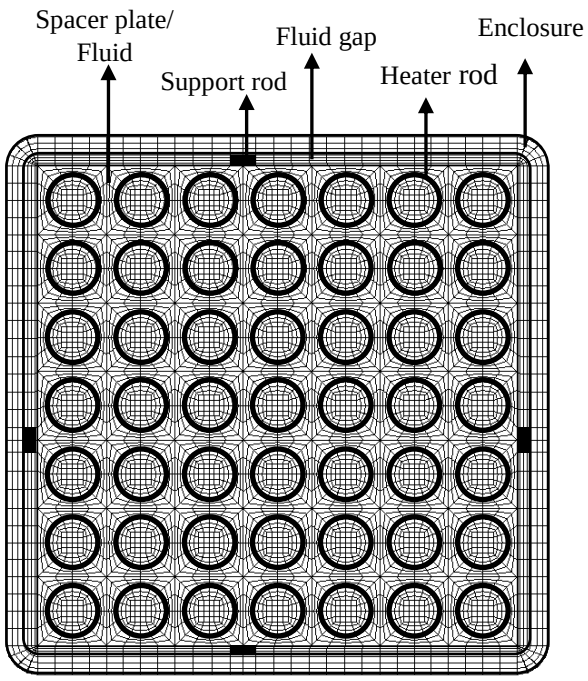

Figure 1: Computational domain in *x-y* plane.

It is important to maintain the temperature of the fuel claddings below 400 °C during vacuum drying [6] to prevent the formation of radial hydrides in the fuel cladding and thus reduce the likelihood of cladding embrittlement [26, 27]. To assure that the cladding temperature is within this limit, over-conservatism in predicting the peak cladding temperature during vacuum drying of canisters is applied. This can lead to unnecessarily long-storage times for the fuel assemblies in the water pool and fewer fuel assemblies being stored in the canister for long-term storage. Hence, an accurate method for predicting the cladding temperature during vacuum drying is necessary.

The long term objective of this work is to develop and experimentally-benchmarked computational fluid dynamics (CFD) models of vacuum drying process that includes the effect of temperature-jump thermal resistance. Similar validation work has been conducted by the authors for pressurized helium conditions [28, 29]. For the benchmark process, a portion of a fuel assembly between two spacer plates and steel basket is considered. An experimental apparatus is constructed using stainless-steel enclosure, electrically heated rods, and two spacer

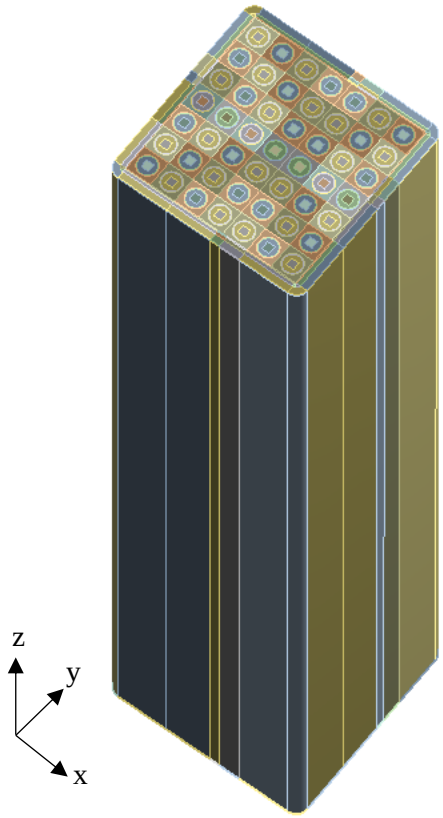

Figure 2: 3D computational domain.

plates. The experiments are conducted for two heat generation rates (Q) of 50 W and 100 W for nine pressures (P) ranging from 10^5 to approximately 50 Pa. The details of the experiment is presented in a separate paper [30]. A geometrically-accurate computational domain of the experimental apparatus is constructed in ANSYS. Numerical simulations are carried out using ANSYS/FLUENT by applying the temperature-jump condition at the gas-surface interfaces to take into account the rarefaction conditions. The numerical simulations were compared to the experimental results for all conditions of heat generation and pressure.

NUMERICAL SIMULATION

Computational Domain

A three-dimensional geometrically-accurate computational mesh representing the experimental apparatus is generated using ANSYS meshing. The domain consists of an enclosure body, heater rods, spacer plates and helium. Figure 1 shows a cross section view of the computational mesh. The outer region represents the stainless steel enclosure. It contains the regions for 49 heater rods which are composed of stainless steel sheath and magnesium oxide core. The darkened circles in this figure represents stainless steel sheaths. Helium gas is modeled in space between the rods and enclosure. The rectangular dark regions on

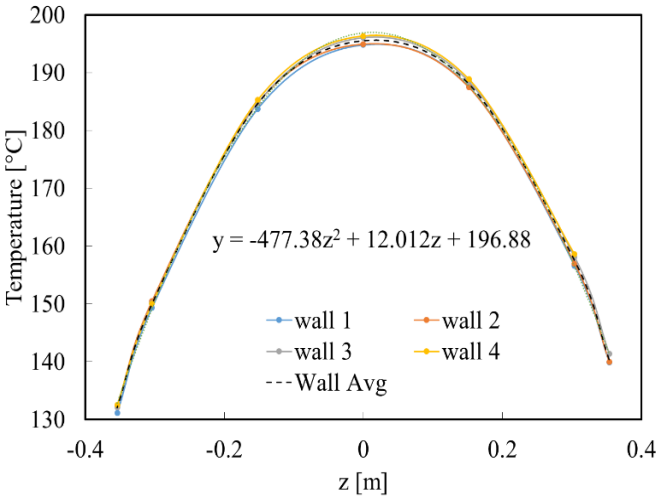

Figure 3: Temperature profile of all four enclosure walls for P = 77 Pa and Q = 100 W

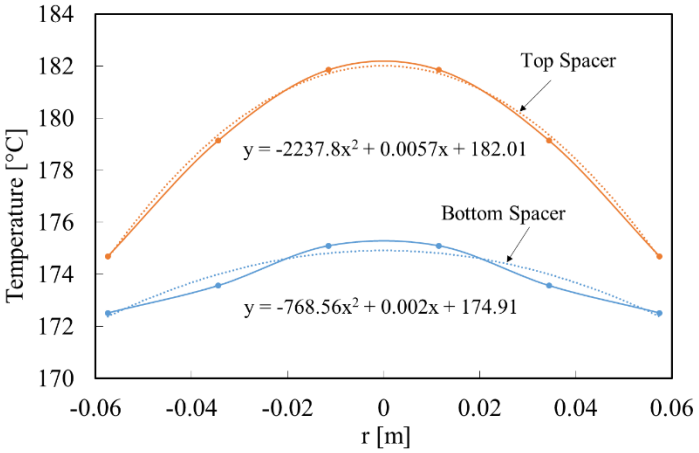

Figure 4: Top and bottom spacer plates temperature profiles as function of distance from plates' center for P = 77 Pa and Q = 100W.

four sides are small part of the support rods that maintain equal gap between spacer plate and enclosure on opposite sides. The mesh is extruded in the z-direction (normal to the plane of the mesh) to form the three-dimensional (3D) mesh. At the end of the extrusion, the properties of 1.5 mm thick regions on both ends are modified to represent two stainless steel spacer plates and small parts of support rod. Figure 2 shows the complete 3D model used in the numerical simulation. The center of the domain is the origin and z = 0 plane is used as the mid-plane. The total number of mesh elements in the domain is 2,180,416 with average orthogonal quality of 0.9.

Temperature dependent material properties are assigned to stainless steel and helium. Heat is generated uniformly along the heater rods. The outer surface of the enclosure and the spacer

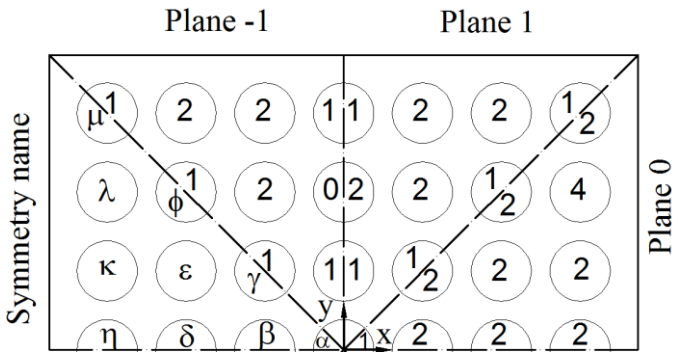

Figure 5: Symmetry groups and number of heater rods with thermocouples in three different axial planes (-1, 0, and 1).

plates use the temperature profile generated from the experimental data as boundary condition.

Conduction, natural convection and radiation heat transfer within the domain are simulated using ANSYS/Fluent. For density of helium, ideal compressible gas is used. The emissivity of the stainless steel used for heater rod, enclosure tube and spacer plates were measured and applied in the simulation. The discrete-ordinate radiation model is used to take into account radiation heat transfer. The steady-state momentum and energy equations are solved using pressure-based solver. The pressure-velocity coupling is achieved by using the SIMPLE scheme and a second order upwind scheme is used for discretization [31].

Temperature-jump boundary condition described by Eq. 1-3 were applied to the gas/solid interfaces using a User Define Function (UDF).

Boundary Condition

The temperatures of the enclosure wall and the spacer plates measured from the experiment are used as boundary condition for the simulations. To get accurate temperature profile of the enclosure wall, 13 thermocouples are installed in each wall [30]. The measurements in all 18 cases show that the deviation of temperatures measured across the wall at same *z* location is less than 1°C. Hence, only the temperatures measured along center of the wall are used as boundary condition. The enclosure temperature profiles are plotted in Fig. 3 for Q = 100 W and P = 77 Pa. To use these profiles as boundary condition, the temperature from four walls are averaged and a second degree polynomial function is generated to fit the data. This polynomial is used as boundary condition for the enclosure wall in CFD simulation. The comparison of wall temperatures at different pressure showed that the variation in wall temperature is insignificant with change in pressure.

Both top and bottom spacer plate temperatures are measured using 14 thermocouples. The temperature profile along the diagonal is used to develop circular temperature profiles for each spacer plate with highest temperature at the center. These

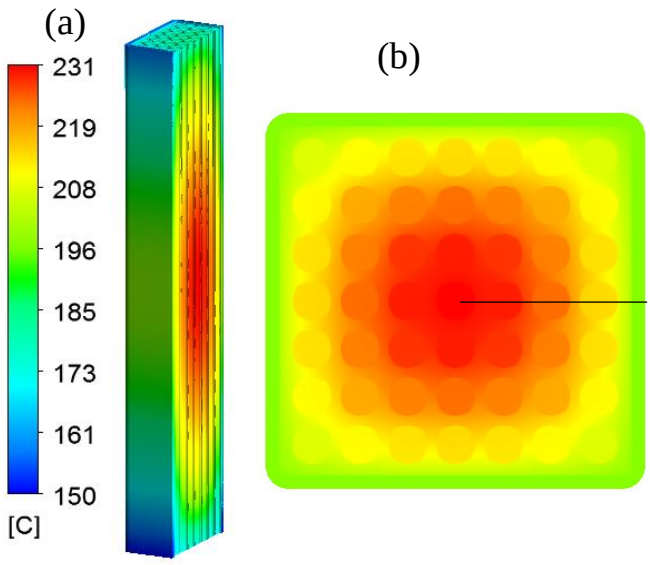

Figure 6: Computational results for P = 77 Pa and Q = 100 W (a) Temperature contour of half domain (b) Temperature contour at mid-plane.

profiles are used as boundary condition in the simulations for both spacer plates. The solid lines with marker in Fig. 4 shows the measured temperature along the diagonal, whereas the dotted lines shows the best polynomial fit lines for the data. These results are shown for the case with Q = 100 W and P = 77 Pa. The equations of the best fit polynomials are used as temperature profile of the spacer plates in simulation.

Symmetry Group

Due to the geometric symmetry and use of same boundary condition on four walls, there is symmetry across *xz* plane, *yz* plane and planes passing through opposite corners of the square enclosure (shown by dashed line in Fig. 5). Hence, only 1/8th portion can completely represent whole computational domain. The detailed description of the use of symmetry to place thermocouple in the heater rods is described in Ref [30]. Figure 5 shows four 1/8th model with name of symmetry group and number of heater rods with thermocouple at same symmetric locations in three different axial planes. There are 10 symmetry groups which are named with Greek letters from α to μ. The three axial planes are z = 0 cm (Plane 0, mid-plane), z = 25 cm (Plane 1) and z = -25 cm (Plane -1).

SIMULATION RESULTS

Figure 6a shows the temperature contour of the computational domain cut by *yz*-plane to show the center of the array for the case P = 77 Pa and Q = 100 W. The central heater rod experiences the maximum temperature of 231 °C at mid-plane, z = 0 cm. Figure 6b shows the cross-sectional temperature

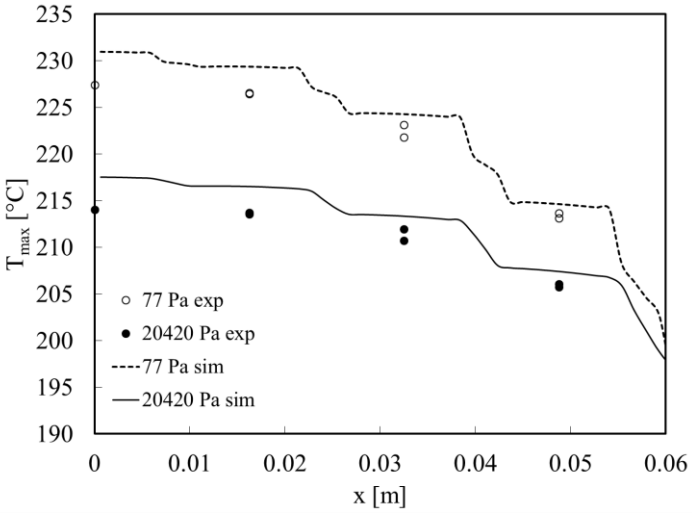

Figure 7: Comparison of temperature along horizontal line in Fig. 3b from simulation and experiment for Q = 100 W.

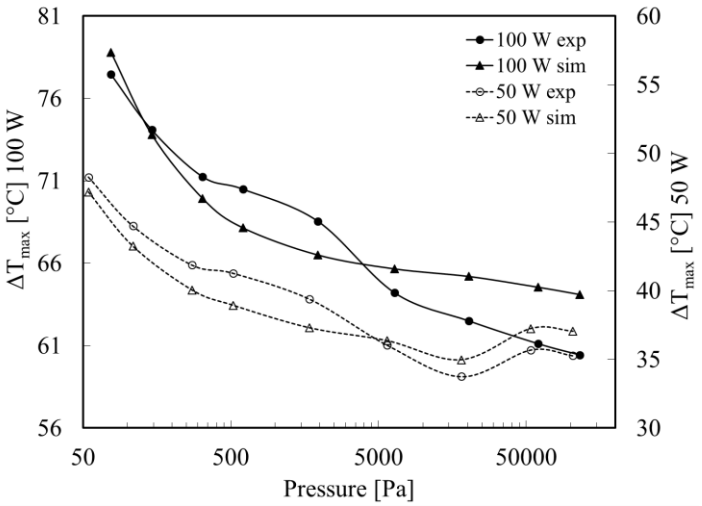

Figure 8: Comparison of maximum temperature from experiment and simulation for Q = 50W and 100W.

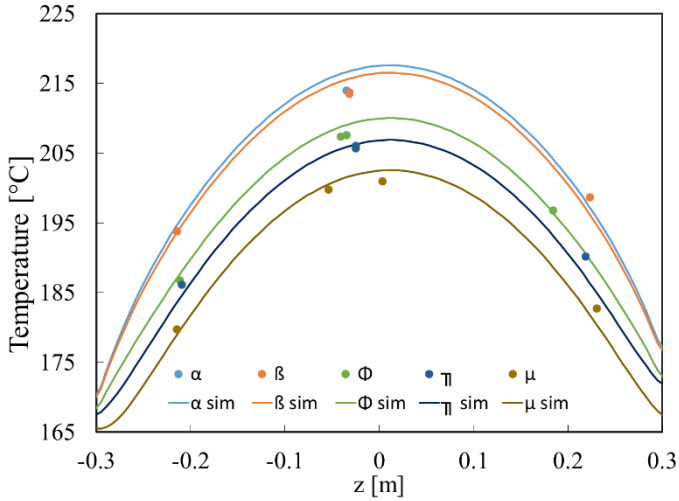

Figure 9: Comparison of simulation and experimental result along 5 symmetry groups for P = 20420 Pa Q = 100 W.

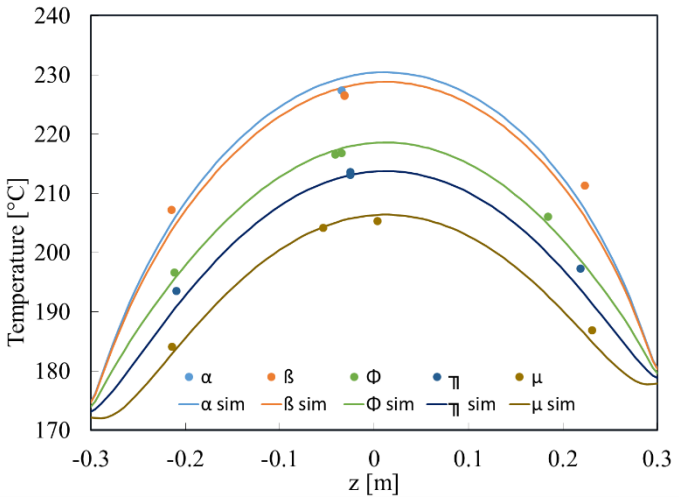

Figure 10: Comparison of simulation and experimental result along 5 symmetry groups for P = 77 Pa and Q = 100 W.

profile at the mid-plane. The temperature is highest at the central region and drops rapidly towards the enclosure wall.

Comparison of experimental and simulation result

Figure 7 shows the temperature profiles along the horizontal line drawn in Fig 6b, for Q = 100 W and for two pressures P = 77 Pa and 20420. The simulation results show that for both pressure values, the temperature gradient is higher near the enclosure wall compared to the center. For almost same enclosure wall temperatures, the maximum temperature obtained for the case P = 77 Pa is 13.4 °C higher than that of P = 20420 Pa case. At pressure of 77 Pa helium is in the slip regime, which causes a temperature jump at the gas/solid interfaces, however, at pressure of 20420 Pa, helium is in the continuum regime (no temperature-jump condition). The temperature jump at the heater rod wall and the enclosure wall can be observed as steep gradient lines for 77 Pa. The circular markers in Fig. 7 shows the experimental results for the heater rods that lie in symmetry group along the horizontal line shown in Fig. 6b. The temperatures obtained from the experimental results are consistently lower than simulation results for both pressure values. However, this is not necessarily the case for all the heater rods. The maximum difference between simulations and experiments in all cases is below 4°C.

Comparison of the maximum temperature from the simulation and experiment for all cases is shown in Fig. 8. The plotted data shows the maximum temperatures obtained from experiments or simulations minus the minimum enclosure wall temperature. The left axis shows the results for the cases Q = 100 W, whereas the right axis shows the results for the case Q = 50

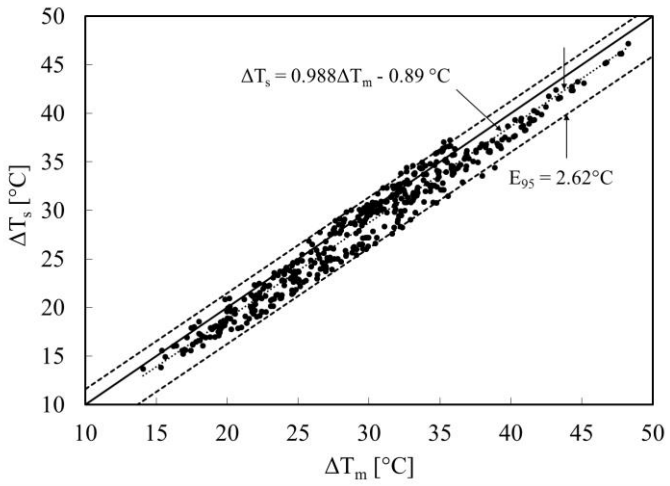

Figure 11: Simulated vs measured temperature for Q = 50 W for all pressures.

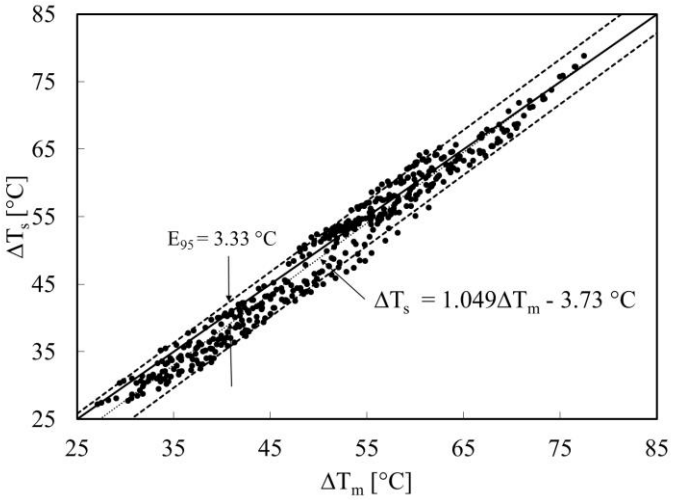

Figure 12: Simulated vs measured temperature for Q = 100W for all pressures

W. The solid lines are for 100 W and the dashed lines are for 50 W. For both heat generations, circular markers represent the experimental results, whereas triangular markers represent the simulation results. The simulation predicts the maximum measured temperature fairly good along all pressures especially for 50 W heat generation rate cases. For Q = 100 W, the maximum difference is 4 °C at higher pressure values. For both heat generation rates, at pressures between 500 and 5000 Pa, there is a 'bump' in the maximum measured temperatures, whereas the simulation results do not show such behavior. This behavior is not well understood. Further investigation will be carried out to explain this behavior.

Since most of the symmetry groups have thermocouples at three axial planes, axial temperature profile can be generated for all the groups from experiment. Figure 9 and 10 compare the axial temperature profiles of few symmetry groups from simulation with experiment for P = 77 and 20420 Pa, respectively with Q = 100 W. The solid lines represent the simulation results whereas the circular markers represent the experimental data. Results for five symmetry groups (α, ß, Φ, η and μ) are shown. The measured axial profile of heater rods correlate well with simulated profile with difference less than 2 °C for most of the heater rods.

The comparisons of measured and simulated results are done for certain symmetry groups and/or at certain locations so far. To see how all the measured temperatures compare to simulated results, direct comparison between simulated and measured temperatures is carried out and is presented in Figs. 11 and 12 for Q = 50 W and 100 W, respectively. The measured temperatures of all 49 heater rods for all 9 pressures (441 points) are presented. The comparison is made between the measured heater rod minus minimum measured wall temperature (ΔT_m) and the simulated heater rod temperature at same location minus minimum measured wall temperature (ΔT_s) for each case. This way, the variation in wall temperature resulted mainly due to variation in the ambient temperature is negated. The temperature differences are as large as 48 °C for Q = 50W and 79 °C for Q = 100 W. The solid line represents $\Delta T_m = \Delta T_s$ and if simulations perfectly recreated the measured data, all the data points would lie on this solid line. The results are scattered in fairly narrow band for both heat generation rates. The dotted lines represent the best linear fit of all the data. The slope (a) and intercept (b) for the case Q = 50W are 0.988 and -0.89 °C, respectively and for Q = 100 W is 1.049 and -3.73 °C.

The scatter of the results above and below the best fit line is an indication of random difference between the simulations and measurements. The estimation of best fit line's random error with 95% confidence level is given by

$$E_{95} = 2\sqrt{\frac{\Sigma(m\Delta T_m + b - \Delta T_s)^2}{N-2}} \quad (4)$$

This summation is carried out for all N = 441 measured values. The value of E_{95} represents the vertical distance from the best fit line that statistically contains 95% of the data. In Figs. 10 and 11, two dashed lines above and below the best fit line should contain 95% of the total data points. For Q = 50W case, E_{95} = 2.62 °C, whereas for Q = 100 W case, E_{95} = 3.33 °C.

The random difference between the measured and simulated temperatures are affected by inaccuracies of the simulations, inaccuracies of the measurements, tolerance in size of different parts and high uncertainty in the location of thermocouple in the heater rods. Considering these inaccuracies, the standard error of estimate for 95% confidence interval given by E_{95} for both Q = 100 and 50 W is fairly low. Thus, the implementation of the temperature jump condition in the CFD simulations was successful.

CONCLUSION

The main objective of this work is to experimentally benchmark CFD simulations of a three-dimensional model of a 7×7 array of heated rods enclosed in a stainless steel square-cross section pressure vessel. The model is relevant a BWR nuclear fuel assembly between two consecutive spacer plates. The numerical model was constructed in ANSYS and simulations were conducted in FLUENT. The description of the experimental apparatus and results were presented in separate paper published in the same conference [30]. A total of 18 experiments were conducted for different pressures and two heat generation rates of 50 W and 100 W. For the numerical simulation, boundary conditions were obtained from experiment for each pressure and heat generation rate.

The comparison between the simulation and experimental results showed that the difference is less than 4°C. The simulations mostly under-predicted the measured temperatures. The maximum increase of temperature caused by the pressure decrease (rarefaction effect) for the case of Q = 100 W, was 13.4 °C from simulation results compared to 15.2°C from experimental results. The direct comparison of all the data points showed that the random errors for 95% confidence interval for 50W is 2.62 °C and for 100 W is 3.33 °C.

ACKNOWLEDGEMENT

This work was supported by the US Department of Energy Office of Nuclear Energy University Program.

REFERENCES

[1] Office of Civilian Radioactive Waste Management (OCRWM), U. S. D. o. E., 1987, "Characteristics of Spent Nuclear Fuel, High-Level Waste, and Other Radioactive Wastes which may Require Long-Term Isolation."

[2] Saling, J. H., and Fentiman, A. W., 2002, Radioactive Waste Management, Taylor and Francis, New York.

[3] International, H., 2010, "HI-STORM 100 FSAR."

[4] Large, W. S., and Sindelar, R. L., 1997, "Review of Drying Methods for Spent Nuclear Fuel," Westinghouse Savannah River Company, report number WSRC-TR-0075, Savannah River Site, Aiken, SC.

[5] Bracey, W., and Smith, P., "Transnuclear drying experience and lessons learned," Proc. ASTM Workshop.

[6] NRC, 2003, "Cladding Considerations for the Transportation and Storage of Spent Fuel," Interim Staff Guidance Report for the Spent Fuel Project Office of the U.S. NRC, ISG-11 R3.

[7] Schaaf, S. A., and Chambre, P. L., 1961, Flow of Rarefied Gases, Princeton University Press, New Jersey.

[8] Bird, G. A., 1983, "Definition of mean free path for real gases," Phys. Fluids, 26(11).

[9] Bird, G. A., 1994, Molecular Gas Dynamics and the Direct Simulation of Gas Flows, Oxford Science Publications.

[10] Sone, Y., and Onishi, Y., "Heat transfer through a rarefied gas between coaxial circular cylinders with large temperature difference," Proc. In Rarefied Gas Dynamics, Proc. 10th Int. Symp.

[11] Sharipov, F., and Bertoldo, G., 2006, "Heat transfer through a rarefied gas confined between two coaxial cylinders with high radius ratio," J. Vac. Sci. Technol. A, 24, p. 2087.

[12] Colmont, D., and Roblin, P., 2008, "Improved thermal modeling of SNF shipping cask drying process using analytical and statistical approaches," Packaging, Transport, Storage & Security of Radioactive Material, 19(3), pp. 160-164.

[13] Manzo, T., Green, R., Hadj-Nacer, M., Greiner, M., Li, J., and Liu, Y., 2014, "Prediction of Cladding Temperatures within a used Nuclear Fuel Transfer Cask Filled with Rarefied Helium," ASME PVPAnaheim, CA.

[14] Hadj-Nacer, M., Manzo, T., Ho, M., Graur, I., and Greiner, M., 2015, "Phenomena Affecting Used Nuclear Fuel Cladding Temperatures during Vacuum Drying Operations," International High Level Radioactive Waste Management Conference.

[15] Hadj-Nacer, M., Manzo, T., Ho, M., Graur, I., and Greiner, M., 2016, "Effects of Gas Rarefaction on Used Nuclear Fuel Cladding Temperatures during Vacuum Drying," Nuclear Technology, 20, pp. 1-13.

[16] Kennard, E. H., 1938, Kinetic Theory of Gases, McGraw-Hill Book Company, Inc., New York.

[17] Kogan, M. N., 1995, Rarefied Gas Dynamics, Springer US.

[18] Hadj-Nacer, M., Maharjan, D., Ho, M., Stefanov, S., Graur, I., and Greiner, M., 2016, "Continuum and Kinetic Simulations of Heat Transfer through Rarefied Gas in Annular and Planar Geometries in the Slip Regime," ASME Journal of Heat Transfer.

[19] Maharjan, D., Hadj-Nacer, M., Ho, M., Stefanov, S., Graur, I., and Greiner, M., 2015, "Simulation of Heat Transfer across Rarefied Gas in Annular and Planar Geometries: Comparison of Navier-Stokes, S-Model and DSMC Methods Results," ASME International Conference Nanochannels, Microchannels and Minichannels (InterPACK/ICNMM2015)San Francisco, California.

[20] Maxwell, J. C., 1878, "On stress in rarefied gases arising from inequalities of temperature," Phil.Trans. R. Soc. Lond.,, 170, pp. 231–256.

[21] Goodman, F. O., 1980, "Thermal Accommodation Coefficients," J. Phys. Chem., 84, pp. 1431-1445.

[22] Song, S., and Yovanovich, M. M., "Correlation of thermal accommodation coefficient for 'engineering' surfaces," Proc. Proceedings of the Twenty-fourth ASME National Heat Transfer Conference.

[23] Trott, W. M., Castañeda, J. N., Torczynski, J. R., Gallis, M. A., and Rader, D. J., 2011, "An experimental assembly for precise measurement of thermal accommodation," Review of scientific instruments, 82(035120).

[24] Thomas, L., and Loyalka, S., 1982, "Determination of Thermal Accommodation Coefficient of Helium, Argon,

and Xenon on a Surface of Zircaloy-2 at about 25 C," Nuclear Technology, 57(2), pp. 213-219.
[25] Green, R., Hadj-Nacer, M., and Greiner, M., 2015, "Design of an Experiment to Measure the Thermal Accommodation Coefficient between Helium and Stainless-Steel in Concentric Cylinders," ASME PVPBoston MA.
[26] Daum, R. S., Majumdar, S., Liu, Y. Y., and M.C., B., 2006, "Radial-hydride Embrittlement of High-burnup Zircaloy-4 Fuel Cladding," J. Nucl. Sci. Tech., 43(9), pp. 1-14.
[27] Daum, R. S., Majumdar, S., and Billone, M. C., 2008, "Experimental and Analytical Investigation of the Mechanical Behavior of High-Burnup Zircaloy-4 Fuel Cladding," J. ASTM Intern., 5(5).
[28] Maharjan, D., Hadj-Nacer, M., Chalasani, N., and Greiner, M., 2016, "Experimentally Benchmarked Computational Fluid Dynamics Simulations of an Array of Heated Rods within a Square-Cross-Section Helium-Filled Pressure Vessel," ASME PVP ConferenceVancouver, BC.
[29] Maharjan, D., Hadj-Nacer, M., Chalasani, N., and Greiner, M., 2017 (Under review), "Experimental Validation of Heat Transfer Simulations for a Vertical Heated Rod Array within a Square-Cross-Section, Helium-Filled Isothermal Enclosure," ASME Journal of Thermal Science and Engineering Applications.
[30] Maharjan, D., Hadj-Nacer, M., and Greiner, M., "Temperature measurement of an array of heated rods subjected to vacuum drying conditions," Proc. PVP2017, ASME.
[31] Inc., A., 2015, "ANSYS Fluent User's Guide," www.ansys.com.